Galaxy Dancers : a dynamical study of globular star clusters

Eduardo Farinazzo Vitral

École doctorale n° 127:
Astronomie et Astrophysique d'Ile de France

Doctorat à l'Institut d'astrophysique de Paris

THÈSE

pour obtenir le grade de docteur délivré par

Sorbonne Université

Spécialité doctorale "Astrophysique"

présentée et soutenue par

EDUARDO FARINAZZO VITRAL

le 8 septembre 2022

GALAXY DANCERS:
A DYNAMICAL STUDY OF GLOBULAR STAR CLUSTERS

Directeur de thèse : **Gary A. Mamon**

Jury

M^me. **Françoise Combes,**	Observatoire de Paris	Présidente
M. Denis Erkal,	University of Surrey	Rapporteur
M. Rodrigo Ibata,	Observatoire de Strasbourg	Rapporteur
M^me. **Paola Di Matteo,**	Observatoire de Paris	Examinatrice
M. Eugene Vasiliev,	University of Cambridge	Examinateur
M^me. **Natalie Webb,**	Université Toulouse III - Paul Sabatier	Examinatrice

Institut d'astrophysique de Paris
UMR CNRS 7095, PARIS, France

The cosmos is within us. We are made of star-stuff.
We are a way for the universe to know itself.

— Carl Sagan

To Nina, my forever shining star.

ABSTRACT

Globular clusters are roughly spherical collections of $10^5 - 10^7$ stars, that orbit a host galaxy. Very old, with typical ages similar to the one of their hosts, these dense clusters hold many interesting aspects that make them a great laboratory to study astrophysics. For instance, their dense environment contributes to increased dynamical interactions between its stars, sometimes giving birth to exotic objects like black holes with masses within the pair-instability gap, cataclysmic variables and pulsars. Their continuous tidal interactions with their host galaxy might also produce long and prominent stellar streams that tell much about the past dynamical history of themselves, and of their host. Other aspects such as different chemical populations and the fact that there is still no consensus on how globular clusters were formed makes the study of these sources challenging and exciting.

Given the interesting possibilities that globular clusters offer to learn physics, this thesis was focused in understanding and modelling their internal and external dynamical interactions, using both simulations and state-of-the-art data from the *Hubble Space Telescope* (*HST*) and the *Gaia* astrometric mission. I have analysed aspects such as core-collapse, tidal interactions and mass segregation, how they can be measured from data and how they influence different aspects of stellar and orbital evolution.

Among the noteworthy accomplishments of this thesis, it is important to mention (1) the improvements in data modelling concerning density profiles, proper motion measurements and Jeans kinematic modelling; (2) the detection of sub-clusters of stellar remnants in the cores of nearby globular clusters, which might be associated to exquisite events like fast radio bursts, compact object mergers, and gravitational waves; and (3) the presentation of new constraints on globular cluster formation scenarios, especially the one pertaining the presence of a dark matter mini-halo. The results obtained over the course of this work and the methods that I developed will contribute to the overall effort to better understand the internal and external evolution of globular clusters, and to make the best use of large astrometric data sets like *Gaia* and *HST*, and in the future, the *James Webb Space Telescope* and the *Nancy Grace Roman Space Telescope*.

RÉSUMÉ / SOMMAIRE

À première vue, les amas globulaires peuvent en effet sembler des sources simples : non seulement leur symétrie sphérique permet une modélisation plus simple que les structures en forme de disque ou irrégulières, mais ce sont aussi des systèmes très anciens[1], impliquant probablement des populations stellaires d'à peu près le même âge. Cependant, de nombreuses découvertes récentes ont perturbé cette vision classique des amas globulaires, et révélé de nombreuses particularités liées à leur morphologie et leur composition. Plus précisément, de nombreux amas globulaires semblent avoir de longs bras de marée en raison de leurs interactions de marée avec leur galaxie hôte (e.g., Ibata et al., 2019; Ibata et al., 2021), ensemble avec une ellipticité relativement élevée, s'écartant ainsi d'une représentation sphérique idéale. De plus, depuis l'étude de Carretta et al., 2009a, la séparation des première et deuxième générations stellaires dans les amas globulaires est largement acceptée, de sorte que la définition d'un amas globulaires a été mise à jour pour inclure leurs anti-corrélations parmi les abondances d'éléments légers, impliquant des populations stellaires de composition chimique différente (voir Gratton et al. 2019 pour une revue). Comme si cela ne suffisait pas, les amas globulaires font également partie des environnements les plus dynamiques de l'Univers. Leurs densités internes très élevées permettent de nombreux effets dynamiques tels que la ségrégation de masse (e.g., Goldsbury, Heyl, and Richer, 2013), l'effondrement du noyau (Lynden-Bell and Wood, 1968) et les fusions successives (Portegies Zwart et al., 1999), qui peuvent aider à leur tour la formation d'objets compacts (Bhattacharya and van den Heuvel, 1991), accélèrent l'évolution stellaire (Bailyn, 1995) et produisent des sources astronomiques exquises, telles que des trous noirs de masse intermédiaire (ci-après, IMBH ; voir González et al. 2021).

Enfin, il n'y a pas de consensus sur la façon dont les amas globulaires sont formés. Peebles, 1984 a proposé un scénario de formation dans lequel les amas globulaires se forment à l'intérieur de leur propre mini-halo de matière noire (comme les galaxies), mais ils pourraient également se former sous forme de nuages de gaz liés (Peebles and Dicke, 1968), sous forme de fragments de galaxies (par exemple, Searle and Zinn 1978; Abadi, Navarro, and Steinmetz 2006), en tant que reliques de jeunes amas massifs (Portegies Zwart, McMillan, and Gieles 2010a; Longmore, Kruijssen, Bastian, Bally, Rathborne, Testi, Stolte, Dale, Bressert, and Alves 2014) formés dans l'Univers à décalage vers le rouge élevé (Kruijssen, 2014; Kruijssen, 2015), ou en tant que débris d'un disque galactique après des événements de fusion (scénario *in-situ*). Dans l'ensemble, plus nous en découvrons sur les amas globulaires, plus nous réalisons qu'ils cachent de nombreux secrets encore à résoudre.

Compte tenu de ce vaste champ de possibilités d'étudier l'astrophysique qu'offrent les amas globulaires, ma thèse s'est donc concentrée sur la com-

1 Les amas globulaires ont des âges typiques allant jusqu'à $\sim$ 13 Gyr (par exemple, Marin-Franch et al., 2009), ce qui est cohérent avec le fait que beaucoup d'entre eux se sont formés avant la réionisation.

préhension des processus dynamiques propres aux amas globulaires. Grâce à de nouveaux outils de modélisation, de traitement de données et de simulations, cela nous a permis, espérons-le, de mieux comprendre comment ils se sont formés, comment ils sont connectés à une image plus large de la formation des galaxies et comment leur dynamique interne est liée à la présence de sources compactes. Dans ce qui suit, je détaille les grandes lignes de ce manuscrit, qui résume mon travail au cours des trois dernières années. Ils servent de guide au lecteur pour mettre les chapitres suivants en contexte.

- **Déprojection du profil de Sérsic** : la déprojection analytique du modèle de densité de Sérsic (Sérsic, 1963; Sersic, 1968) en trois dimensions implique des fonctions mathématiques compliquées généralement non disponibles dans les routines classiques de modélisation de masse, ou dans les langages de logiciels communes. Pour mieux modeliser la structure interne des amas globulaires, nous avons dérivé dans Vitral and Mamon, 2020 une approximation analytique de cette déprojection en considérant un ajustement polynomial d'ordre 10 dans une vaste gamme de rayons de Sérsic (R_e) et d'indices (n) . Notre approximation présente, à cette date, les erreurs relatives les plus faibles par rapport à la véritable déprojection (dans la vaste région $R_e \times n$ que nous avons analysée), parmi d'autres modèles présents dans la littérature, et était particulièrement mieux adaptée pour des indices de Sérsic faibles, qui concordent mieux avec les profils de densité de la plupart des amas globulaires.

- **Détection d'une population de rémanents stellaires dans NGC 6397** : les amas globulaires devraient contenir de nombreux rémanents stellaires dans leur noyau, compte tenu des masses plus élevées de ces derniers et de l'équipartition de l'énergie. En particulier, le deuxième amas globulaire le plus proche de nous, NGC 6397, a vu son budget de masse analysé plusieurs fois (Heyl et al., 2012; Watkins et al., 2015; Baumgardt, 2017), avec un travail récent de Kamann et al., 2016 revendiquant la détection d'un trou noir de masse intermédiaire de masse 600 ± 200 $M_\odot$. Dans Vitral and Mamon, 2021, nous avons analysé cet amas avec des données de mouvement propres de *Gaia* et *HST*, et avons détecté un excès de masse interne similaire à celui de Kamann et al., 2016, mais étendu jusqu'à quelques pour cent du rayon de l'échelle lumineuse de l'amas, plutôt qu'une masse ponctuelle attendue pour un trou noir de masse intermédiaire. Cet ouvrage[2] a attribué cette masse à un compact sous-amas de rémanents stellaires, et a proposé que sa masse puisse être dominée par des trous noirs de masse stellaire, sur la base d'hypothèses simples sur la fonction de masse initiale. Dans Vitral et al., 2022, cet amas a été ré-analysé et une masse excédentaire interne a de nouveau été solidement ajustée comme une population sombre étendue, qui cette fois a été contrainte d'être composée de centaines de naines blanches massives, à l'aide de modèles plus réalistes (Modèles évolutifs de Monte Carlo). Ceci est cohérent avec ce qui est attendu des amas globulaires ayant subi un effondrement de cœur (e.g., Rui et al., 2021b; Kremer et al., 2021).

2 L'ouvrage de Vitral and Mamon, 2021 a également fait l'objet de nombreux communiqués de presse, dont la *NASA/ESA* et le *New York Times*.

- **Détection d'une population de rémanentes stellaires dans NGC 3201** : Comme mentionné ci-dessus, des groupes de rémanentes stellaires dans les noyaux d'amas globulaires peuvent être attendus. En particulier, si la densité initiale de l'amas n'était pas trop grande, on peut s'attendre à des échelles de temps dynamiques plus élevées (c'est-à-dire $\gtrsim$ 10 Gyr) pour l'éjection de trous noirs de masse stellaire au moyen d'interactions dynamiques. L'amas globulaire NGC 3201, étant un amas moins dense, est particulièrement bien adapté à la recherche de trous noirs, avec une détection préalable de trous noirs individuels (Strader et al., 2012; Giesers et al., 2018; Giesers et al., 2019) et de nombreuses simulations indiquant la présence d'une population de trous noirs conséquente (Kremer et al., 2019a; Weatherford et al., 2020). En Vitral et al., 2022, nous avons effectué une modélisation Jeans de cet amas et contraint une population de trous noirs d'environ 1000 $M_\odot$, avec un rayon d'échelle d'environ 0,1 pc, en trouvant des correspondances remarquables entre nos ajustements des données *Gaia* et *HST* aux modèles Monte Carlo du logiciel `CMC` (Rodriguez et al., 2022).

- **Nouvelles méthodes de modélisation de Jeans pour l'ajustement des données** : la modélisation de la masse de Jeans reste l'une des méthodes les plus fiables pour mesurer la masse de systèmes sphériques isolés non rotatifs, auxquels les amas globulaires sont généralement des analogues raisonnables. Dans cette thèse, l'ancienne version du code de modélisation de Jeans MAMPOSSt (Mamon, Biviano, and Boué, 2013), initialement conçue pour gérer les données de ligne de visée, a été améliorée pour tenir compte des mouvements propres (Mamon & Vitral en prép.) à partir des catalogues astrométriques de pointe *Gaia* et *HST*. Les nouvelles équations de ce logiciel ont été utilisées dans Vitral and Mamon, 2021; Vitral et al., 2022 pour dévoiler la dynamique interne des amas globulaires proches. De plus, de nouvelles méthodes ont été proposées pour contraindre différents modèles de masse et la composition des masses non lumineuses provenant des rémanentes stellaires. En particulier, l'utilisation d'ensembles de données virtuels construits avec AGAMA pour sélectionner entre différents modèles de masse et l'utilisation de modèles `CMC` Monte Carlo pour démêler la composition des sous-amas de restes stellaires (par exemple, est-ce composés de trous noirs, de naines blanches ou d'autres objets ?) ont d'abord été employés, simultanément, dans Vitral et al., 2022.

- **Nouvelle description du scénario de formation de matière noire pour les amas globulaires** : Il n'y a pas de consensus sur la façon dont les amas globulaires se sont formés, et il est probable qu'ils partagent différents scénarios de formation. Dans cette thèse, j'ai étudié le scénario où ils se forment à l'intérieur de leurs propres mini-halos de matière noire (comme les galaxies dans un cadre ΛCDM), initialement proposé par Peebles, 1984. Le travail présenté dans Vitral and Boldrini, 2022 rejoint les tentatives précédentes de Mashchenko and Sills, 2005 et Peñarrubia et al., 2017 pour contraindre les différences entre les amas globulaires formés à l'intérieur des mini-halos de matière noire et ceux qui ne l'étaient pas. Nous avons montré avec des simulations de N-corps qu'initialement, le mini-halo de matière noire se comporte comme un bouclier dynamique,

en étant dépouillé avant de l'amas d'étoiles, et le protégeant ainsi des effets de marée. Un tel mécanisme de blindage pourrait en effet expliquer pourquoi certains amas semblent moins affectés par les marées que ce à quoi on pourrait s'attendre dans le scénario où seule la matière baryonique est considérée. Dans Boldrini and Vitral, 2021, nous avons montré en comparant les simulations avec les données de *Gaia* qu'en fait, NGC 6397 semble appartenir à cette catégorie, avec des empreintes de marée observées beaucoup plus petites que ce que prédisaient nos simulations sans matière noire.

Ce manuscrit se compose de trois parties (une quatrième étant les annexes), avec un total de neuf chapitres. La première partie, qui comprend les chapitres 1, 2, 3 et 4, est destinée à donner au lecteur un contexte général de l'astrophysique impliquée dans mon travail, ainsi que les instruments et ensembles de données que j'ai utilisés. La deuxième partie, du chapitre 5 à 7, vise à expliquer les méthodes que j'ai utilisées pour analyser les données des amas globulaires, ce qui inclut également ma propre contribution pour améliorer les outils utilisés dans ces analyses. Enfin, la troisième et dernière partie, avec les chapitres 8 et 9, apporte les principaux résultats concernant la modélisation en masse de Jeans de la dynamique interne de NGC 6397 et NGC 3201, et concernant les empreintes dynamiques du scénario de formation de matière noire des amas globulaires.

- **Chapitre 1 : Introduction** : Ce chapitre vise à fournir une brève définition des amas globulaires et à motiver le lecteur à poursuivre les prochains chapitres. Il se termine en résumant les principaux points saillants de la thèse, pour le contexte, ainsi qu'en posant le format du manuscrit.

- **Chapitre 2 : Évolution stellaire** : je présente les principaux aspects de l'évolution stellaire qui concernent la physique des amas globulaires, avec un accent particulier sur la description des objets compacts, qui seront évoqués plus en détail au chapitre 8. Je commente également les différentes populations stellaires trouvées dans les amas globulaires, y compris le phénomène de populations chimiques multiples (Gratton et al., 2019).

- **Chapitre 3 : Processus dynamiques** : J'ai mis en scène les principaux processus dynamiques qui régissent la cinématique interne des amas globulaires, ainsi que leur cinématique externe, résultat de leur statut satellitaire, plongé dans le champ de marée de leur galaxie hôte. Une attention particulière est accordée au phénomène de core-collapse, qui est d'une grande importance pour la discussion du chapitre 8.

- **Chapitre 4 : Instruments & Données** : Je présente et commente les jeux de données et les logiciels que j'ai utilisés tout au long de mon travail, en précisant l'apport et la situation où chacune de ces données était nécessaire.

- **Chapitre 5 : Profils de densité** : ce chapitre introduit les nombreux profils de densité de la littérature que j'ai utilisés pour modéliser la dynamique des amas globulaires, ainsi qu'une éventuelle problématique qui leur est

associée (en particulier, la déprojection des Profil Sérsic dérivé de Vitral and Mamon 2020). Elles sont d'une extrême importance pour les équations du Chapitre 7, ainsi que pour les résultats du Chapitre 6.

- **Chapitre 6 : Astrométrie & Photométrie** : J'explique les principaux outils astrométriques et photométriques que j'ai codés dans BALRoGO, et je fournis l'application de ces outils à plus d'une centaine d'amas globulaires de la Voie lactée, et neuf naines sphéroïdales du groupe local, ainsi qu'une discussion sur la robustesse de ces méthodes. Ce chapitre résume les principaux résultats présentés dans Vitral, 2021 et les sujets mineurs de mes autres travaux.

- **Chapitre 7 : Masse & Anisotropie Modélisation** : ce chapitre présente le formalisme mathématique derrière la routine de modélisation de masse de MAMPOSSt-PM, le logiciel que j'ai utilisé et aidé à développer (cf., Mamon & Vitral en prép.) pendant ma thèse. Ce formalisme a été appliqué aux données astrométriques des amas globulaires proches, comme mentionné au chapitre 8.

- **Chapitre 8 : Cimetières stellaires** : Je présente ici les analyses et les résultats de Vitral and Mamon, 2021 et Vitral et al., 2022, concernant l'agrégation des restes stellaires dans les cœurs des amas globulaires NGC 6397 et NGC 3201.

- **Chapitre 9 : Sur l'origine des amas globulaires** : ce chapitre vise à résumer les principales caractéristiques d'un système d'amas globulaires qui s'est formé à l'intérieur d'un mini-halo de matière noire et subit un champ de marée, comme présenté dans Vitral and Boldrini, 2022. La dernière partie de ce chapitre présente brièvement les résultats de Boldrini and Vitral, 2021, qui plaident en faveur de ce scénario de formation.

PUBLICATIONS

As of August 2022.

Refereed publications:

Properties of globular clusters formed in dark matter mini-halos
Vitral E., Boldrini P., 2022, Link: A&A, in press

Stellar graveyards: clustering of compact objects in globular clusters NGC 3201 and NGC 6397
Vitral E., Kremer K., Libralato M., Mamon G. A., Bellini A., 2022,
Link: MNRAS, 514, 806

Absence of obvious tidal tails around the globular cluster NGC 6397
Boldrini P., **Vitral E.**, 2021, Link: MNRAS, 507, 1814

BALRoGO: Bayesian Astrometric Likelihood Recovery of Galactic Objects – Global properties of over one hundred globular clusters with Gaia EDR3
Vitral E., 2021, Link: MNRAS, 504, 1355

Does NGC 6397 contain an intermediate-mass black hole or a more diffuse inner subcluster?
Vitral E., Mamon G. A., 2021, Link: A&A, 646, A63

A precise analytical approximation for the deprojection of the Sérsic profile
Vitral E., Mamon G. A., 2020, Link: A&A, 635, A20

Publications in preparation:

Vitral E., Libralato M., Kremer K., Mamon G., Bellini A., Bedin L., Anderson J.

Mamon G. A., **Vitral E.**

It is the time you have wasted for your rose that makes your rose so important.

— Antoine de Saint-Exupéry, The Little Prince.

ACKNOWLEDGEMENTS

Sam: *"This is it."*

Frodo: *"What?"*

Sam: *"If I take one more step, I'll be the farthest away from home I've ever been."*

Frodo: *"Come on, Sam. Remember what Bilbo used to say: 'It's a dangerous business, Frodo, going out your door. You step onto the road, and if you don't keep your feet, there's no telling where you might be swept off to.' "*

— Jackson, Peter (2001). The Lord of the Rings: The Fellowship of the Ring. New Line Cinema.

I am not sure if my journey towards here started when I was first presented to the alien worlds of *Star Wars*, or when I found an astronomy book about the Solar System lost in my grandmother's library to discover that other planets have different sizes, compositions and year lengths, or finally if it was when I left home in my 17s to pursue my dream of studying in a high quality university, leaving my friends and family behind. The truth is that, as much as the end of this journey, which I have no idea where it will be, the beginning is also not that important. What matters most is whom I spent this journey with, and how it shaped who I am. Here, I shall make the hopeless effort of thanking the many people that participated in my path towards getting a Ph.D., with the ambition that at least, I might get a glimpse of a smile from them.

[Continuation provided in the printed version...]

CONTENTS

LIST OF FIGURES

LIST OF TABLES

Part I

CONTEXT: GLOBULAR CLUSTERS

1 INTRODUCTION

This nebula is beautiful & round.

— Charles Messier's notes on M10 (Messier, 1781)

1.1 HISTORY & PRESENT

1.1.1 *First impressions*

At first, globular clusters were perceived as bright nebulae, with no stars. For instance, in his famous catalog, Charles Messier (Messier, 1781) stated, while commenting on the source M22:

(June 5, 1764) *"Nebula, below the ecliptic, between the head and the bow of Sagittarius, near a star of 7th magnitude, 25 Sagittarii, according to Flamsteed, this nebula is round, it doesn't contain any star, & one can see it very well in an ordinary telescope of 3.5-foot [FL];"*

Indeed, M22 was probably the first globular cluster discovered[1], being misinterpreted as a star-less nebulae, and not only later, globular clusters were constrained to be large, round collections of stars. It was William Herschel who coined the term *globular cluster* (hereafter, GC), in his *Catalogue of Nebulae and Clusters of Stars* (Herschel, 1786), by which time, the perception of them being star clusters was already accepted. Today, GCs are generally defined as spherically shaped collections of roughly $10^5 - 10^7$ stars, having very high inner densities[2], and orbiting a host galaxy. Our Milky Way galaxy has itself more than 150 known GCs (e.g., Gaia Collaboration et al., 2018a), with probably more still undetected. Figure 1 displays an image of Omega Centauri, the most massive GC in the Milky Way.

1.1.2 *A second glance*

After a first glance, GCs may indeed seem simple sources: Not only spherical symmetry allows for more straightforward modelling than disc-shaped or irregular structures, but they are also very old systems[3], likely implying quasi coeval stellar populations. However, many recent findings perturbed this classic vision of GCs, and revealed many particularities related to their morphology and composition. Specifically, many globular clusters seem to have long

1 Abraham Ihle, a German amateur astronomer, discovered it in 1665, while observing Saturn (Messier, 1781).

2 The densest GCs have inner densities as much as $\sim 10^6$ times greater than what is observed in our solar neighbourhood (McKee, Parravano, and Hollenbach, 2015).

3 GCs have typical ages up to $\sim$ 13 Gyr (e.g., Marin-Franch et al., 2009), which is consistent with many of them being formed before re-ionisation.

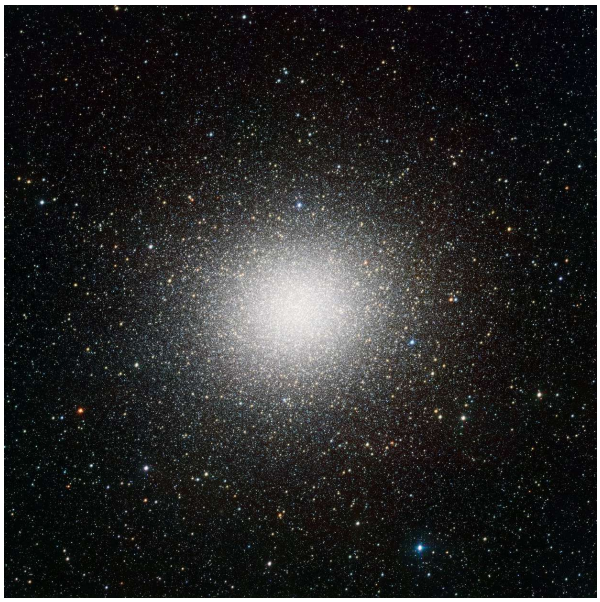

Figure 1: *Globular cluster:* Image from the globular cluster Omega Centauri. Credit: ESO/INAF-VST/OmegaCAM. Acknowledgement: A. Grado, L. Limatola/INAF-Capodimonte Observatory.

stellar streams as a result of their tidal interactions with their host galaxy (e.g., Odenkirchen et al., 2001; Ibata et al., 2019; Ibata et al., 2021), altogether with relatively high ellipticity[4], thus departing from an ideal spherical representation. Moreover, since the study from Carretta et al., 2009a, the separation of first and second stellar generations in GCs is wildly accepted, such that the definition of a GC has been updated to include their anti-correlations among the abundances of light-elements, implying stellar populations of different chemical composition (see Gratton et al. 2019 for a review). On top of that, GCs are also among the most dynamically active environments in the Universe. Their very high inner densities allow for many dynamical effects such as mass-segregation (e.g., Goldsbury, Heyl, and Richer, 2013), core-collapse (Lynden-Bell and Wood, 1968) and runaway mergers (Portegies Zwart et al., 1999), which can in turn propel compact object formation (Bhattacharya and van den Heuvel, 1991), accelerate stellar evolution (Bailyn, 1995) and produce exquisite astronomical sources, such as intermediate-mass black holes (hereafter, IMBHs; see González et al. 2021).

Finally, there is no consensus on how GCs are formed. Peebles, 1984 proposed a formation scenario where GCs are formed inside their own dark matter mini-halo (such as galaxies), but they could also be formed as bound gas clouds (Peebles and Dicke, 1968), as galaxy fragments (e.g., Searle and Zinn 1978; Abadi, Navarro, and Steinmetz 2006), as relics of young massive clusters (Portegies Zwart, McMillan, and Gieles 2010a; Longmore, Kruijssen, Bastian, Bally, Rathborne, Testi, Stolte, Dale, Bressert, and Alves 2014) formed in the high-redshift Universe (Kruijssen, 2014; Kruijssen, 2015), or as debris from the

4 Also referred to as flattening. Throughout the manuscript, we shall use "ellipticity", defined as $e = \sqrt{1-(b/a)^2}$, where b and a are the semi-minor and semi-major axes of the projected stellar distribution.

galactic disc after merger events (*in-situ* scenario). All in all, as more we discover about GCs, more we realise that they hide many secrets yet to be solved.

Given this vast realm of possibilities to study astrophysics that GCs offer, my thesis has thus focused on understanding the dynamical processes respective to GCs. By means of new modelling tools, data handling and simulations, it has hopefully led us to a better grasp on how they were formed, how are they connected to a broader galaxy formation picture, and how their inner dynamics relates to the presence of compact sources. In the following, I detail the outline of this manuscript, which summarises my work during the past three years.

1.2 THESIS OVERVIEW

1.2.1 *Main results*

Below, I summarise the highlights of the work I performed in these three years, which are thoroughly explained in more detail throughout this manuscript. They serve as a guide for the reader to put the further chapters into context.

- **Deprojection of the Sérsic profile**: The analytical deprojection of the Sérsic density model (Sérsic, 1963; Sersic, 1968) into three dimensions involves complicated mathematical functions usually not available in classic mass-modelling routines, or common software languages. In order to better model the internal structure of globular clusters, we derived in Vitral and Mamon, 2020 an analytical approximation to this deprojection by considering a 10-th order polynomial fit in a vast range of Sérsic radii (R_e) and indices (n). Our approximation presented the lowest relative errors compared to the true deprojection (in the broad $R_e \times n$ region we analysed), among other models present in the literature, and was particularly better suited for lower Sérsic indices, which mimic better the density profiles of most globular clusters.

- **Detection of a population of stellar remnants in NGC 6397**: Globular clusters are expected to hold many stellar remnants in their cores, given to the latter's higher masses and to equipartition of energy. In particular, the second closest globular cluster to us, NGC 6397, had its mass budget analysed several times (Heyl et al., 2012; Watkins et al., 2015; Baumgardt, 2017), with a recent work by Kamann et al., 2016 claiming the detection of an intermediate-mass black hole of mass 600 ± 200 $M_\odot$. In Vitral and Mamon, 2021, we analysed this cluster with proper motion data from *Gaia* and *HST*, and detected a similar inner excess mass than Kamann et al., 2016, but extended up to a few percent of the cluster luminous scale radius, rather than a point-like mass expected for an intermediate-mass black hole. This work[5] assigned this mass to a compact sub-cluster of stellar remnants, and proposed that its mass could be dominated by stellar-mass black holes, based in simple assumptions on the initial mass function. In Vitral et al., 2022, this cluster was re-analysed and an inner excess mass was again robustly fitted as an extended dark population,

5 The work from Vitral and Mamon, 2021 was also subject of many press releases, including one in *NASA/ESA* and in one the *New York Times*.

which this time was constrained to be composed of hundreds of massive white dwarfs, with the help of realistic Monte Carlo N-body evolutionary models. This is consistent with what is expected from globular clusters having experienced core-collapse (e.g., Rui et al., 2021b; Kremer et al., 2021).

- **Detection of a population of stellar remnants in NGC 3201**: As mentioned above, groups of stellar remnants in the cores of globular clusters can be expected. In particular, if the cluster's initial density was not too great, one can expect higher dynamical timescales (i.e., $\gtrsim$ 10 Gyr) for the ejection of stellar-mass black holes by means of dynamical interactions. The globular cluster NGC 3201, being a lesser dense cluster, is particularly well suited to search for black holes, with previous detections of individual black holes (Strader et al., 2012; Giesers et al., 2018; Giesers et al., 2019) and many simulations indicating the presence of a consequent black hole population (Kremer et al., 2019a; Weatherford et al., 2020). In Vitral et al., 2022, we performed Jeans modelling of this cluster and constrained a black hole population of roughly 1000 $M_\odot$, with a scale radius of roughly 0.1 pc, by finding remarkable matches between our fits from *Gaia* and *HST* data to the Monte Carlo models from the `CMC` software (Rodriguez et al., 2022).

- **New methods of Jeans modelling for data fitting**: Jeans mass modelling remains one of the most reliable methods to measure the mass of non-rotating, isolated spherical systems, to which globular clusters are generally reasonable analogues. In this thesis, the former version of the Jeans modelling code MAMPOSSt (Mamon, Biviano, and Boué, 2013), originally crafted to handle line-of-sight data, was improved to account for proper motions (Mamon & Vitral in prep.) from the state-of-the-art *Gaia* and *HST* astrometric catalogues. The new equations from this software were employed in Vitral and Mamon, 2021; Vitral et al., 2022 to unveil the internal dynamics of nearby globular clusters. In addition, new methods were proposed to constrain different mass models and the composition of non-luminous masses coming from stellar remnants. In particular, the use of mock data sets constructed with AGAMA (Vasiliev, 2019a) to select between different mass models and the use of `CMC` Monte Carlo models to disentangle the composition of sub-clusters of stellar remnants (e.g., is it composed of black holes, white darfs, or other objects?) were first employed, simultaneously, in Vitral et al., 2022.

- **New astrometric methods for data fitting**: The *Gaia* astrometric mission represented a revolution in the understanding of the dynamics of our Milky Way, and along with its unprecedent amount of astrometric data, there comes the need of state-of-the-art tools to extract the best of its information. In Vitral, 2021, I provided the main recipes of my public[6] software code BALROGO: BAYESIAN ASTROMETRIC LIKELIHOOD RECOVERY OF GALACTIC OBJECTS, which aims at selecting members from globular clusters and dwarf spheroidal galaxies, satellites from the Milky Way, as

6 https://gitlab.com/eduardo-vitral/balrogo.

well as providing fits to their structural parameters in a Bayesian frame. Along with Vasiliev and Baumgardt, 2021, Vitral, 2021 was the only work to provide bulk proper motions for over a hundred Milky Way globular clusters (in very good agreement with the other work) from *Gaia* EDR3 data, using new methods. This was of great scientific relevance, since it is important to have more than a single measurement, by means of different methods, in order to add more robustness to a given result.

- **New constraints on a dark matter formation scenario for globular clusters**: There is no consensus on how globular clusters were formed, and it is likely that they may share different formation scenarios. In this thesis, I studied the scenario where they are formed inside their own dark matter mini-halos (such as galaxies in a ΛCDM framework), originally proposed by Peebles, 1984. The work presented in Vitral and Boldrini, 2022 joined the previous attempts from Mashchenko and Sills, 2005 and Peñarrubia et al., 2017 to constrain the differences between globular clusters formed inside dark matter mini-halos and those that were not. We showed with N-body simulations that initially, the dark matter mini-halo behaves as a dynamical shield, by being stripped beforehand the cluster stars, and thus protecting the stellar component from tidal effects. Such shielding mechanism could indeed explain why some clusters seem less affected by tides than one would expect in the scenario where just baryonic matter is considered. In Boldrini and Vitral, 2021, we showed by comparing simulations with *Gaia* data that in fact, NGC 6397 seems to fall in this category, with observed tidal imprints much smaller than what our dark matter-free simulations predicted.

1.2.2 *Organisation note*

This manuscript consists of three Parts (with a fourth being the appendixes), with a total of nine Chapters. The first Part (Chapters 1, 2, 3 and 4) is intended to give the reader a general context of the astrophysics involved in my work, as well as the instruments and data sets I used. The second Part, from Chapter 5 to 7, aims at explaining the methods I used to analyse the data of globular clusters, which also includes my own contribution to improve the tools used in those analyses. Finally, the third and last Part, with Chapters 8 and 9, bring the main results concerning the Jeans mass-modelling of the internal dynamics of NGC 6397 and NGC 3201, and concerning the dynamical imprints of the dark matter formation scenario of globular clusters.

- **Chapter 1: Introduction**: The present Chapter aims at providing a brief definition of globular clusters, and motivating the reader to pursue the next Chapters. It ends by summarising the main highlights of the thesis, for context, as well as laying the format of the manuscript.

- **Chapter 2: Stellar Evolution**: I provide the main aspects of stellar evolution that relate to the physics of globular clusters, with special emphasis on the description of compact objects, which will be further evoked in Chapter 8. I also comment on the different stellar populations found

in GCs, including the multiple chemical populations phenomenon (e.g., Gratton et al., 2019).

- **Chapter 3: Dynamical Processes**: I set the stage for the main dynamical processes that govern the internal kinematics of globular clusters, as well as their outer kinematics, impacted by their satellite status, plunged in the tidal field of their host galaxy. Special attention is given to the phenomenon of core-collapse, which is of great importance for the discussion from Chapter 8.

- **Chapter 4: Instruments & Data**: I present and comment on the data sets and software I used throughout my work, specifying the contribution and situation where each of these data were necessary.

- **Chapter 5: Density Profiles**: This Chapter introduces the many density profiles in the literature that I used to model the dynamics of globular clusters, as well as an eventual problematic associated to them (in particular, the deprojection of the Sérsic profile derived in Vitral and Mamon 2020). They are of extreme importance for the equations in Chapter 7, as well as for the results in Chapter 6.

- **Chapter 6: Astrometry & Photometry**: I explain the main astrometric and photometric tools that I coded into BALRoGO, and provide the application of these tools to over a hundred Milky Way globular clusters, and nine Local Group dwarf spheroidals, along with a discussion on the robustness of those methods. This Chapter summarises the main results presented in Vitral, 2021 and minor topics from my other works.

- **Chapter 7: Mass & Anisotropy Modelling**: This Chapter introduces the mathematical formalism behind the mass modelling routine of MAMPOSSt-PM, the software I used and helped to develop (cf., Mamon & Vitral in prep.) during my thesis. This formalism was applied to astrometric data of nearby globular clusters, as mentioned in Chapter 8.

- **Chapter 8: Stellar Graveyards**: I present here the analyses and results from Vitral and Mamon, 2021 and Vitral et al., 2022, concerning the clustering of stellar remnants in the cores of globular clusters NGC 6397 and NGC 3201.

- **Chapter 9: On The Origin Of Globular Clusters**: This Chapter aims to summarise the main characteristics of a globular clusters system that was formed inside a dark matter mini-halo and experiences a tidal field, as presented in Vitral and Boldrini, 2022. The final part of this Chapter briefly presents the results from Boldrini and Vitral, 2021, which argue in favour of this formation scenario.

2 STELLAR EVOLUTION

It often seems to me that the night is even more richly coloured than the day, coloured in the most intense violets, blues and greens. If you look carefully you'll see that some stars are lemony, others have a pink, green, forget-me-not blue glow. And without labouring the point, it's clear that putting little white dots on a blue-black surface is not enough.

— Vincent van Gogh, on a letter to his sister, 1888

The different stellar populations visible in the sky are, indeed, too rich and numerous to be simplified as simple white dots in a dark emptiness. Stars can have different colours, meaning that their temperature and chemical composition are not alike, and they can also shine in many different intensities. This vast range of stellar types is largely correlated with the star's initial mass and composition. For example, heavier stars tend to evolve faster, such that by burning more fuel, they reach higher temperatures, which on its turn is associated with bluer wavelengths. As these blue stars evolve very rapidly, soon undergoing a supernova explosion[1], we associate them with younger stellar populations formed from debris of other past supernovae events. On the other side of the spectrum, stars with low initial mass take more time to evolve, producing less energy, and looking redder. Because these low mass stars have a more gradual evolution, they are generally associated with longer timescales, hence being older.

Many stellar trends and evolutionary tracks can emerge by looking how different physical properties such as temperature, luminosity and mass correlate altogether. Indeed, by the beginning of the 20th century, astronomers Ejnar Hertzsprung (Hertzsprung, 1911) and Henry Norris Russell (Russell, 1914) had independently noticed a common behaviour when plotting the luminosity versus the effective temperature of different stars. It might not be an overstatement to claim that the behaviour they noticed became later the most popular diagram in astrophysics, which is now known as the Hertzsprung–Russell diagram, abbreviated as HR diagram. The relations portrayed on this diagram, or on the *colour magnitude diagram* (hereafter, CMD[2]) display not only different stellar types grouped in different sections, but also an evolutionary track enlightening the life journey of a star, from its birth to its death as a white dwarf or a supernova.

In this chapter, we shall present and study different aspects of the CMD, which in turn will help us to better grasp the different stellar types present in GCs. These, in particular, present a very characteristic CMD shape, that can

1 Stellar lifetimes in this scenario are usually within less than 1 Gyr (Harwit, 1988).

2 An equivalent plot using colour gradients rather than temperatures, and magnitudes instead of luminosities.

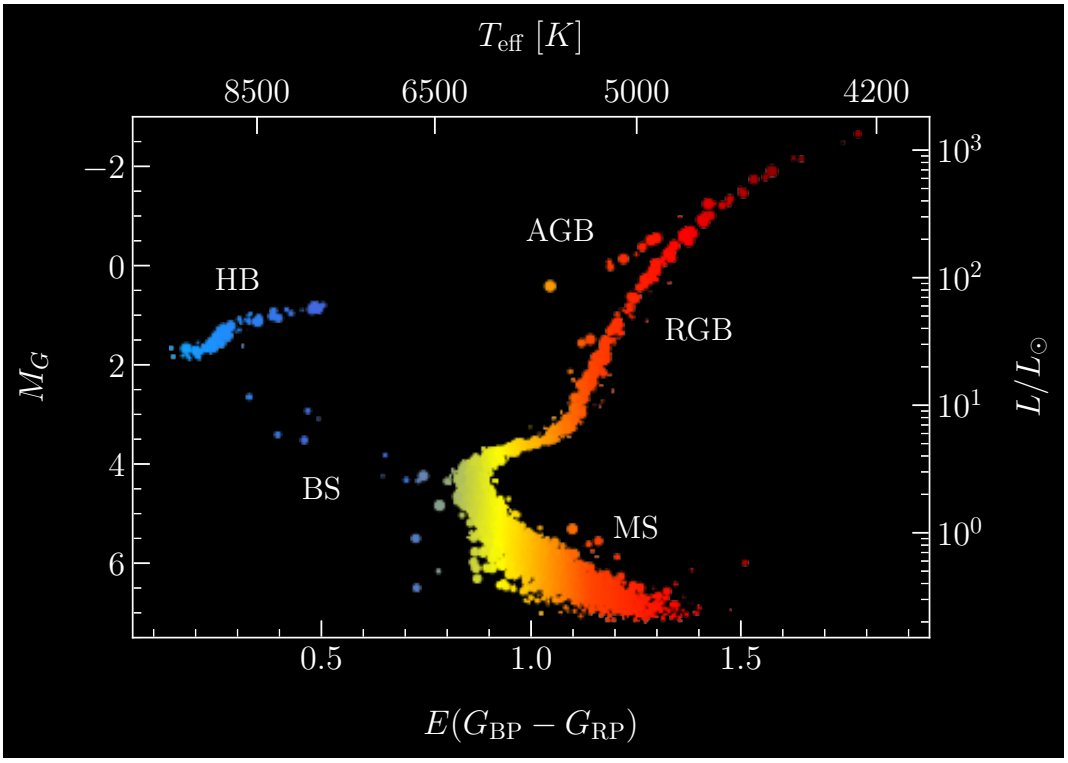

Figure 2: *Colour magnitude diagram:* Example of a colour magnitude diagram, indicating the position of the *Main Sequence* (MS); the *Red-Giant Branch* (RGB); the *Horizontal Branch* (HB) the *Asymptotic-Giant Branch* (AGB) and *Blue Stragglers* (BS). The image uses data from Gaia EDR3, filtered with the BALRoGO software (Vitral, 2021), with temperature and luminosity values derived with the Parsec code (Bressan et al., 2012; Chen et al., 2014; Chen et al., 2015; Marigo et al., 2017; Pastorelli et al., 2019). The globular cluster exemplified here is NGC 6397.

be used to infer their ages, distances, metallicities and stellar binary content. We shall also focus on a few exotic populations of compact objects, and briefly present the multiple stellar population event in GCs, which is now part of their definition (Gratton et al., 2019).

2.1 COLOUR MAGNITUDE DIAGRAMS

Figure 2 displays the CMD of the GC NGC 6397, with the locations of a few stellar populations labelled throughout it. In the following, we shall comment on these different stellar phases, keeping in mind that the CMD can be seen as an evolutionary track, with the direction of time starting at the *Main Sequence* and going up to the *Asymptotic Giant Branch*, before the star becomes a compact object. Hence, we will present these stellar populations in their order of evolution, with exception of the *Blue Stragglers*, which follow a different evolutionary path. Much of this section has been inspired by the book of (Ashman and Zepf, 2008), and the reader can refer to this work for more details.

2.1.1 *Main sequence*

The lightest stars in GCs still burn hydrogen in very slow rates, such that their temperatures are lower than other stars. Along with the fact that they are less luminous, this places them in the lower right region of Figure 2, labelled the *Main Sequence* (MS). The main sequence is characterised by a relatively thin line which increases in luminosity and temperature with the star's mass, up to bluer wavelengths, and is associated with a hydrogen burning core (thus, stars in their initial stage of life) whose thermal pressure balances the gravitational pull. As mentioned, the location of a star in the main sequence is primarily related to its initial mass, but also to its composition and age. Even though GCs are know to have more than a single stellar population (see Section 2.3), these populations are still considerably homogeneous with respect to other GCs, and one can, in a first moment, consider GCs as a single system with a given age and metallicity, for pedagogical purposes. Because of that, the CMD of GCs is also referred to as an isochrone.

GCs present very old stellar populations, with typical ages of the order of 13 Gyr (Marin-Franch et al., 2009), meaning that they were likely formed alongside the galaxies where they are hosted. This also means that the visible stars that we see today in these clusters are all very light (i.e., $\lesssim 1\ M_\odot$), otherwise they would have already evolved onto a compact object. This mass limit sets a boundary in the MS, since heavier stars would have already burnt their hydrogen core. This boundary is known as the MS turn-off, located where the cluster's MS changes direction, moving towards lower temperatures in the CMD. The location of the MS turn-off is therefore defined mainly by the age of the GC system: older GCs display a MS turn-off at both lower temperatures and luminosities, meaning that most of its stars had enough time to burn their hydrogen core.

The chemical composition of the GC influences the overall colour and spread of the MS. Clusters with higher metallicities present a thicker layer of electrons (from the metals) in their star's atmospheres (Reiz, 1954; Schwarzschild, Searle, and Howard, 1955), which in turn intensifies scattering, allowing preferentially redder wavelengths to reach us. Hence, low metallicity clusters have a bluer MS, and high-metallicity ones have a redder MS. Given this trend, clusters with a higher metallicity spread also display a thicker, more spread MS as well, which is characteristic of a system with more than a single chemical composition. The lower limit of the MS is set whether by the quality of the observational material, which might not reach fainter magnitudes, or by the theoretical mass limit of roughly $0.08\ M_\odot$ where hydrogen burning no longer takes place in the stellar core (in this later case, we have a brown dwarf, no longer considered as a star).

2.1.2 *Red-giant branch*

Once having left the MS, the star starts to burn hydrogen in shells surrounding the core, and the gravitational pull is outbalanced by the new stronger radiation pressure. This leads the star to inflate, with outer shells of stellar material increasing the opacity of the system, which becomes redder. This new redder,

giant star is therefore called a *red giant*, and its location in the CMD is labelled the *Red Giant Branch* (RGB).

RGBs follow roughly the same intuition of MS stars, with different chemical compositions relating to a bluer or redder RGB, and its overall spread. The tip of the RGB is reached when the pressure in the core is high enough to start burning helium. At this point, such burning is associated with much higher temperatures, which drifts the star's location on the CMD towards the *Horizontal Branch* (HB).

2.1.3 *Horizontal branch and asymptotic giant branch*

The HB is characterised by a higher spread in temperature but with equivalent values of luminosity, which renders it horizontal in the CMD. This trend however is not a strict rule, and many GCs show a luminosity decrease towards increasing temperatures (this feature is often referred to as a blue tail). The exact behaviour of the HB is mostly defined by the mass loss history during the RGB phase, but many other aspects are in play, such as the cluster's metallicity, temperature and eventually other parameters (e.g., Rood, 1973; Stetson, Vandenberg, and Bolte, 1996; Fusi Pecci et al., 1993). Finally, the HB is also important for the study of RR-Lyrae variable stars, which can serve as a probe for distance measurements and formation history of the GC (Oosterhoff, 1939; Sandage, 1993).

Once the helium in the core is burnt, helium starts to burn in outer shells, following by further hydrogen shells, which increases the star luminosity and opacity at the same time. This moves the star once again towards the giant region in the CMD, asymptotic located at the left of the RGB. This new branch is called the *Asymptotic Giant Branch* (AGB). An important point about AGB stars is that they have significant mass loss (Cohen, 1976), which will be later useful to explain some multiple stellar population formation models. All in all, the physics and location of AGB stars are more complex (in part due to the modelling of mass loss) and are beyond the scope of this thesis. Further information about these stars can be found in Iben and Renzini, 1983.

2.1.3.1 *Blue stragglers & Binaries*

When gazing the CMD, one might be surprised by the sparse blueish thread of stars connecting the MS to the HB. These stars seem to continue a normal MS path, instead of following the MS turn-off. As we mentioned, the MS turn-off location is imposed primarily by the age of the cluster, which points to these outlier stars as younger siblings of the MS stars. Because they appear blue in the CMD and depart from the expected trend, they are referred to as *Blue Stragglers* (BSs). Nevertheless, the difference in age from BSs and classic MS stars, given their location, should imply more recent stellar formation in an environment mostly devoid of gas (which could not have formed new stars). BSs are, thus, not compatible with a recent stellar formation picture, and its behaviour characteristic of younger stars is rather due to a rejuvenating process than a recent birth.

Different rejuvenating processes have been proposed to explain BS formation, and they may indeed coexist under different environmental conditions.

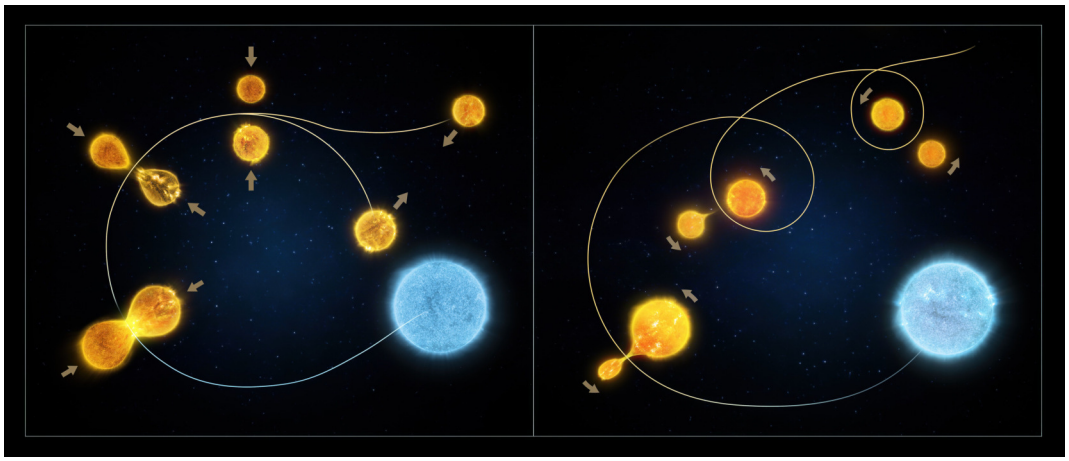

Figure 3: *Blue stragglers:* Illustrative scheme indicating different ways of producing a *Blue Straggler*, through a collision model (**left**) and a slow coalescence model **right**). Credits: NASA & ESA.

For instance, BSs can be formed through a slow coalescence model where a binary system consisting of a lower mass star and higher mass one exchanging material (from the more to the less massive), so that the final product is a single, bluer star that appears younger, due to its higher mass, which exceeds the typical mass of the turn-off point (McCrea, 1964; Iben, 1986). In addition, BSs can also be formed through a collision scenario, where two stars collide and rotate, subsequently merging to form a new bluer, apparently younger star (Hills and Day, 1976). Given the high inner densities of GCs, the collision scenario is more likely to happen in their cores, while the slow coalescence scenario is more typical of the cluster outskirts, such that both processes are probably common in GCs (Bailyn, 1995). Figure 3 illustrates these two formation scenarios. For more information on BSs, the reader is invited to see the works of Stryker, 1993; Bailyn, 1995; Leonard, 1996.

Finally, another interesting unexpected behaviour concerns the stars right above the MS, which in a first glance, seem to be correlated with noise, rather than any other population. However, those are unresolved binary stars, whose combined luminosity is greater than what is expected for their temperature. Of course, some of the outliers could indeed be related to noisy measurements or poorly filtered Milky Way field stars.

2.2 COMPACT OBJECTS

Once a stars burns all of its initial fuel supply through thermonuclear fusion, the gravitational pull becomes balanced (or not) by other means, and the remnant stellar corpse is referred to as a compact object. Depending on the mass of the star prior to fuel exhaustion, it can turn into three different classes: lower mass stars turn into white dwarfs, medium mass stars turn into neutron stars and finally, stars massive enough so that the gravitational pull is stronger than any other pressure mechanism turn into black holes. Dynamical processes and interactions with other stars might eventually accelerate or change the kind of compact object it turns into. In the following, we briefly describe some useful

characteristics of these stellar remnants, that might be further invoked in this manuscript.

2.2.1 *White dwarfs*

If a star is born with a mass below $\sim 8\ M_\odot$, the source of energy that will prevent its core from collapsing once all the available fuel has been burnt is the electron degeneracy pressure from its remaining core. Most of those remnants will have a core composed of carbon and oxygen, for which reason they are called [CO] white dwarfs.

For some specific stars, with masses between $\sim 8 - 10\ M_\odot$, they might be massive enough to fuse carbon into neon or magnesium, but their core is not yet massive to fuse neon to iron (Nomoto, 1984), which would in turn be a non-fusing core of mass higher than what can be supported by electron degeneracy pressure. In that case, it will have an oxygen, neon and magnesium core, and will be called a [ONeMg] white dwarf. Finally, there are also helium ([He]) core white dwarfs, thought to be formed in close binary systems (Benvenuto and De Vito, 2005).

White dwarfs remain stable and cool down unless their mass exceeds the Chandrasekhar limit (Chandrasekhar, 1931), above which they can no longer be supported by the electron degeneracy pressure. In dense systems like GCs, it is likely that they will end up interacting with other stars, or even other compact objects, which will change the course of its evolution. In particular, when accreting material from a companion, a white dwarf can surpass the Chandrasekhar limit and explode into a type Ia supernova (Mazzali et al., 2007).

A question of interest regarding GCs and white dwarfs is which white dwarf population is more massive, which in turn will influence their spatial location throughout the cluster due to mass segregation processes (see chapter 3). The difference in mass from [CO], [He] and [ONeMg] white dwarfs depends not only on the initial stellar mass (in which case, [ONeMg] would be forcibly more massive), but also on the amount of mass loss during the previous stellar phases. In general, [CO] white dwarfs have a very broad range of masses, with some of them being closer to the Chandrasekhar limit and others being of very low mass. [ONeMg] are generally more massive, given that they come from more massive stars, but there are still, nonetheless, some [ONeMg] white dwarfs less massive than the more massive [CO] white dwarfs, due to different processes of mass loss. Finally, [He] white dwarfs are believed to be less massive in general (Calcaferro, Althaus, and Córsico, 2018).

Given that most of the original GC stars with mass above $\sim 1\ M_\odot$ have already became white dwarfs due to high GC ages (Heggie and Hut, 1996), white dwarfs are thought to dominate the mass of many GCs, although they are more difficultly detected (because of their lower luminosities). They play an important role in clusters having undergone core-collapse (see chapter 3), and they will be of crucial importance in chapter 8.

Figure 4: *First image of a black hole:* First image of a black hole released by the Event Horizon Telescope Collaboration, in the core of the M87 galaxy. Credit: Event Horizon Telescope Collaboration.

2.2.2 *Neutron stars*

Stars having masses higher than $\sim 8-10\ M_\odot$, but lower than $\lesssim 25\ M_\odot$ (Fryer, 1999) will explode as a supernova once an iron core is formed. The remnant stellar corpse will not actively produce heat through thermonuclear fusion, and will be in equilibrium only due to degenerate neutron pressure and, most importantly, due to repulsive nuclear forces (Douchin and Haensel, 2001). These forces are able to hold the object against its on gravitational pull up to roughly $2\ M_\odot$. Beyond that limit (which happens for stars with initial mass $\gtrsim 25\ M_\odot$), the remnant is no longer able to hold the gravitational forces, and it becomes a black hole.

2.2.3 *Black holes*

Black holes are among the most fascinating objects in astrophysics, given the very interesting phenomena related to them, including space-time dilation, gravitational wave mergers with extremely high energies, and their important role in galaxy formation. Once formed, a region called the event horizon is created around them where not even light can escape[3]. Although these sources hold still many secrets, much advance has been made on black holes since the first detection of gravitational waves by the Laser Interferometer Gravitational-Wave Observatory (LIGO, Abbott et al., 2016a), followed by the first image of a black hole by the Event Horizon Telescope (EHT, Event Horizon Telescope Collaboration et al., 2019), depicted in Figure 4.

3 The size of the event horizon is given by the Schwarzschild radius: $r_s = 2GM_{BH}/c^2$, where c is the speed of light, M_{BH} is the black hole mass and G is the gravitational constant.

Yet, black holes have been treated as more than a theoretical object for a considerable amount of time, starting in 1939, when Oppenheimer and Snyder proposed them to be the final step of the life of massive stars ($\gtrsim 10\ M_\odot$) after their final gravitational collapse into stellar-mass black holes, with masses in between $\sim 2\ M_\odot$ (Thompson et al., 2020) and $\approx 52\ M_\odot$ (Woosley, 2017), but also when Hoyle and Fowler, 1963 identified the then recently discovered quasars (Schmidt, 1963) as super massive black holes (SMBHs). This latter class of black holes, which reside in the centres of massive galaxies, are responsible for extremely luminous sources in the Universe, such as quasars and active galactic nuclei (AGN), sometimes unleashing powerful jets of relativistic matter, along with outflows that have a profound impact on star formation and galaxy evolution (e.g., Croton et al. 2006; Hopkins et al. 2006). In addition, some black holes may have formed during the early moments of the Universe (e.g. Zel'dovich and Novikov 1966; Hawking 1971), and these primordial black holes may constitute an important mass fraction of black holes below the SMBH mass.

Since there is no theoretical constraint to the mass of a black hole, it would be reasonable to believe that intermediate-mass black holes (IMBHs) could exist, filling the considerable gap between stellar-mass black holes and SMBHs (i.e., with masses between 100 and $10^5\ M_\odot$). Furthermore, SMBHs are understood to grow by mergers, where the first seeds are stellar-mass black holes (Madau and Rees, 2001) or metal-free primordial gas clouds (Loeb and Rasio, 1994), so IMBHs may be a transitory stage in the growth of black holes. However, there is currently little evidence for IMBHs (see reviews by Volonteri 2010 and Greene, Strader, and Ho 2020), with some important candidates highlighted (e.g., Kaaret et al. 2001; Chilingarian et al. 2018 in dwarf galaxies, and recently Lin et al. 2020 in a GC) and one gravitational wave confirmation (The LIGO Scientific Collaboration et al. 2020). Furthermore, IMBHs could help to explain many enigmas in astrophysics, such as filling up part of the dark matter mass budget (e.g., Haehnelt and Rees 1993 and Loeb and Rasio 1994) or providing massive seeds for high redshift quasars, whose high masses at such early times represent a challenge to current theories (Haiman, 2013). Therefore, great efforts have been undertaken to detect IMBHs to better understand their origin and evolution.

GCs appear to be a unique laboratory to test the existence of IMBHs. These quasi-spherical star clusters are known to have old stellar populations, indicating that they formed at early epochs. Their high stellar number densities provide an excellent environment to increase stellar interactions that could give birth to compact objects. More precisely, contrary to galaxies, the rates of stellar encounters in the inner parts of GCs containing half their stellar mass are sufficiently high to statistically affect the orbits of their stars by two-body relaxation (Chandrasekhar, 1942).

Several scenarios have been proposed for the existence of IMBHs in GCs. One is the direct collapse of population III stars (Madau and Rees, 2001), but the link of population III stars with GCs is not clear. Another is the accretion of residual gas on stellar-mass BHs formed in the first generation of stars (Leigh et al., 2013), but the availability of the gas is unclear as the first massive stars will blow it out of the GC by supernova explosions. Stellar mergers are a popular mechanism for IMBH formation. Portegies Zwart and McMillan, 2002 proposed a runaway path to IMBH formation in GCs, where an initially massive star suf-

fers multiple physical collisions with other stars during the first few Myr of the GC, before they have time to explode as supernovae or simply lose mass. During these collisions, the most massive star will lose linear momentum, ending up at the bottom of the gravitational potential well. At the same time, its mass will grow during the successive stellar mergers, to the point that it will end up as a BH, possibly reaching 0.1 per cent of the GC stellar mass.

Miller and Hamilton, 2002 proposed a slower process for IMBH formation, where dynamical friction (Chandrasekhar, 1943) causes the most massive stellar remnant BHs to sink to the centre of the gravitational well over a Gyr. Thus a $\gtrsim 50\ M_\odot$ stellar remnant BH, sufficiently massive to avoid being ejected from the GC by dynamical interactions, would grow in mass through mergers with these other massive BHs as well as other typically massive stars, reaching a mass of $1000\,M_\odot$ over the Hubble time, which they argued generates IMBHs in some ten per cent of GCs. Finally, Giersz et al., 2015 proposed that hard binaries containing stellar-mass BHs merge with other stars and binaries, which can be a fast or slow process.

These models present, however, drawbacks: The short relaxation time needed in the Portegies Zwart and McMillan scenario usually requires primordial mass segregation in order not to eliminate too many GCs candidates, while the assumption by Miller and Hamilton, 2002 of BH seeds $\gtrsim 50\,M_\odot$ is not expected as the massive progenitors are fully exploded in pair-instability supernovae (e.g., Woosley 2017).

Unfortunately, attempts to detect IMBHs have been somewhat inconclusive: Dynamical modeling is still dependent on the assumptions concerning the confusion between the IMBH and a central subcluster of stellar remnants (e.g., den Brok et al. 2014, Mann et al. 2019 and Zocchi, Gieles, and Hénault-Brunet 2019). Furthermore, these analyses usually rely on too few stars inside the sphere of influence of the IMBH, which can lead to false detections (see Aros et al., 2020, for a comparison of different outcomes). Besides, searches for signs of accretion indicate no strong evidence for $> 1000\ M_\odot$ black holes in galactic GCs (e.g., Tremou et al. 2018).

Apart from IMBHs, black holes are also very important to regulate the internal dynamics of GCs, being particularly crucial to explain the delay in core-collapse observed in Milky Way GCs. In particular, dynamical processes in GCs can also help to generate black holes with masses above which pair-instability supernovae fully explode the progenitor star (thus, leaving no remnant). This limit is set as $M_{\mathrm{BH,max}} = 45\ M_\odot$ (Farmer et al., 2019) or $52\ M_\odot$ (Woosley, 2017).

2.3 MULTIPLE STELLAR POPULATIONS

In this section, we briefly comment on the multiple stellar population phenomenon in GCs. This is a vast theme well detailed in Gratton et al., 2019 and we do not aim to provide a complete picture of it. Instead, we focus on some dynamical aspects that might differentiate these contrasting populations, and quickly discuss the possible origin scenarios that have been so far highlighted in the literature.

Indeed, many GCs show signs of different chemical populations (e.g., Carretta et al., 2009b; Milone et al., 2018; Bonatto et al., 2019; Cordoni et al., 2019).

The advance of techniques using different colour filters from the ultraviolet up to the infrared, allowed by the high quality data obtained with telescopes such as *Hubble Space Telescope* as well as ground based telescopes, has made possible to rule out the vision of GCs as composed by a single isochrone. It is yet not clear why and how these different populations came to be, neither why most GCs possess a bi-modal separation between first and second generations (hereafter, 1G and 2G respectively), while a few of them, like Omega Centauri, have even more populations (e.g., Bellini et al., 2017). We discuss below some of the most widely discussed scenarios in the literature, with the caveat that they are still not able to quantitatively reproduce the observations (Bastian, Cabrera-Ziri, and Salaris, 2015).

2.3.1 *Possible origins*

Many of the formation scenarios suggested in the literature propose that 2G stars are formed from the debris, or expelled material from 1G stars. This directly implies multiple star formation bursts in GCs, which is not yet confirmed observationally. Two prominent scenarios in that line are the ones invoking ejecta from AGB stars (D'Ercole et al., 2008) and from fast rotating massive stars (Decressin et al., 2007).

As mentioned in section 2.1.3, AGB stars are associated with a high amount of mass loss. These stars would also be more massive because of their fast evolution that places them in the AGB phase in a first place. Being more massive, they are thus more likely to mass segregate to the cluster's core through dynamical friction (see chapter 3), and their lost stellar ejecta would therefore also occupy the internal regions of the GC. D'Ercole et al., 2008 performed hydrodynamical and N-body simulations to show that such inner gas reservoir could indeed create future stellar generations. However, it was also shown that in order for that to happen, the initial GC mass should be roughly $10-100$ times greater than observed today (e.g., Bekki, 2011), which seems too large from what we expect from mass loss due to tidal effects or evaporation. The scenario proposed by Decressin et al., 2007 on the other hand proposes that the processed material that forms 2G stars would come from the wind of fast rotating stars located in the cluster's centre due to their assumed higher masses. In fact, this scenario requires the amount of very massive stars (e.g., with masses up to 60 $M_\odot$) to be considerably higher than what we expect from classical initial mass functions, which in turn renders this scenario less likely.

Another scenario, which does not rely on multiple star formation bursts was proposed by Bastian et al., 2013, who suggested that both 1G and 2G stars generate from the same original cluster material, but due to the presence of an early disc in stars at the centre of GCs, stars that pass in this region would be enriched/polluted forming the observed 2G. Nevertheless, the timescale needed for this disc to survive in order to reproduce the amount of 2G stars we see today is somewhat larger than expected in the presence of the high velocity dispersion/dynamical heating in observed clusters. Furthermore, D'Antona et al., 2014 also argued that the necessary mixing of the enriched material in the early disc would not be achieved considering the structure of the disc seed stars and the timescales related to their activity. Hence, the matter of how 2G stars form

in GCs remains a subject of considerable interest in the GC community, and it is still open to debate.

2.3.2 *Dynamical implications*

Although the means by which 2G stars form in GCs is still unknown, dynamical differences between the two populations have been highlighted, and might be of interest when performing mass modelling of the stellar populations present in these clusters. Here, we summarise some of the main dynamical attributes differentiating 1G and 2G stars. On observational terms, we present below some constraints from recent papers:

- Milone et al., 2018 reported that 2G stars were more radially anisotropic than the 1G in 47 Tuc.
- Lee, 2017 showed that in M5, 2G stars had significant rotation, while 1G ones had none.
- When analysing NGC 6752, Lee, 2018 found that 1G stars rotated more rapidly than 2G ones, in opposition with the previous item.
- Dalessandro et al., 2018 found that in NGC 6362, 1G stars had a more increased line-of-sight velocity dispersion than 2G stars.
- Dalessandro et al., 2019 showed that less dynamically evolved clusters have 2G stars centrally more concentrated than 1G ones, while more dynamically evolved clusters show no significant difference between spatial locations.

Indeed, it has been shown by Tiongco, Vesperini, and Varri, 2019, with N-body simulations, that centrally located 2G stars would eventually diffuse towards outer GC envelopes, which would be characterised by a more radial velocity (Milone et al., 2018) observations. Due to the lack of 3D measurements of the velocity anisotropy in many modelling approaches, there is still space for development in this area, and a more significant amount of analysed clusters is needed in order to better understand the constraints from dynamics on the different formation scenarios of 1G and 2G stars.

Finally, Cordoni et al., 2020, who analysed the spatial distributions and kinematics of seven GCs split by their two detected chemical populations, found that only the two GCs with the highest two-body relaxation times showed signs of different kinematics between their two chemical populations. Hénault-Brunet et al., 2015 also provide an interesting study highlighting which are the main dynamical signatures expected from each formation scenario: they mention that rotation at the cluster's outskirts is a unique kinematical imprint to be distinguished between multiple star bursts and accretion scenarios, and that the inner cluster dynamics is mixed too early for us to derive significant distinctions between 1G and 2G stars in Milky Way GCs. In fact, if the two populations have roughly the same mass functions, then two-body relaxation should wash out any differences in their positions in projected phase space (Vesperini et al., 2013), except in their outer regions where two-body relaxation is incomplete.

In sum, most of this information implies that mass-modelling analyses of the inner regions of GCs should not be considerably affected by neglecting of multiple stellar populations, and when targeting the outer regions, it would still be difficult to separate the dynamical imprints of the different populations if the two-body relaxation times are relatively small.

3 DYNAMICAL PROCESSES

Looking at these stars suddenly dwarfed my own troubles and all the gravities of terrestrial life. I thought of their unfathomable distance, and the slow inevitable drift of their movements out of the unknown past into the unknown future.

— H. G. Wells, *The Time Machine* (Wells, 1898).

As previously stated, GCs are among the most dynamically active environments in the Universe. In such dense environments, cluster evolution is shaped by the internal and external dynamics by means of phenomena such as runaway mergers, mass segregation, core collapse and tidal interactions. In this Chapter, I will introduce these themes from a theoretical point of view, and further comment about recent developments in the literature. Many of the mathematical developments in this Chapter are inspired from Binney and Tremaine, 2008, where the reader can seek a more detailed description of such phenomena.

3.1 BINARY ENCOUNTERS

Binary stars form naturally in GCs. Not only there are primordial binaries, but also due to dynamical interactions, it is common to form new such companions. We will briefly analyse their impact on the energy budget of the cluster, which will come in hand, when discussing the development of *core-collapse*. For a start, we write below the total energy of a binary system on their centre of mass frame, formed by two smaller components of mass m_1 and m_2, with velocities (respective to the centre of mass) v_1 and v_2, with a distance r from each other:

$$E = \frac{1}{2}(m_1 v_1^2 + m_2 v_2^2) - \frac{G m_1 m_2}{r}. \tag{1}$$

From Kepler's laws of planetary motion, we can re-write v_1 and v_2 as a function of the stellar masses and involving the gravitational constant G, so that the total energy of the system can be written as:

$$E = -\frac{G m_1 m_2}{2a}, \tag{2}$$

where a is the semi-major axis of the ellipse describing the orbit. If the typical mass of nearby stars is m_a, and the velocity dispersion in such environment is σ, we can define the quantity $|E|/(m_a \sigma^2)$, which compares the dynamical energy of a binary encounter with another star, and its own binding energy. Binaries where $|E|/(m_a \sigma^2) > 1$ are called *hard* binaries, while *soft* binaries relate

to $|E|/(m_a\sigma^2) < 1$. The step-by-step mathematical development of this factor following the binary encounter is beyond the scope of this manuscript.

Instead, we will report the results from Heggie, 1975; Hut and Bahcall, 1983; Hut, 1983, which summarise the general behaviour of such interactions. Indeed, they showed that in typical environments of GCs, hard binaries tend to get harder, meaning that their binding energy increases (thus expelling out energy to the system), while soft binaries get softer, by increasing their total energy budget (i.e., equation 2); this result is known as Heggie's law. Hence, these energy exchanges mediated by binary interactions with GC field stars are of great importance to balance and determine the further dynamical evolution of the cluster.

3.2 RELAXATION

We can estimate the timescale for a star inside a GC to lose memory of its initial conditions, by computing the number of relaxation interactions it would take for its velocity to change by an order of magnitude similar to its initial value, i.e. $|v/\delta v|$. Then, one can multiply this number of relaxing interactions by the crossing time needed for a star to cross the typical length of the cluster, which would cause the velocity variation δv. Spitzer and Hart, 1971 propose a median relaxation time given by

$$t_{rh} = \frac{0.14N}{\ln(0.4N)}\sqrt{\frac{r_h^3}{GM}}, \tag{3}$$

where N is the number of particles in the system, M the total system's mass, G the gravitational constant and r_h the system's median radius. Typical values of relaxation time for GCs span from 10^7 yr to 10^{11} yr, with the bulk of GC having $t_{rh} \sim 10^9$ yr (Webbink, 1985).

3.3 DYNAMICAL FRICTION

If we consider the encounter of two bodies, with masses M (higher) and m (lower), they will exchange energy and will likely (from a statistical view), share a similar energy budget by the end of the interaction. This will lead to the deceleration of the higher mass M (see Chapter 7 from Binney and Tremaine 2008). Next, considering that the mass M is now in a medium with many more tracers of mass m, Chandrasekhar, 1943 derived the variation of the velocity of the mass M with respect to time as:

$$\frac{d\mathbf{v}_M}{dt} = -16\pi^2(\ln\Lambda)G^2m(m+M)\frac{\int_0^{v_M} f(v_m)v_m^2 dv_m}{v_M^3}\mathbf{v}_M, \tag{4}$$

where G is the gravitational constant, v_i is the velocity of the body of mass i and $\ln\Lambda$ is the Coulomb natural logarithm, with Λ defined as

$$\Lambda \equiv \frac{b_{max}V_0^2}{G(M+m)}, \tag{5}$$

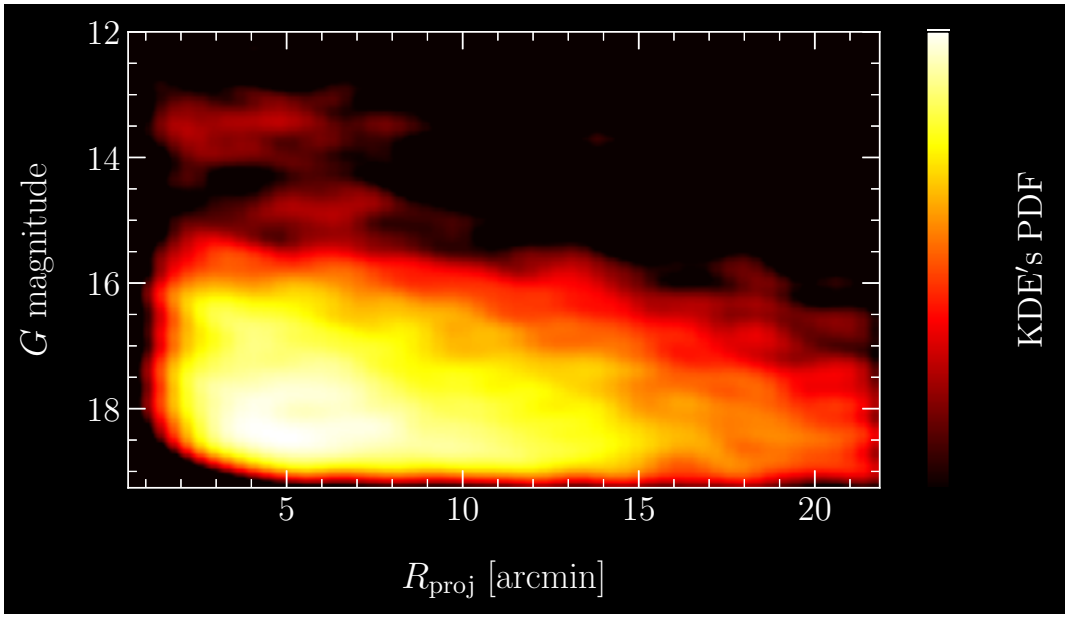

Figure 5: *Mass segregation:* Plot of G magnitude versus projected distance (in arcmin) to the centre of a globular cluster system, illustrating that more massive stars (thus, with smaller magnitudes) tend to be more common in the cluster's inner regions. The colour bar indicates the probability distribution function (PDF) of the data computed through a *Kernel Density Estimation* (KDE) with darker tones indicating less dense regions, and brighter tones indicating denser ones. The image uses data from GAIA EDR3, filtered with the BALROGO software (Vitral, 2021). The globular cluster exemplified here is NGC 6397.

where b_{max} is the largest impact parameter[1] considered, and V_0 is the modulus of the original velocity difference between the two bodies. Indeed, equation 4 shows that the impact of such interaction is to decrease the velocity, or kinetic energy of the body of higher mass. This dragging force is thus described as dynamical friction.

3.3.1 *Mass segregation*

Although the stellar populations in GCs can be considered homogeneous for many applications, in reality we have different mass ranges among the dynamical tracers in these sources. From low mass main-sequence stars, up to heavy compact objects (see Chapter 2), the differences in mass between different stars can impact their respective location in the cluster.

Indeed, as seen above, if a star of higher mass M interacts with many less heavy stars in the GC, it will decelerate, such that the centripetal force associated with the orbit of the star of mass M will be smaller, and will not be able to endure the gravitational pull at such position, thus moving into inner orbits. Similarly, less heavy stars will move onto outer orbits, which will create a gradient of masses, with higher masses in the cluster inner regions, and lower

1 An impact parameter is here defined as the perpendicular projection of the distance between a the body of mass M and the body of mass m, whilst the orbital path of the former is yet not altered by their mutual interaction.

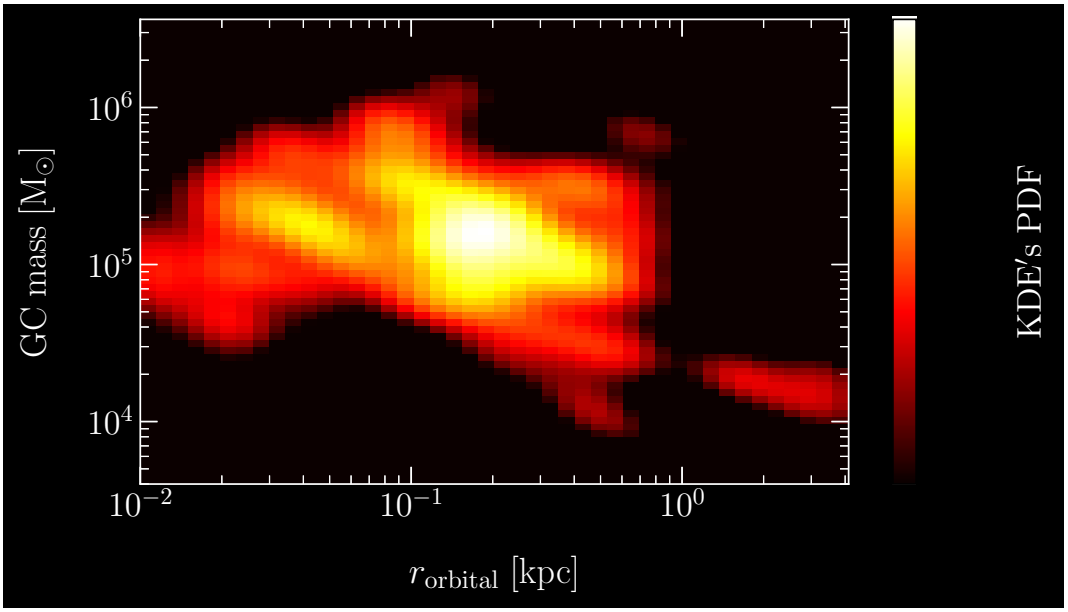

Figure 6: *Orbital decay:* Plot of globular cluster mass (in $M_\odot$) versus orbital radius (in kpc) for Milky Way globular clusters, illustrating that more massive clusters tend to be more common in the galactic inner regions. The colour bar indicates the probability distribution function (PDF) of the data computed through a *Kernel Density Estimation* (KDE) with darker tones indicating less dense regions, and brighter tones indicating denser ones. The image uses data from Holger Baumgardt's website catalogue (© H. Baumgardt, A. Sollima, M. Hilker, A. Bellini & E. Vasiliev).

masses in the outskirts. This phenomenon is labelled as mass segregation, and is illustrated in Figure 5.

3.3.1.1 *Orbital decay*

Another consequence of dynamical friction is the orbital decay of satellites like GCs. Indeed, GCs being much more massive than the stars that compose the galaxies they orbit, the natural tendency is for GCs to interact with these stars, and decelerate. Hence, the cluster's orbit shrinks with time, and it falls down into the gravitational potential well of the host galaxy. This is illustrated in Figure 6.

Naturally, the more massive a GC is, the more the deceleration described in equation 4 will be stronger, which will culminate in a faster orbital decay. However, during infall, satellites may lose mass due to tidal interactions, which renders this evolution more complicated. If ones disconsiders the mass loss though, Binney and Tremaine, 2008 provide the following relation for the timescale needed for a satellite to fall to the centre of its host:

$$t_{fric} = \frac{1.17}{\ln \Lambda} \frac{r_i^2 v_c}{G M}, \tag{6}$$

where r_i is the initial orbital radius of the satellite, and v_c its circular velocity. Using typical values of Milky Way GCs for the constants present in equation 6, we find that typical dynamical friction times are of the order of 10 Gyr. One

application of this was suggested by Tremaine, Ostriker, and Spitzer, 1975, who proposed that the nuclei of major galaxies are enriched with debris from GCs that have completely sunk to the centre due to dynamical friction.

3.4 NEGATIVE HEAT CAPACITY OF SELF-GRAVITATING SYSTEMS

3.4.1 *The Virial theorem*

A GC can be, in principle, simplified as a spherical collection of particles having similar masses, such as an ideal gas composed of mono-atomic particles. From this, one can deduce important trends of the cluster's long term evolution, among which the most notorious is probably the cluster's core-collapse. Indeed, if we consider the cluster in equilibrium, and governed only by self gravitating forces, the overall modulus of the gravitational pull will be equal to the internal pressure gradient due to the motions of its particles (stars):

$$\vec{\nabla} P = \rho \vec{g}, \tag{7}$$

where P is the pressure, ρ is the local mass density and $\vec{g}$ is the acceleration imposed by the gravity field, given by $\vec{g}(r) = -e_r \times GM(r)/r^2$, with e_r the unity radial vector of the coordinate system. Moreover, due to the spherical symmetry of the system, we can thus write that $dP/dr = \rho(r)g(r)$. By multiplying it by $V(r)dr$ ($V(r)$ is the volume enclosed at radius r), and further integrating over the whole system, we get

$$\int_\star V(r)dP = \frac{1}{3}\int_\star -\frac{GM(r)}{r}dM, \tag{8}$$

where we use $\rho(r) = \frac{dM(x)}{dV(x)}|_{x=r}$, and $V(r) = 4\pi r^3/3$. The right member integral is the definition of the gravitational potential energy, E_g, of the system. When integrating by parts the left member integral[2], we end up with:

$$-3\int_\star P\, dV = E_g. \tag{9}$$

By defining the mean pressure over the volume as $\overline{P} = \frac{1}{V(R)}\int_\star P\, dV$, we get a simplified version of the Virial theorem:

$$3\overline{P}\, V = -E_g, \tag{10}$$

where, for simplicity, we note $V(R) = V$. Still using the analogy of the mono-atomic gas, we can use the ideal gas law:

$$\frac{P}{\rho} = \frac{kT}{m}, \tag{11}$$

2 This calculation leads to a term $[V(r)P(r)]_0^R$, which is zero, since $V(0) = 0$ and $P(R) = 0$.

where T is the system's temperature[3], m the particle mass and k the Boltzmann constant. Here, we can use Mayer's relation that gives $c_P - c_V = k/m$, where c_P and c_V are the specific heat capacities (per mass) under constant pressure and volume, respectively. Moreover, with the definition of the internal energy (per mass) being $u = c_V T$, we have:

$$\frac{P}{\rho} = (\gamma - 1)u, \tag{12}$$

where γ is the ratio c_P/c_V. Injecting back this relation in the Virial theorem equation, we have:

$$3(\gamma - 1)E_i = -E_g, \tag{13}$$

where E_i is the total internal energy of the system. Finally, for a mono-atomic gas, the ratio γ is $5/3$, which delivers the final simplified form of the Virial theorem governing the internal dynamics of GCs:

$$2\,E_i = -E_g. \tag{14}$$

Hence, the total energy of the system is $E_{\text{Total}} = E_i + E_g = -E_i$, which implies a negative heat capacity system. Such negative heat capacity is completely counter-intuitive, meaning that an energy input in the system will decrease its overall temperature, i.e., it gets colder.

3.4.2 *Core-collapse*

We now describe the long term evolution of GCs based on the implications of equation 14. For that, imagine that the system is embedded in a heat bath, which in practice can be considered as the outskirts of GCs. These outskirts are likely non-self-gravitating systems with a positive heat capacity, as they feel the influence of Milky Way tides, and its stars are much less bound to the cluster. In such scenario, if both systems (i.e., the inner GC regions, which we will just refer as the GC, and the heat bath) start with roughly the same temperature, and a small amount of energy is exchanged from the GC to the heat bath, the former's temperature will increase due to its negative heat capacity, and become hotter than the bath. As a consequence of the second law of thermodynamics, the energy flow will thus continue to proceed indefinitely from the warmer to the colder system, i.e., from the GC to the heat bath. Similarly, if the initial energy exchange happens from the heat bath to the GC, the later will now decrease its temperature until it reaches the absolute zero.

In systems like GCs, the energy flow tends to naturally go from the inner regions to the outskirts, by means of core stars that reach escape velocity and diffuse outwards. Moreover, inner regions tend indeed to be hotter given a

3 For a GC, the temperature can be associated with the mean squared velocity $\overline{v^2}$ of its stars, according to the relation $\frac{1}{2}m\overline{v^2} = \frac{3}{2}kT$.

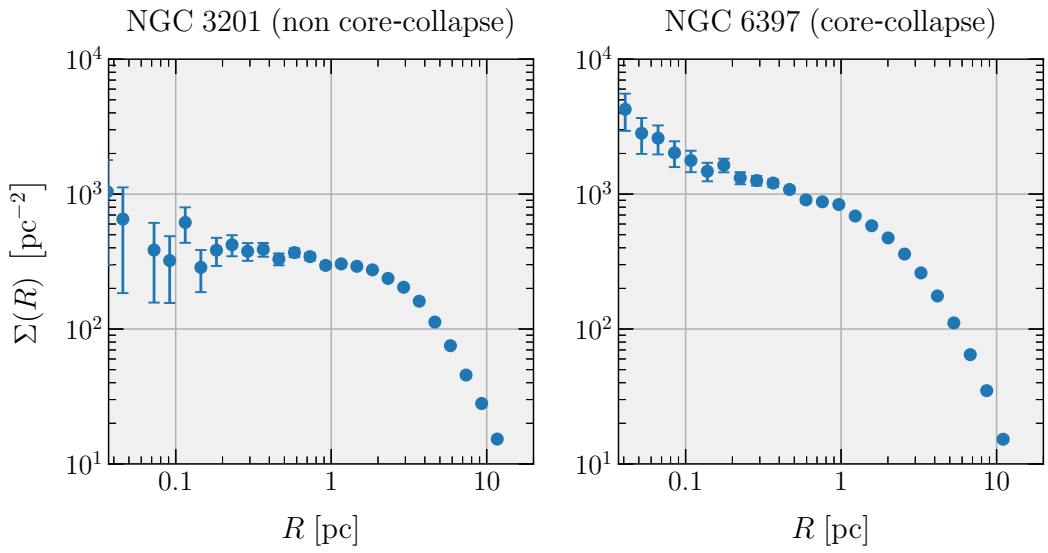

Figure 7: *Core-collapse:* Plot of the surface number density (in pc^{-2}) as a function of projected distance to the cluster's centre (in pc) for two Milky Way globular clusters: NGC 3201 (non core-collapse) and NGC 6397 (post core-collapse). The panels use data from Gaia EDR3, within the same range of absolute magnitudes. The angles are converted to distances with the distances from Baumgardt and Vasiliev, 2021. A uniform contribution from Milky Way interlopers (from fits with BALRoGO Vitral 2021) is subtracted. The error bars are a quadratic sum from the Poisson errors plus the errors on the fits. One clearly observes that in the case after core-collapse (i.e., NGC 6397), the inner regions of the cluster show a power-law shape of increasing densities.

high dispersion velocity induced by higher central densities. Under these circumstances, the scenario in which we are placed is the one where both the temperatures of the GC and its heat bath increase indefinitely. Because of the Virial theorem, we can connect the temperature increase witht the expected variation in the gravitational potential energy with $E_g = -2\,E_i$. Thus, if E_i increases (i.e., the system grows hotter), E_g becomes more negative. Since $E_g \propto -1/r$, becoming more negative means that the GC core's typical radii decrease, and the inner regions become denser and denser.

This phenomenon, where the core becomes increasingly denser is known and referred to as *core-collapse* or *gravothermal catastrophe* (Hénon, 1961; Lynden-Bell and Wood, 1968), and about a fifth of the Milky Way GCs are known to have experienced it (Djorgovski and King, 1986). Observationally, it is characterised by a steep increase in the cluster's inner densities, in a shape similar to a power law, such as in Figure 7.

Although such increase in the inner densities is indeed well observed in many clusters, it is eventually halted, the reason being that an energy input from hard binary mediated interactions helps to counter balance the gravothermal catastrophe, a process known as *binary burning*. As previously seen above in Section 3.1, hard binaries, which are naturally formed in such dense GC environments release a great amount of energy by getting harder after an encounter, and this energy is proportional to their masses and inversely proportional to their distance. Due to mass segregation, we also expect that the stars in the inner regions that will eventually form binaries are also more massive, relat-

ing to a higher binding energy that is able to halt core-collapse (Hills, 1975; Ostriker, 1985). Thus, although the fate of GCs in isolated environments is to naturally arrive to a post core-collapse state, they also naturally stop further core shrinking due to formation of hard binaries.

3.4.2.1 *Timescales of core-collapse: the role of black holes*

The core-collapse process has been studied through many aspects (e.g., Heggie 1979; Cohn 1980; Makino and Hut 1991; Goodman 1993), but an important disparity arises when analysing the timescales expected for core-collapse from classic dynamical arguments and the ages of Galactic GCs: Many Milky Way GCs are sufficiently dense to have experienced enough relaxation for core-collapse to occur in their lifetimes[4] (e.g., Spitzer 1987; Quinlan 1996 and equation 5 from Portegies Zwart and McMillan 2002). However, there is a clear bi-modality of core-collapsed and non core-collapsed clusters among the roughly 150 GCs observed in our galaxy, with only a fifth of them presenting a core-collapse structure (Djorgovski and King, 1986; Harris, 2010).

More recently, Chatterjee et al., 2013 showed that the bi-modality between core-collapsed and non core-collapsed clusters could indeed be associated with clusters having reached or not, respectively, the binary-burning phase. However, this study needed to assume relatively low initial cluster densities (with respect to recent observations of young massive star clusters – the expected local universe analogues of GC progenitors; Bastian et al., 2005; Scheepmaker et al., 2007; Portegies Zwart, McMillan, and Gieles, 2010b) in order to obtain correct timescales of core-collapse, which still seemed to arrive too fast. Thus, the question remains: What mechanism is able to effectively delay core-collapse, in order to explain the relatively small core-collapsed GC population in the Milky Way?

The answer to this question has been gradually shaped in the last decade, especially thanks to the improvement of our knowledge of black hole populations in GCs (e.g., Strader et al. 2012; Giesers et al. 2018; Giesers et al. 2019). In fact, by means of realistic N-body simulations (e.g., Morscher et al., 2015; Wang et al., 2016; Askar et al., 2017; Kremer et al., 2020a; Rodriguez et al., 2022), black holes are now suggested to be behind the observed delay of core-collapse in many GCs (Merritt et al. 2004; Mackey et al. 2007; Breen and Heggie 2013; Askar, Arca Sedda, and Giersz 2018; Kremer et al. 2018b; Kremer et al. 2019a). Black holes in GCs form and sink early (on $\lesssim 100\,\mathrm{Myr}$ timescales) to the cluster's centre due to a combination of their high masses and energy equipartition. Once in the inner regions of GCs, black holes dynamically interact with one another and with luminous stars. Those living in hard binaries thus provide a similar energy exchange towards the cluster's interior as in the classical stellar binary-burning scenario, but amplified due to the relative high masses of black holes compared to stars. This phenomenon has been referred to as *black hole binary-burning* (Kremer et al., 2020c).

This new theoretical comprehension of the physics governing GCs suggests that the ones without the characteristic inner cuspy structure of core-collapse probably harbour a segregated black hole population, responsible for the delay

4 GCs are particularly old systems with ages ranging up to 13 Gyrs (Marin-Franch et al., 2009).

of core-collapse. Nevertheless, black holes are expected to eventually leave the cluster, primarily from repeated dynamical encounters between black hole binaries and other black holes. These encounters harden the black hole binaries (e.g., Heggie, 1975) and also pump linear momentum into the black hole binaries and single black holes, ultimately leading to ejection of black holes from their host clusters (e.g., Kulkarni, Hut, and McMillan, 1993; Morscher et al., 2015; Kremer et al., 2020a). Also, when binary black holes merge, the massive amount of energy released in the form of gravitational waves is in general anisotropic (e.g., Barausse and Rezzolla, 2009; Lousto et al., 2012; Gerosa and Kesden, 2016), and conservation of linear momentum leads to gravitational kicks (Peres, 1962), whose amplitudes (Lousto et al., 2010) should be usually sufficient to eject the resulting black hole from its host cluster. Ultimately ($\gtrsim 10\,\mathrm{Gyr}$ timescales), the clustered black hole population becomes negligible, allowing other luminous stellar components to sink, as well as less massive compact objects such as neutron stars and white dwarfs. When these more luminous components collapse in the centre, forming the characteristic core-collapse inner cusp, *stellar* and *white dwarf* binary-burning effectively halts further shrinking of the core (Kremer et al., 2021).

3.5 TIDAL INTERACTIONS

Although GCs are many times modelled as isolated sources, they are in fact satellites that orbit a host galaxy, and are thus under constant effect of its gravitational field. Moreover, the extended shape of GCs imply that at different points of the cluster, the gravitational pull from the host is different, which induces tidal effects. In this section, we explore some of the features expected from systems undergoing tidal interactions with a more massive host.

3.5.1 *Tidal radius*

First, it is important to define a region wherein the satellite is better protected from tidal effects from the host. In a first moment, we can use the Jacobi radius r_J, which is the point where the effective potential of the two bodies (host and satellite) has a saddle point. To the first order, in a system with two point-like masses (i.e. Keplerian potential), this radius is given by:

$$r_J = r_{\mathrm{orbit}} \left[\frac{m}{M(3 + m/M)} \right]^{\frac{1}{3}}, \tag{15}$$

where r_{orbit} is the orbital radius of the satellite, m its mass and M the host's mass. The Jacobi radius is just a simplification of what we are really aiming for, since it assumes a very simple scenario that does not really take into account tidal effects. Binney and Tremaine, 2008 define the *tidal radius* r_t as the distance from the satellite's centre where the tidal effects from the host prune the satellite's tracers, which become unbound in such circumstances. It can be computed empirically as the distance where the density profile of the satellite displays a cut-off radius. Among the main simplifications of r_J over r_t, Binney and Tremaine, 2008 mention the non-sphericity of the system, non-circular or-

bits, and the extended shape of the satellites, implying a different gravitational pull at different points.

Given all the arguments above, the proper computation of the tidal radius within the frame of a realistic situation is better estimated empirically than with models assuming a similar radius for all the directions departing from the cluster's centre. However, for the sake of understanding the orders of magnitude and the extension of tidal effects, we use the theoretical tidal radius derived by Bertin and Varri, 2008a:

$$r_t = \left(\frac{GM_{sat}}{\Omega^2 \upsilon} \right)^{1/3} , \tag{16}$$

where the orbital frequency Ω at r_{orbit}, the epicyclic frequency κ at r_{orbit}, and a positive dimensionless coefficient υ related to the orbit's eccentricity, are defined as:

$$\Omega^2 = (d\Phi_{host}(r)/dr)_{r_{orbit}} / r_{orbit} , \tag{17}$$

$$\kappa^2 = 3\Omega^2 + \left(d^2\Phi_{host}(r)/dr^2 \right)_{r_{orbit}} , \tag{18}$$

$$\upsilon = 4 - \kappa^2/\Omega^2 . \tag{19}$$

Throughout the manuscript, this measure will be useful to probe the differences of GCs formed according to different theoretical scenarios, under the tidal effects of its host.

3.5.2 *Stellar streams*

As a stellar system orbits a host galaxy, its stars follow roughly the same bulk velocity, and thus the same path in the gravitational field. As a star reaches the escape velocity of the cluster, and evaporates through diffusion or ejection after a certain encounter, it is expected that, if its kinetic energy is not too high, it will nevertheless keep on the same orbital path as its progenitor system. This behaviour, extended to a system with a vast amount of stars such as GCs, will produce stellar streams formed by the debris of past tidal interactions. Figure 8 displays the stellar streams of a GC simulated in the work of Vitral and Boldrini, 2022, while orbiting a dwarf galaxy.

Such stellar streams provide useful information about the orbital path from its progenitor, which in turn helps to constrain the gravitational potential of the host where it belongs. The further analysis of stellar streams can also reveal interesting information about the past morphology and dynamical history of the progenitor satellite, which can help to constrain different formation scenarios of the satellite and its host. This field dedicated to decipher the past from relics of past dynamical, chemical and energetic evolution is known as *galactic archaeology*. The field of galactic archaeology was undoubtedly pushed forward with the discovery of the Sagittarius dwarf galaxy ongoing merger with the Milky Way (Ibata, Gilmore, and Irwin, 1994), and has much advanced since then. Algorithms such as the StreamFinder code (Malhan and Ibata, 2018) managed

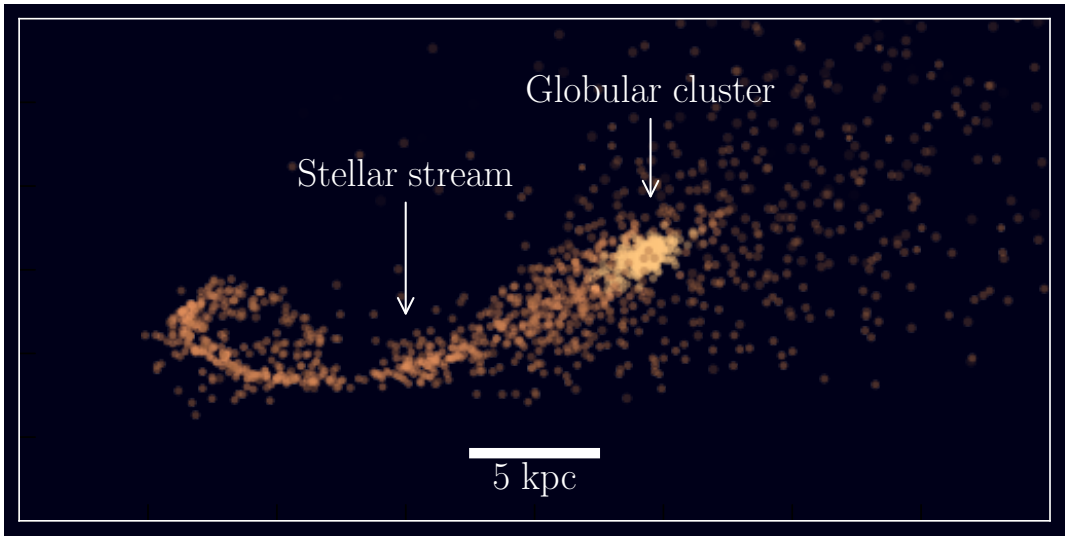

Figure 8: *Stellar stream:* Spatial distribution of a stellar stream formed along the orbital path of a simulated globular cluster, in the tidal field of its host galaxy. The figure uses data from Vitral and Boldrini, 2022.

to unveil several stellar streams in the Milky Way (e.g., Ibata et al., 2021; Martin et al., 2022; Malhan et al., 2022), along with other studies having detected streams of different GCs (e.g., Odenkirchen et al., 2001; Shipp et al., 2018; Ibata et al., 2019) and past galactic mergers (e.g., Helmi et al., 1999; Helmi et al., 2018; Haywood et al., 2018).

Although the detection of stellar streams remains difficult given observational difficulties such as contamination and low brightness, the large number of streams already unveiled by the works mentioned above now allows to constrain the kinematics, morphology and general structure of these streams from both observational (e.g., Erkal, Koposov, and Belokurov, 2017) and theoretical (e.g., Helmi and White, 1999) points of view. In particular, these constraints can be used to better understand the role of dark matter and gravity in astrophysics (Erkal and Belokurov, 2015; Thomas et al., 2018; Banik et al., 2021; Vitral and Boldrini, 2022). In this manuscript, we will not focus on the detailed mathematics that describes and allows us to detect stellar streams, but we will rather comment on its morphology and extension, from a more qualitative point of view, whenever studying the development of tidal streams in GCs orbiting a host galaxy. If the reader whises to learn more about these very interesting structures, the recent review by Helmi, 2020 is highly recommended.

4

INSTRUMENTS & DATA

... with nice instruments and the spirit of experiment, the progress of human knowledge will be rapid and discoveries made of which we have at present no conception. I begin to be almost sorry I was born so soon, since I cannot have the happiness of knowing what will be known a hundred years hence.

— Benjamin Franklin, (Franklin and Sparks, 1839).

4.1 GAIA

The releases of the *Gaia* astrometric mission undoubtedly marked a turning point in galactic dynamics, with an overall astrometric coverage of parallaxes, stellar velocities (mostly proper motions, but also a few line-of-sight velocities), positions and magnitudes for more than 10^9 stars in the Milky Way and beyond. During the time-span of my thesis, I managed to work extensively with both the *Gaia* Data Release 2 (DR2) and Early Data Release 3 (EDR3). Among the main qualities of the *Gaia* EDR3 data set that impacted my work (for a summary of the main aspects of this mission, see Gaia Collaboration et al. 2021; Lindegren et al. 2021), I highlight, compared to the previous *Gaia* DR2 data, the ~ 2 times better precision on proper motion measurements and better photometry precision, rendering more homogeneous CMDs. In practice, this yielded not only more reliability to the data I treated, but also improved completeness, especially for nearby clusters such as the ones analysed in the thesis.

Gaia EDR3 data presents an inconvenient issue related to spatially correlated systematic errors (e.g., Lindegren et al., 2021), which is usually associated to the telescope scan directions, even though there has been significant improvement from DR2 to EDR3. The modelling and correction of these systematics in our data was beyond the scope of our work, and we only used the statistical errors provided in the catalogue. In fact, the impact of these systematics on GCs is not yet very clear, with recent works focusing more on describing them rather than presenting a method to correct for them (e.g., Fardal et al., 2021). The most robust correction for these systematics in GCs is perhaps the one given in Vasiliev and Baumgardt, 2021 where the authors calculate an uncertainty floor of $\epsilon_\mu \sim 0.026$ mas yr^{-1}. The use of *Gaia* proper motions, magnitudes and spatial data was necessary in the works Vitral and Mamon, 2021; Vitral, 2021; Boldrini and Vitral, 2021; Vitral et al., 2022, according to the necessities listed below:

- Vitral and Mamon, 2021; Vitral et al., 2022: *Gaia* data was used to probe the outer dynamics and stellar distribution of the GCs NGC 6397 and NGC 3201. By doing so, the integration of the velocity distribution function over the line-of-sight could be better constrained by the data at outer

Figure 9: *Hubble Space Telesope:* The telescope Hubble photographed by the crew from the Discovery Space Shuttle during its second servicing mission. Credit: STS-82 Crew, STScI, NASA.

projected radii, giving more reliability for the measurements of the outer velocity anisotropy and projection effects in the cluster's centre, for example.

- Vitral, 2021: In this work, *Gaia* EDR3 data was used to derive values of centre, half-number radii, and bulk proper motions of over a hundred GCs from the NGC catalogue, along with nine Local Group dwarf spheroidal galaxies. This catalogue of bulk proper motions was one of the two single catalogues for GCs available for *Gaia* EDR3 (along with Vasiliev and Baumgardt, 2021), hence allowing for an independent cross-check of results.

- Boldrini and Vitral, 2021: *Gaia* data was used to compare the outcome of N-body simulations with real data, concerning the possible existence of massive stellar streams related to the cluster NGC 6397.

4.2 HUBBLE SPACE TELESCOPE

Saying the Hubble Space Telescope (HST) was the most important telescope since Galileo's invention risks to to be an understatement, giving not only the mission's unprecedent impact on science, but also its influence on the general public, which in turn was inspired by the beautiful images from the cosmos unveiled by this telescope. During my thesis, HST data was used in Vitral and Mamon, 2021 and Vitral et al., 2022, in order to probe the internal regions of nearby GCs, in particular NGC 3201 and NGC 6397. A precise motivation and explanation of these works is discussed in Chapter 8.

4.2.1 *Vitral & Mamon, 2021*

The HST data from Vitral and Mamon, 2021 were kindly provided by A. Bellini, who measured proper motions for over 1.3 million stars in 22 GCs, including NGC 6397 (Bellini et al., 2014). This dataset was provided in a particular master frame shape (for details, see Table 29 from Bellini et al. 2014 as well as Anderson et al. 2008), with both GC centre and proper motion mean shifted to zero. The first step in our analysis was to convert the positions and proper motions to the absolute frame.

We applied the Rodrigues, 1840 rotation formula to shift the relative positions back to their original centre to translate the GC stars to their true positions on the sky. We used the centre of Goldsbury et al., 2010, which was the one considered by Bellini et al., 2014. We then rotated the subset with respect to its true center, so that the stars originally parallel to the dataset's increasing x axis remained parallel to the right ascension increasing direction. We then verified our method by matching the stars in sky position with *Gaia*.

The HST PMs were measured relative to the bulk proper motion of the GC. We corrected the relative PMs of Bellini et al., 2014 with their provided PM corrections. We just added columns 4 and 5 to columns 31 and 32 from Table 29 of Bellini et al., 2014, respectively. We then converted the relative PMs to absolute proper motions by computing the bulk PM of NGC 6397 using the stellar proper motions provided by *Gaia*.

The small field of view of HST and the few pointed observations do not allow the observation of sufficiently numerous background quasars to obtain an absolute calibration of HST proper motions. On the other hand, the *Gaia* reference frame obtained with more than half a million quasars provides a median positional uncertainty of 0.12 mas for $G < 18$ stars (Gaia Collaboration et al., 2018d) and therefore allows us, by combining its accuracy with HST's precision, to know NGC 6397 proper motions with unprecedented accuracy.

4.2.2 *Vitral et al., 2022*

The HST data reduction and proper-motion computation from Vitral et al., 2022 were performed following the prescriptions of Bellini et al. (2014); Bellini et al. (2018) and Libralato et al. (2018); Libralato et al. (2019). In this Section, we briefly summarise the salient points. The detailed description of the workflow will be provided in an upcoming paper (Libralato et al., in preparation). The clusters targeted in this study were NGC 3201 and NGC 6397.

We made use of all suitable `_flc` exposures taken before 2019 with the Wide-Field Channel (WFC) of the Advanced Camera for Surveys (ACS) and with the Ultraviolet-VISible (UVIS) channel of the Wide-Field Camera 3 (WFC3). In a first pass, an initial set of positions and fluxes for the brightest and most isolated sources in each exposure was estimated via fits of the point-spread-function (PSF) to the brighter sources. The PSF model varies across the frame and depends on the frame. These sources, in combination with the *Gaia* Data Release 2 catalogue (Gaia Collaboration et al., 2016; Gaia Collaboration et al., 2018c), were then used to setup a common reference-frame system. Once onto the same reference system, all images were used at once to re-determine po-

sition and flux of all detectable sources, this time PSF-subtracting all close-by neighbours prior to the final fit. This second-pass-photometry stage is designed to enhance the contribution of faint sources, and yields better measurements in crowded regions (by subtracting all detected close-by neighbours before estimating position and flux of an object)[1].

Finally, proper motions were computed following Bellini et al., 2014, i.e. by fitting geometric-distortion-corrected positions transformed onto the same reference system as a function of epoch with a least-squares straight line. The slope of the straight line provides an estimate of the proper motion. Spatial patterns in proper motions indicate systematic errors, which were also corrected, both for low and high spatial frequency, with the prescriptions of Bellini et al., 2018 and Libralato et al., 2018; Libralato et al., 2019.

Various HST data sets were used to compute the astro-photometric catalogues of NGC 3201 and NGC 6397. We considered in the analysis only objects that were measured in both GO-10775 (ACS/WFC images in F606W and F814W filters; PI: Sarajedini) and GO-13297 (WFC3/UVIS exposures in F275W, F336W, and F438W filters; PI: Piotto) data. Finally, as described in, e.g., Bellini et al., 2017 and Libralato et al., 2018, the procedure used to compute proper motions removes any signature of the systemic rotation of the GC in the plane of the sky. Thus, one cannot infer rotation directly from our HST proper motions.

4.3 MULTI-UNIT SPECTROSCOPIC EXPLORER

In the work from Vitral and Mamon, 2021, we complemented the proper motions from NGC 6397 by using line-of-sight velocities that Husser et al., 2016 acquired with the Multi-unit spectroscopic explorer (MUSE) spectrograph on the Very Large Telescope (VLT) of the European Southern Observatory (ESO), in Chile, which operates in the visible wavelength range. Due to adaptive optics, this instrument's capability is elevated, providing exquisite resolution even though it is a ground based instrument.

A mosaic of 5×5 MUSE pointings led to an effective square field of view of 5 arcmin on the side. The bulk line-of-sight velocity from NGC 6397 was measured as $\langle v_{\rm LOS} \rangle = 17.84 \pm 0.07$ km s^{-1} (Husser et al., 2016). In a companion article, Kamann et al., 2016 assigned membership probabilities to this cluster's stars according to their positions in the space of line-of-sight velocity and metallicity, compared to the predictions for the field stars from the Besançon model of the Milky Way (Robin et al., 2003). The data, kindly provided by S. Kamann, contained 7 130 line-of-sight velocities, as well as the membership probabilities.

4.4 SOFTWARES

Whenever studying the outcomes of N-body simulations, the works of my thesis used the initial condition code MAGI (Miki and Umemura, 2018). Adopting

1 NGC 6397 was analyzed by Vitral and Mamon, 2021 using the proper-motion catalogue made by Bellini et al., 2014. The data reduction carried out in this manuscript mainly differs from that of Bellini et al., 2014 by the addition of the second-pass-photometry stage. As exhaustively described in Bellini et al., 2018 and Libralato et al., 2018; Libralato et al., 2019, second-pass photometry provides better results for faint sources and crowded environments than first-pass photometry.

a distribution-function-based method, it ensures that the final realisation of the cluster is in dynamical equilibrium (Miki and Umemura, 2018). Pierre Boldrini kindly performed our simulations with the high performance collision-less N-body code GOTHIC (Miki and Umemura, 2017). This gravitational octree code runs entirely on GPU and is accelerated by the use of hierarchical time steps in which a group of particles has the same time step (Miki and Umemura, 2017). On what concerns mock data sets of GCs, the velocities and spatial positions of its stars were derived with the AGAMA (Vasiliev, 2019a) software, and many of the dynamical analyses were performed with BALROGO (Vitral, 2021), which on its turn will be better described in Chapter 6.

Part II

METHODS

5 DENSITY PROFILES

Among the most remarkable objects in the sky
must be reckoned the globular clusters.
They suggest a number of interesting problems,
the most elementary and fundamental of which
is concerned with the statistical arrangement
of the stars they contain.

— Henry Crozier Keating Plummer, (Plummer, 1911).

The density profiles of GCs are a necessary and important component of Jeans mass-modelling (see Chapter 7), allowing to infer masses and extended shapes of these clusters. In particular, for Bayesian parametric approaches, the knowledge of various parametric forms is of great help to select between different mass models. Furthermore, the density profile can be used to infer membership probabilities of GCs stars with respect to the supposed constant contribution from field stars, or interlopers.

In this thesis, some specific parametric forms, highlighted here, were used to test different mass models of GCs. In particular, great effort has been put in well modelling the Sérsic model, which we not only explain in Section 5.1, but also present the issues and solutions related to the 3D deprojection of the known surface density parametrisation. Among the main qualities of this model, is the possibility to fit the inner slope, thus well accounting for both kind of GCs: the ones presenting cored density profiles (which are equally well fitted by King and Plummer models) with low Sérsic indexes, but also the ones with more cuspy inner densities (such as in the case of core-collapsed GCs), associated with higher Sérsic indexes. In the end, we also briefly comment about other models and present their analytical form.

5.1 SÉRSIC PROFILE

The Sérsic model (Sérsic, 1963; Sersic, 1968) is the generalisation of the $R^{1/4}$ law (de Vaucouleurs, 1948) to describe the surface brightness profiles of elliptical galaxies (Caon, Capaccioli, and D'Onofrio, 1993) and the bulges of spiral galaxies (Andredakis, Peletier, and Balcells, 1995). It has also been used to describe the surface density profiles of nuclear star clusters (Graham and Spitler, 2009), resolved dwarf spheroidal galaxies (Battaglia et al., 2006) and GCs (Barmby et al., 2007). The surface (mass or number) density (or equivalently surface brightness) of the Sérsic model is

$$\Sigma(R) = \Sigma_0 \exp\left[-b_n \left(\frac{R}{R_e}\right)^{1/n}\right], \tag{20}$$

where R is the projected distance to the source centre in the *plane-of-sky* (POS), R_e is the effective radius containing half of the projected luminosity, n is the

Sérsic index and Σ_0 is the central surface density. The term b_n is a function of n, obtained by solving the equation:

$$\Gamma(2n)/2 = \gamma(2n, b_n) \,, \tag{21}$$

where $\gamma(a, x) = \int_0^x t^{a-1} e^{-t} dt$ is the lower incomplete gamma function.

Since the Sérsic model represents well astronomical objects viewed in projection, it is important to know its corresponding three-dimensional (3D) density and mass profiles. These serve as a reference to compare to other possible observational tracers, as well as to dark matter. Moreover, the 3D density profile is required for modelling the kinematics of spherical structures, since it appears in the Jeans equation of local dynamical equilibrium. Since the Jeans equation also contains the total mass profile, the 3D mass profiles of stellar components are required to estimate the dark matter mass profile of elliptical and dwarf spheroidal galaxies.

Many authors assume that simple three-dimensional models resemble Sérsic models for certain values of the Sérsic index: It is often assumed that massive ellipticals and spiral bulges are well represented by the Hernquist, 1990 model (e.g., Widrow and Dubinski, 2005). On the other hand, dwarf spheroidal galaxies are often described as a Plummer, 1911 model (e.g. Muñoz et al., 2018, who also tried Sérsic and other models), while ultra diffuse galaxies have been described by the Einasto (Einasto, 1965; Navarro et al., 2004 [1] model (Nusser, 2019). Łokas and Mamon, 2001 noted that the projected Navarro, Frenk, and White (1996, hereafter NFW) model resembles an $n = 3$ Sérsic for reasonable concentrations. Finally, $n = 4$ Sérsic models are considered to resemble the Jaffe, 1983 model (Ciotti, Mancino, and Pellegrini, 2019). In Section 5.1.5, we compare these models to the deprojected Sérsic.

Unfortunately, the deprojection of the Sérsic surface density profile to a 3D (mass or number)[2] density profile, through Abel, 1826 inversion

$$\rho(r) = -\frac{1}{\pi} \int_r^{+\infty} \frac{d\Sigma}{dR} \frac{dR}{\sqrt{R^2 - r^2}} \,, \tag{22}$$

(e.g., Binney and Mamon, 1982), as well as the corresponding 3D mass (or number) profile

$$M(r) = \int_0^r 4\pi s^2 \rho(s)\, ds \,, \tag{23}$$

both involve the complicated Meijer G special function (Mazure and Capelato, 2002 for integer values of n, and Baes and Gentile, 2011 for general values of n) or the other complicated Fox H function (Baes and van Hese, 2011), neither of which are available in popular computer languages.

1 Navarro et al., 2004 showed how the Einasto model represents very well the density profiles of dark matter halos in dissipationless cosmological simulations, while Merritt et al., 2005 were the first to note the similar form to the Sérsic model, and Merritt et al., 2006 were first to realise that this model had been previously introduced by Einasto.

2 The number profile always has the same form as the mass profile, and is obtained by simply replacing $M(r)$ by $N(r)$ and M_∞ by N_∞, e.g. in Eqs. (25a), (25b), and (32c).

Following the shape of the analytical approximation to the $R^{1/4}$ law by Mellier and Mathez, 1987, Prugniel and Simien, 1997 (hereafter, PS) proposed an analytical approximation for the 3D density of the Sérsic profile:

$$\rho_{PS}(r) = \rho_0 \left(\frac{r}{R_e}\right)^{-p_n} \exp\left[-b_n \left(\frac{r}{R_e}\right)^{1/n}\right], \tag{24}$$

which yields a simple analytical form for the 3D mass profile

$$M_{PS}(r) = M_\infty \frac{\gamma[(3-p_n)\,n, b_n\,(r/R_e)^{1/n}]}{\Gamma[(3-p_n)\,n]}, \tag{25a}$$

$$M_\infty = 4\pi\,\rho_0\,R_e^3\,\frac{n\,\Gamma[(3-p_n)\,n]}{b_n^{(3-p_n)\,n}}, \tag{25b}$$

where p_n is a function depending only on n. PS calculated this dependence to be:

$$p_{n,PS} = 1 - \frac{0.594}{n} + \frac{0.055}{n^2}, \tag{26}$$

while Lima Neto, Gerbal, and Márquez, 1999 (hereafter, LGM) later improved this approximation with

$$p_{n,LGM} = 1 - \frac{0.6097}{n} + \frac{0.05463}{n^2}. \tag{27}$$

LGM indicate that equation (27) is good to 5 per cent relative accuracy for $0.56 \leqslant n \leqslant 10$ and $-2 < \log(r/R_e) < 3$. However, the power-law approximation at small radii is unjustified for small n. Indeed, as shown by Baes and Gentile, 2011, the central density profile converges to a finite value for $n < 1$ (and the inner density profile diverges only logarithmically for $n = 1$), as we will illustrate in Sect. 5.1.4.

Simonneau and Prada, 1999; Simonneau and Prada, 2004 (hereafter, SP) proposed the quasi-Gaussian expansion for the density profile

$$\rho_{SP}(r) = \frac{2}{\pi}\frac{b_n}{(n-1)}\frac{\Sigma_0}{R_e}\left(\frac{r}{R_e}\right)^{1/n-1}\sum_{j=1}^{5}\rho_j \exp\left[-b_n\lambda_j\left(\frac{r}{R_e}\right)^{1/n}\right], \tag{28}$$

where

$$\lambda_j = \left(1-x_j^2\right)^{-1/(n-1)}, \tag{29a}$$

$$\rho_j = w_j \frac{x_j}{\sqrt{1-\left(1-x_j^2\right)^{2n/(n-1)}}}, \tag{29b}$$

where x_j and w_j are 10 fit parameters. The individual SP density profiles (the terms inside the sum of Eq. 28) have a similar (but not the same) form as the PS/LGM one, hence a similar shape for the mass profile:

$$M_{SP}(r) = M_\infty \frac{4}{\pi\,(n-1)\,\Gamma(2n)}\sum_{j=1}^{5}\frac{\rho_j}{\lambda_j^{2n+1}}\gamma\left[2n+1, b_n\lambda_j\left(\frac{r}{R_e}\right)^{1/n}\right]. \tag{30}$$

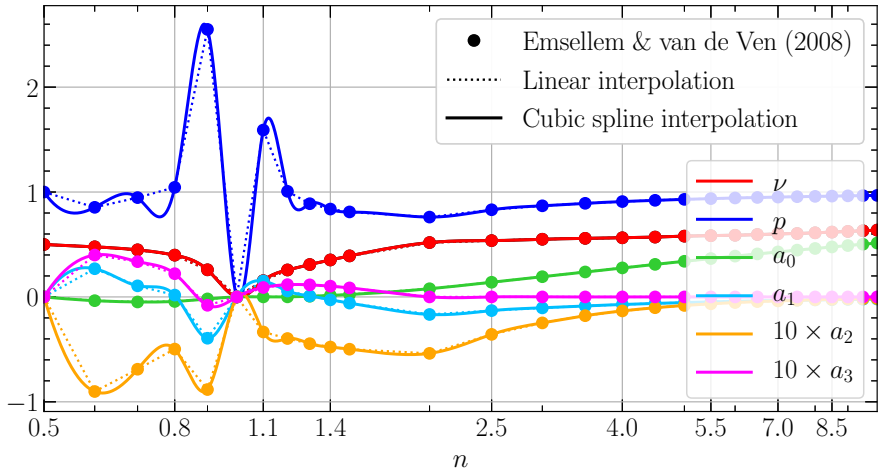

Figure 10: Variation with Sérsic index of the different parameters of the analytical approximation of Emsellem and van de Ven, 2008 for the deprojected Sérsic density profile (*filled circles*). The *solid* and *dotted* curves show the spline cubic and linear interpolations, respectively. At small n, the parameters vary abruptly and the interpolations (both linear and cubic) are thus uncertain. This figure was originally published in Vitral and Mamon, 2020.

Trujillo et al., 2002 proposed an ellipsoid formula, which in the limit of spherical symmetry becomes

$$\rho_T(r) = \frac{2^{(n-1)/(2n)}\, b_n}{\pi\, n}\, \frac{\Sigma_0}{R_e}\, r^{p_n(1/n-1)}\, \frac{K_{\nu_n}(r/R_e)}{1-\sum_{i=0}^{2} a_{n,i} \log^i (r/R_e)}\,, \tag{31}$$

where $K_\nu(x)$ is the modified Bessel function of the 2nd kind[3] of index ν, while ν_n, p_n, $a_{n,0}$, $a_{n,1}$, and $a_{n,2}$ are empirical functions of index n. Trujillo et al. only provided their results for integer and half-integer values of n for $n \leqslant 5$ and only integer values of n beyond. Emsellem and van de Ven, 2008 (hereafter, EV) repeated their analysis on a finer grid of n, with steps of 0.1 for $0.5 \leqslant n \leqslant 1.5$ and with one more term, $a_{n,3}$, in equation (31), involving 168 parameters. Unfortunately, as shown in Figure 10, these functions vary abruptly for $n \lesssim 1.2$. Moreover, neither Trujillo et al. nor Emsellem and van de Ven provide analytical forms for the mass profile.

In summary, all the previous approximations to the deprojected Sérsic model have drawbacks:

- PS, LGM (and Márquez et al., 2000, which is the same as LGM, but with a slightly different last term for p_n, which was a typo) are inappropriate for low n (Baes and Gentile, 2011) and less precise than claimed (Emsellem and van de Ven, 2008).
- SP is limited to $n \geqslant 1$, and is generally less precise than EV.
- Trujillo et al., 2002 is only given for half-integer values of n and their parameters vary wildly with n for $n \leqslant 1.5$. They do not provide a formula for the mass profile.

3 Trujillo et al., 2002 call this the modified Bessel function of the 3rd kind, as some others do.

- EV also suffers from discrete values of n, even though the grid is finer ($\Delta n = 0.1$ for $n \leqslant 1.5$). EV also did not provide a formula for the mass profile.

In Vitral and Mamon, 2020, we provided polynomial fits to the log residuals of the LGM approximation, allowing to reach high accuracy for both the 3D density and 3D mass profiles in a wide range of Sérsic indices. We present below the mathematical formalism and briefly explain our numerical integration method. We then show in Sect. 5.1.4 how our polynomial plus LGM approximation is orders of magnitude more precise than the formulae of LGM, SP, and Trujillo et al., 2002, as well as that of EV for low n and only slightly worse for $n \geqslant 3$.

5.1.1 *Equations using dimensionless profiles*

We expressed the general surface density, 3D density, and 3D mass (or number) profiles in terms of dimensionless functions:

$$\Sigma(R) = \frac{M_\infty}{\pi R_e^2}\,\widetilde{\Sigma}\left(\frac{R}{R_e}\right)\,, \tag{32a}$$

$$\rho(r) = \left(\frac{M_\infty}{4\pi R_e^3}\right)\,\widetilde{\rho}\left(\frac{r}{R_e}\right)\,, \tag{32b}$$

$$M(r) = M_\infty\,\widetilde{M}\left(\frac{r}{R_e}\right)\,. \tag{32c}$$

Hereafter, we will use $x = r/R_e$ and $X = R/R_e$. For the Sérsic model (see Graham and Driver, 2005 for a thorough review of the Sérsic profile), the dimensionless surface density profile is

$$\widetilde{\Sigma}_S(X) = \frac{b_n^{2n}}{2n\,\Gamma(2n)}\,\exp\left(-b_n\,X^{1/n}\right)\,, \tag{33}$$

while for the PS model, one can write the dimensionless 3D density and mass profiles as

$$\widetilde{\rho}_{PS}(x) = \frac{b_n^{(3-p_n)\,n}}{n\,\Gamma\left[(3-p_n)\,n\right]}\,x^{-p_n}\,\exp\left[-b_n x^{1/n}\right]\,, \tag{34}$$

$$\widetilde{M}_{PS}(x) = \frac{\gamma\left[(3-p_n)\,n, b_n\,X^{1/n}\right]}{\Gamma((3-p_n)\,n)}\,. \tag{35}$$

It is easy to show that the deprojection equation (22) becomes

$$\widetilde{\rho}(x) = -\frac{4}{\pi}\int_x^{+\infty}\frac{d\widetilde{\Sigma}}{dX}\frac{dX}{\sqrt{X^2-x^2}}\,, \tag{36}$$

where

$$\frac{d\widetilde{\Sigma}}{dX} \equiv \widetilde{\Sigma}'(X) = -\frac{b_n^{2n+1}}{2n^2\,\Gamma(2n)}\,X^{-1+1/n}\,\exp\left(-b_n x^{1/n}\right)\,. \tag{37}$$

The dimensionless mass profile is

$$\widetilde{M}(x) = \int_0^x y^2\,\widetilde{\rho}(y)\,dy = -\frac{4}{\pi}\int_0^x y^2\,dy\int_y^\infty \frac{\widetilde{\Sigma}'(X)}{\sqrt{X^2-y^2}}\,dX \tag{38a}$$

$$= -\int_0^x X^2\,\widetilde{\Sigma}'(X)\,dX - \frac{2}{\pi}\int_x^\infty X^2\,\sin^{-1}\left(\frac{x}{X}\right)\widetilde{\Sigma}'(X)\,dX$$

$$= +\frac{2}{\pi}\int_x^\infty x\,\sqrt{X^2-x^2}\,\widetilde{\Sigma}'(X)\,dX\,, \tag{38b}$$

where equation (38b) is obtained by inversion of the order of integration in the second equality of Eq. (38a).

5.1.2 *Numerical integration*

We numerically evaluated the dimensionless 3D density (Eq. [36]) and mass (Eq. [38b]) profiles by performing the numerical integrations in cells 50×100 of $[\log n, \log(r/R_e)]$, with $\log 0.5 \leqslant \log n \leqslant 1$ and $-3 \leqslant \log(r/R_e) \leqslant 3$. Numerical calculations were done with Python's SCIPY.INTEGRATE.QUAD. For both density and mass profiles, we split the numerical integration in two, i.e.

$$\int_a^b f(X)\,dX = \int_a^{X_{crit}} f(X)\,dX + \int_{X_{crit}}^b f(X)\,dX\,, \tag{39}$$

where $\exp\left(-b_n X_{crit}^{1/n}\right) = 10^{-9}$ and $a \leqslant X_{crit} \leqslant b$. We used a relative tolerance of `epsrel` $= 10^{-4}$ and `limit` $= 1000$ in both integrals. If $X_{crit} \notin [a, b]$, we also used `epsrel` $= 10^{-4}$ and `limit` $= 1000$, but for a single integral from a to b.

We performed our analysis using either the highly accurate approximations for b_n of Ciotti and Bertin, 1999 (hereafter, CB) or the exact (numerical) solutions of Eq. (21). We noticed that the difference between these two approaches was negligible (see Sect. 5.1.4).

We then fit two-dimensional polynomials to both $\log[\widetilde{\rho}_{LGM}(x,n)/\widetilde{\rho}(x,n)]$ and $\log\left[\widetilde{M}_{LGM}(x,n)/\widetilde{M}(x,n)\right]$, for geometrically spaced x and n, i.e. writing

$$\log\left[\widetilde{f}_{LGM}/\widetilde{f}\right] = -\sum_{i=0}^{k}\sum_{j=0}^{k-i} a_{ij}\log^i x\,\log^j n \tag{40}$$

with polynomial orders $2 \leqslant k \leqslant 12$. For this, we used Python's package NUMPY.LINALG.LSTSQ. We found the smallest residuals for order 10 polynomials when using both the b_n approximation of CB and b_n by numerically solving Eq. (21). The coefficients are provided in Appendix A.1. In the following, we present the results relative to the CB approximation, since it is a simpler and more used model, and also because our order 10 polynomial fits remarkably well the exact b_n case.

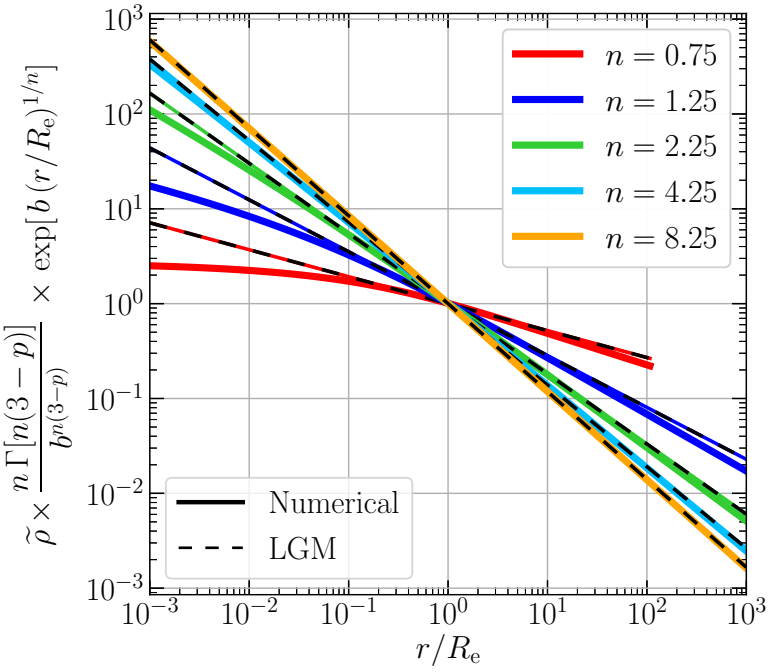

Figure 11: Illustration of the accuracy of the PS formula with the LGM coefficients for p_n. The *solid curves* show the numerically estimated profiles, while the *coloured-dashed curves* show the LGM approximation. This figure was originally published in Vitral and Mamon, 2020.

5.1.3 *Numerical precision: Tests for known simple analytical deprojections ($n = 0.5$ and 1)*

For Sérsic indices $n = 0.5$ and $n = 1$, there are analytical solutions for the 3D density profile:

$$\widetilde{\rho}(x) = \begin{cases} 4\,\dfrac{b_{0.5}^{3/2}}{\sqrt{\pi}}\,\exp\left[-b_{0.5}\,x^2\right] & (n = 0.5)\,, \\ \\ 2\,\dfrac{b_1^3}{\pi}\,K_0(b_1 x) & (n = 1)\,, \end{cases} \tag{41}$$

where $K_0(x)$ is the modified Bessel function of the second kind of index 0. We can therefore verify the numerical integration of Eq. (36) for these two Sérsic indices.

For the interval $-3 \leqslant \log(r/R_e) \leqslant 3$, we compared the densities from numerical integration with the analytical formulae of Eq. (41), using the CB approximation for b_n. The match was very good, with *root-mean-square* (rms) values of $\log(\widetilde{\rho}_{ana}/\widetilde{\rho}_{num})$ of 1.5×10^{-7} and 2×10^{-8} for $n = 0.5$ and $n = 1$, respectively. The same comparison using the exact b_n yields 7×10^{-5} and 2×10^{-8}, respectively (with one particular value of r causing the higher rms for $n = 0.5$).

5.1.4 *Results*

As seen in Figure 11, the 3D density profiles depart from the power laws proposed by LGM at low n, especially for low radii, as expected by the asymptotic

expansions of Baes and Gentile, 2011 for $n < 1$. Interestingly, the LGM formula is also inadequate at low radii for $n = 1.25$ and 2.25, although the asymptotic expansion of Baes and Gentile indicate power-law behaviour at small radii. This poor accuracy of the LGM approximation at low radii is a serious concern when performing kinematic modelling of systems with possible central massive black holes. For example, *Gaia* positions and proper motions for stars in nearby GCs extend inwards to 0.7 arcsec from the centre, which translates to $0.002\,R_e$.

We now compare the accuracy of the different analytical approximations for the 3D density and 3D mass profiles. Figure 12 displays the ratio $\log\left(\widetilde{f}_{\rm model}/\widetilde{f}\right)$, for $\widetilde{f} = \widetilde{\rho}$ and $\widetilde{f} = \widetilde{M}$, for the main analytical approximations available in the literature, along with our new model

$$f_{\rm new}(x,n) = f_{\rm LGM}(x,n)\ {\rm dex}\left[\sum_{i=0}^{10}\sum_{j=0}^{10-i} a_{i,j}\log^i x\,\log^j n\right]\ , \tag{42}$$

where f is either the 3D density or 3D mass profile. One sees that our model presents a more continuous behavior over the full range of Sérsic indices and radii. Our approximation displays the smallest residuals among all models for $n \leqslant 3$ (except that SP outperforms our model for mass estimates at $r > 3\,R_e$ for $n > 1.3$).

The variation of accuracy with Sérsic index can be seen in more detail in Figure 13, which displays the rms of $\log\left(\widetilde{f}_{\rm model}/\widetilde{f}\right)$, over the radial domain where $\rho(r) > 10^{-30}\,\rho(R_e)$, of the main analytical approximations, using 1000 log-spaced Sérsic indices. Figure 13 indicates that the SP (respectively, EV) approximation for density has rms relative accuracy worse than 2.3% (0.01 for $\log\left(\widetilde{f}_{\rm model}/\widetilde{f}\right)$) for $n < 1.6$ (respectively 1.3). Our approximation (Eq. [42]) is more accurate than SP for $n < 4.3$ (density) and $n < 3.1$ (mass), and is more accurate than EV for $n < 3.4$ (density), except for their particular choices of n. Figure 13 shows that the EV approximation is much more accurate at specific values of n (note that our grid does not contain all of these values precisely, so the EV approximation is even more accurate at these specific values of n). However, these specific values of n represent a negligible measure compared to the full continuous range of $0.5 \leqslant n \leqslant 10$. Therefore, the EV approximation at low n is not reliable for estimating the 3D density profile.

We analyzed the results shown in Figure 13 using b_n from either CB or by numerically solving Eq. (21), and the results were very similar. In fact, the results are similar if we adopt one form of b_n in the numerical integration and the other in the analytical approximations. This can be explained by the fact that $\log\left(\widetilde{f}_{\rm LGM}/\widetilde{f}\right)$ is practically the same for both estimates of b_n, yielding a very similar fit of Eq. (40).

Finally, we provide in Table 1 the rms accuracies computed over the full range of radii $-3 \leqslant \log(r/R_e) \leqslant 3$ and $0.5 \leqslant n \leqslant 10$, except for the SP formula, which does not allow $n \leqslant 1$, and also avoiding the domain where $\rho(r) < 10^{-30}\,\rho(R_e)$. One sees that, averaging over all Sérsic indices, our approximation is much more accurate than all others (with over 10 times lower rms).

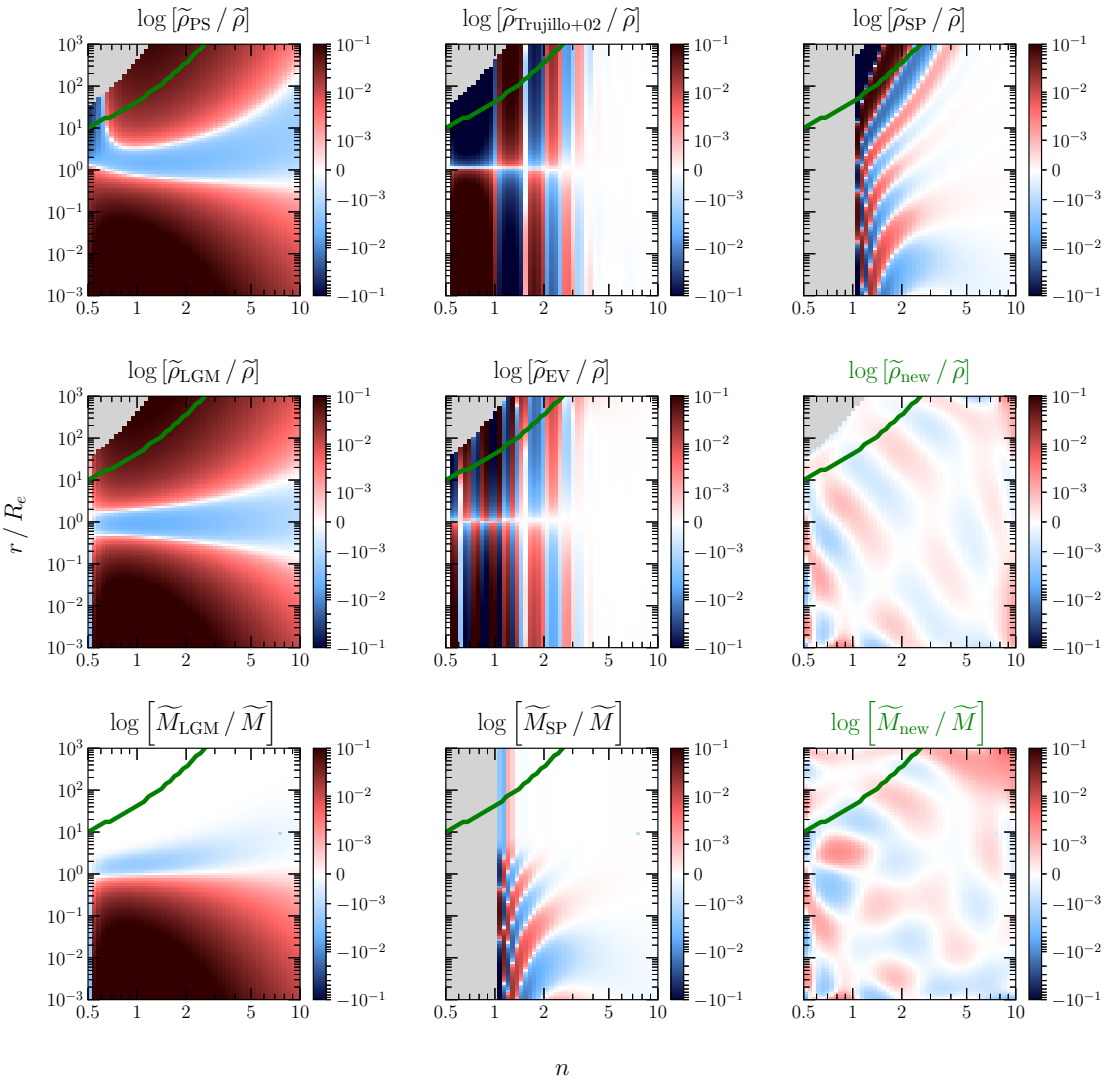

Figure 12: Accuracy of deprojected density (*top 6 panels*) and mass (*3 bottom panels*) of the different analytical approximations (LGM: Lima-Neto et al. 1999; SP: Simonneau & Prada 1999, 2004; Trujillo+02: Trujillo et al. 2002; EV: Emsellem & van de Ven 2008; our new one (Eq. [42], with green-coloured titles) as a function of both Sérsic index (abscissae) and radii (ordinates). The colour scale given in the *vertical colour bars* are linear for log ratios between –0.001 and 0.001 and logarithmic beyond. The *grey region* and *green curves* in the upper left of the density panels are for regions where the numerical integration reached the underflow limit or density 10^{-30} times $\rho(R_e)$, respectively, because of the very rapid decline of density at large radii for low n, and also covers $n < 1$ that is not covered by the SP model. Note that the EV and Trujillo+02 models perform better at specific values of n that are often missed in our grid. This figure was originally published in Vitral and Mamon, 2020.

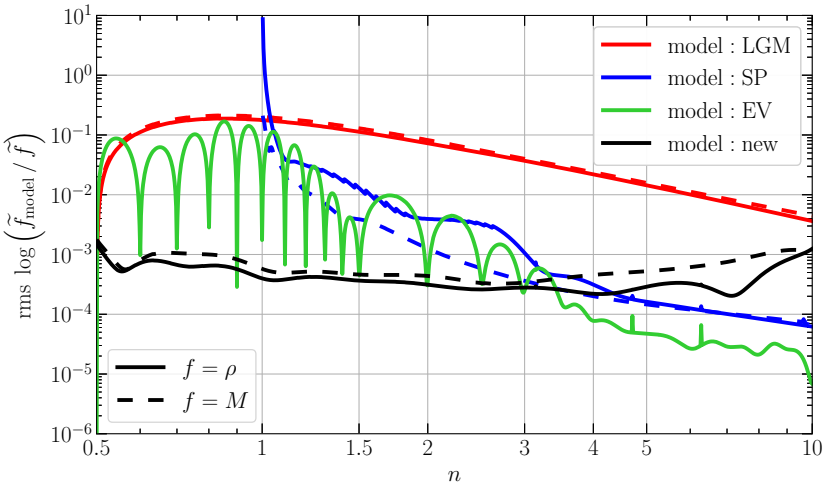

Figure 13: Accuracy of different approximations (LGM: Lima-Neto et al. 1999; SP: Simonneau & Prada 1999, 2004; EV: Emsellem & van de Ven 2008; our new one (Eq. [42]) as a function of Sérsic index. Note that the EV model performs better at specific values of n that are often missed in our logarithmic grid of 1000 values of n. This figure was originally published in Vitral and Mamon, 2020.

Table 1: Accuracy of approximations to 3D density and mass profiles

Author	rms $\log\left(\frac{\widetilde{\rho}_{\rm approx}}{\widetilde{\rho}_{\rm num}}\right)$	rms $\log\left(\frac{\widetilde{M}_{\rm approx}}{\widetilde{M}_{\rm num}}\right)$
Prugniel & Simien 97	0.1052	0.1187
Lima Neto et al. 99	0.0905	0.1021
Simonneau & Prada 04 ($n > 1$)	0.0238	0.0098
Trujillo et al. 02	0.1496	–
Emsellem & van de Ven 08	0.0382	–
new	**0.0005**	**0.0007**
hybrid-1 (optimized for $n_{\rm cut}$)	**0.0004**	**0.0005**
hybrid-2 (optimized for $r_{\rm cut}$)	**0.0004**	**0.0005**

Notes: The rms accuracies are computed over the full range of radii $-3 \leqslant \log(r/R_e) \leqslant 3$ (100 steps) and $0.5 \leqslant n \leqslant 10$ (50 steps), except for the SP formula, which does not allow $n \leqslant 1$, and also avoiding the domain where $\rho(r) < 10^{-30}\,\rho(R_e)$. Trujillo et al., 2002 and EV do not provide analytical mass profiles. The lower two rows display hybrid models, both with our new approximation $\widetilde{\rho}_{\rm new}$ for $n < 3.4$ and $\widetilde{\rho}_{\rm eV}$ for $n \geqslant 3.4$. The first hybrid model has a mass profile $\widetilde{M}_{\rm new}$ for $n < 3$ and $\widetilde{M}_{\rm SP}$ for $n \geqslant 3$, while in hybrid model 2, the mass profile is $\widetilde{M}_{\rm new}$ for $r < R_e$ and $\widetilde{M}_{\rm LGM}$ for $r \geqslant R_e$. This table was originally published in Vitral and Mamon, 2020.

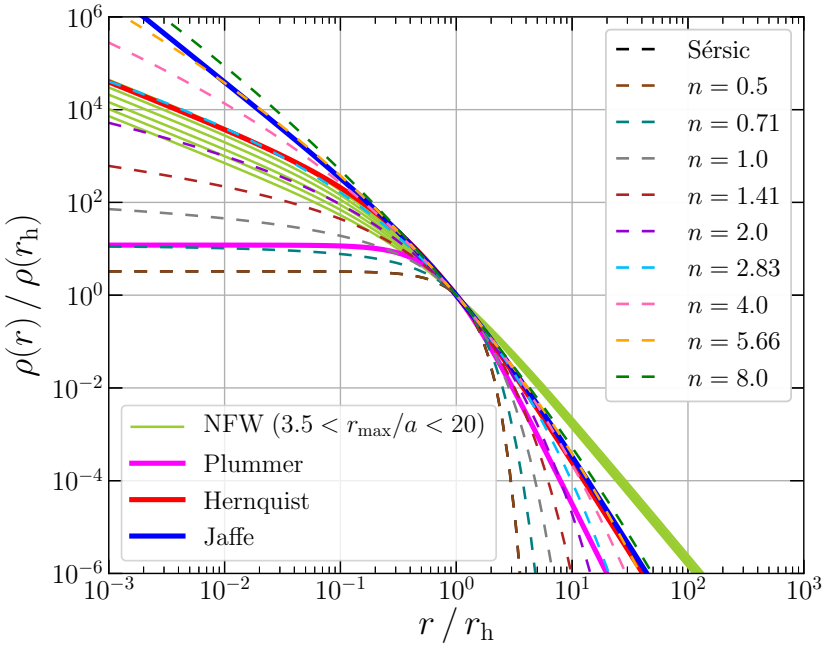

Figure 14: Comparison of other known three-dimensional density profiles and the deprojected Sérsic density profile for certain values of the Sérsic index n. All density profiles are normalised to the value at the three-dimensional half-mass radius, $r_{\rm h}$ (see text). The different NFW models can be distinguished at low radii, where the density increases with $r_{\rm max}/a$. This figure was originally published in Vitral and Mamon, 2020.

5.1.5 *Comparison of deprojected Sérsic to other popular models*

Figure 14 compares the density profiles, normalised to the half-mass radius $r_{\rm h}$, for which we applied the following relations:

$$\rho(r) \propto \begin{cases} \left[1+\left(\frac{r}{a}\right)^2\right]^{-5/2} & \text{(Plummer)}\,, \\ \left(\frac{r}{a}\right)^{-2}\left[1+\left(\frac{r}{a}\right)\right]^{-2} & \text{(Jaffe)}\,, \\ \left(\frac{r}{a}\right)^{-1}\left[1+\left(\frac{r}{a}\right)\right]^{-3} & \text{(Hernquist)}\,, \\ \left(\frac{r}{a}\right)^{-1}\left[1+\left(\frac{r}{a}\right)\right]^{-2} & \text{(NFW)}\,, \\ \exp\left[-\left(\frac{r}{a}\right)^{1/n}\right] & \text{(Einasto)}\,. \end{cases} \tag{43}$$

The ratio of half-mass radius to scale radius r_h/a is given by

$$\frac{r_h}{a} = \begin{cases} \left[\left(1+2^{1/3}\right)/\sqrt{3}\right] & \text{(Plummer)}\,, \\ 1 & \text{(Jaffe)}\,, \\ \left(1+\sqrt{2}\right) & \text{(Hernquist)}\,, \\ \mathrm{dex}\left(-0.209+0.856\,\log c-0.090\log^2 c\right) & \text{(NFW)}, \\ \left[P^{(-1)}(3n,1/2)\right]^n & \text{(Einasto)}\,. \end{cases} \tag{44}$$

In Eq. (44) for NFW, $c = r_{max}/a$, where r_{max} is the maximum allowed radius (because, contrary to all other models discussed here, the NFW model has logarithmically divergent mass). Also, for Einasto, $P^{(-1)}(a,y)$ is the inverse regularized lower incomplete gamma function, i.e. $x = P^{(-1)}(a,y)$ satisfies $\gamma(a,x)/\Gamma(a) = y$.[4] For Sérsic, the conversion was done by fitting an order 3 polynomial and recovering the relation $r_h/R_e = \sum_{j=0}^{3} a_i \log^i n$, where $\{a_0, a_1, a_2, a_3\} = \{1.32491, 0.0545396, -0.0286632, 0.0035086\}$. The dex function stands for the power of ten of the argument.

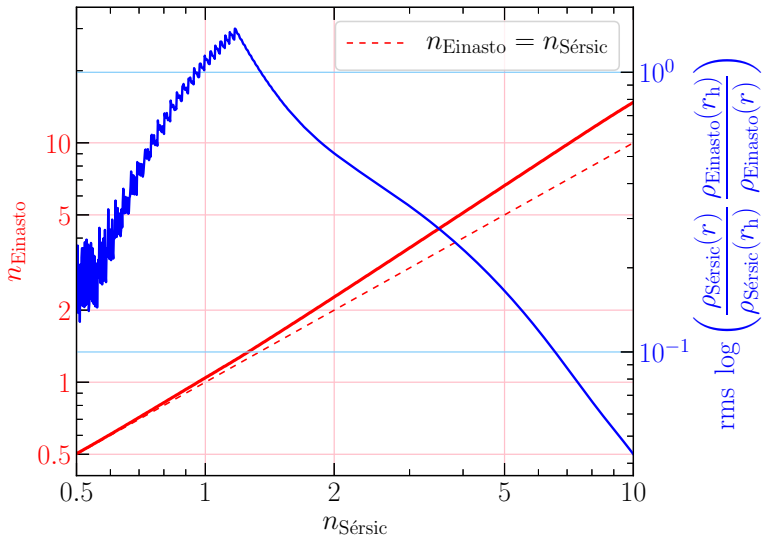

Figure 15: Comparison of Einasto and deprojected Sérsic density profiles (both normalised to half-mass radius). **Red**: best-fit Einasto index (dashed line is $n_{\rm Einasto} = n_{\rm Sérsic}$). **Blue**: rms of best fit, over the radial range $10^{-3} < r/R_e < 10^3$. This figure was originally published in Vitral and Mamon, 2020.

The Einasto model, which is the 3D analog of the Sérsic model, resembles the deprojected Sérsic model. Figure 15 shows the best-fit values of the Einasto index, $n_{\rm Einasto}$ in terms of the Sérsic index. The relation (red curve) is almost one-to-one (dashed line). The figure also shows the rms over all radii and best-fit indices (blue curve).

4 The inverse (regularized) incomplete gamma function is available in many computer languages, e.g. Python (SCIPY package), Fortran, Matlab, Mathematica, and Javascript.

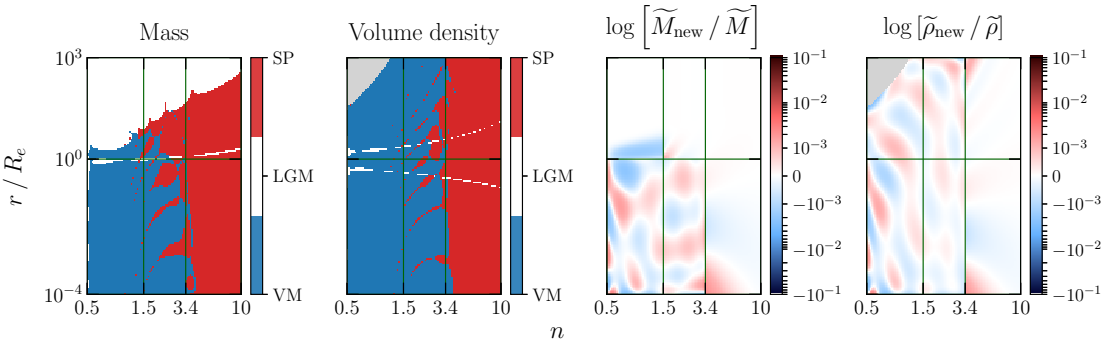

Figure 16: Characteristics of approximations to the mass and density profiles of the deprojected Sérsic model. **Left two panels**: Most precise approximation. SP stands for Simonneau and Prada, 2004, LGM stands for Lima Neto, Gerbal, and Márquez, 1999 and VM stands for the new VM20bis coefficients applied to the Vitral and Mamon, 2020 method. The white curves indicate a thin region preferred by the LGM approximation. **Right two panels**: Accuracy of deprojected mass (*left*) and density (*right*) of the hybrid model using VM20bis coefficients, LGM and SP, with respect to the numerical integration done with MATHEMATICA. This is the analog of figure 3 of VM20: The color scale is linear for log ratios between –0.001 and 0.001 and logarithmic beyond. Both sets of figures employ a $[100 \times 150]$ grid of $[\log n \times \log(r/R_e)]$, which is shown in all four panels. The *gray region* in the upper left of each of the density panels is for regions where the numerical integration of MATHEMATICA reached the underflow limit because of the very rapid decline of density at large radii for low n. This figure was originally published in Vitral and Mamon, 2021.

5.1.6 *New coefficients for VM20 approximation extending to very low radii*

The coefficients of the VM20 approximation were originally calculated for a logarithmic grid of $[n \times r/R_e]$ with $-3 \leqslant \log(r/R_e) \leqslant 3$ (100 steps) and $0.5 \leqslant n \leqslant 10$ (50 steps). However, data from both Gaia and HST could extend to even lower radii than $0.001\,R_e$. We therefore recomputed, in Vitral and Mamon, 2021, the VM20 approximation, using a different region of the $[n \times r/R_e]$ domain, and an even finer grid.

We used the same approach as in VM20, but this time we performed the numerical deprojection of the Sérsic profile with MATHEMATICA 12, instead of PYTHON. Given Figure 12 and the lower limit of r/R_e we needed to attain, we calculated the best VM20 parameters for a new logarithmic spaced region $[n \times r/R_e]$ limited to $-4 \leqslant \log(r/R_e) \leqslant 3$ (150 steps) and $0.5 \leqslant n \leqslant 3.5$ (100 steps). The resulting coefficients $a_{i,j}$, presented in the same way as VM20 (see their Eq. [28]), can be found online[5] and we hereafter refer to them as VM20bis.

5.1.6.1 *Choice of deprojection approximation*

The two left panels of Figure 16 display the best fitting approximations in 100×150 grid in $[\log n \times \log(r/R_e)]$. We included in MAMPOSSt-PM a simpli-

5 https://gitlab.com/eduardo-vitral/vitral_mamon_2020b.

fied choice of best approximations to the deprojected Sérsic mass and density profiles. For the mass profile we used

- $n \times r/R_e \in [0.5; 1.5] \times [1; 10^3]$: LGM
- $n \times r/R_e \in [0.5; 3.4] \times [10^{-4}; 1)$: VM20bis
- $n \times r/R_e \in (3.4; 10] \times [10^{-4}; 1) \cup (1.5; 10] \times [1; 10^3]$: SP

For the density profile, the division was even simpler:

- $n \times r/R_e \in (3.4; 10] \times [10^{-4}; 10^3]$: SP
- $n \times r/R_e \in [0.5; 3.4] \times [10^{-4}; 10^3]$: VM20bis

The outcome of this approximation is highly accurate, as seen in the right panels of Figure 16 (which are the equivalent of figure 3 in VM20), with the grid lines indicating the divisions adopted for the 3 approximations. The reader can verify that the relative precision of this hybrid model is on the order of $\sim 0.1\%$.

5.2 KING MODELS

King-Michie models (King, 1966; Michie, 1963) depart from a given distribution function in phase space, usually of the form

$$f(E) = \begin{cases} 0 & \text{for } E \geqslant E_0 \\ K\left[e^{-\beta(E-E_0)} - 1\right] & \text{for } E < E_0 \end{cases}, \tag{45}$$

where K, β, and E_0 are constants, $E = v^2/2 + \phi(r)$, $\phi(r)$ is the gravitational potential and $f(E)$ is the mass probability distribution function in phase space. These models have been shown to fit remarkably well some of the galactic GCs, but still present some inconveniences. For instance, their density profile, obtained by integrating $f(E)$ over the velocity space, is a function of the potential rather than the distance to the cluster's centre, which forces the user to solve the Poisson equation, thus requiring more information on the system than just the radial positions. If we define $W = -\beta\phi(r)$, and fix $\nabla^2 W = -9$, then one derives a relation very close to an empirical representation of this density profile, presented in King, 1962:

$$\rho(r) = \frac{k}{\pi r_c \left[1 + (r_t/r_c)^2\right]^{\frac{1}{2}}} \frac{1}{z^2}\left[\frac{1}{z}\cos^{-1} z - \left(1 - z^2\right)^{\frac{1}{2}}\right], \tag{46}$$

where $k = Ke^{\beta\phi_0}$, with ϕ_0 the gravitational potential at $r = 0$, r_c the core radius, where the surface density reaches half its value at $r = 0$, and r_t a cut-off tidal radius which the model supposes to be the maximum extend of the cluster. This tidal radius is shown to have a similar dependence on $r_{orbit}\left(\frac{M_{sat}}{M_{host}}\right)^{1/3}$ (here, r_{orbit} is the orbital radius of the satellite, M_{sat} its mass and M_{host} the

host's mass), such as the Jacobi radius from Eq. 15 and the theoretical tidal radius from Eq. 16. Finally, z is defined as

$$z = \left[\frac{1 + (r/r_c)^2}{1 + (r_t/r_c)^2}\right] . \tag{47}$$

This expression can be used, when one does not wish to solve the Poisson equation above, but regards an specific scenario. In any case, another drawback from King models is that it always presents an inner cored profile, and it is known that some clusters, such as the ones who have undergone core-collapse, can have an inner cusp in their density profiles. Thus, an analytical model whose the inner cusp can be fitted, such as the Sérsic model, is in principle more advantageous for studies targeting the cluster's inner dynamics. The existence of a tidal cut in the King models can also be worrying, specially when targeting clusters with an extended envelope, such as presented in Kuzma et al., 2016; Kuzma, Da Costa, and Mackey, 2018. Models with an extended shape that converges at infinity can, in principle, better model these structures.

5.3 PLUMMER PROFILE

The Plummer model (Plummer, 1911), is assumed to reproduce well the density profiles of many cored GCs. It can be derived by developing the potential of a polytropic gas of index equals 5. The respective density profile is given by

$$\rho(r) = \frac{\rho_0}{[1 + (r/a_P)^2]^{5/2}} , \tag{48}$$

where a_P is the Plummer scale radius (that happens to be also the 2D half-mass radius) and ρ_0 is the density at $r = 0$. This model has a total mass (at infinity) of $M_\infty = \frac{4\pi}{3}\rho_0 a_P^3$.

5.4 KAZANTZIDIS PROFILE

The Kazantzidis et al., 2004 profile is motivated from dynamical simulations of repeated tidal encounters, and its density profile is given by

$$\rho(r) = \rho_a (r/a_K)^{-1} \exp(1 - r/a_K) , \tag{49}$$

where a_K is the Kazantzidis scale radius (it is also the radius of density slope -2), and ρ_a is a the density at radius $r = a_K$. Notice that this profile diverges towards $r = 0$.

5.5 HERNQUIST PROFILE

The Hernquist, 1990 profile is a very good approximation to the deprojection of the $R^{1/4}$ de Vaucouleurs, 1948 law, and has a density profile described as below

$$\rho(r) = \rho_a \frac{8(r/a_H)^{-1}}{(1 + r/a_H)^3} , \tag{50}$$

where a_H is the Hernquist scale radius, and ρ_a is the density at radius $r = a_H$. Notice that this profile diverges towards $r = 0$.

6 ASTROMETRY & PHOTOMETRY

It [The Universe] is written in mathematical language, and its characters are triangles, circles and other geometric figures, without which it is impossible to humanly understand a word; without these, one is wandering in a dark labyrinth.

— Galileo Galilei (Galilei and GRASSI, 1618).

During my thesis, I constructed different algorithms and methods to fit astrometric and photometric data from mainly *Gaia* and *HST* GCs, but that can also be applied to other data sets. In this Chapter, I will explain the fitting procedures used in those algorithms, aimed at measuring centres, bulk proper motions and structural parameters of spherical stellar systems, as well as confidence regions of colour-magnitude diagrams. I will also comment on the non-Gaussianity of field stars proper motions, and propose the solutions related to its modelling.

The compilation of these methods has been reported in Vitral and Mamon, 2020; Vitral, 2021; Boldrini and Vitral, 2021; Vitral and Boldrini, 2022, and are available as an open source Python code called BALRoGO: Bayesian Astrometric Likelihood Recovery of Galactic Objects. The link to access this repository is available at the footnote link[1].

6.1 FITS OF CENTRE & SURFACE DENSITY

6.1.1 *Centre estimation*

Although BALRoGO allows for an iterative frequentist approach to estimate the cluster's centre, this can be dangerous when dealing with objects that suffer from crowding issues (Arenou et al. 2018), since the amount of stars decreases when one approaches the centre too much. Therefore, as for many other steps, we opted for a Bayesian fit of the galactic object centre.

This is done by fitting a Plummer profile (Plummer 1911) plus a constant contribution of interlopers to the surface density of the stars inside a cone in the field of view. Such approach aims for nothing more than finding a centre of mass of the stellar distribution, by fitting the centre that best suits an spherical shaped collection of stars. Even if the galactic object does not follow precisely a Plummer model (e.g., core-collapsed GCs), other profiles, such as Sérsic (Sérsic, 1963; Sersic, 1968), Hernquist (Hernquist, 1990) or Kazantzidis (Kazantzidis et al., 2004) for example also follow a circular symmetry, and therefore should have their centres well determined by a Plummer fit. In addition, allowing for the contribution of interlopers in the fit enables the user not to lose many

1 https://gitlab.com/eduardo-vitral/balrogo.

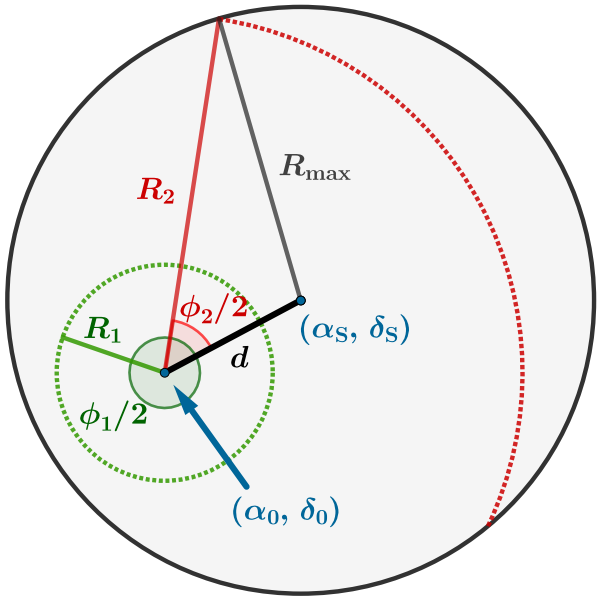

Figure 17: *Geometry of the centre estimation:* The original cone search, centred in (α_S, δ_S) is shown as the gray circle of radius R_{max}, while the new fitted centre is (α_0, δ_0). The angles ϕ_1 and ϕ_2 represent the effective circular sections (of respective radii R_1 and R_2) where one considers circular symmetry. The distance between the two centres is labelled as d, and we consider this value to approach zero for the cone searches around the centres from the SIMBAD data base. This figure was originally published in Vitral, 2021.

galactic object stars and thus have a better knowledge of the radial extent of the source, as well as the radial membership probability of a star with respect to the galactic object.

Following the normalisation of Vitral and Mamon (2020, equations 15–17), the surface density and projected number of stars are:

$$\Sigma(R) = \frac{N_\infty}{\pi R_{scale}^2} \widetilde{\Sigma}\left(\frac{R}{R_{scale}}\right) , \tag{51a}$$

$$N(R) = N_\infty \widetilde{N}\left(\frac{R}{R_{scale}}\right) , \tag{51b}$$

where N_∞ is the projected number of tracers at infinity. One can write the global surface density as:

$$\widetilde{\Sigma}(X) = \widetilde{\Sigma}_{sys}(X) + \mathcal{R}\,\frac{\widetilde{N}_{sys,tot}}{X_{max}^2 - X_{min}^2} , \tag{52}$$

where $\mathcal{R} = N_{ilop,tot}/N_{sys,tot}$ is the ratio between the number of interlopers and system (galactic object) stars, $\widetilde{N}_{sys,tot} = \widetilde{N}_{sys}(X_{max}) - \widetilde{N}_{sys}(X_{min})$ is the total number of system stars, and $X = R/a$ is the normalised projected radius, with a being the Plummer scale radius, or the Plummer projected, two-dimensional,

half number radius. The normalised surface density of the analysed system, for a Plummer profile reads:

$$\widetilde{\Sigma}_{sys}(X) = \frac{1}{(1+X^2)^2} \, , \tag{53}$$

while the normalised projected number of stars for the same model is:

$$\widetilde{N}_{sys}(X) = \frac{1}{\pi} \int_{X_{min}}^{X_{max}} \phi(X)\, X\, \widetilde{\Sigma}_{sys}(X) dX \, , \tag{54}$$

where $\phi(X)$ is the angle corresponding to the effective circular section where one analyses the data (see Fig 17), and whose analytical expression for small cone apertures (i.e. $R_{max} \ll 1$ radian) is:

$$\phi(X = R/a) = \begin{cases} 2\,\pi & , \text{ if } R \leqslant R_{max} - d \, , \\ 2 \arccos\left[\dfrac{R^2 + d^2 - R_{max}^2}{2\,R\,d}\right] & , \text{ if } R > R_{max} - d \, , \end{cases} \tag{55}$$

where R_{max} is the maximum radius of the original cone search and d is the distance between the fitted centre and the centre from the original cone search (α_S, δ_S), set as the source centre on SIMBAD[2] by the automatic *Gaia* advanced query. The projected radius R is defined, in spherical trigonometry, as:

$$R = \arccos[\sin\delta\, \sin\delta_0 + \cos\delta\, \cos\delta_0\, \cos(\alpha - \alpha_0)] \, , \tag{56}$$

where (α_0, δ_0) is the centre of the galactic object. The likelihood function is therefore written as:

$$\mathcal{L} = \prod_i \frac{\phi(X)}{\pi} \frac{X}{a} \frac{\widetilde{\Sigma}(X)}{\widetilde{N}_{sys,tot}\,(1+\mathcal{R})} \, . \tag{57}$$

We minimise $-\log\mathcal{L}$ with the DIFFERENTIAL_EVOLUTION routine from the SCIPY.OPTIMIZE method and find the centres that best fit the data. For simplicity, since one expects the quantity d to approach zero, given the reliable previous measurements of the centres in SIMBAD, one can assume the case where $\phi(X) = 2\,\pi$, and thus derive:

$$\widetilde{N}_{sys}(X) = \frac{X^2}{1+X^2} \, . \tag{58}$$

Notably, for more general cases, the BALRoGO routine allows to use the more general representation of $\phi(X)$, and thus to account for a more complicated expression for $\widetilde{N}_{sys}(X)$, presented in appendix A.2.

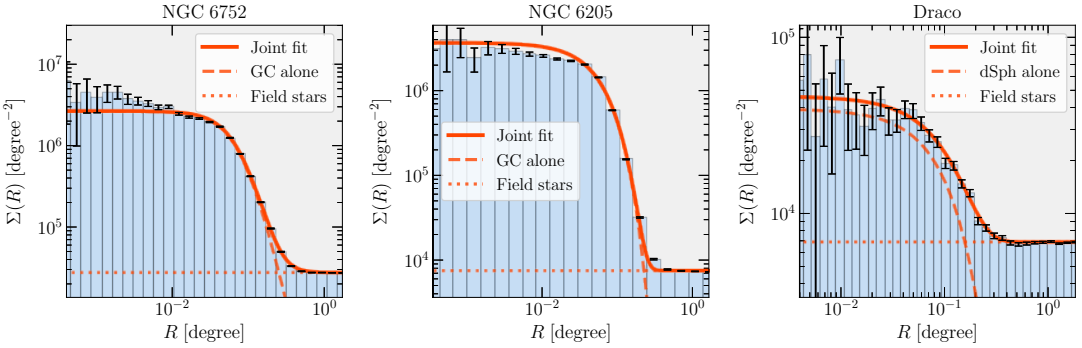

Figure 18: *Surface density fits:* Fits for the surface density of the galactic object (NGC 6752, NGC 6205 or M 13 and the Draco dSph, respectively) plus a constant contribution of interlopers, according to section 6.1.2. The *histogram* shows the empirical profile, using logarithmic radial bins extending from the innermost bin point to 2 degrees. The *curves* show different models: our MLE fit (*red*) of a Plummer, Sérsic and Sérsic models respectively (*dashed*) plus constant field stars surface density (*dotted*), as well as the total (*solid*) to compare with the data. The error bars were calculated considering only Poisson noise. This figure was originally published in Vitral, 2021.

6.1.2 *Surface density*

BALRoGO also allows to fit the surface density of the galactic object plus interlopers, using other density profiles through a maximum likelihood estimation (MLE), but with fixed centres. It not only allows for Plummer profiles, but also Sérsic models (Sérsic, 1963; Sersic, 1968), which can be useful for core-collapsed clusters such as NGC 6397, the Kazantzidis model, which is motivated from dynamical simulations of repeated tidal encounters (Kazantzidis et al., 2004), King, 1962 models, and the generalised Plummer shape (Zhao, 1996).

Different models can be compared by means of Bayesian inference, using the corrected Akaike Information Criterion (AICc, Sugiura 1978):

$$\mathrm{AICc} = \mathrm{AIC} + 2\,\frac{\mathrm{N_{free}}\,(1+\mathrm{N_{free}})}{\mathrm{N_{data}}-\mathrm{N_{free}}-1}\,, \tag{59}$$

where AIC is the original Akaike Information Criterion (Akaike, 1973):

$$\mathrm{AIC} = -2\,\ln \mathcal{L}_{\mathrm{MLE}} + 2\,\mathrm{N_{free}}\,. \tag{60}$$

Our motivation for this criterion is the same one portrayed in Vitral and Mamon, 2021, section 8.2. The results of our fits of surface density model plus constant interloper contribution are displayed in Figure 18 for NGC 6752, NGC 6205 (M 13) and the Draco dSph, respectively.

6.2 PROPER MOTION MIXTURE MODELS

6.2.1 *Kurtosis of the interlopers proper motions*

When analysing GC data from *Gaia*, it often extends to much greater projected radii from the GC centre than in *HST* data. Thus, to lower GC surface densities,

2 http://simbad.u-strasbg.fr/simbad/

the GC stands out less prominently from the field stars (FS) in proper motion space, and the selection of cluster members is less straightforward. This can be related to the FS proper motions following a wider distribution than a Gaussian, and we address now the interpretation of this result. Such an effect could be explained by the fact that the proper motions delivered by *Gaia* are not a direct measurement of the velocity, i.e. a measure of space variation per time, but rather a measurement of angular velocity, which neglects the distance of the stars.

According to the central limit theorem (Laplace, 1810), when one considers the ensemble of independent and identically distributed random variables sharing the same dispersion and mean, their properly normalised sum tends toward a normal distribution regardless of the variables original distribution. In the case of GCs and dSph, this can be considered as an adequate approximation, since these sources contain generally tens or hundreds of thousands of stars (Binney and Tremaine, 2008) which are located at distances that can be considered barely the same for a distant observer. This means that when converting the spatial velocities of its stars into angular velocities (i.e., dividing by their distance and turning them into proper motions), their originally quasi-independent and identically distributed velocities remain as such, as well as their similar dispersion, and therefore the variation around their mean is close to a Gaussian.

In the case of Milky Way FS however, since they have completely different distances, the distribution of proper motions is drawn away from an independent and identically distributed assumption, with each random measurement having a particular dispersion. In fact, their variation around their mean depends on the distance they lie from the observer, some of them much closer and others much farther than the galactic object analysed. As a consequence, one expects to find more outliers, i.e., stars with proper motions that deviate more strongly from their mean, and thus a higher kurtosis (wider tails) in the distribution.

6.2.2 *Methods*

Vasiliev, 2019b and McConnachie and Venn, 2020 used Bayesian approaches based on Gaussian mixture models (a Gaussian distribution for both cluster and interloper clumps), while the original work from Gaia Collaboration et al., 2018b used an iterative method based on clustering approaches and Baumgardt et al., 2019 performed an iterative cleaning routine based on an $n - \sigma$ outlier rejection. Even though Bayesian approaches tend to be more reliable, the use of Gaussian mixtures (which is admittedly more tempting) must, however, be taken with caution, since the distribution of FS has often much wider wings than a Gaussian distribution (it was first noticed in Vitral and Mamon 2021), as explained just above. This can be cleverly bypassed by assigning multiple Gaussians to the interloper component, such as in Vasiliev and Baumgardt, 2021, which increases the number of free parameters to be estimated, on the other hand.

This means that stars on the other side of the GC, relative to the centre of the field star component (i.e., its bulk motion) in proper motion space are more

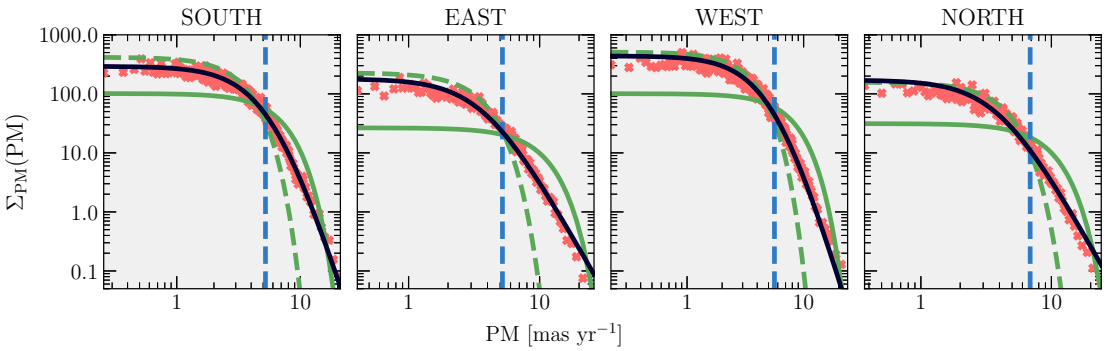

Figure 19: Surface density of proper motion moduli (defined in eq. [62]) for the four 5 degrees distant regions around NGC 6397 (for simplicity, we call them SOUTH, EAST, WEST and NORTH), represented by *red crosses*. *Solid green curves* display the best MLE fit for a Gaussian distribution, while *dashed green curves* display the best Gaussian MLE fit when only considering the regions with proper motions inside the limit of the *dashed blue vertical line*. The best MLE fit using Eq. (61) is displayed as the *black curves*. This figure was originally published in Vitral and Mamon, 2021.

likely to be FS than assumed by the Gaussian model. We found that the PM-modulus "surface density" profile (the velocity analogue of the surface density profile) is well fit by a Pearson type VII distribution (Pearson 1916), as explained in detail below. This distribution relies on two free parameters, a scale radius a and an outer slope γ, and can be written as:

$$f_\mu(\boldsymbol{\mu}) = -\frac{\gamma+2}{2\pi a^2}\left[1+\left(\frac{\mu}{a}\right)^2\right]^{\gamma/2}, \tag{61}$$

where $\boldsymbol{\mu} = (\mu_{\alpha,*}, \mu_\delta)$ and

$$\mu_i = \sqrt{(\mu_{\alpha,*i} - \overline{\mu_{\alpha,*i}})^2 + (\mu_{\delta,i} - \overline{\mu_{\delta,i}})^2}\,, \tag{62}$$

where the suffix i stands for the component analysed, which in the case of Eq. (61) is the interlopers (i.e., FS). The reader can verify that, indeed, $\int f_\mu(\boldsymbol{\mu})\,d\boldsymbol{\mu} = 1$, with $d\boldsymbol{\mu} = 2\pi\mu\,d\mu$.

In Vitral and Mamon, 2021, we downloaded *Gaia* DR2 proper motion data in four regions around NGC 6397 (and also for two other GCs, M4 and NGC 6752, in order to check for generality). These four regions were chosen by doing a cone search, with a $30'$ aperture, for positions 5 degrees distant from the GC centres (α_{GC}, δ_{GC}), north, south, east, and west. We applied the same quality flags that we had applied to the NGC 6397 data in Vitral and Mamon, 2021.

We then fitted the distribution of proper motion moduli using both a Gaussian and the form of Eq. (61). We estimated the mean $\mu_{\alpha,*}$ and mean μ_δ for both distribution functions, a dispersion σ for the Gaussian assumption and for Eq. (61), we estimated the scale radius and outer slope. Finally, we took into account the convolution of both distributions with Gaussian errors.

Figure 19 shows the distribution of proper motion moduli, for the four regions surrounding NGC 6397. One can easily verify that the new expression

fits much better than a Gaussian in Figure 19. Moreover, the calculated kurtosis excess of both $\mu_{\alpha,*}$ and μ_δ always gave huge values (from 16 to over 400, compared to zero, expected for a Gaussian), which clearly implies a non-Gaussian behaviour. To check for robustness of our fits, we also verified that whenever limiting the fitting range to exclude the wider wings of the FS distribution, a Gaussian distribution is well fitted.

It is important to notice that the convolution of the field star distribution with Gaussian errors cannot be reduced to an analytic function and numerical evaluation of the convolution integrals for each star would dramatically increase the calculation time. In Vitral and Mamon, 2021, we thus used the analytical approximation for the ratio of convolved to raw probability distribution functions of proper motion moduli, (which is also incorporated in MAMPOSSt-PM), as briefly described in Chapter 7. This allowed us to perform our mixture model fit to the proper motion data, to estimate bulk motions of both the GC and the FS and assign probabilities of GC membership for each star.

6.2.2.1 *Asymmetric shape*

In Vitral and Mamon, 2021, we opted for a symmetric Pearson VII distribution for the interlopers and the results were much more robust than the common Gaussian assumption. In Vitral, 2021, we employed a refined version of the previous Bayesian method, by assigning a symmetric Gaussian distribution for the galactic object plus a non-symmetric Pearson VII distribution for interlopers. The choice of a non-symmetric distribution allows for a much better adjustment of the interlopers, which improves the membership probability of the stars in the subset, while the impact on the bulk proper motions of the galactic object varies from cluster to cluster[3].

The main drawback of such an approach is that in order to introduce a non-symmetric Pearson VII distribution, which is analytically more complicated than a symmetric distribution, we abandon the convolution of the interloper distribution with Gaussian errors. This was not an issue for Vitral and Mamon, 2021, who used a polynomial approximation to this convolution for the symmetric case, which was simpler, in order to avoid extra integrals. This becomes much more computationally costly whenever accepting the non symmetricity of the data. We therefore try to counter this issue by trusting in our data cleaning, which applied conservative cuts on proper motion errors (i.e., tracers with large proper motion errors are removed). Moreover, ignoring the error convolution for the non-Gaussian field population should not impact significantly the fits, since the interlopers show a much broader distribution, which is less affected than the narrow galactic object component (Gaussian). We further test this assumption in section 6.2.3. To construct the probability distribution function (PDF) of the analysed subset, we consider the PDF from these tracers and from the Milky Way contaminants:

$$\mathrm{PDF} = f_{GO}\,\mathrm{PDF}_{GO} + (1 - f_{GO})\,\mathrm{PDF}_{MW}\,, \tag{63}$$

3 For example, there is no strong difference when using symmetric and non-symmetric interloper distributions for some GCs such as NGC 6397 and NGC 6121 (M4)

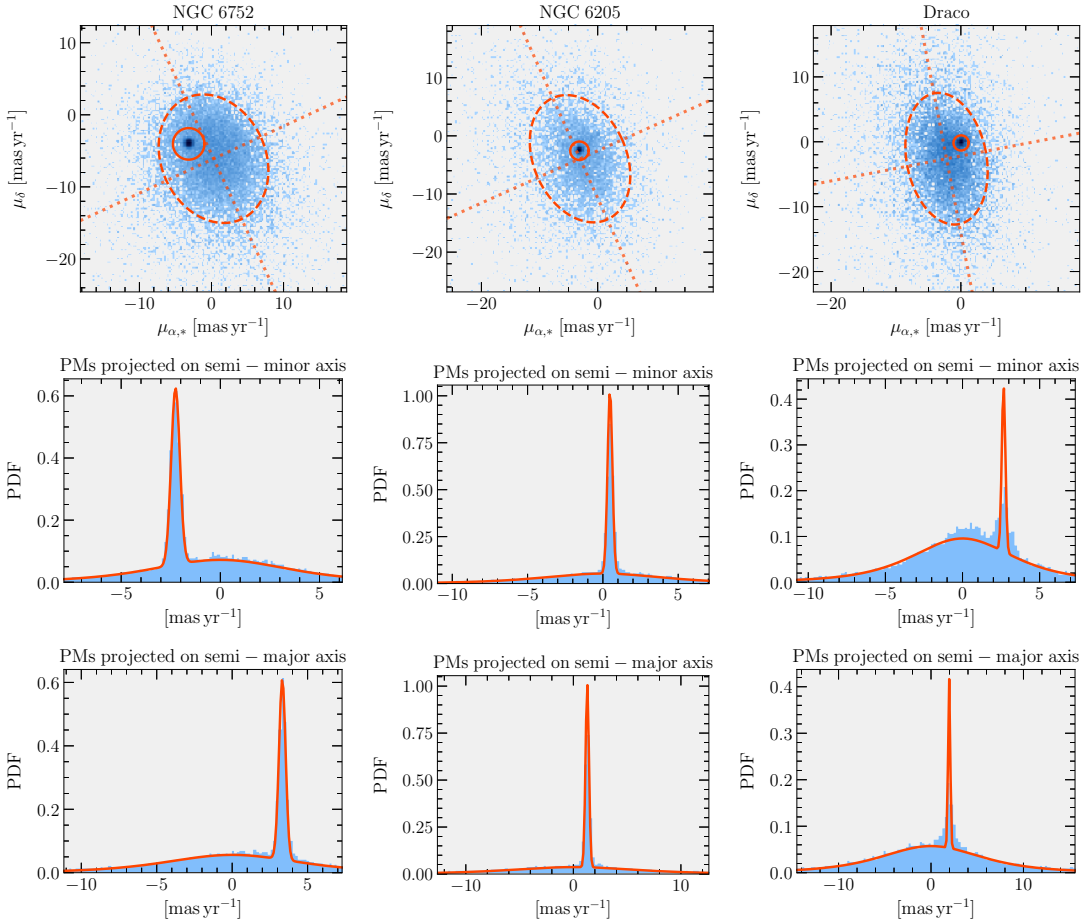

Figure 20: *Proper motion fits:* We display here the results of the proper motion fits of NGC 6752, NGC 6205 (M 13) and the Draco dSph in the first, second and third columns, respectively. The first row displays the entire proper motion subset color-coded by stellar counts, from light blue to dark blue. The dashed ellipse displays the Pearson VII asymmetric distribution, with its semi-minor and semi-major directions as two perpendicular dotted lines, while the continuous circle represents the galactic object (globular cluster or dwarf spheroidal) proper motion mean with a radius equals ten times its intrinsic dispersion, for better visualization. The second and third rows display the fits (solid red) projected on the semi-minor and semi-major axis respectively, with the data in blue. This figure was originally published in Vitral, 2021.

where f_{GO} is the fraction of galactic object stars. The PDF of galactic objects is a straightforward Gaussian:

$$\mathrm{PDF}_{GO}(\mu_{\alpha,*}, \mu_\delta) = \frac{\exp\left(-\zeta^2\right)}{2\,\pi\,\sigma_{GO}^2}\,, \tag{64a}$$

$$\zeta^2 = \frac{(\mu_{\alpha,*} - \mu_{\alpha,*\,GO})^2 + (\mu_\delta - \mu_{\delta,GO})^2}{2\,\sigma_{GO}^2} \tag{64b}$$

where σ_{GO} is the convolved proper motion dispersion of the galactic object stars, and $\mu_{\alpha,*\,GO}$ and $\mu_{\delta,GO}$ are their bulk proper motions in (α, δ). The convolution of the Gaussian component is done by considering $\sigma_{GO}^2 = \sigma_{GO,int}^2 + \epsilon^2$, where ϵ is the proper motion error (see equation [20] from Vitral and Mamon 2021) and $\sigma_{GO,int}$ is the intrinsic dispersion of the source. For the PDF of interlopers, we first shift the origin to the bulk proper motions of the interlopers clump, and then rotate the reference frame into the main axis of the interlopers proper motion ellipsoidal distribution:

$$\mu_x = (\mu_{\alpha,*} - \mu_{\alpha,*\,MW})\,\cos\theta + (\mu_\delta - \mu_{\delta,MW})\,\sin\theta\,, \tag{65a}$$

$$\mu_y = -(\mu_{\alpha,*} - \mu_{\alpha,*\,MW})\,\sin\theta + (\mu_\delta - \mu_{\delta,MW})\,\cos\theta\,, \tag{65b}$$

where $\mu_{\alpha,*\,MW}$ and $\mu_{\delta,MW}$ are the contaminants bulk proper motions in (α, δ) and θ is the angle between the original ($\mu_{\alpha,*}$, μ_δ) frame and the new one. Then, if we call the semi-major and semi-minor axis of the Pearson VII ellipsoidal distribution a_x and a_y, one can write the interlopers PDF as:

$$\mathrm{PDF}_{MW} = \left[\frac{\Gamma\left(-\frac{1}{2} - \frac{\tau}{2}\right)}{\Gamma\left(-1 - \frac{\tau}{2}\right)}\right]^2 \frac{\left\{\left[1 + \left(\frac{\mu_x}{a_x}\right)^2\right]\left[1 + \left(\frac{\mu_y}{a_y}\right)^2\right]\right\}^{(1+\tau)/2}}{\pi\,a_x\,a_y}\,, \tag{66}$$

where $\Gamma(x)$ is the gamma function of x and τ is an intrinsic slope of the distribution (with $\tau < -2$). Thus, we had ten free parameters, which were fitted by an MLE routine using the DIFFERENTIAL_EVOLUTION method in PYTHON.

In Figure 20, we present the outcome of those fits for NGC 6752, NGC 6205 (M 13) and the Draco dSph, respectively. The first row shows the fit over the entire proper motion space, where one can verify the asymmetry of the interlopers distribution, while the second and third rows display the fits projected on the semi-minor and semi-major axis respectively.

6.2.2.2 *Handling errors*

In order to derive statistical errors of our Bayesian estimates, such as bulk proper motion uncertainties, we used PYTHON's NUMDIFFTOOLS.HESSIAN method to compute the Hessian matrix of the proper motion PDF (i.e., eq [63]). After,

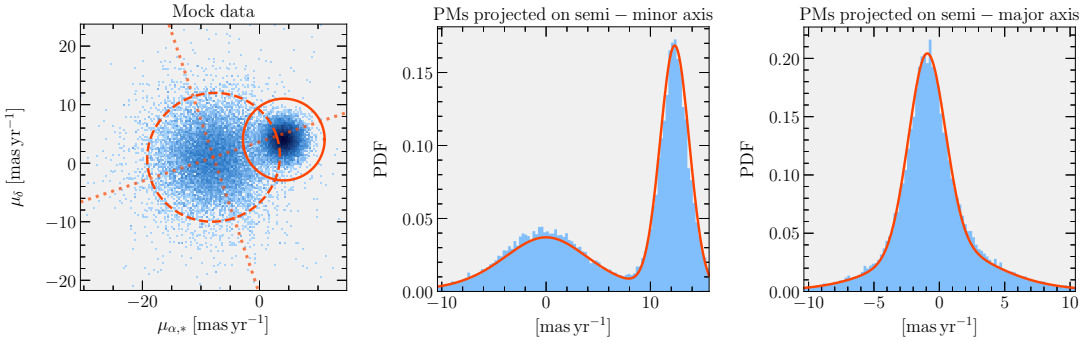

Figure 21: *Mock data:* We display here the results of the proper motion fits of our mock data set with realistic *Gaia* EDR3 errors. The image on the first column displays the entire proper motion subset colour-coded by stellar counts, from light blue to dark blue. The dashed ellipse displays the fitted Pearson VII symmetric distribution, with its main axis directions as two perpendicular dotted lines, while the continuous circle represents the galactic object (mock globular cluster) proper motion mean with a radius equals five times its intrinsic dispersion, for better visualisation. The second and third columns display the fits (solid red) projected on the semi-minor and semi-major axis respectively, with the data in blue. This figure was originally published in Vitral, 2021.

Table 2: Comparison of estimates on the bulk $\mu_{\alpha,*}$ and μ_δ from the clean and inaccurate mock data sets (see section 6.2.3). This table was originally published in Vitral, 2021.

Data set	$\mu_{\alpha*}$	μ_δ
	[mas yr^{-1}]	[mas yr^{-1}]
Clean	4.141 ± 0.011	4.040 ± 0.011
Inaccurate	4.146 ± 0.012	4.039 ± 0.012

we assigned the uncertainties of each parameter as the square root of the respective diagonal position of the inverted Hessian matrix. To these statistical uncertainties, one should expect to incorporate a systematic error at the level of ~ 0.025 mas yr^{-1} for *Gaia* EDR3 (as estimated by Lindegren et al. 2021 and Vasiliev and Baumgardt 2021) and of ~ 0.06 mas yr^{-1} for *Gaia* DR2 (Vasiliev 2019c).

6.2.3 *Convolution with Gaussian errors*

In order to test if a conservative data cleaning which removes tracers with high proper motion errors is sufficient to disconsider the convolution of the field star Pearson VII distribution with Gaussian errors, Pierre Boldrini kindly provided a GC mock using the initial condition N−body generator MAGI (Miki and Umemura, 2018). Adopting a distribution-function-based method, it ensures that the final realisation of the cluster is in dynamical equilibrium (Miki and Umemura, 2018). This GC mock was inspired by the real cluster NGC 6397, and therefore followed a Sérsic profile with stellar mass of 1.17×10^5 M$_\odot$, Sérsic radius of 3.14 pc, Sérsic index of 3.3 (Vitral and Mamon, 2021), along with

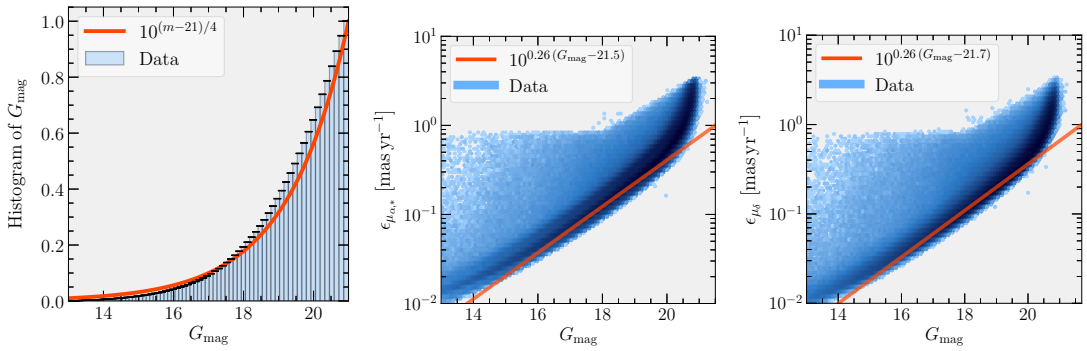

Figure 22: *Gaia EDR3 uncertainties:* On the **left**, we show the cumulative histogram of *Gaia* EDR3 G magnitudes in blue, along with the function $10^{(m-21)/4}$ in red. In the **middle**, we display the *Gaia* EDR3 $\mu_{\alpha,*}$ uncertainties blue color-coded by stellar counts, with the function $10^{0.26\,(m-21.5)}$ in red. In the **right**, we display the *Gaia* EDR3 μ_δ uncertainties blue color-coded by stellar counts, with the function $10^{0.26\,(m-21.7)}$ in red. The *Gaia* EDR3 data used for those plots is the stack of all stars in a two degrees cone search around the nearby globular clusters NGC 6121 (M 4), NGC 5139 (ω Cen), NGC 6397 and NGC 6752. This figure was originally published in Vitral, 2021.

orbital and tidal radius of 5.91 kpc (Vasiliev, 2019b) and 59.9 pc (using the relation from Bertin and Varri 2008b), respectively.

To this data, composed of 57500 stars, we added five times more stars, following spatial and velocity distributions of *Gaia* EDR3 FS, as described in section 6.3. From this new data set, we created an extra one with realistic *Gaia* EDR3 proper motion uncertainties, constructed accordingly to section 6.3, in order to test if the lack of convolution with Gaussian errors could significantly impact our results. We randomly selected 10^4 stars in both subsets (hereafter clean and inaccurate subsets, for simplicity) and ran BALRoGO's routine on them. Figure 21 displays the proper motion fits of the inaccurate subset, similar to Figure 20.

The fitted bulk $\mu_{\alpha,*}$ and μ_δ from the clean and inaccurate subsets, along with their respective uncertainties are displayed in Table 2. One can verify that even without convolving the global proper motion PDF with Gaussian errors, the fits on the bulk proper motion from the data sets with and without uncertainties agree within the $1-\sigma$ error bars, and their disagreement lies below the *Gaia* EDR3 uncertainty floor of 0.025 mas yr^{-1}. This strengthens the confidence in the proper motion cleaning routine from BALRoGO, as well as in its fits.

6.3 MOCK DATA

For astronomers interested in generating mock data sets, BALRoGO has a MOCK method equipped with many capabilities such as (1) Projecting cartesian data into sky coordinates[4], (2) Adding field stars uniformly distributed in an spherical cap and following a Pearson VII distribution in proper motions space, and (3) Adding realistic *Gaia* EDR3 errors to velocities. We describe below these three functionalities.

4 α, δ, $\mu_{\alpha,*}$ and μ_δ

6.3.1 *Coordinate transformation*

BALRoGO's method CART6D_TO_GAIA is able to convert cartesian coordinates into plane of sky coordinates, allowing the users to decide weather they want a realistic data set with proper motion uncertainties of not. Moreover, if the users want to shift a certain source from one (α, δ) position in the sky to another one, this can be promptly done by calling the method ANGLE.TRANSROT_SOURCE, which takes into account the spherical symmetry of the sky projection.

6.3.2 *Field stars*

When observing regions of the sky narrow enough (such as the two degrees cone searches we made in this work), one can expect to find uniformly distributed field stars in the field of view. By taking into account spherical trigonometry, one can generate such random distribution by inverting the probabilities $\Pr\{r < R\}$ and $\Pr\{\theta < \Theta\}$, where R and Θ are the angular distance of a tracer from the source's center and the angle between this tracer and the source's center with respect to the increasing declination axis. One has, thus:

$$R = \arccos\left[(1 - U) + U\,\cos\left(R_{lim}\right)\right] , \tag{67a}$$

$$\Theta = 2\,\pi\,U , \tag{67b}$$

where R_{lim} is the maximum distance from the source's center and U is a random variable uniformly distributed between zero and one. Similarly, one is able to generate random proper motions from a symmetric Pearson VII distribution ($a_y = a_x$ in equation [66]) by inverting the probability $\Pr\{|\mu| < M\}$:

$$M = a\,\sqrt{U^{1/(1+\tau/2)} - 1} , \tag{68}$$

where a and τ are the scale radius and slope from the Pearson VII distribution, and once again U is a random variable uniformly distributed between zero and one. We distribute those proper motion moduli azimuthally by choosing angles from a distribution such as the one from equation (67b). The precise derivation of the probabilities above is presented in appendix B.1.

6.3.3 *Realistic Gaia EDR3 uncertainties*

The proper motion uncertainties in *Gaia* EDR3 present a clear dependence on the apparent magnitude: In Figure 22, we stacked all *Gaia* EDR3 stars in a two degrees cone search around the nearby GCs NGC 6121 (M 4), NGC 5139 (ω Cen), NGC 6397 and NGC 6752, in order to show that dependence. For that reason, to generate realistic *Gaia* EDR3 proper motion uncertainties, BALRoGO first generates random magnitudes, again, by inverting the probability $\Pr\{G_{mag} < m\}$, which can be easily derived from the cumulative distribution of

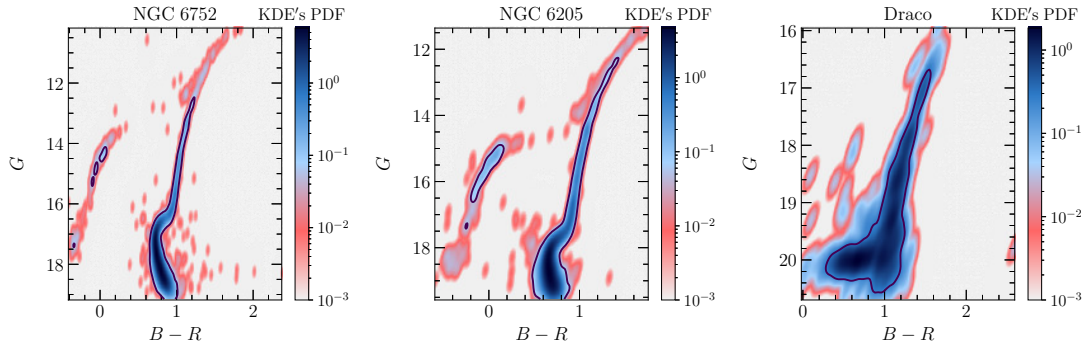

Figure 23: *Color-magnitude diagram fits:* We display the color-magnitude diagram (CMD) of NGC 6752, NGC 6205 (M 13) and the Draco dSph color-coded by the Kernel Density Estimation (KDE) non-parametric PDF. The black line contours indicate $3-\sigma$ ($2.5-\sigma$, for Draco) confidence regions, which we used to filter out interlopers and binaries that lie away from the CMD. This figure was originally published in Vitral, 2021.

G_{mag} magnitudes from *Gaia* EDR3 (i.e., the `phot_g_mean_mag` parameter), by imposing a threshold magnitude m_{lim}. The respective equations for a distribution of magnitude m are:

$$\Pr\{G_{mag} < m\} = 10^{(m-m_{lim})/f} \,, \tag{69a}$$

$$m = f \log_{10} U + m_{lim} \,, \tag{69b}$$

where U is a random variable uniformly distributed between zero and one, and $m_{lim} = 21$ and $f = 4$, according to the fits displayed in Figure 22. Once one has a random set of magnitudes from equation (69b), we can again make use of the fits displayed in Figure 22 to assign:

$$\epsilon_{\mu_{\alpha,*}} = 10^{0.26\,(m-21.5)} \,, \tag{70a}$$

$$\epsilon_{\mu_\delta} = 10^{0.26\,(m-21.7)} \,. \tag{70b}$$

Those uncertainties are provided to the user, after adding Gaussian errors to $\mu_{\alpha,*}$ and μ_δ, with respective standard deviation of $\epsilon_{\mu_{\alpha,*}}$ and ϵ_{μ_δ}.

6.4 COLOUR MAGNITUDE DIAGRAM

Once one has a precise analytical description of both the surface density and the proper motion distribution of the ensemble of field stars plus the analysed galactic object, it is much easier to extract tracer members by means of membership probabilities. However, the incredible amount of astrophysical information from the *Gaia* releases allows to go even further, by analysing how likely it is for a star to be part of the colour-magnitude diagram of the tracer. It also allows

to spot particular groups of stars such as binaries and blue stragglers that lie away from the CMD.

The last step of our default filtering routine aims at constraining the region covered by the galactic object on the color-magnitude diagram (CMD). Since we do not have an analytical form to correctly describe the CMD, we opt, for the first time until now, to not use a Bayesian method, but rather a non-parametric Kernel Density Estimation (KDE) approach. We do so with the PYTHON method SCIPY.STATS.GAUSSIAN_KDE, similarly to Vitral and Mamon, 2021. Nevertheless, our approach has some few differences:

- We first select stars with a membership probability greater than 0.8 (this limit is a modifiable parameter in BALROGO).
- We used a KDE bandwidth of half the one derived by the Silverman's rule (Silverman, 1986).
- We used the membership probabilities of each star as weights to the KDE routine.
- We selected stars inside a $n-\sigma$ density contour in the CMD (this $n-\sigma$ limit is a modifiable parameter in BALROGO).

The CMD of NGC 6752, NGC 6205 (M 13) and the Draco dSph are presented in Figure 23, with the $3-\sigma$ ($2.5-\sigma$, for the dSph) contour region displayed as a black thick line.

6.5 APPLICATION TO MILKY WAY SATELLITES

In Vitral, 2021, these methods were directly applied to more than 100 Milky Way GCs and 9 Local Group dwarf spheroidals, with *Gaia* EDR3. This section aims to compare our results with previous estimates and discuss the implications of our new methods. The complete table from Vitral, 2021, with different structural parameters for all these sources is available at the footnote link[5].

6.5.1 *Centres*

Our GC centers, derived according to section 6.1.1, were compared to the estimates from Goldsbury et al., 2010 for a robustness check: The median separation between their centres and ours is of 0.12 arcsec, while the median of their reported uncertainties is of 0.2 arcsec. Similarly, we compared our estimates with the sources from the Harris, 2010 catalogue, and obtained a median separation of 0.67 arcsec.

This strengthens our initial assumption of small separations (i.e., $d \approx 0$, in Figure 17), and gives us confidence in our Bayesian centre estimation. The maximum separation between our measurements and those from Goldsbury et al., 2010 and Harris, 2010 was of 26.5 arcsec, for the GC NGC 4147, followed by NGC 6553, with a separation of 26.1 arcsec and then by NGC 6558, with a separation of 9.5 arcsec.

5 https://gitlab.com/eduardo-vitral/balrogo/-/raw/master/table_gc_dsph.dat.

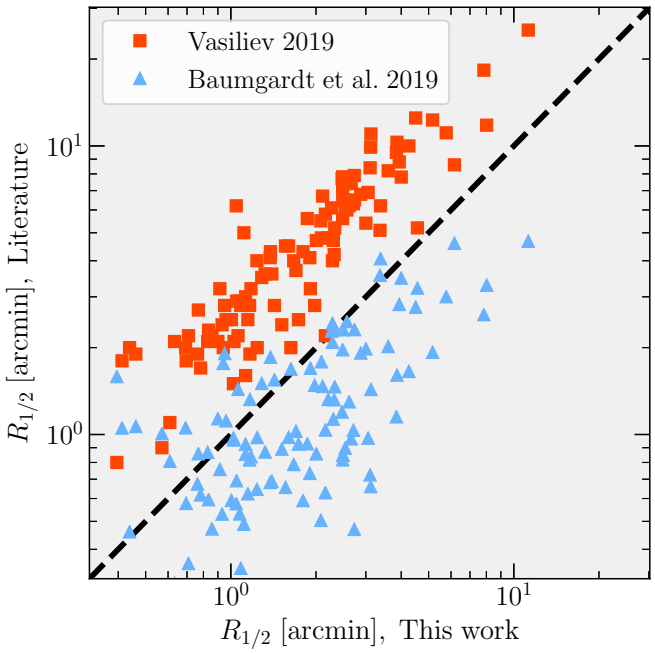

Figure 24: *Effective radii:* Comparison between the half number radii in arcmin derived by BALRoGO from *Gaia* EDR3 data in the x-axis, and the same quantity derived by Baumgardt et al. (2019, blue triangles) and Vasiliev (2019, red squares) from *Gaia* DR2 data in the y-axis. We display the $x = y$ line in dashed black. This figure was originally published in Vitral, 2021.

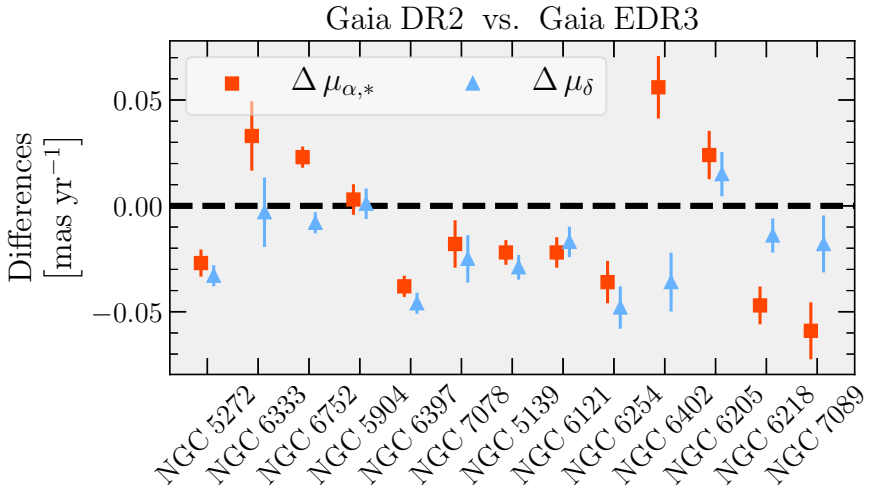

Figure 25: *Improvement of the Gaia catalogue:* Comparison of proper motion means derived by BALRoGO from *Gaia* DR2 and *Gaia* EDR3 data for the first ten globular clusters from the Messier catalogue plus NGC 6397, NGC 6752 and NGC 5139 (ω Cen). We display, in the y-axis, the differences $\Delta\mu_{\alpha,*} = \mu_{\alpha,*\,\mathrm{DR2}} - \mu_{\alpha,*\,\mathrm{EDR3}}$ and $\Delta\mu_{\delta} = \mu_{\delta\,\mathrm{DR2}} - \mu_{\delta\,\mathrm{EDR3}}$ as red squares and blue triangles, respectively, for the 13 globular clusters mentioned above, distributed along the x-axis. The errors bars were calculated as explained in section 6.5.3, and we plot a dashed black horizontal line at the value of zero as a reference. This figure was originally published in Vitral, 2021.

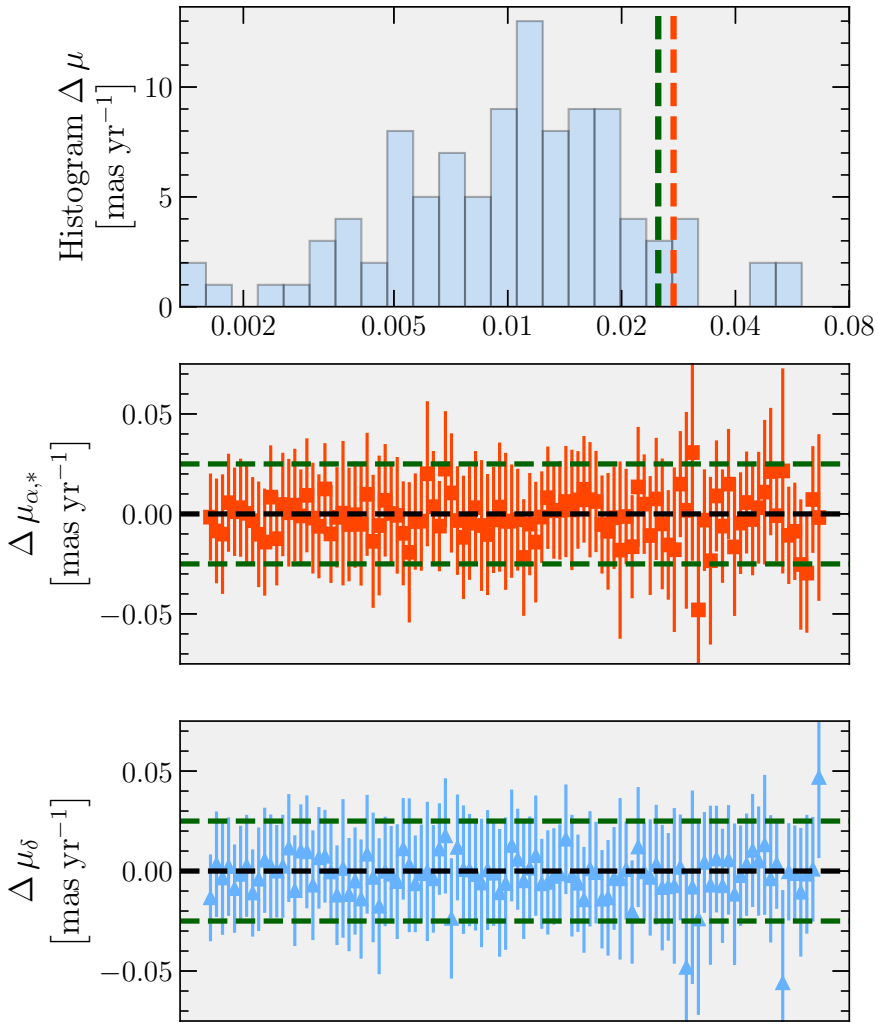

Figure 26: *Bulk proper motions:* Comparison of proper motion means derived from *Gaia* EDR3 data by BALRoGO and Vasiliev and Baumgardt, 2021 for all the globular clusters in Vitral, 2021. The two *bottom plots* display, in the y-axis, the differences $\Delta\mu_{\alpha,*} = \mu_{\alpha,*\,\mathrm{this\ work}} - \mu_{\alpha,*\,\mathrm{other\ work}}$ and $\Delta\mu_{\delta} = \mu_{\delta\,\mathrm{this\ work}} - \mu_{\delta\,\mathrm{other\ work}}$ as red squares and blue triangles, respectively, for the globular clusters in Vitral, 2021, distributed along the x-axis in a similar fashion than Figure 25. In the *top plot*, we display the histogram of $\Delta\mu = \sqrt{(\Delta\mu_{\alpha,*})^2 + (\Delta\mu_{\delta})^2}$ in mas yr^{-1}, with the uncertainty floor of the *Gaia* EDR3 data reported in Vasiliev and Baumgardt, 2021, of 0.025 mas yr^{-1} as a dashed green line and the median uncertainty in these differences, calculated with uncertainty propagation, as a dashed red line. This figure was originally published in Vitral, 2021.

6.5.2 *Effective radii*

Figure 24 displays the effective (two-dimensional) radii derived from *Gaia* EDR3 by BALRoGO in the x-axis along with the same quantity derived from *Gaia* DR2 by Vasiliev, 2019b and Baumgardt et al., 2019, in red and blue respectively, in the y-axis. The conversion to projected half number radii was straightforward for both Sérsic and Plummer fits, since the scale radius used in both models was already the half number radius. For the Kazantizidis model, we multiplied the Kazantizidis scale radius a_K by 1.257 in order to retrieve the equivalent half number radius.

The values from Vasiliev, 2019b are in general higher, which he mentions in his Figure C.1 to be a consequence of the incompleteness in the central regions of his filtered *Gaia* catalogue, which may lead his derived scale radius to be much larger than the actual half number radius of the cluster computed from all stars. In contrast, the measurements from Baumgardt et al., 2019 seem slightly smaller than ours, which in turn may indicate that our measurements are also slightly overestimated due to the intrinsic incompleteness of *Gaia*.

In any case, it is impressive that BALRoGO stands right in the middle of both estimates, which can be considered as a reliable indicator of an adequate goodness of fit. This highlights one of the strengths of our surface density fit method, which is taking into account a constant distribution of MW field stars, and neglecting any data filtering in this first step: It avoids a forced incompleteness towards both the cluster center and outskirts, due to crowdness and fainter stars respectively, which are associated with worse astrometric solutions that would be filtered out in most filtering routines.

6.5.3 *Proper motions*

6.5.3.1 *Gaia DR2 vs. Gaia EDR3*

In this subsection, we stress the important difference between the bulk proper motions derived with *Gaia* DR2 and *Gaia* EDR3. In order to make such a comparison possible, we decided to perform the same analysis, but this time using *Gaia* DR2, for 13 GCs: the first ten GCs of the Messier catalogue, plus NGC 6397, NGC 6752 and NGC 5139 (ω Cen). We show, in Figure 25, the differences between the bulk proper motions ($\mu_{\alpha,*}$, μ_δ) estimated by BALRoGO from *Gaia* DR2 and from *Gaia* EDR3.

The uncertainty of those mean values was calculated as $\epsilon = \sqrt{\epsilon_{DR2}^2 + \epsilon_{EDR3}^2}$, where ϵ_i stands for the uncertainties on the estimated values from the catalog i. One can notice that the disagreements, dominated by DR2 errors, lie in-between the uncertainty floor of the *Gaia* DR2 mission reported in Vasiliev, 2019c, of ~ 0.06 mas yr^{-1}. This is an important indicator of the improvement of *Gaia* EDR3, with more reliable measurements and a longer baseline, which in turns leads to smaller systematic uncertainties of the order of ~ 0.025 mas yr^{-1} (e.g., Lindegren et al. 2021 and Vasiliev and Baumgardt 2021).

6.5.3.2 *Comparison with the literature*

Gaia Collaboration et al., 2018b, Baumgardt et al., 2019 and Vasiliev, 2019b measured bulk proper motions for over a hundred GCs with *Gaia* DR2 by using different methods previously mentioned. In this work, we update those information with the new *Gaia* EDR3, which has more precise and robust measurements of proper motions given its longer baseline. Due to this fact, the values of proper motions means for nearly all GCs changed by more than their respective errors published in the works mentioned above. Therefore, it would be unfair to compare our results using *Gaia* EDR3 with their results obtained from *Gaia* DR2 modelling.

Fortunately, Vasiliev and Baumgardt, 2021 recently provided bulk proper motion fits for 170 GCs, which allow for such comparison. We show, in Figure 26, the differences between the bulk proper motions ($\mu_{\alpha,*}$, μ_δ) estimated from *Gaia* EDR3 by BALRoGO and by their work in the two bottom panels, in a similar fashion than displayed in Figure 25, but for all GCs in Vitral, 2021. The upper plot displays the histogram of $\Delta\mu = \sqrt{(\mu_{\alpha,*\,\mathrm{VB21}} - \mu_{\alpha,*\,\mathrm{V21}})^2 + (\mu_{\delta\,\mathrm{VB21}} - \mu_{\delta\,\mathrm{V21}})^2}$ in mas yr^{-1} (VB21 stands for Vasiliev and Baumgardt 2021 and V21 for this work) with the uncertainty floor of the *Gaia* EDR3 data reported in Lindegren et al., 2021 and Vasiliev and Baumgardt, 2021, of 0.025 mas yr^{-1} as a dashed green line and the median uncertainty in these differences, calculated with uncertainty propagation, as a dashed red line.

One observes a very good agreement between the measurements using BALRoGO and the measurements from Vasiliev and Baumgardt, 2021: Most of the sources lie below the median uncertainty of ≈ 0.03 mas yr^{-1}, with the exception of NGC 6440, NGC 6453, NGC 6522, NGC 6528 and NGC 6540, which present a $\Delta\mu \approx 0.05$ mas yr^{-1}, with high statistical uncertainties, on the order of 0.05 mas yr^{-1}. The reason for such disagreement is likely the small amount of tracers of NGC 6453, NGC 6522, NGC 6528, NGC 6540, which all have a small extension (i.e., $R_{1/2} \lesssim 0.6$ arcmin), and are therefore more affected by data cleaning and also the increased amount of interlopers in the proper motion space of NGC 6440. In this plot, it is important to mention that the differences are certainly smaller than what could be expected from formal error bars, since both studies use the same EDR3 data (different from Figure 25), in which case the systematic uncertainty cancels out (it could be viewed as the calibration error on the proper motion zero-point, which varies across the sky at this level).

In addition to the comparison between GCs made above, our proper motion fits of dSphs provide a very good agreement with the estimates from McConnachie and Venn, 2020, with differences $\lesssim 0.05$ mas yr^{-1} for all of our fits. In the very late stages of this work, Li et al., 2021 also provided bulk proper motion fits[6] for 46 dSphs, presenting a very good overall agreement with our measurements, a part from the Bootes I dSph, for which our measurements are closer to those from McConnachie and Venn, 2020. This gives confidence to the use of a non-Gaussian mixture in our Bayesian fit, along with the choice of a Pearson VII non-symmetric distribution of proper motions for interlopers, even though we neglected the convolution of the field stars component with Gaussian errors, after cleaning the data.

6 They apply a similar method than presented in Vasiliev, 2019b, therefore also relying on Gaussian mixtures.

7 MASS & ANISOTROPY MODELLING

Today we not only have no perfect model [of the atom]
but we know that it is of no use to search for one.

— Sir James Jeans, (Jeans, 1942).

One of the main points of my thesis has been to perform mass-modelling of spherical stellar systems by means of the Jeans equations. Hence, I describe here the steps and considerations used to derive these equations, and the special formalism used to apply them to data from *HST* and *Gaia*. The first part, where I derive the Jeans equation is largely inspired by chapter 4 from Binney and Tremaine, 2008, while the application of this formula is based on the equations from Mamon and Łokas, 2005; Mamon, Biviano, and Boué, 2013 and Mamon & Vitral in prep.

7.1 LOCAL EQUILIBRIUM

7.1.1 *Boltzmann equation*

Suppose that we have a stellar system formed by particles whose movement is entirely described by the gravitational potential $\Phi(\vec{x}, t)$. In this system, the probability density function (PDF) of the phase space (i.e., position and velocity) is denoted $f(\vec{x}, \vec{v}, t)$, and if we consider that the particles move smoothly from one point to another of the phase space (i.e., no collisions are considered), we can write a continuity equation similar to the classical mass conservation equations in fluid dynamics

$$\frac{\partial f}{\partial t} + \sum_{i=1}^{3} \left(\frac{\partial (f \dot{x}_i)}{\partial x_i} + \frac{\partial (f \dot{v}_i)}{\partial v_i} \right) = 0 \, . \tag{71}$$

When developing this equation, we use the fact that $\dot{x} = v$ and x are independent variables (thus, $\partial \dot{x}_i / \partial x_i = 0$), that the only source of acceleration is the gravitational potential and that it does not depend on the velocity field, to further write

$$\frac{\partial f}{\partial t} + \sum_{i=1}^{3} \left(v_i \frac{\partial f}{\partial x_i} - \frac{\partial \Phi}{\partial x_i} \frac{\partial f}{\partial v_i} \right) = 0 \, , \tag{72}$$

which is known as the *collisionless Boltzmann equation*, or also, the *Vlasov equation*.

7.1.2 *The Jeans equation*

The previous subsection presents one of the most important equations of physics, and that can be used to infer the probability of different mass configurations and thus fit most likely profiles for an analysed system. One of the methods to do so is the Jeans equation. For that, we start by integrating Eq. 72 over the velocity space

$$\int \frac{\partial f}{\partial t} d^3\vec{v} + \int v_i \frac{\partial f}{\partial x_i} d^3\vec{v} - \frac{\partial \Phi}{\partial x_i} \int \frac{\partial f}{\partial v_i} d^3\vec{v} = 0 \,, \tag{73}$$

where we have noted $\sum_i a_i \equiv a_i$, for simplicity of notation (i.e., repeated indices are summed over so we suppress the sum notation). We can also consider $\nu \equiv \int f d^3\vec{v}$ and $\bar{v}_i \equiv \frac{1}{\nu} \int f v_i d^3\vec{v}$, so the equation can be written in a simpler form

$$\frac{\partial \nu}{\partial t} + \frac{\partial (\nu \bar{v}_i)}{\partial x_i} = 0 \,. \tag{74}$$

Now, we keep Eq. 74 in hand, and come back to Eq. 72 by v_j and integrate over the velocity space

$$\frac{\partial}{\partial t} \int f v_j d^3\vec{v} + \int v_i v_j \frac{\partial f}{\partial x_i} d^3\vec{v} - \frac{\partial \Phi}{\partial x_i} \int v_j \frac{\partial f}{\partial v_i} d^3\vec{v} = 0 \,, \tag{75}$$

where the last term can be written as $\int v_j \frac{\partial f}{\partial v_i} d^3\vec{v} = -\delta_{ij}\nu$, after integrating by parts. This equation thus becomes

$$\frac{\partial (\nu \bar{v}_j)}{\partial t} + \frac{\partial (\nu \overline{v_i v_j})}{\partial x_i} + \nu \frac{\partial \Phi}{\partial x_j} = 0 \,, \tag{76}$$

where $\overline{v_i v_j} \equiv \frac{1}{\nu} \int v_i v_j f d^3\vec{v}$. Eq. 76 is called the Jeans equation, and when written in spherical coordinates and considering $\bar{v}_r = \bar{v}_\phi = \bar{v}_\theta = 0$ (i.e., no rotation, expansion or contraction), a steady state ($\partial/\partial t = 0$), it reads

$$\frac{d(\nu \overline{v_r^2})}{dr} + \frac{\nu}{r} \left[2\overline{v_r^2} - \left(\overline{v_\theta^2} + \overline{v_\phi^2} \right) \right] = -\nu \frac{d\Phi}{dr} \,, \tag{77}$$

where we use the definition of the velocity anisotropy $\beta(r) = 1 - \left[\overline{v_\theta^2} + \overline{v_\phi^2} \right] / \left[2\overline{v_r^2} \right]$, the notation $\sigma_i^2 = \overline{v_i^2} - \overline{v_i}^2$ and the fact that we consider an spherical potential (i.e., $d\Phi/dr = GM/r^2$, where M is the mass and G is the gravitational constant), to re-write the final version of the Jeans equation that we will use further on

$$\frac{d\left(\nu \sigma_r^2\right)}{dr} + 2\frac{\beta(r)}{r} \nu(r) \sigma_r^2(r) = -\nu(r) \frac{G\,M(r)}{r^2} \,. \tag{78}$$

7.2 MAMPOSST-PM

Once we have the Jeans equation, one of the big questions is how to apply it to astrometric data in order to infer masses and velocity dispersion profiles from systems such as GCs, dwarf spheroidal galaxies and clusters of galaxies. Many algorithms were designed for this purpose and have been successfully tested (see Read et al., 2021, for a review), but in my thesis, we have specifically focused on the Bayesian approach from MAMPOSSt-PM, an updated version of MAMPOSSt (Mamon, Biviano, and Boué, 2013) which dealt with line-of-sight data alone. MAMPOSSt-PM also deals with proper motion data and for that reason, is ideal to treat data from *Gaia* and *HST*. In the following, I describe some of the formalism of MAMPOSSt-PM, using equations from Mamon and Łokas, 2005; Mamon, Biviano, and Boué, 2013 and new work, tailored to proper motions, produced on the context of my thesis.

7.2.1 *General solutions*

The general solution of the Jeans equation (van der Marel, 1994; Mamon and Łokas, 2005) is given by

$$\nu(r)\sigma_r^2(r) = \frac{1}{f(r)}\int_r^{+\infty} f(s)\nu(s)\frac{GM(s)}{s^2}ds\ , \tag{79}$$

where the function f is the solution to the equation $d\ln f/d\ln r = 2\beta(r)$, $\beta(r)$ being the anisotropy profile at radius r. MAMPOSSt-PM, being a Bayesian code, uses parametrisations to fit the observed phase space, and for the velocity anisotropy profile in particular, three shapes are allowed:

- The generalised Osipkov, 1979; Merritt, 1985 profile:

$$\beta_{gOM}(r) = \beta_0 + (\beta_\infty - \beta_0)\ \frac{r^2}{r^2 + r_\beta^2}\ . \tag{80}$$

- The generalised Tiret et al., 2007 profile:

$$\beta_{gTiret}(r) = \beta_0 + (\beta_\infty - \beta_0)\ \frac{r}{r + r_\beta}\ . \tag{81}$$

- The isotropic profile:

$$\beta_{iso}(r) = 0\ . \tag{82}$$

In the equations above, β_0 and β_∞ are the velocity anisotropy value at $r = 0$ and at infinity, and r_β is the velocity anisotropy scale radius. For the particular case of $\beta_{gOM}(r)$, which I used extensively during my thesis, and that can easily be adapted to the isotropic case by fixing $\beta_0 = \beta_\infty = 0$, Eq. 79 becomes

$$\nu(r)\sigma_r^2(r) = \frac{G}{r^{2\beta_0}\left[r^2 + r_\beta^2\right]^{(\beta_\infty - \beta_0)}}\int_r^{+\infty}\nu(s)M(s)\left[\frac{s^{2\beta_0} + \left(s^2 + s_\beta^2\right)^{(\beta_\infty - \beta_0)}}{s^2}\right]ds\ .$$

(83)

Next, we aim at describing the velocity dispersion in the plane-of-sky (R and T, for radial and tangential) and in the line-of-sight (Z) projected in the sky, using the relation

$$\sigma_i^2(R) = \frac{2}{\Sigma(R)} \int_R^{+\infty} \frac{\sigma_i^2(R|r)\,\nu(s)\,r}{\sqrt{r^2 - R^2}} dr \,, \tag{84}$$

where $\Sigma(R)$ is the surface density profile at projected radius R, i stands for R, T and Z, and $\sigma_i^2(R|r)$ are given by the relations from Binney and Mamon, 1982; Strigari, Bullock, and Kaplinghat, 2007 below

$$\sigma_R^2(R\,|\,r) = \left[1 - \beta(r) + \beta(r)\,\frac{R^2}{r^2}\right]\,\sigma_r^2(r) \,, \tag{85a}$$

$$\sigma_T^2(R\,|\,r) = [1 - \beta(r)]\,\sigma_r^2(r) \,, \tag{85b}$$

$$\sigma_Z^2(R\,|\,r) = \left[1 - \beta(r)\,\frac{R^2}{r^2}\right]\,\sigma_r^2(r) \,. \tag{85c}$$

With those equations, one is then able to fit the mass and anisotropy profiles to the phase space data.

7.2.2 *Probability distribution function*

In practice, MAMPOSSt-PM considers a PDF in projected phase space (PPS), $(R, \overrightarrow{v})$, to recover the likelihood of the data. The PPS PDF is given by

$$g(R, \overrightarrow{v}) = \Sigma(R) p(\overrightarrow{v}|R) \tag{86}$$

where $p(\overrightarrow{v}|R)$ is the probability density of having a tracer with velocity $\overrightarrow{v}$ at a given projected radius R, and $\Sigma(R)$ is the surface density profile. Notice that $g(R, \overrightarrow{v})$ satisfies

$$\int\int 2\pi R g(R, \overrightarrow{v}) dR d\overrightarrow{v} = N \tag{87}$$

where N is the number of tracers inside the space integrated. As this thesis focus on GCs, we will refer to the tracers as stars and to the system as GC, for simplicity, keeping in mind that this can be enlarged to other systems like clusters of galaxies for example.

7.2.2.1 *Surface density priors*

MAMPOSSt-PM can operate in two modes, considering both complete and incomplete data in projected radius R. In the absence of mass segregation, the tracer mass density profile, $\rho(r)$ is proportional to the number density profile $\nu(r)$, which is deprojected from the surface mass density profile, $\Sigma(R)$, using

spherical symmetry. But the surface distribution of kinematic tracers is usually incomplete, in particular in the inner regions of the GCs, for the data sets used in this thesis (i.e., *Gaia* and *HST*). In this case, a previous fit of the surface density $\Sigma(R)$ is required, in order to provide realistic priors to the density parameters.

One can, therefore, estimate the surface density profile in two steps, such as in Vitral et al., 2022:

1. First, we use Gaussian priors based on MCMC fits of a certain density model plus a uniform field surface density to the distribution of projected radii. For this, we do not restrict our sample to the stars whose kinematics we later analyse with MAMPOSSt-PM. We therefore consider all stars in a magnitude range, but also emphasise that spatial incompleteness can still strongly affect our results in the cluster's centre due to crowdness (Arenou et al., 2018), especially for denser clusters. We try several maximum allowed projected radii, R_{max}^{allow} and adopt the MCMC means for the surface density parameters in the middle of the plateau of R_{max}^{allow}, where the means are roughly constant (see left panel of fig. 10 of Vitral and Mamon, 2021).

2. Since MAMPOSSt-PM takes into account not only the distribution of projected radii, but also kinematic data, a second pass that uses it should add more constraints on our fits (and future priors, consequently), and decrease the spatial incompleteness intrinsic to the data (see previous step). Hence, we run MAMPOSSt-PM with these means for the simplest model (i.e., with fewer free parameters[1], using Gaussian priors with fairly wide uncertainties for the density parameters, centred on the means of the fits of the first step.

For each mass model, we then run MAMPOSSt-PM with the mean and uncertainties on surface density parameters returned by MAMPOSSt-PM in that first run.

7.2.2.2 *Likelihoods*

With these priors, one can focus on fitting $p(\overrightarrow{v}|R)$ with wider priors, and even considering the contribution of interlopers (we will denote them by the letter 'i'):

$$p(\overrightarrow{v}|R) = \frac{g_{GC}(R, \overrightarrow{v}) + g_i(R, \overrightarrow{v})}{\Sigma_{GC}(R) + \Sigma_i(R)} \, . \tag{88}$$

The system contribution to the PPS density is the mean local velocity distribution function h, averaged along the line of sight (Mamon, Biviano, and Boué, 2013)

$$g_{GC}(R, \overrightarrow{v}) = 2 \int_R^\infty h(\overrightarrow{v}|R, r)\, \nu(r)\, \frac{r}{\sqrt{r^2 - R^2}}\, dr \, . \tag{89}$$

1 We test other mass-anisotropy models to check if the derived priors were too different.

MAMPOSSt-PM then assumes that the *local* velocity ellipsoid, i.e. the local 3D velocity distribution function, is separable along the three spherical coordinates $(r,\,\theta,\,\phi)$ where each component is a Gaussian of zero mean, with respective standard deviations σ_r, σ_θ, and σ_ϕ:

$$h(\overrightarrow{v}|R,r) = \mathcal{G}\left[v_r, 0, \sigma_r(r)\right]\,\mathcal{G}\left[v_\theta, 0, \sigma_\theta(r)\right]\,\mathcal{G}\left[v_\phi, 0, \sigma_\phi(r)\right]\ . \tag{90}$$

This Gaussian assumption for the local velocity distribution function, $h(\overrightarrow{v}|R,r)$, is much better than the very popular Gaussian assumption for the integrated velocity distribution function, $g_{GC}(\overrightarrow{v}|R)$, because velocity anisotropy affects the shape of $g_{GC}(\overrightarrow{v}|R)$ (Merritt, 1987).

Once one has defined $h(\overrightarrow{v}|R,r)$ as in Eq. 90, the next step is to write it down in observable astrometric coordinates. Here, we use the radial and tangential direction in the plane-of-sky (R and T), and the Z direction of the line-of-sight. Eq. 90 thus becomes, in this new coordinate system,

$$\begin{aligned} h(\overrightarrow{v}|r,R) =& \frac{\exp\left[-\frac{v_R^2\sigma_Z^2}{2\sigma_r^2\sigma_T^2}\right]}{\sqrt{2\pi\sigma_T^2}}\,\frac{\exp\left[-\frac{v_Z^2\sigma_R^2}{2\sigma_r^2\sigma_T^2}\right]}{\sqrt{2\pi\sigma_T^2}}\,\frac{\exp\left[-\frac{v_T^2}{2\sigma_T^2}\right]}{\sqrt{2\pi\sigma_T^2}} \\ & \frac{\exp\left[\frac{\mathrm{sgn}(\beta)\,\sqrt{|1-(\sigma_Z/\sigma_r)^2|}\,\sqrt{|1-(\sigma_R/\sigma_r)^2|}\,v_R v_Z}{\sigma_T^2}\right]}{(\sigma_r/\sigma_T)}\ . \end{aligned} \tag{91a}$$

where $\mathrm{sgn}(x)$ is the sign function[2] of the variable x, and we used the conversions of the $(r,\,\theta,\,\phi)$ system into the new (Z, R, T) where the observer is placed at infinity:

$$v_\phi = -v_T \tag{92}$$

$$v_\theta = \frac{\sqrt{r^2-R^2}\,v_R - R\,v_Z}{r} \tag{93}$$

$$v_r = \frac{R\,v_R + \sqrt{r^2-R^2}\,v_Z}{r} \tag{94}$$

and considered the symmetry $\sigma_\phi^2 = \sigma_\theta^2 = \sigma_r^2\,[1-\beta(r)]$. If ever one has no data on line-of-sight, one should use the function $h(\overrightarrow{v}|r,R)$ integrated in the v_Z domain:

$$\begin{aligned} h(\overrightarrow{v}|r,R)_{RT} &= \int_{-\infty}^{+\infty} h(\overrightarrow{v}|r,R)\,dv_Z \\ &= \frac{1}{2\pi\sigma_T\sigma_R}\,\exp\left[-\frac{v_T^2}{2\,\sigma_T^2}\right]\exp\left[-\frac{v_R^2}{2\,\sigma_R^2}\right]\ . \end{aligned} \tag{95a}$$

2 $\mathrm{sgn}(x) = x/|x|$, if $x \neq 0$, and $\mathrm{sgn}(x) = 0$ otherwise.

Analogously, if one only has proper motion data, the shape of the function becomes:

$$h(\overrightarrow{v}|r,R)_Z = \int_{-\infty}^{+\infty}\int_{-\infty}^{+\infty} h(\overrightarrow{v}|r,R)\,dv_R\,dv_T = \frac{1}{\sqrt{2\pi}\,\sigma_Z}\,\exp\left[-\frac{v_Z^2}{2\,\sigma_Z^2}\right]. \tag{96a}$$

Admittedly, the data used for the MAMPOSSt-PM fit will contain errors, which should be accounted when computing the distribution functions above. For that, MAMPOSSt-PM convolves $h(\overrightarrow{v}|r,R)$ with Gaussian errors, for each of the coordinates analysed. The cases with no line-of-sight or with no proper motions are trivial, since they are separable Gaussians, and the convolution with another Gaussian yields a new Gaussian with mean equal to the sum of means, and dispersion equal to the quadratic sum of dispersions. Thus, we just substitute, in Eqs. 95a and 96a, $\sigma_{i,new}^2 = \sigma_i^2 + \epsilon_i^2$, where i stands here for R, T or Z, and ϵ_i is the uncertainty on the velocity i, provided by the dataset used. In the case where the MAMPOSSt-PM user has 3D data, then the convolution of Eq. 91a with Gaussian errors is not that straightforward, but good mathematical handling yields

$$\begin{aligned} h(\overrightarrow{v}|r,R)_{new} &= h(\overrightarrow{v}|r,R) * \mathcal{G}(0,\epsilon_T) * \mathcal{G}(0,\epsilon_R) * \mathcal{G}(0,\epsilon_Z) \\ &= \frac{\exp\left[-\frac{v_T^2}{2(\sigma_T^2+\epsilon_T^2)}\right]}{\sqrt{2\pi(\sigma_T^2+\epsilon_T^2)}}\;\frac{\exp\left[\frac{\mathrm{sgn}(\beta)\sqrt{(\sigma_r^2-\sigma_Z^2)\,(\sigma_r^2-\sigma_R^2)}\,v_R v_Z}{\Delta^4}\right]}{2\pi\,\Delta^2} \\ &\quad \exp\left[-\frac{v_Z^2\,(\sigma_R^2+\epsilon_R^2)}{2\,\Delta^4}\right]\exp\left[-\frac{v_R^2\,(\sigma_Z^2+\epsilon_Z^2)}{2\,\Delta^4}\right], \end{aligned} \tag{97a}$$

where we have noted $*$ as the symbol for convolution, and defined

$$\Delta^4 = \sigma_r^2\,\sigma_T^2 + \epsilon_R^2\,\sigma_Z^2 + \epsilon_Z^2\,\sigma_R^2 + \epsilon_R^2\,\epsilon_Z^2\,. \tag{98}$$

Finally, MAMPOSSt-PM considers the likelihood

$$\mathcal{L} = \prod_i p(\overrightarrow{v}_i|R_i)\,, \tag{99}$$

and maximises it with the CosmoMC[3] (Lewis and Bridle, 2002) algorithm by running a Markov Chain Monte Carlo (MCMC) routine that determines the marginal distributions of the free parameters and their covariances.

3 https://cosmologist.info/cosmomc/.

7.2.2.3 *Interlopers*

The proper motion distribution of interlopers is not a Gaussian, as shown in Chapter 6, which yields no analytical convolution with Gaussian errors. We describe here how we convolve the the distribution of interloper proper motions with measurement errors, in the framework of MAMPOSSt-PM.

Let $R = PM$ (the proper motion vector) and $R_o = PM_o$, where index 'o' stands for observed (R is not the projected radius but its proper motion analog), and let ϵ be the proper motion error. We followed the recipe of Binney and Mamon (1982, appendix C) for convolution of two-dimensional data with circular symmetry (Vitral and Mamon, 2021):

$$p_{conv}(R_o) = \frac{R_o}{\epsilon^2} \int_0^\infty dR\, p(R)\, \exp\left(-\frac{R^2+R_o^2}{2\,\epsilon^2}\right) I_0\left(\frac{R,R_o}{\epsilon^2}\right) . \tag{100}$$

We evaluated Eq. (100) in tight bins of R_o/a_{PM}, ϵ/a_{PM}, and δ using the more analogous equation, which is more robust to underflows

$$p_{conv}(R_o) = \frac{R_o}{\epsilon^2} \left\{ \int_0^{R_o} dR\, p(R)\, \exp\left[-\frac{(R-R_o)^2}{2\epsilon^2}\right] F\left(\frac{R\,R_o}{\epsilon^2}\right) + \int_{R_o}^\infty dR\, p(R)\, \exp\left[-\frac{(R-R_o)^2}{2\epsilon^2}\right] F\left(\frac{R\,R_o}{\epsilon^2}\right) \right\} , \tag{101}$$

where

$$F(X) = \begin{cases} e^{-X}\, I_0(X) & \text{for } X < 4 \\ \dfrac{1}{\sqrt{2\pi X}} \left(1 + \dfrac{1}{8X \left(1 + \frac{9/2}{8X\left(1+\frac{25/3}{8X}\right)} \right)} \right) & \text{for } X \geqslant 4 \end{cases} , \tag{102}$$

where the expression for large X represents the first terms of the nested series of Olver (1972, eq. [9.7.1]).

To avoid fitting a three-dimensional function to $p_{conv}(R_o|\delta, \epsilon/a_{PM})$, it was used that the ratio of convolved to raw pdf varies from a constant value y_0 at small R_o to unity at large R_o, with a possible maximum in between, which can be approximated as

$$\frac{p_{conv}(R_o, a_{PM}, \delta|\epsilon)}{p(R_o, a_{PM}, \delta)} = \left(\left\{ y_0 \left[1 + \left(\frac{X}{X_1} \right)^A \right] \right\}^g + \left[\left(1 + \left(\frac{X}{X_2} \right)^B \right]^g \right)^{1/g} , \tag{103}$$

where $X = R_o/a_{PM}$. We performed non-linear fitting of our 6 free parameters, y_0, A, X_1, B, X_2, and g to the logarithm of the ratio of Eq. (103), where y_0 was predetermined from the median of the ratios for $R_o/a_{PM} < 0.1$ (allowing it to vary by 2%), while the 5 other free parameters were constrained to $A > 0 \simeq 2$, $X_1 > 0 \simeq 1$, $B < 0 \simeq -2.5$, $X_2 > 0 \simeq 2$, and $g < 0 \simeq -1$. We used 21 bins of R_o/a

geometrically spaced between 0.01 and 1, also 9 bins of ϵ/a_{PM} geometrically spaced between –2 and 0, and 9 bins of δ between –8 and –4.

We then derived functional forms as a function of $\log \epsilon/a_{PM}$ and δ for our 6 free parameters, using 6th order two-dimensional polynomial fits for $\log y_0$, A, $\log(-B)$, $\log X_1$, $\log X_2$, and $\log(-g)$. These polynomial fits to our model of Eq. (103) lead to a factor 80 gain in computational speed relative to the numerical integration of Eq. (101). We used Monte Carlo simulations to test that our polynomial fits to our model of Eq. (103) recovered $p_{conv}(R_o, a_{PM}, \delta|\epsilon)$. With 1000 trials, with random values of R_o/a_{PM} (geometrically spaced between 0.01 and 10), ϵ/a_{PM} (geometrically spaced between 0.01 and 1), and δ (between –8 and –4), we found that our model with the polynomial fits recovered the numerical value of p_{conv} to an accuracy of 0.002 dex (median absolute deviation), 0.13 dex (rms), and 1.67 dex (max). The median value is slightly improved by not allowing $p_{conv}(R_o) < p(R_o)$ for $R_o/a_{PM} > 5$.

Part III

RESULTS

8 STELLAR GRAVEYARDS

Somewhere, something incredible
is waiting to be known.

— Carl Sagan.

By means of the methods explained in the previous chapters, Vitral and Mamon, 2021 and Vitral et al., 2022 analysed two Milky Way GCs, NGC 6397 and NGC 3201, and modelled the cluster mass and anisotropy from their outskirts down to their inner regions. In this chapter, I explain the criteria used to select these two GCs, how we handled their *HST* and *Gaia* data, and the results and implications of these studies. The data cleaning and handling procedure was somewhat similar for the two works, and for that reason, I chose only to report the one in the most recent work, Vitral et al., 2022. Concerning the results, I will do it chronologically, by first discussing the results from Vitral and Mamon, 2021 for NGC 6397, and then the ones reported in Vitral et al., 2022 for both NGC 3201 and NGC 6397.

8.1 TARGET GLOBULAR CLUSTERS

The choice of which clusters to study depends on the availability of good quality data as well as on structural characteristics that facilitate our modelling. For instance, strong imprints of rotation, or non-spherical sources are not ideal, as our mass-modelling routine considers a spherical system with no rotation when solving the Jeans equation (see Chapter 7). Similarly, sources that are located too far away from us (e.g., $\gg 5$ kpc) usually have characteristic uncertainties much higher than the local velocity dispersion, which could induce an error underestimation that undermines our study. For those reasons, we chose to work with NGC 3201 and NGC 6397, whose main features we comment below.

8.1.0.1 *NGC 3201*

NGC 3201 is a 10.4 Gyr old cluster that orbits the Milky Way in a retrograde orbit and recedes from the Sun with a velocity of nearly 500 km s^{-1} (Marin-Franch et al., 2009; Gaia Collaboration et al., 2018b). It is located at 4.74 kpc from the Sun (Baumgardt and Vasiliev, 2021), it had its dynamics studied many times (e.g., Bianchini, Ibata, and Famaey 2019; Wan et al. 2021) and its ellipticity is of 0.12, according to Harris, 1996; Harris, 2010[1]. The median and maximum *HST* proper motion baselines among the stars are 4 and 8 years, for this cluster.

Rotation in this cluster can be overestimated when disregarding perspective rotation (see van de Ven et al. 2006; Wan et al. 2021, for details) due to its

1 Ellipticity is defined in this catalogue as $e = 1 - b/a$, where a and b are the semi-major and minor axis of the isophote projected ellipse, respectively.

Figure 27: *NGC 6397:* Image of NGC 6397 in the night sky. Credits: Julian Shaw, AstroBin.

high line-of-sight velocity, but recent studies that treat this issue tend to agree that a rotation signal of amplitude $\sim$ 10 per cent of the velocity dispersion is present in its innermost regions (Sollima, Baumgardt, and Hilker, 2019), a feature that is erased, by construction, on our *HST* subset. The outskirts of our *Gaia* data however, could have an increasing rotation pattern, but recent studies using *Gaia* proper motions found that its rotation is much smaller than its velocity dispersion (Bianchini et al., 2018; Sollima, Baumgardt, and Hilker, 2019; Vasiliev, 2019c). Along with the fact that our *Gaia* data actually represents only $\sim$ 14 per cent of our NGC 3201 subset, we thus ignore this cluster's rotation and assume it to have an weak effect on our mass-modelling.

Among the many interesting features of NGC 3201, we stress that it is far from a core-collapse state (Djorgovski and King, 1986). Giesers et al., 2018 recently provided solid evidence for a stellar-mass[2] black hole dynamical detection near the cluster's centre and follow-up observations revealed additional black holes (Giesers et al., 2019).

8.1.0.2 *NGC 6397*

NGC 6397 is the second closest GC to our Sun, at only 2.48 kpc away (Baumgardt and Vasiliev, 2021), and is a very metal-poor ([M/H]$= -1.54$), old (12.87 Gyr) cluster (Marin-Franch et al., 2009). It is very spherical ($e = 0.07$, Harris 1996; Harris 2010) and its rotation is negligible relative to its velocity dispersion (Bianchini et al., 2018; Sollima, Baumgardt, and Hilker, 2019; Vasiliev, 2019c). As a matter of fact, recent mass-modellings of this cluster have neglected rotation and argued that such assumption did not affect its overall modelling (e.g.,

2 They measured a mass of 4.36 ± 0.41 $M_\odot$.

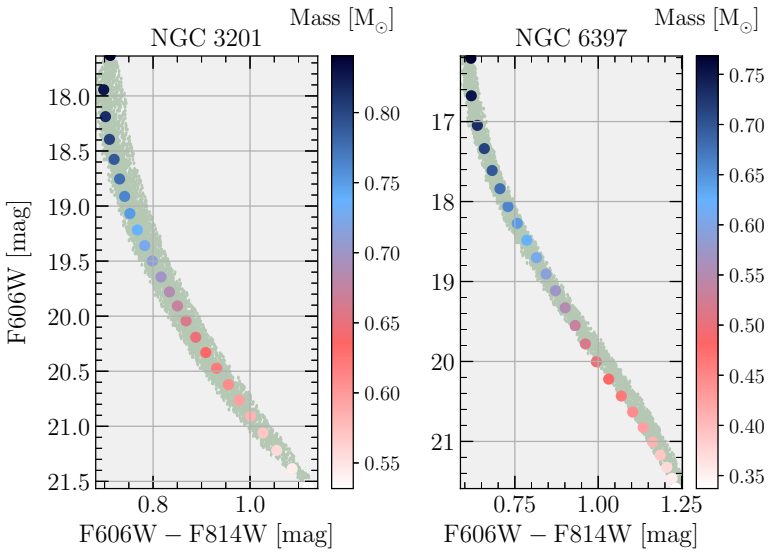

Figure 28: *Colour-magnitude diagrams of the two globular clusters:* The *small gray-green points* are the *HST* data, cleaned according to Section 8.2, while the *filled circles* are the predictions from the *Parsec* code, colour-coded by stellar mass. This figure was originally published in Vitral et al., 2022.

Kamann et al. 2016). The median and maximum *HST* proper motion baselines among the stars are 9.7 years (both statistics), for this cluster.

Claims of a central dark mass in this cluster were recurrent. Larson, 1984 first proposed that a central 1600 $M_\odot$ component formed by compact remnants could reside int the cluster's core, while Kamann et al., 2016 fitted line-of-sight data of this cluster to claim a 600 $M_\odot$ intermediate-mass black hole (IMBH) detection.

8.2 DATA HANDLING IN VITRAL ET AL. (2022)

8.2.1 *Parsec isochrones*

In order to handle mass-magnitude conversions, as well as to relate the magnitude systems from *Gaia* EDR3 and *HST*, we used PARSEC isochrones[3] (e.g., Bressan et al. 2012; Chen et al. 2014; Chen et al. 2015; Marigo et al. 2017; Pastorelli et al. 2019). The input parameters we used and their references are displayed in Table 3 (along with a few other assumptions from our modelling).

For the value of total extinction of NGC 3201, we used a value between the ones presented in Harris, 2010 and VandenBerg et al., 2013, which yielded a better fit to our data (as well as to the combination of other parameters). Figure 28 displays the isochrones of the two analysed clusters, with respect to the cleaned *HST* data (according to the sections below).

3 http://stev.oapd.inaf.it/cgi-bin/cmd

Table 3: Main assumptions.

Cluster ID	Distance [kpc]	η_R	Age [Gyr]	A_v	[M/H]	(α_0, δ_0) [deg]
NGC 3201	4.74	0.492	10.40	0.8215	−1.02	(154°.40346, −46°.41249)
NGC 6397	2.48	0.468	12.87	0.558	−1.54	(265°.17540, −53°.67441)

Notes: Columns are: (1) Cluster ID; (2) Distance to the Sun, in kpc (Baumgardt and Vasiliev 2021); (3): Reimers scaling factor (McDonald and Zijlstra 2015); (4) Age, in Gyr (Marin-Franch et al. 2009); (5) Total extinction, considering the reddening parameter $R_v = 3.1$ (Harris 1996; Harris 2010 and VandenBerg et al. 2013 for NGC 3201 and just Harris 1996; Harris 2010 for NGC 6397); (6) Metallicity, in log solar units (Marin-Franch et al. 2009); (7) Cluster centre, in degrees (calculated with BALRoGO, Vitral 2021). For the total extinction of NGC 3201, we selected values between the different ones provided in the literature, so that we had a better adjustment of *Parsec* isochrones. This table was originally published in Vitral et al., 2022.

8.2.2 *Maximum projected radius*

Passages close to the Milky Way's disk, as well as possible amounts of dark matter in its outskirts can provide an important source of dynamical heating to the outer regions of GCs. As our modelling does not include dark matter components, neither encompasses the influence of the Milky Way tidal field, we chose to analyse our data up to a maximum allowed radius, where we expect such effects to be negligible.

The mean plane-of-sky velocities in the frame aligned with the position of the star, $\overline{v_{POSr}}$ and $\overline{v_{POSt}}$, are equal up to $2\,R_e$, where R_e is the *effective radius* containing half the projected number of stars. The mean velocity profiles diverge further out, for both NGC 6397 (see Vitral and Mamon, 2021, fig. 6) and NGC 3201. Also, for both NGC 6397 (fig. 6 of Vitral and Mamon, 2021) and NGC 3201, the velocity dispersion profiles σ_{POSr} and σ_{POSt} decrease up to $5\,R_e$ and increase further out. We therefore set the maximum allowed projected radius as $2\,R_e$.

8.2.3 *Quality indicators*

The first step in our data cleaning was to remove stars with poor photometric and astrometric measurements. We detail below this cleaning procedure for both *Gaia* EDR3 and *HST*.

8.2.3.1 *Gaia EDR3*

We retained *Gaia* stars that satisfied:

- **Astrometric accuracy**: $\texttt{RUWE} < \eta_{90}(\texttt{RUWE})$, where RUWE is *Gaia*'s Renormalised Unit Weight Error and $\eta_n(x)$ is the n-th percentile of the x data ($\eta_{90}(\texttt{RUWE}) \simeq 1.1$, close to the threshold of 1.15 chosen by Vasiliev and Baumgardt 2021).

- **Photometric accuracy**:

$$C(r) - f(G_{BP} - G_{RP}) < 3\,\sigma_C\ , \tag{104}$$

where $C(r)$ is *Gaia*'s `phot_bp_rp_excess_factor`, $f(x) = \sum_i a_i\, x^i$, with the polynomial coefficients a_i taken from Table 2 of Riello et al., 2021, and $G_{BP} - G_{RP}$ is given by `bp_rp`.

Eq. (104) performs an additional filter for unreliable astrometric solutions (mainly in the cases of blended stars), affecting mainly faint sources in crowded areas.

8.2.3.2 *HST*

Our *HST* astro-photometric catalogues include several diagnostic parameters to select trustworthy objects for the analysis. For each cluster, a sample of well-measured objects in the *HST* data is defined with the following criteria (similarly to Libralato et al. 2019, but with some small changes labelled as 'new' or 'changed').

- the star is unsaturated;
- the number of single exposures used to compute the magnitude of a star in the second-pass-photometry stage differs by less than 15 per cent from the number of images in which a star was actually found (new);
- the star flux is greater than the flux from neighbours within the PSF fitting radius of the star.
- the photometric rms uncertainty is lower than 0.2 mag (changed);
- the quality, `QFIT` of the PSF fit is greater than 0.8 (changed);
- the absolute value of the shape parameter `RADXS` (Bedin et al., 2008) is lower than 0.15 (changed). The `RADXS` parameter represents the excess/deficiency of flux outside of the fitting radius with respect to the PSF prediction and helps discerning stars from other objects like galaxies or cosmic rays;
- all photometry-based selections above must be fulfilled in both (ACS/WFC) F606W and F814W filters;
- the acceptance rate in the proper-motion fit (number of measurements used to compute the proper motion (PM) of a star before and after all outlier rejections; see Bellini et al. 2014) is greater than 85 per cent (changed);
- an a posteriori correction was applied to the proper motion to account for spatial and magnitude-dependent systematics (see Libralato et al., in prep.).

8.2.4 *Proper motion error threshold*

Even though our mass-modelling routine takes into account the distribution of errors by convolving it with the local velocity distribution, it is wise to limit the tracers to a maximum error threshold, for robustness. Indeed, if the proper motion errors are underestimated, which can be the case for stars with very high errors, an artificial increase of the velocity dispersion (and thus, of the mass) can take place. We therefore removed stars with error greater than or equal to a constant times the local (mass and position) velocity dispersion of stars of given mass. The local velocity dispersion (for each star) was computed empirically, without relying on a particular model, according to the following steps:

1. We converted F606W magnitudes (G magnitudes for *Gaia*) into mass by interpolating the magnitude with respect to the respective *Parsec* isochrone of the cluster, disregarding the horizontal branch, which could cause a degeneracy in the interpolation and would be eventually removed further on. and $\log R$, where R is the projected distance to the cluster centre (hereatfer *projected radius*). The distance ξ in the $\log M_\star$ vs. $\log R$ plane was calculated as:

$$\xi = \sqrt{(\Delta x_{new})^2 + (\Delta y_{new})^2} \,, \tag{105}$$

with $x \equiv \log M_\star$, $y \equiv \log R$, and

$$\Delta x_{new} = \Delta x / [\eta_{84}(x) - \eta_{16}(x)] \,, \tag{106a}$$
$$\Delta y_{new} = \Delta y / [\eta_{84}(y) - \eta_{16}(y)] \,, \tag{106b}$$

where, once again, $\eta_n(x)$ designates the n-th percentile of the variable x.

2. We computed the velocity dispersion of this subset according to:

$$\sigma_\mu = \sqrt{\sigma^2_{POSr} + \sigma^2_{POSt}} \,, \tag{107}$$

where POSr and POSt stand for *plane of sky radial (tangential)* directions, respectively. Moreover, the PM in the radial direction is corrected for perspective rotation (causing apparent expansion) according to eq. (4) of Bianchini et al., 2018, by using the line-of-sight velocity displayed on the website of H. Baumgardt[4]

We finally applied $\epsilon_\mu < \sigma_\mu$, where the proper motion error ϵ_μ was calculated according eq. B2 from Lindegren et al., 2018:

$$\epsilon_\mu = \sqrt{\frac{1}{2}(C_{33} + C_{44}) + \frac{1}{2}\sqrt{(C_{44} - C_{33})^2 + 4C^2_{34}}} \,, \tag{108a}$$
$$C_{33} = \epsilon^2_{\mu_{\alpha*}} \,, \tag{108b}$$
$$C_{34} = \epsilon_{\mu_{\alpha*}}\, \epsilon_{\mu_\delta}\, \rho \,, \tag{108c}$$
$$C_{44} = \epsilon^2_{\mu_\delta} \,, \tag{108d}$$

4 https://people.smp.uq.edu.au/HolgerBaumgardt/globular/, Copyright H. Baumgardt, A. Sollima, M. Hilker, A. Bellini & E. Vasiliev.

where ρ is the correlation coefficient between $\mu_{\alpha*}$[5] and μ_δ. Notice that ρ is zero for *HST* stars since $\mu_{\alpha*}$ and μ_δ were independently calculated for this catalogue.

The steps above were repeated iteratively for each star, until no more star was discarded from the cluster. This assures that at least the most discordant stars will be removed, so that they will not affect the dispersion of their network. The procedure usually consisted of $5-10$ iterations.

8.2.4.1 *Caveats*

During the procedure described above, it was possible (mostly for *Gaia* data) that a strong amount of Milky Way interlopers could bias the dispersion measurements. That is why, at each iteration, when picking the 100 closest stars in order to compute the velocity dispersion, we considered only a naively filtered subset, with less interlopers. We did this by first selecting stars whose errors were smaller than the previously computed σ_μ and whose PM moduli[6] was smaller than five times the cluster velocity dispersion fitted jointly with the Milky Way contaminants by BALRoGO (Vitral, 2021).[7]

8.2.5 *Proper motion interloper filtering*

MAMPOSSt-PM can handle the presence of interlopers in proper motion space. However, we have noticed that the best-fit MAMPOSSt-PM parameters that linked to the visible components appear more physically realistic when the interloper fraction is much less than one-half.

This model assigns a fat-tailed Pearson VII (Pearson, 1916) distribution to the Milky Way contaminants (as discovered by Vitral and Mamon, 2021), and a Gaussian to the cluster members, which allows us to compute membership probabilities to each star.[8] We then filtered out stars whose membership probabilities are smaller than 90 per cent.

8.2.5.1 *HST bulk proper motion*

In contrast with the *Gaia* data, the original *HST* PMs are relative to the bulk motion of the clusters and do not provide information about the absolute motions of stars on the sky. Before applying our mixture model mentioned above, we registered the *HST* relative PMs onto an absolute reference frame by cross matching well-measured *Gaia* and *HST* stars and computing the PM offset between them.

Well-measured stars in the *Gaia* catalogue were defined as those with `RUWE` < 1.3 and $\epsilon_\mu < 0.1$ mas yr^{-1}. For *HST* data, we selected only unsaturated stars with `QFIT` > 0.99 and magnitude rms lower than 0.1 mag in both F606W and F814W data. We refined this sample by including only objects whose proper motions have a rejection rate lower than 20 per cent, $\chi^2_x < 2$ and $\chi^2_y < 2$, and error lower than 0.1 mas yr^{-1}. Some of these quality selections are less severe than those described in Sect. 8.2.3.2 and represent a good compromise between the

5 We use the standard notation $\mu_{\alpha*} = \cos\delta\, d\alpha/dt$, $\mu_\delta = d\delta/dt$.
6 We define the PM modulus as in eq. (19) of Vitral and Mamon, 2021.
7 https://gitlab.com/eduardo-vitral/balrogo
8 Following Vitral, 2021 we allow asymmetric Pearson VII profiles.

need of a statistically-significant sample of objects to compute the offset, and the rejection of poorly-measured stars in both catalogues. Our final estimates had separations, with respect to those computed in Vasiliev and Baumgardt, 2021, of the order of the *Gaia* systematics (i.e., $\sim 0.025\,\mathrm{mas\,yr^{-1}}$).

8.2.6 *Colour-magnitude filtering*

Filtering the colour-magnitude diagram (CMD) not only removes field stars whose PMs coincide by chance with those of GC stars, but also removes GC members that are unresolved binary stars and lie in the edges of the stellar Main Sequence, as well as particular Blue Stragglers, which are believed to be associated with GC mergers and binaries (Leonard 1989; Davies 2015). Removing binaries and stars that have gone through mergers is wise because their kinematics could be dominated by two-body interactions (i.e., their motions might be more affected by the companion or by previous encounters than by the cluster's potential), while our modelling (Chapter 7) assumes that stellar motions are dominated by the global gravitational potential of the GC.

Mass-orbit modelling of line-of-sight data is biased by the presence of binaries whose velocities are more affected by their mutual interaction than by the gravitational potential of the GC (e.g., Rastello, Carraro, and Capuzzo-Dolcetta 2020). In contrast, mass-orbit modelling based on PM-based fits are not very affected by them (Bianchini et al., 2016b). Our study is entirely based on PMs, and therefore, the influence of those binaries should be almost negligible, but we still filter them, for the reasons mentioned above.

We filter these outliers according to the BALRoGO Kernel Density Estimation (KDE) confidence limits explained in Vitral, 2021, by keeping stars inside a $2-\sigma$ confidence contour. The KDE bandwidth was set as half the one derived by the Silverman rule (Silverman, 1986), to access a better resolution.

8.2.7 *Data stitching*

In order to stitch our cleaned *Gaia* EDR3 and *HST* data sets, we performed a similar approach to the one from Vitral and Mamon, 2021: First, we removed *Gaia* stars which had an angular separation in the sky from *HST* stars smaller than one arcsec. Second, we selected only *Gaia* stars with magnitudes within the range of magnitudes of our cleaned *HST* data.

The conversion of *Gaia* G magnitude into the *HST* F606W filter, for comparison purposes, was done by interpolating the output of *Parsec* isochrones for a same cluster, with different filters, in a similar fashion as what is described in Section 8.2.4 for the mass-magnitude interpolation.

8.2.8 *Multiple population treatment from Vitral & Mamon (2021)*

We explored the range of masses of the stars in our data sets by comparing synthetic CMDs from Parsec isochrones to our observed ones. In fact, mass segregation is visible in NGC 6397 (Heyl et al., 2012; Martinazzi et al., 2014). Analysing HST stars in the range $3' < R < 7'5$, Heyl et al. found mass segregation of main-sequence stars: brighter stars show 4% lower median projected

radius and 12% lower median PM moduli than fainter stars. In a subsequent study by the same team, Goldsbury, Heyl, and Richer, 2013 showed that two characteristic radii scale as a M^{γ}, with $\gamma = -1.0 \pm 0.1$ for NGC 6397. Martinazzi et al. found that the mean mass of main-sequence stars drops with *physical* radius (after deprojection) from $> 0.7\,M_{\odot}$ for $r < 10''$ to $\simeq 0.56\,M_{\odot}$ for $r > 100''$ (after correcting for the completeness with magnitude, estimating it by adding artificial PSF-convolved stars to the images), thus a 20% effect. MAMPOSSt-PM is able to treat multiple stellar populations together. We therefore also performed SD fits with two populations of stars, as we explain below.

The magnitude threshold we chose to separate the two population of stars was based on the analysis of Heyl et al., 2012: Their figures 7 and 12 indicate that NGC 6397 main-sequence stars present a (small) variation of radial distribution and velocity dispersion profiles, respectively, at a magnitude of $F814W \sim 18.75$, which corresponds to $F606W = 19.76$. We thus used this limit to divide our cleaned subset of 8255 stars into two populations, one with brighter magnitudes (6527 heavier stars) and the other with fainter ones (1728 less massive stars).

Unfortunately, we could not perform a surface density fit as robust as for the single population case because 1) our data was considerably incomplete at higher magnitudes (the fainter subset) and 2) the HST plus *Gaia* stacked subset presented discontinuous trends when allowing stars with fainter magnitudes ($G > 17$). We therefore let MAMPOSSt-PM fit the SD profile of each population from the kinematics only, more precisely from the conditional probabilities $p(\mathbf{v}|R)$. We adopted Gaussian priors for $\log R_e$, with mean equal to that found by our previous SD fit of the single population and a wide (0.2 dex) uncertainty. We also considered Gaussian priors for the Sérsic indices, but with lower uncertainties to avoid a degeneracy in its marginal distribution.

We helped MAMPOSSt-PM by providing narrow Gaussian mass priors for each population. We derived mass fractions for each population using the power-law main-sequence stellar mass function of slope $\alpha = -0.52$,[9] together with the mass limits of our subsets. Indeed, a power-law relation $dN/dm \propto m^{\alpha}$ implies a total stellar mass in the range of stellar masses (m_1, m_2) of

$$M_{\text{total}} \propto \int_{m_1}^{m_2} m \frac{dN}{dm} dm = \frac{m_2^{2+\alpha} - m_1^{2+\alpha}}{2+\alpha}\,, \tag{109}$$

and thus derive

$$\frac{M_{\text{bright}}}{M_{\text{faint}}} = \frac{m_{\text{bright}}^{2+\alpha} - m_{\text{cut}}^{2+\alpha}}{m_{\text{cut}}^{2+\alpha} - m_{\text{faint}}^{2+\alpha}}\,, \tag{110}$$

where M_{bright} and M_{faint} are the masses of the brighter and fainter populations, respectively and m_{bright}, m_{faint} and m_{cut} are the respective highest, lowest and two-population threshold masses of the global subset. With $m_{\text{bright}} = 0.77\,M_{\odot}$, $m_{\text{cut}} = 0.51\,M_{\odot}$, and $m_{\text{faint}} = 0.25\,M_{\odot}$, Eq. (110) yields a bright mass fraction of 0.56. Since our main mass estimates of NGC 6397's mass with one

9 The slope $\alpha = -0.52$ of the main-sequence stellar mass function of NGC 6397 is given in H. Baumgardt's very useful web site on GCs, https://people.smp.uq.edu.au/HolgerBaumgardt/globular.

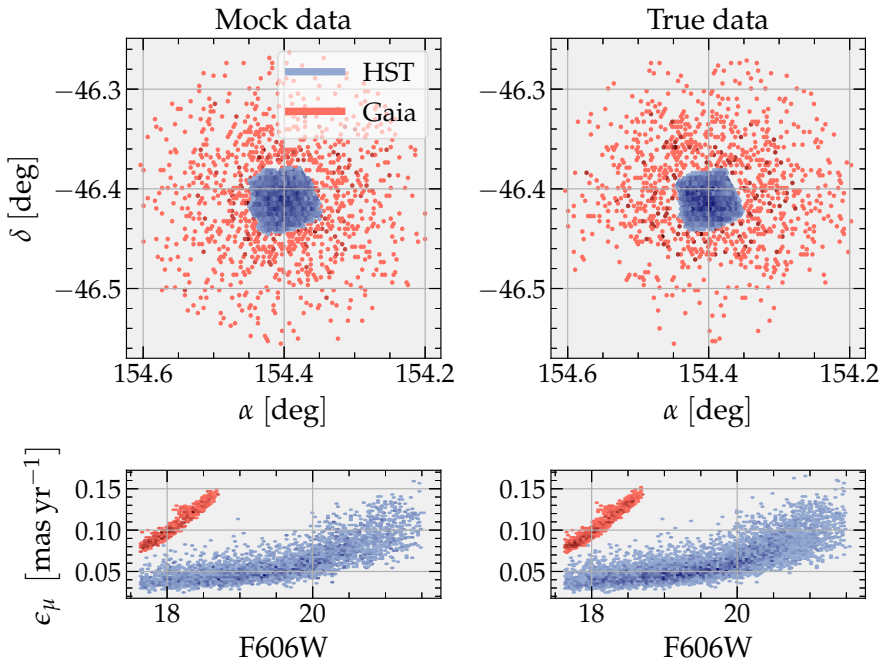

Figure 29: *Mocks:* Comparison of our mock data (*left*) and the true data set (*right*), for NGC 3201. Stars associated with *HST* are in *blue*, while the ones associated with *Gaia* EDR3 are in *red*. The *upper panels* show the positions on the sky, while the *lower panels* show the dependence of proper motion errors with magnitude. The axis limits are the same between mock and data. The colours go from *faint tones* in less populated regions to *darker tones* in more populated regions). This figure was originally published in Vitral et al., 2022.

single population were centred around 10^5 $M_\odot$, we passed logarithmic Gaussian priors to each population, centred at $\log(M/M_\odot) = 4.7$, with standard deviation of 0.05.

8.2.9 *Mock data*

We built mock datasets to test the ability of MAMPOSSt-PM to recover central mass excesses, either point-like (IMBH) or extended as a cluster of unresolved objects (CUO). For each GC, we generated four mocks, one with no central excess mass, one with an IMBH, one with an extended central mass, and one with both IMBH and an extended central mass.

8.2.9.1 *Positions and velocities in a cartesian frame*

The mocks were constructed with the Agama software (Vasiliev, 2019a). For each GC, we used information obtained from our MAMPOSSt-PM runs: i.e. with the same mass profiles as determined by MAMPOSSt-PM. Therefore, the GC followed a Sérsic profile and the CUO, if present, followed a Plummer profile, while the GC Main Sequence and CUO stars had isotropic velocities. The mean tracer mass of each population (i.e., GC and CUO) is required by Agama for the construction of the mock.

- For GC tracers, we estimated the mean mass assuming a power-law mass function (MF), dN/dM:

$$\bar{m}_\star = \frac{\int_{m_{min}}^{m_{max}} m\,[dN/dm]dm}{\int_{m_{min}}^{m_{max}} [dN/dm]dm} = \frac{m_{max}^{\alpha+2} - m_{min}^{\alpha+2}}{m_{max}^{\alpha+1} - m_{min}^{\alpha+1}} \tag{111}$$

  where we used the MF slopes α available at the website of H. Baumgardt, see footnote 4), while m_{min} and m_{max} are the minimum and maximum stellar masses of our data, derived from PARSEC isochrones (see Fig. 28).

- For CUO tracers, we used the mean mass of the compact objects from the Monte Carlo models described in Section 8.2.11, up to twice the 3D half mass radius we derived from the real data with MAMPOSSt-PM.

8.2.9.2 *Sky membership*

We transformed the Cartesian coordinates into astrometric data (i.e., α, δ, $\mu_{\alpha,*}$, and μ_δ) positioned similarly to the studied clusters with the routine ANGLE.CART_TO_RADEC from BALROGO. We used the same values of cluster centre, mean bulk motion[10], line-of-sight velocity and distance we considered for the true data.

Next, for each star, we assigned *Gaia* EDR3 and *HST*-like memberships by mimicking the membership of the closest star in the true data set. The top panels of Figure 29 show the mock data used for NGC 3201 next to the true data for this cluster.

8.2.9.3 *Proper motion errors*

We estimated proper motion errors in our mock GC stars, separately for the *HST* and *Gaia* EDR3 data sets, according to the following steps:

1. We constructed an empirical cumulative distribution function (CDF) of magnitudes (the original F606W for *HST* data, and the converted G_{mag} to F606W for *Gaia*) for the true data, by sorting and arranging it from zero to one.

2. We interpolated the CDF with the respective magnitudes for a uniformly distributed array (from zero to one) of length equal the mock *Gaia* EDR3 or *HST*-like data set, which is greater than the length of the true data set. This creates a random distribution of magnitudes following the same shape as the true data.

3. From those magnitudes, we associated an error (both in α and δ) by picking the same $\epsilon_{\alpha,*}$ and ϵ_δ from the star with the closest magnitude from the true data set. In this way, the proper motion errors follow the same trend and scatter with magnitude as the observed ones, as can be seen from the similarity of the bottom panels of Fig. 29.

10 We considered the *HST* bulk motion as calculated in Section 8.2.5.1 for *HST*-like stars, and the bulk motion values from Vasiliev and Baumgardt, 2021 for the *Gaia*-like stars. Having two different bulk motions may surprise the reader, and we tested in Vitral et al., 2022 the robustness of our results to the choice of bulk motions.

4. Having those errors, we add them up to the proper motions by sorting random Gaussian variables with zero mean and standard deviation equal to the respective error. The original errors are saved and taken into account during the mass modelling, when convolving the velocity distribution function of the tracers.

Finally, we randomly selected, from each data set, a number of tracers equal to the amount of respective *Gaia* and *HST* stars from our true data set, which artificially (and intentionally) adds incompleteness to our subset.

8.2.10 *Statistical tools*

We first use Bayesian evidence to compare our four basic models for each GC: no excess inner mass, a central IMBH, a CUO, and a combination of IMBH and CUO. This model selection involves comparing the maximum log posteriors using a Bayesian information criteria. We then measure how well the posterior distributions obtained by MAMPOSSt-PM on the observations match those obtained on mock data constructed to mimic these observations.

8.2.10.1 *Bayesian inference*

We use the corrected Akaike Information Criterion (derived by Sugiura 1978 and independently by Hurvich and Tsai 1989 who demonstrated its utility for a wide range of models)

$$\mathrm{AICc} = \mathrm{AIC} + 2\,\frac{\mathrm{N_{free}}\,(1+\mathrm{N_{free}})}{\mathrm{N_{data}}-\mathrm{N_{free}}-1}\,, \tag{112}$$

where AIC is the original Akaike Information Criterion (Akaike, 1973)

$$\mathrm{AIC} = -2\,\ln\mathcal{L}_{\mathrm{MLE}} + 2\,\mathrm{N_{free}}\,, \tag{113}$$

and where $\mathcal{L}_{\mathrm{MLE}}$ is the maximum likelihood estimate found when exploring the parameter space, $\mathrm{N_{free}}$ is the number of free parameters, and $\mathrm{N_{data}}$ the number of data points. We prefer AICc to the other popular simple Bayesian evidence model, the Bayes Information Criterion (BIC, Schwarz 1978), because AIC(c) is more robust for situations where the true model is not among the tested ones (for example our choice of Sérsic density profiles is purely empirical and not theoretically motivated), in contrast with BIC (Burnham and Anderson, 2002).

The likelihood (given the data) of one model relative to a reference one is

$$\exp\left(-\frac{\mathrm{AIC}-\mathrm{AIC_{ref}}}{2}\right) \tag{114}$$

(Akaike, 1983) and we assume strong evidence for one reference model over another whenever 95 per cent confidence is attained (i.e., $\mathrm{AICc} > \mathrm{AICc_{ref}} + 6$). We consider AICc differences smaller than 4.5 (i.e., less than 90 per cent confidence) are usually not enough to consistently distinguish two models, based on purely statistical arguments (thus, no astrophysics involved).

8.2.10.2 *Distance on parameter space*

To correctly compare the mass-modelling outputs of the mock data and the true, observed data, we also compute the distance on parameter space from the maximum likelihood[11] solutions of the real data and the mock data set. For each free parameter k, we define the distance between the maximum likelihood solutions λ_{ik}^{MLE} and λ_{jk}^{MLE} from the set of chains from the data and mock, $\mathcal{C}_i$ and $\mathcal{C}_j$ as:

$$\Delta_{ij}(k) = |\lambda_{ik}^{MLE} - \lambda_{jk}^{MLE}| \, . \tag{115}$$

With this information, we follow the iteration below:

1. For each parameter k, select a random value from the chain $\mathcal{C}_i$, and another one from the chain $\mathcal{C}_j$.
2. Evaluate if the modulus of the difference between these two values is greater than $\Delta_{ij}(k)$.
3. Repeat it 10^6 times.

Then, we compute the fraction $\phi_{\Delta k}$ of times where the absolute difference between the random values from $\mathcal{C}_i$ and $\mathcal{C}_j$ is greater than $\Delta_{ij}(k)$. If this fraction is high, it means that the distance between the fits from the mock and true data is small when compared to the overall difference of MCMC chain values. On the opposite, small fractions (e.g., $\lesssim 50\%$) indicate a disagreement between the fits of mock and true data. We test this statistic for the free parameters of a dark central component fit (i.e., mass and scale radius of the dark component), in order to better evaluate its composition.

8.2.10.3 *AD and KS statistics*

In some cases, the marginal distribution of the posterior might be very broad, indicating higher uncertainties for the maximum likelihood solutions. In that case, it is interesting to compare the *shapes* of the marginal distributions obtained by MAMPOSSt-PM on the mock and observed datasets, to probe the expected contrast between different mass models. For this purpose, we used Kolmogorov-Smirnov (Kolmogorov 1933; Smirnov 1939, hereafter KS) as well as Anderson-Darling (Anderson and Darling 1952, hereafter AD) statistics to quantify the disagreement between mock and observed marginal distributions of mass and scale radius of a dark central component.

Since the KS and AD tests quantify whether two 1-D distributions arise from a single parent distribution, they will be sensitive to any shift between them. We adapt these statistics to compare the distribution of shapes without being sensitive to any offset. For this, we translated (shifted) the two marginal distributions by a proxy of their respective median. In practice, we performed the following iteration three times:

11 Since some of our priors are Gaussians, our maximum likelihood parameter vectors are really maximum posteriors, but we will refer to these as 'maximum likelihood' to avoid confusion with the modes of the marginal parameter distributions.

Table 4: Number of compact objects in our CMC Monte Carlo N-body models.

ID	BH	NS	WD [ONeMg]	WD [CO]	WD [He]
(1)	(2)	(3)	(4)	(5)	(6)
NGC 3201	108	334	1954	78501	315
NGC 6397	0	191	620	31941	73

Notes: Columns are: (1) Cluster ID; (2) Number of black holes; (3) Number of neutron stars; (4) Number of [ONeMg] white dwarfs; (5) Number of [CO] white dwarfs; (6) Number of [He] white dwarfs. This table was originally published in Vitral et al., 2022.

1. We first consider only the intersection of the two chains $\mathcal{C}_i$ and $\mathcal{C}_j$, to be compared.
2. We assign this intersection to an auxiliary pair of chains $\widetilde{\mathcal{C}}_i$ and $\widetilde{\mathcal{C}}_j$.
3. We translate the distributions of $\mathcal{C}_i$ and $\mathcal{C}_j$ by a respective amount of $M\left[\widetilde{\mathcal{C}}_i\right]$ and $M\left[\widetilde{\mathcal{C}}_j\right]$, where M[x] is the median of a distribution x.

This iteration removes undesirable effects on the borders of the distributions, where there may be artefacts of our choice of priors. This iteration thus allows a more honest comparison between the shapes of the distributions than just a single shift by the difference of medians, because our distributions can be skewed non-Gaussians (the median does not necessarily follow the mode of a skewed distribution). We considered the intersection of the translated mock and observed marginal distributions of a specific parameter, and computed the KS and AD statistics associated with them.

8.2.11 *Monte Carlo* N*-body models*

To facilitate interpretation of our results, we use Monte Carlo N-body cluster models of NGC 3201 and NGC 6397, computed using the cluster dynamics code CMC (Kremer et al., 2020a; Rodriguez et al., 2022). CMC is a Hénon-type Monte Carlo code that includes various physical processes relevant to the dynamical evolution of clusters including two-body relaxation, tidal mass loss, and direct integration of small-N resonant encounters. For strong binary-mediated encounters, CMC computes the energy exchange between binaries and stars directly, by performing direct N-body integrations using the Fewbody code (Fregeau and Rasio, 2007), now updated to include post-Newtonian effects for black hole encounters (Rodriguez et al., 2018). Although individual distant encounters (with pericentre distances much larger than the characteristic hard-soft boundary) are not modelled directly, the cumulative effect of many distant encounters is computed as a single *effective* encounter at each time step using the scheme described in Stodolkiewicz (1982); Joshi, Rasio, and Portegies Zwart (2000). This method captures the effect of distant encounters on the cluster as a whole, in particular upon the two-body relaxation process. For a detailed and current explanation of the methods implemented in CMC, see Rodriguez

et al. (2022, specifically Section 2.1 for discussion of the treatment of weak encounters and two-body relaxation, and Section 2.2 for the treatment of strong encounters). The Monte Carlo approach employed in CMC has been shown to agree well with direct N-body models, especially pertaining to dynamical evolution of black holes (e.g., Rodriguez et al., 2016). Finally, by employing the COSMIC single/binary star evolution code (Breivik et al., 2020), CMC tracks various evolution features (including stellar type, mass, radius, luminosity, etc.) for all N stars as the model cluster evolves dynamically. This makes it straightforward to compute standard observed cluster features from the CMC snapshots, in particular surface brightness and velocity dispersion profiles, binary fractions, and colour-magnitude diagrams (e.g., Rui et al., 2021a).

Previous studies have identified specific CMC models that match accurately both NGC 3201 and NGC 6397 (using observed surface brightness and velocity dispersion profiles as the key diagnostic to evaluate goodness of fit; for details, see Rui et al. 2021a). For NGC 3201, we use the CMC model presented in Kremer et al., 2019a. For NGC 6397, we use the models published in Kremer et al., 2021 and also compute a few additional models in an effort to more accurately match the compact object distributions inferred from our analysis.[12] In both clusters, CMC starts with isotropic stellar orbits (e.g., assumes standard King profiles as initial conditions; King, 1966), and despite 3-body encounters and natal kicks, the models remain roughly isotropic over time. In Table 4, various features of our best-fit models for both of these clusters are listed.

8.3 RESULTS FROM VITRAL & MAMON (2021)

The results of the mass-anisotropy fits from Vitral and Mamon, 2021 can be seen in their table 3, for various mass models.

8.3.1 *Velocity anisotropy*

The combination of *HST* data properly probing the inner regions of NGC 6397 with the *Gaia* data probing the outer regions allows us to estimate the velocity anisotropy across the cluster. We ran MAMPOSSt-PM using different priors on the anisotropy. Our standard prior had isotropic velocities throughout the GC. Our other priors assume the gOM anisotropy model (we found that the softer varying Tiret et al. 2007 model performs almost as well, but not better).

In summary, there was strong evidence for isotropy with BIC, but weaker evidence with AICc. However, even the anisotropic runs produce anisotropy profiles that were very close to isotropic throughout. We thus concluded that the visible stars in NGC 6397 have quasi-isotropic orbits, at least for the stars brighter than F606W $= 19.76$ and up to R $= 8'$ (i.e., the limits of the data in this paper). We therefore adopted isotropic orbits as our standard when investigating other quantities.

12 The CMC N-body models are intended to provide a basic numerical supplement that complements the Jeans modelling constraints. We are not claiming to have performed an exhaustive match between the models and observed cluster properties, which may include other diagnostics such as mass segregation measurements (e.g., Weatherford et al., 2020), blue straggler

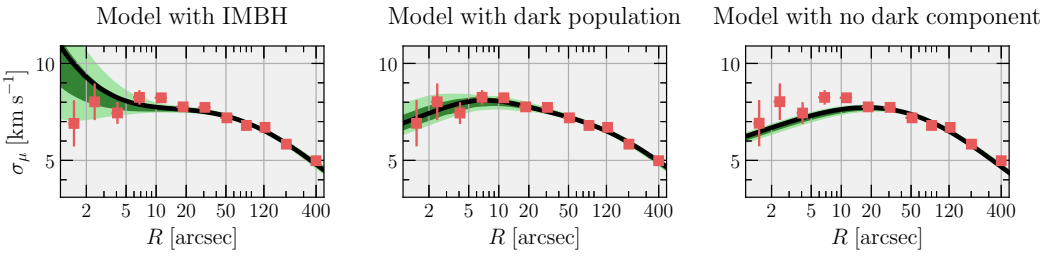

Figure 30: Goodness of fit plots of plane of velocity dispersions as a function of the projected radius for no dark component (**left**), IMBH (**middle**) and central unresolved objects (**right**). The *black curves display* the maximum likelihood solutions, while the *darker and lighter shaded regions* show the [16, 84] and [2.5, 97.5] percentiles, respectively. The *red squares* show the data in logarithmic spaced bins. The vertical error bars were calculated using a bootstrap method, while the horizontal error bars considered the radial quantization noise. This figure uses data from Vitral and Mamon, 2021.

8.3.2 *Intermediate mass black hole*

We tested the scenario with an IMBH and no CUO. The most likely one and very strongly favoured by AICc yields an IMBH mass of $511^{+158}_{-207}\,M_\odot$. Furthermore, AICc (resp. BIC) indicates very strong (resp. quite strong) evidence for the presence of an IMBH in the absence of a central diffuse component.

However, both AICc and BIC indicate strong evidence against the IMBH hypothesis in comparison with the presence of a CUO, with differences of 15.9 in AICc and 8.9 in BIC between isotropic, single-population models. Hence, the unseen inner matter of NGC 6397 is very likely to be diffuse. We therefore now investigate the CUO model in more detail. Figure 30 illustrates the quality of the 3 classes of models in reproducing the observed velocity dispersion profiles. The model with no additional dark component, clearly underestimates the velocity dispersions below 10″. The model with an IMBH, overestimates it below 4″. Finally, the model with a CUO does best.

8.3.3 *Inner sub-cluster of unresolved objects (CUO)*

8.3.3.1 *CUO density profile*

If the dark component is diffuse as a CUO instead of a singular IMBH, we first need to measure its extent. We first assumed a Plummer, 1911 model for the CUO with the same effective radius as that of the GC stars (4′5), but with a wide standard deviation (1 dex) for the Gaussian prior on log scale radius. Interestingly, as seen in Figure 31, MAMPOSSt-PM converged to $r_{-2} = 7''$, thus an effective (half-projected number) radius of only 4″3 for the CUO, which is 60 times lower than the median of the prior, thus confirming our suspicion that the CUO might indeed be significantly more concentrated than the main-sequence stars.

populations, cataclysmic variables, etc. Such a comparison would be a much more intensive endeavour than is intended here.

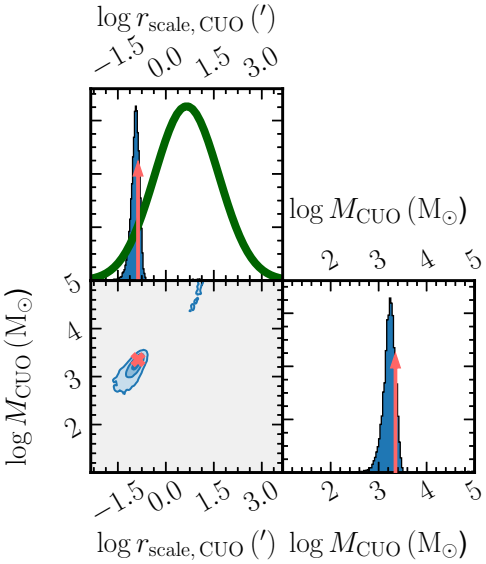

Figure 31: Selected marginal distributions of the CUO effective radius and mass, and their covariance, for a preliminary MAMPOSSt-PM run for an isotropic, single-population plus Plummer CUO SD profile, with an unrealistic prior on the log CUO scale radius centred at $r_{-2,CUO} = R_{e,GC} = 4'51$. This figure was originally published in Vitral and Mamon, 2021.

We then ran MAMPOSSt-PM for three models with a much smaller scale radius prior for the CUO (30″), to allow for more accurate fits. We used three different CUO density models: a Sérsic model, a Plummer model, and a Hernquist, 1990 model. All three led to very small scale radii, which convert to effective (half projected number) radii $R_e = 9''6, 17''4$ and $4''4$ for the Sérsic, Hernquist and Plummer models, respectively.

AICc has a weak preference for the Plummer model, while BIC prefers the Plummer model, with strong evidence against the more complex Sérsic model, but weak evidence against the Hernquist model. The model with the Sérsic CUO density profile produced a low Sérsic index of $n = 0.92$, which leads to a shallow inner slope that is not too different from the zero slope of the inner Plummer density profile (see Figure A.1 from Vitral and Mamon 2020). The steeper inner profile of the Hernquist density profile makes it less similar to the $n = 0.92$ Sérsic model than is the Plummer profile, as confirmed by the Hernquist model producing the lowest likelihood (highest $-\ln\mathcal{L}$) among the three models. In summary, it is hard to distinguish which is the best density model for the CUO scenario. There was weak evidence for a shallow slope. We adopted the Plummer model given that it is the preferred of the three density models for both AICc and BIC, albeit with weak evidence for both.

8.3.3.2 *Presence of an IMBH in addition to the CUO*

One may ask whether the centre of NGC 6397 can host both an IMBH and a diffuse dark component. We tested this model, but it is somewhat less likely than the CUO case, and in comparison it is strongly disfavoured by BIC, although only weakly disfavoured by AICc. We note that the Plummer model used for the CUO is the one that best distinguishes the CUO from a possible

additional IMBH. Moreover, the recovered mass of the additional IMBH is so small $42^{+92}_{-26}\,M_\odot$ that it can no longer be called an IMBH.

8.3.4 *Two-mass populations*

In Vitral and Mamon, 2021, we also tested our 4 models with two populations, split by apparent magnitude, hence by mass. The model with a CUO but no IMBH, had the highest likelihood of the three models considering isotropy. It was very strongly favoured with AICc over the models with IMBH but no CUO and no IMBH nor CUO. This preference of the CUO model over the IMBH model resembles that found for the single population (Sect. 8.3.2).

But there are differences in the MAMPOSSt-PM results between single-population and two-population models, both in their Bayesian evidence and in their best-fit parameters. In particular, comparing two-population models to their single-population equivalents, with strong AICc evidence.

MAMPOSSt-PM yielded interesting results on the differences between the bright and faint populations. First, the two-population runs can be tested for the respective masses in each. Despite our prior of equal masses for each, MAMPOSSt-PM returned best-fit bright population mass fractions of 0.49, 0.44, and 0.57 for the models IMBH without CUO, no IMBH nor CUO, and CUO without IMBH. Only one model (CUO without IMBH) had a bright fraction close to the expected value of 0.56 (from the IMF).

Secondly, in all three two-population models, the brighter population had a much lower scale radius than its fainter counterpart, by factors of ~ 2. These lower scale radii for the bright population were highly statistically significant. Indeed, the fractions of MCMC chain elements leading to higher scale radius of the brighter population were very small. Therefore, MAMPOSSt-PM is able to find very strong kinematic signatures of luminosity (hence mass) segregation, by fitting $p(\mathbf{v}|R)$ with the same priors on the scale radii of the two populations, without directly fitting the distribution of projected radii.

8.3.5 *Composition of the CUO*

Below, we present the discussion from Vitral and Mamon, 2021 on the nature of the subcluster of unresolved objects that we found in the centre of NGC 6397. The much smaller scale radius for the CUO indicates that the objects must be more massive than the stars that we studied, thus more massive than $m_{bright} \sim 0.77\,M_\odot$ (Figure 28). Indeed, such unresolved massive objects would sink to the centre by dynamical friction Chandrasekhar, 1943.

We compared the radial distribution from our cleaned sample and from X-ray binaries from Bahramian et al., 2020. Figure 32 shows the cumulative distribution function (CDF) of these two datasets in the range of $2.7 - 100''$. It is clear that these two populations do not follow the same radial distribution (we find a KS p-value of 1.7×10^{-4}). Furthermore, the bulk of the X-ray binaries seems to be located within $6'' - 50''$ arcsec (Figure 32). This is consistent with the CUO effective radius of 2.5 to $5''$.

One may ask which among white dwarfs, neutron stars, BHs and massive binaries dominates the mass of the CUO. We can first discard unresolved binaries

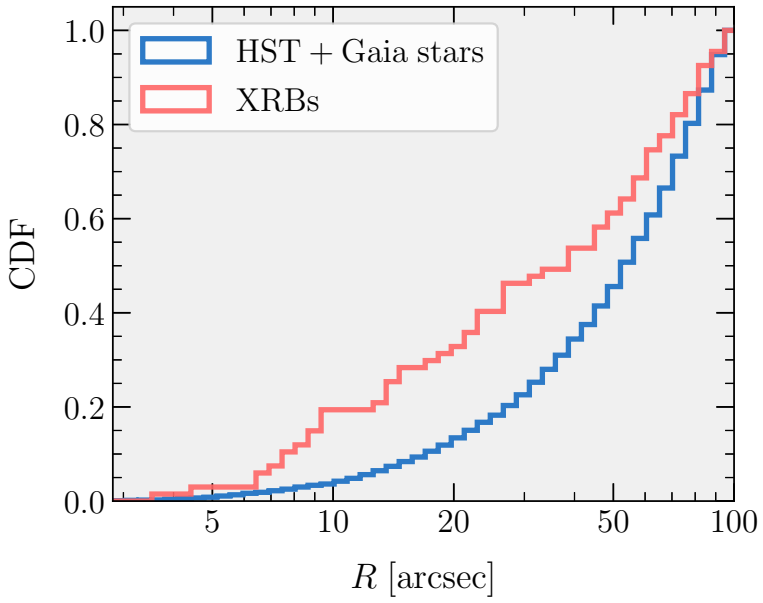

Figure 32: Cumulative distribution functions of projected radii for our HST+*Gaia* subset in blue and for the X-ray binaries from Bahramian et al., 2020 in red. We considered the subsets in the range of $2.7'' < R_{proj} < 100''$. This figure was originally published in Vitral and Mamon, 2021.

of main-sequence stars. Indeed, if they are unobserved, their total magnitude must be fainter than F606W $= 22$, which is the rough magnitude limit of our HST sample (*Gaia* is not relevant given the very low effective radius of the CUO). There is no way that their total mass can exceed that of the bulk of our sample. We could then have unresolved binaries of a main-sequence star with a compact star (white dwarf or neutron star) or possibly a BH. But the main-sequence star will have a mass of $m_{faint} = 0.25\,M_\odot$ (Figure 28), thus at least three times lower than our cut at $m_{bright} = 0.77\,M_\odot$ and at least 20 times lower than that of a BH. Therefore, the main-sequence mass can be neglected.

In Vitral and Mamon, 2021, we compared the total mass in white dwarfs, neutron stars and BHs, by integrating over the zero-age (stellar mass function of the) main sequence (ZAMS):

$$\int_{m_{min}}^{m_{max}} m_{remnant}(m)\, n(m)\, dm\,, \tag{116}$$

where $n(m)$ is the ZAMS. We adopted the initial - final (remnant) mass relations from equations (4)–(6) of Cummings et al., 2018 for white dwarfs and from equations (C1), (C2), (C11), and (C15) of Spera, Mapelli, and Bressan, 2015 for neutron stars and BHs. Figure 33 displays these initial - final mass relations. We took a minimum remnant mass of $0.77\,M_\odot$, corresponding to the maximum main-sequence mass (Sect. 8.2.8), below which mass segregation is not effective against the most massive main-sequence stars. The maximum possible neutron star mass is $M \simeq 2.15\,M_\odot$ (Rezzolla, Most, and Weih, 2018). We conservatively assumed a mass gap between 2.15 and $5\,M_\odot$ from the lack of LIGO detections in this mass range. We also considered a maximum stellar BH mass above which pair-instability supernovae fully explode the progenitor star leaving no remnant, adopting $M_{BH,max} = 45\,M_\odot$ (Farmer et al., 2019) or $52\,M_\odot$ (Woosley,

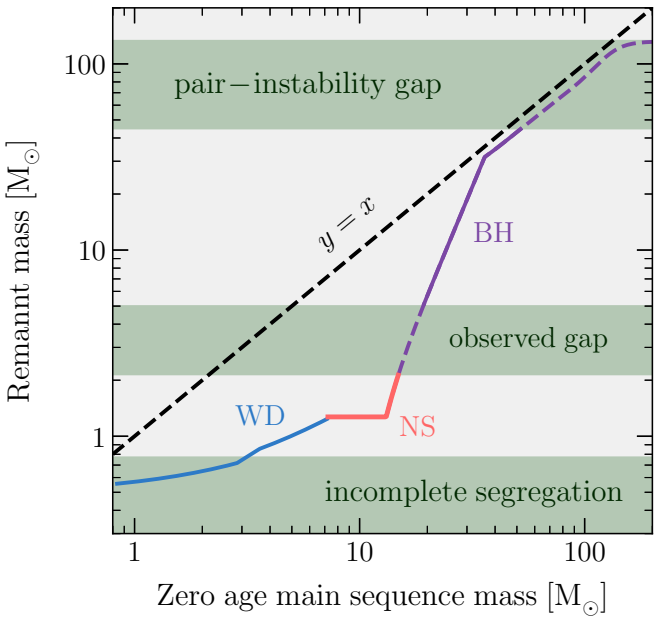

Figure 33: Initial – final mass relation of white dwarfs (WD, MIST model from Cummings et al. 2018, *blue*), neutron stars (NS, *red*) and black holes (BH, *purple*) (PARSEC/SEVN model with Z = 0.0002 from Spera, Mapelli, and Bressan 2015). Factors of two changes in Z are barely visible in the red (purple) line and do not affect the blue line. The *lower green band* indicates incomplete mass segregation because some of the main-sequence stars are more massive than the white dwarfs. The *middle green band* indicates the gap where no BHs have (yet) been detected. The *upper green bands* highlight the gap where pair-instability supernovae fully explode the progenitor star without leaving a black hole. The *black line* shows equality as a reference. This figure was originally published in Vitral and Mamon, 2021.

2017). We ignored the formation of very massive BHs above the pair-instability gap (i.e., $M_{BH} > 133\,M_\odot$ Woosley 2017).

Summing the masses of each component by integrating Eq. (116) over the ZAMS mass function (i.e., the initial mass function, which in this mass range always has the Salpeter 1955 slope of –2.3) leads to BHs accounting for $\approx 58\%$ of the CUO, with only $\approx$ 30% from white dwarfs and $\approx$ 12% from neutron stars. These fractions vary little with the maximum allowed BH mass: with 55% of the CUO mass in BHs with $M_{BH} < 45\,M_\odot$ (Farmer et al., 2019) or 60% with $M_{BH} < 52\,M_\odot$ (Woosley, 2017). These fractions are insensitive to the metallicity of NGC 6397 from $Z = 0.00013$ to 0.0004 (i.e., from 1% to 3% solar, consistent with the metallicities derived for NGC 6397 by Marin-Franch et al. 2009 and Jain et al. 2020, respectively).

However, we must take this CUO mass dominance by BHs with caution because BHs may merge, losing of order of 5% of their mass to gravitational waves (e.g., Abbott et al. 2016a), leading to kicks, some of which are strong enough to drive them out of the GC. Still, one part of the BH population may merge and end up escaping the GC, while another part has not merged, but would nevertheless be located at low radii thanks to orbital decay by dynamical friction. If the CUO mass fraction in BHs were at least $f_0 = 0.55$ or 0.6 before merging and escapes, and if a mass fraction f_d of this BH component disappeared through mergers or escapes, then BHs would still dominate the CUO if $f_0\,(1 - f_d) > 1 - f_0$, i.e. $f_d < 2 - 1/f_0 = 0.19$ or 0.33 considering the maximum BH mass of $45\,M_\odot$ (Farmer et al., 2019) or $52\,M_\odot$ (Woosley, 2017). Put another way, BHs could contribute to half the CUO mass, if the maximum surviving BH mass is $40\,M_\odot$ according to our integrations of Eq. (116). The more massive BHs would sink faster to the centre by dynamical friction and preferentially merge, leaving these lower mass ones. This discussion is a simplification because orbital decay by dynamical friction is stochastic, and one needs to test this with N-body simulations.

A more robust conclusion of our integration of Eq. (116) is that white dwarfs always dominate the neutron stars, by a factor of ≈ 4, regardless of the possible dominance of BHs in the mass of the CUO component. Moreover, neutron stars can also merge together (or with black holes), and such an event has been detected by LIGO (Abbott et al., 2017). Presumably, the gravitational waves emitted will be much weaker and the lower momentum vector of the waves should lead to smaller kicks on the remnant (despite the lower masses of neutron stars compared to BHs). In summary, Vitral and Mamon, 2021 concluded that the CUO mass should be dominated by BHs, but must also contain white dwarfs, contributing four times more mass to the CUO than neutron stars.

8.3.6 *Repercussions of Vitral & Mamon (2021)*

On the basis of the initial mass function and simple stellar evolution, Vitral and Mamon, 2021 argued that the inner mass excess may be dominated by stellar-mass black holes if these avoided merging and escaping from the momentum acquired by the anisotropic emission of gravitational waves. However, we did not consider the importance of black hole ejection from dynamical interactions,

nor that a large black hole population is inconsistent with the core-collapsed structure of NGC 6397 (Rui et al., 2021b).

As discussed in Sect. 3.4.2.1, once formed, black holes mass segregate to the centres of their host clusters, creating a black hole subsystem. Once a central black hole subsystem forms (typically on $\lesssim 100\,\mathrm{Myr}$ timescales), black hole–black hole binaries[13] within this subsystem begin to undergo binary–single and binary–binary dynamical encounters with single black holes and other binary black holes, respectively, on $\mathcal{O}(\mathrm{Myr})$ timescales. On average, these dynamical encounters lead to hardening of the black hole binaries (e.g., Heggie, 1975). Conservation of energy requires that this dynamical hardening is accompanied by an increase in kinetic energy of the single and binary black holes involved: the single and binary black holes receive dynamical "kicks." Inevitably, the consequence of many of these dynamical encounters is for nearly the entire black hole population (both singles and binaries) to be ejected from their host cluster (e.g., Kulkarni, Hut, and McMillan, 1993; Portegies Zwart and McMillan, 2000; Morscher et al., 2015; Wang et al., 2016; Askar, Arca Sedda, and Giersz, 2018; Kremer et al., 2020b).

Although the dynamical ejection of all black holes is expected to be the ultimate fate of all GCs, not all clusters have evolved sufficiently long to have reached this state. Kremer et al., 2020a showed that the initial size at given mass of a GC impacts considerably its dynamical and evolutionary timescales, with denser clusters evolving faster and thus ejecting their black holes faster. Furthermore, while present in a cluster, the dynamical activity of stellar-mass black holes pump energy into their host cluster's luminous stellar population, preventing cluster core collapse (Merritt et al., 2004; Mackey et al., 2007; Breen and Heggie, 2013; Askar, Arca Sedda, and Giersz, 2018; Kremer et al., 2019a; Kremer et al., 2020a; Weatherford et al., 2020). This implies that non-core-collapsed clusters have yet to eject their full black hole population, while core-collapsed clusters should contain a negligible number of stellar-mass black holes. In the absence of black holes in the latter case, the inner regions of core-collapsed clusters are expected to be dominated by white dwarfs, the next most massive stellar population.[14]

Since NGC 6397 is a core-collapsed GC (Djorgovski and King, 1986), its inner mass should be dominated by white dwarfs instead of by stellar-mass black holes. This idea was recently confirmed by Kremer et al., 2021, who found that the observed surface brightness and velocity dispersion profiles of NGC 6397 were effectively reproduced by core-collapsed `CMC` models that included an inner population of hundreds of white dwarfs.

8.4 RESULTS FROM VITRAL ET AL. (2022)

Given the repercussion from Vitral and Mamon, 2021 mentioned above, we decided to perform our data modelling once again with new re-calibrated *HST*

13 Black hole binaries can form from the evolution of primordial massive stellar binaries in the cluster or through the three-body binary formation mechanism involving three single black holes (e.g., Binney and Tremaine, 2008; Ivanova et al., 2010; Morscher et al., 2015).

14 Of course, neutron stars likely have comparable masses to white dwarfs (or even slightly larger masses). However white dwarfs dominate overwhelmingly by number, and thus are expected to dominate the central regions.

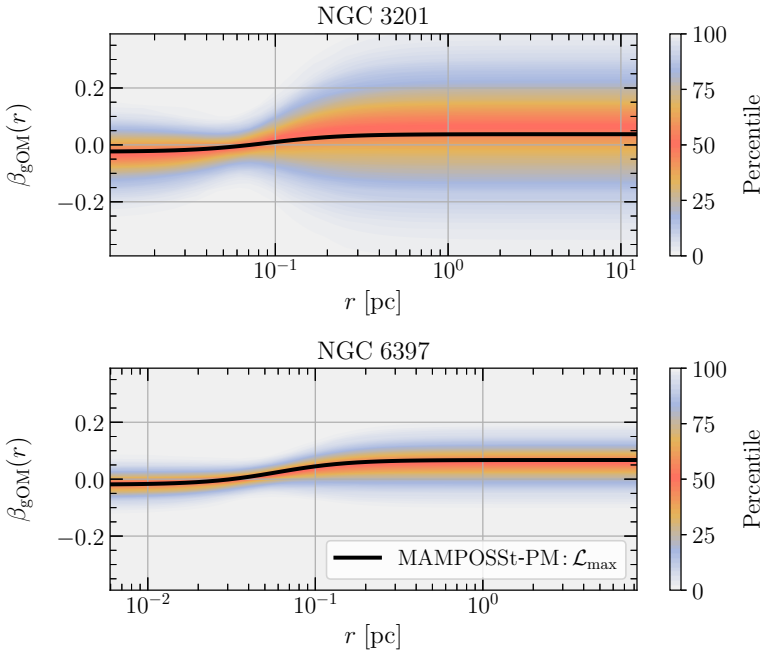

Figure 34: *Velocity anisotropy:* MAMPOSSt-PM fits of the velocity anisotropy, using the gOM parameterization (Eq. [80]), as a function of the distance (in pc) to the respective cluster's centre. The colour bar indicates the percentile of the MCMC chain post burn-in phase. The *black curves* represent the maximum likelihood solution of our fit. The *upper* plot displays the fits for NGC 3201, while the *bottom* plot presents the fits for NGC 6397. The range of physical radii is set to the range of projected radii in the data we analysed. This figure was originally published in Vitral et al., 2022.

data and *Gaia* EDR3 (instead of DR2), and this time using robust constraints from Monte Carlo simulations and mock datasets in order to probe the composition of a possible CUO. We joined forces with Kyle Kremer, with a strong expertise in Monte Carlo simulations, and Mattia Libralato and Andrea Bellini, who both bring great expertise of proper motion data handling, specially with *HST*. After the data cleaning and construction described in Section 8.2, we ran a total of 48 MAMPOSSt-PM fits on the *HST* plus *Gaia* EDR3 data, using different mass models, data cuts, and prior assumptions. In the following, we present our results on velocity anisotropy and on the excess of mass in the centre.

8.4.1 *Velocity anisotropy*

Our MAMPOSSt-PM fits to the kinematic data allow us to constrain the radial profile of velocity anisotropy of the visible (Main Sequence) stars. For each mass model, we performed MAMPOSSt-PM fits to the data using isotropic and gOM velocity anisotropy (Eq. [80]) in turn. For both GCs, all the free anisotropy runs presented roughly isotropic shapes, with a slight tendency for radial anisotropy in the outskirts and tangential anisotropy in the centre. However, the uncertainties in the inner and outer anisotropies encompass the isotropic solution. This can be seen in Figure 34, which displays the radial profiles of velocity anisotropy for the two clusters with the CUO mass model. Admittedly, the uncertainties of the outer anisotropy profile of NGC 3201 are quite large. Thus,

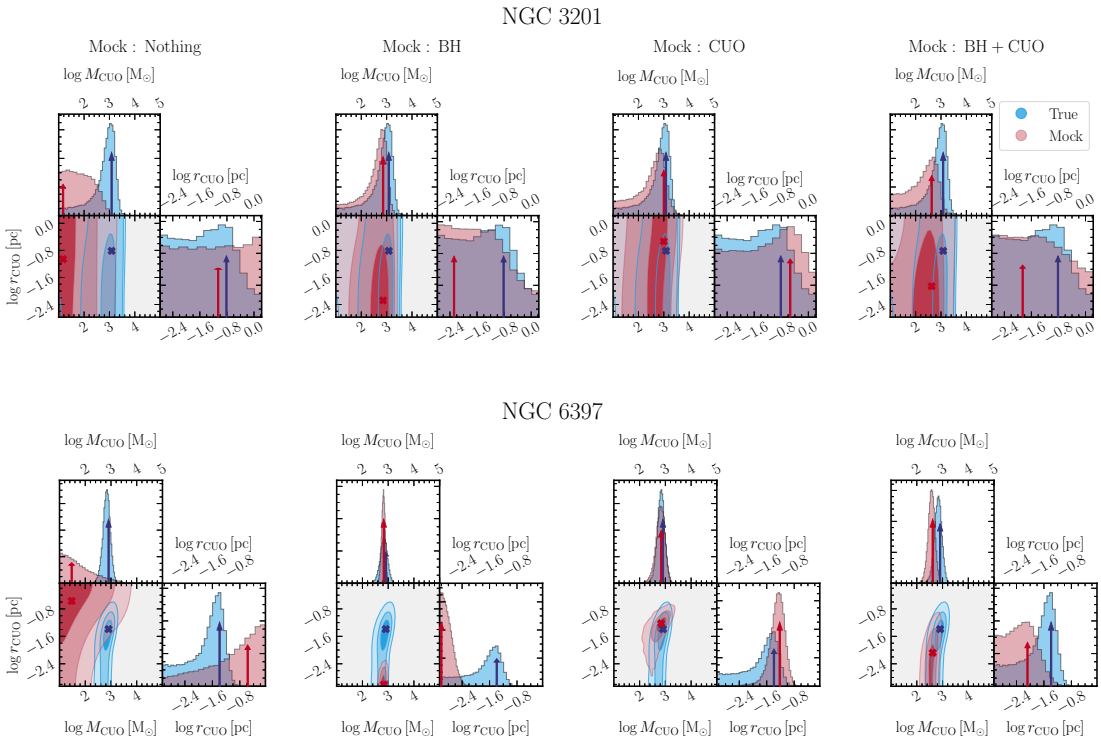

Figure 35: *MAMPOSSt-PM outputs on mock data compared to those on real data:* Marginal distributions of the cluster of unresolved objects (CUO) mass and 2D Plummer half mass radius and their covariances for the true data (*HST* and *Gaia* EDR3) in *blue* and the mock data (constructed with Agama) in *red*, for NGC 3201 **top** and NGC 6397 **bottom**, respectively. The priors are flat for M_{CUO} within the plotted range and zero outside, while they are Gaussian for the scale radii, centred on the middles of the panels and extending to $\pm 3\,\sigma$ at the edges of the panels, and zero beyond. The arrows indicate the respective best likelihood solutions of the Monte Carlo chains. The mock data prescription is, from **left** to **right**: No central dark component (Nothing); a central black hole alone (BH); a central CUO (CUO) and both a central black hole and CUO (BH+CUO). The mocks were constructed with the best values of each respective isotropic mass model. The fits alone indicate preference for a CUO in NGC 6397 and for a central mass excess in NGC 3201, without strong distinction between extended and point-like scenarios (see text for details). This figure was originally published in Vitral et al., 2022.

given the present quantity of kinematic data in both GCs, there is no compelling evidence for anisotropic motions in either cluster. We thus assumed velocity isotropy to better explore other free parameters such as the central unseen mass.

8.4.2 *Central dark component*

8.4.2.1 *MAMPOSSt-PM results on observed data*

We now compare, for both clusters, our four mass models using MAMPOSSt-PM fits to the kinematic data assuming isotropic velocities. We first used AICc to compare our mass models. There is only marginal evidence of an excess mass in NGC 3201 from AICc. On the other hand, there is very strong evidence for an excess inner mass in NGC 6397, yielding a probability of no mass excess of less than 10^{-5} (from Eq. [114]).

In summary, there is marginal evidence of an excess inner mass in NGC 3201, but while there is weak evidence in favour of an IMBH (of mass between $200\,M_\odot$ and $1050\,M_\odot$) relative to a CUO, it is too small to be taken in consideration. This suggests that we need to consider other indicators to compare the models. We will discuss in Sect. 8.4.2.2 whether the CUO model fits produce marginal distributions of the CUO scale radius that match those of MAMPOSSt-PM fits to a mock with an IMBH in their centre.

For NGC 6397, the best fit IMBH model gives a more constrained IMBH mass between 400 and $700\,M_\odot$. But AICc leads to a very weak preference for the CUO over the IMBH model, which, again, is too small to consider. In summary, there was very strong evidence for an excess inner mass in NGC 6397, but it is difficult to tell whether it is extended or not.

8.4.2.2 *Tests with mock data*

We ran MAMPOSSt-PM on our 4 mock datasets, with isotropic velocities, realistic proper motion errors, for our 4 mass models. In all these MAMPOSSt-PM runs, we assumed a CUO mass model, for reasons that will be clear below. Figure 35 compares the marginal distributions of CUO mass and scale radius and their covariance for the MAMPOSSt-PM fit to mock data (light red) to the MAMPOSSt-PM fit to the observed data (light blue), both assuming the CUO mass model. The figure also compares the values of the maximum likelihood estimates.

First, the marginal distributions of CUO mass fit on the mock with no central mass excess (left top panels of left corner plots, in light red) show a significantly different pattern from the true data marginal distribution of CUO mass (light blue in same panels), spanning significantly lower masses. On the other hand, for both clusters, the marginal distributions of the CUO mass obtained on the three other mocks with extra inner mass (second, third and fourth columns of panels) show general agreement on the shape of the marginal CUO mass distributions obtained from the observed data, with some fairly small shifts of the peaks.

The marginal distribution of CUO scale radius is even more interesting. For the fit on the mock with no excess mass, the marginal distribution of CUO

scale radius is flat for NGC 3201, suggesting a CUO scale radius that cannot be determined. For NGC 6397, this distribution is rising, suggesting a large CUO scale radius of the order of the radius of the visible stars. For the black hole mocks, the CUO scale radius marginal distributions also show a different pattern than what is observed: for both clusters, it fails to reproduce the peak in the marginal distribution of CUO scale radius obtained on the observed data: this is very striking for NGC 6397, but is also visible for NGC 3201. On the other hand, as expected, the marginal distributions of the CUO scale radius obtained on the CUO mocks are consistent with those obtained on the data.

Whether or not the CUO model is the correct mass model, one expects that the marginal distributions of the CUO scale radii should have similar shapes when comparing those obtained on a mock that represents the observed data and those directly obtained from the same data. The marginal distribution of CUO scale radii obtained from our CUO fits should therefore be a sensitive discriminator between single BH and a CUO, with no peak or a clear peak in the distribution of CUO scale radii, respectively. Although AICc (based on likelihood) provides a global score for a particular model, it misses the differences in the marginal distributions of CUO scale radii, which appear to be the critical aspect to differentiate black hole and CUO scenarios. In AICc, the differences of these marginal distributions are blurred by small differences in the marginal distributions of the structural properties of GC stars. We therefore favoured the comparison of CUO marginal distributions between mock and observed data to using AICc, and we will hereafter omit model comparisons based on AICc.

The large discrepancy noted between the CUO mass and scale radii marginal distributions between the mock data with no-inner-excess-mass and the observed data indicates that this model is ruled out by these MAMPOSSt-PM fits. Similarly, the lack of a peak in the marginal distributions of CUO scale radii for the black hole mock, for both GCs, suggests that the data prefers an extended extra mass (CUO) compared to a point-like central mass (BH) for both GCs.

We quantified the preferences mentioned above in Table 5, with the statistical indicators presented in Section 8.2.10. One first notices that in both clusters, models without a central dark mass ("Nothing") are quickly ruled out, given their very different maximum likelihood solutions (small percentages in column 3) and disagreeing marginal shapes (high values in columns 5 and 7) concerning the mass fit. We compared the remaining three dark mass models by analysing column 4 to see how distant the maximum likelihood scale radius solutions are, and also columns 6 and 8 to compare the scale radius marginal distributions. The two clusters display extremely unsatisfactory agreements for the case with a central black hole alone ("BH") in column 4, and poor agreements for the case with both a CUO and a black hole ("BH+CUO"). The best match of shapes is for the CUO model in NGC 3201, followed by a "BH+CUO" model. In NGC 6397, this trend is inverted, but the reader should keep in mind that the "BH+CUO" case for this cluster consists of a $\sim 750\,M_\odot$ CUO, with a black hole of only $\sim 20\,M_\odot$, hence nearly a CUO case actually.

Therefore, our comparisons between MAMPOSSt-PM fits of mock and observed data yield robust evidence for a dark central mass in both clusters. While in NGC 3201 we have reasonable, but not strong arguments to defend that this mass is extended, the case for NGC 6397 is more straightforward, with robust

Table 5: Main statistical tests used for model selection.

Cluster ID	Mock model	ϕ M_{dark}	ϕ r_{dark}	AD M_{dark}	AD r_{dark}	KS M_{dark}	KS r_{dark}
(1)	(2)	(3)	(4)	(5)	(6)	(7)	(8)
NGC 3201	Nothing	6%	84%	18346	1709	0.229	0.070
NGC 3201	BH	73%	20%	1307	317	0.045	0.027
NGC 3201	CUO	90%	82%	7778	208	0.127	0.026
NGC 3201	BH+CUO	63%	38%	13979	979	0.179	0.058
NGC 6397	Nothing	33%	59%	56540	29034	0.412	0.290
NGC 6397	BH	63%	11%	15783	50704	0.148	0.361
NGC 6397	CUO	76%	77%	1678	22912	0.050	0.219
NGC 6397	BH+CUO	44%	47%	333	8459	0.022	0.150

Notes: Columns are **(1)** Cluster ID; **(2)** Mass model assigned to the mock data; **(3)** Fraction of chain elements that present absolute dark mass distances greater than the distance between the mock and true data fit's best solutions – Higher values indicate good agreement between the mock and true data fits; **(4)** Same than (3), but considering only the dark radius; **(5)** AD statistic, for M_{dark} – High values indicate poor matches; **(6)** AD statistic, for r_{dark}; **(7)** KS statistic, for M_{dark} – High values indicate poor matches; **(8)** KS statistic, for r_{dark}. This table was originally published in Vitral et al., 2022.

evidence for an extended mass, in agreement with previous fits from Vitral and Mamon, 2021[15].

8.4.3 *Robustness*

In Vitral et al., 2022, several robustness tests were performed to validate the results of the previous section. In particular, we tested if allowing a different error threshold, bulk proper motion and cluster centre for our data in Section 8.2 provided diverging results. For each of these cases, we showed, also using mock datasets, that our results remained well constrained.

A different point of the analysis from Vitral et al., 2022 with respect to Vitral and Mamon, 2021 is that we only fitted single stellar population models for the main sequence stars, instead of allowing for two components eventually. Indeed, it had been shown in Vitral and Mamon, 2021, that the estimated masses in both approaches agreed within the 1-σ error bars and the respective density profiles related such that the prescriptions of the single component fits were alike the ones of the brightest component of the two population fits.

On top of this observation, we computed the differences expected due to mass segregation in our dataset, with the relations from Trenti and van der Marel, 2013; Bianchini et al., 2016a, and noticed that the error budget in our data was higher than the dispersion due to mass segregation. Thus, the presence of systematics and uncertainties in our data effectively erase the imprints

15 We notice however, that in Vitral and Mamon, 2021, their extended mass was roughly twice more massive and twice more diffuse. This difference could be related to a less complete data set in Vitral and Mamon, 2021 and a less conservative data cleaning.

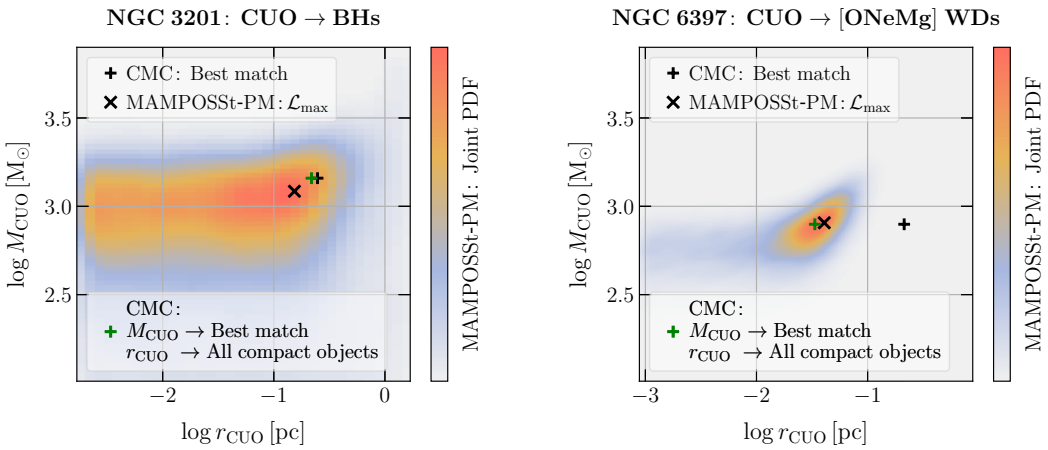

Figure 36: *Comparison between MAMPOSSt-PM fits and* `CMC` *dynamical simulations:* Mass vs. half-mass radius of the sub-cluster of unresolved objects (CUO) for NGC 3201 (**left**) and for NGC 6397 (**right**). In each panel, the *black cross* indicates the position of the maximum likelihood solution of MAMPOSSt-PM, while the MAMPOSSt-PM joint probability distribution function (PDF) is linearly colour-coded from grey to orange. Also, in each panel, the *black plus sign* indicates the CUO mass and scale radius (containing half the projected mass) of the `CMC` simulation snapshot whose surface brightness and velocity dispersion profiles match best the observations, when the CUO is that of the dominant compact component (black holes for NGC 3201 and [ONeMg] white dwarfs for NGC 6397). Other compact objects can also contribute to the sub-cluster, especially in NGC 6397, but they end up mixing themselves within the stellar component (thus, not forming a sub-cluster), so the MAMPOSSt-PM fits of scale radius might be affected. For that reason, we also show the case considering all compact remnants (*green plus sign*): the mass is still that of the main CUO component (black holes or [ONeMg] white dwarfs), but the scale radius corresponds to where the mass contribution of all compact remnants from the `CMC` simulation snapshot reaches half of the CUO mass found by MAMPOSSt-PM (the radii are projected half-mass radii, estimated from the 3D half-mass radius, converted to projected assuming a Plummer model). This figure was originally published in Vitral et al., 2022.

from this segregation, so we decided to only perform the single population modelling in our case.

8.4.4 *Comparison with* `CMC` *models*

The analysis of the internal kinematics of core-collapsed NGC 6397, with a code such as MAMPOSSt-PM, may miss important priors set by the full, complex dynamics of the clusters. Dynamical simulations incorporating the small-range dynamical processes should therefore be used to complement our Jeans modelling. We then selected Monte Carlo simulations from `CMC` according to Section 8.2.11, and picked the snapshot whose surface brightness and veloc-

ity dispersion profiles best match the observed ones. For NGC 6397, this best snapshot was in one of the new models that were run[16].

Figure 36 shows the distinctive match of the CUO mass and scale radius, between our MAMPOSSt-PM mass-modelling fits (black cross) and from the snapshot of the CMC Monte Carlo simulation that best matches the observed surface brightness and velocity dispersion profiles (black plus sign) for NGC 3201 (left) and NGC 6397 (right). We are able to find CMC simulations that predict a CUO mass that agrees well with those found by MAMPOSSt-PM, attesting simultaneously the good performances of both MAMPOSSt-PM and CMC, which are completely different methods arriving at roughly the same result. The match of CUO scale radius is also very good for the black hole population in NGC 3201, but less good for the [ONeMg] white dwarf population in NGC 6397, with the simulations predicting a scale radius roughly five times greater.

This scale radius issue can be explained as follows. The unresolved population in NGC 6397 is composed of two white dwarf components ([CO] and [ONeMg]). The [CO] white dwarfs follow a density profile close to the resolved stars and eventually mix up with the stellar component. In contrast, the [ONeMg] white dwarfs are much more concentrated in the inner regions. It is therefore natural that when MAMPOSSt-PM fits a single clustered dark population, it gets confused if the CUO is made of several components with different density profiles. For that reason, we also highlight in Fig. 36 the CUO half projected-mass radius when considering all compact remnants (green plus sign) instead of the major one (black plus sign). The match is indeed much better for NGC 6397. The difference is not significant for NGC 3201, whose black hole population strongly dominates the mass excess in the centre, and tends to eject other less massive remnants through dynamical interactions.

All in all, our Monte Carlo simulations provide a remarkable agreement with our MAMPOSSt-PM fits, and argue in favour of a central extended mass excess in both clusters, instead of a single central IMBH (or even an IMBH plus a CUO). While in NGC 6397, the CUO is likely to be formed by [ONeMg] white dwarfs with a still important contribution from [CO] white dwarfs (although these are more extended), NGC 3201's CUO is mostly formed by stellar-mass black holes. This is also in agreement with the recent analyses of Giesers et al. (2019), who predicted a population of roughly 50 black holes at present in NGC 3201, and Aros et al. (2021), who showed (see their figure D1) that the binary fractions in NGC 3201 are more consistent with a sub-cluster of stellar-mass black holes than with a single IMBH.

8.5 ASTROPHYSICAL IMPLICATIONS OF BLACK HOLE/WHITE DWARF SUB-CLUSTERS

The presence of black hole sub-clusters and, at late times after their host clusters have undergone core-collapse, white dwarf sub-clusters, leads naturally to a number of interesting astrophysical implications. In both scenarios, compact object binaries form through both three-body encounters (e.g., Morscher et al., 2015) and binary exchange encounters. Once formed, these compact object bi-

16 The new model was similar to the ones presented in Kremer et al., 2021, but with a slightly smaller initial size for the cluster.

naries harden through subsequent dynamical encounters (e.g., Heggie, 1975) until, ultimately, they either merge or are ejected from their host cluster after attaining a sufficiently large dynamical recoil kick. For black hole sub-clusters, this process yields black hole–black hole binary mergers which are detectable as gravitational sources by instruments such as LIGO/Virgo (Abbott et al., 2016b; Abbott et al., 2021). A number of recent analyses have demonstrated that the black hole binary mergers that occur in typical dense star clusters occur at rates comparable to the local Universe rates predicted from the latest LIGO/Virgo results (e.g., Rodriguez et al., 2021). Furthermore, the dynamical processes operating in black hole sub-clusters enable the formation of black hole mergers with components in the proposed pair-instability mass gap (e.g., Rodriguez et al., 2019; Di Carlo et al., 2020; Kremer et al., 2020b; Gerosa and Fishbach, 2021) which may be difficult to produce through alternative formation channels. Black hole sub-clusters are expected to also lead to the formation of compact black hole–luminous star binaries (e.g., Kremer et al., 2018a) similar to those detected in a number of MW GCs (e.g., Strader et al., 2012; Giesers et al., 2019) as well as stellar-mass tidal disruption events (e.g., Perets et al., 2016; Kremer et al., 2019b; Kremer et al., 2022), which may be detectable as bright electromagnetic transients by both current (e.g., Zwicky Transient Facility; Bellm et al., 2019) and upcoming (e.g., Vera Rubin Observatory; LSST Science Collaboration et al., 2009) all-sky surveys.

In the case of core-collapsed clusters like NGC 6397 that are expected to have ejected nearly all of their black holes and host instead a compact sub-cluster of white dwarfs, the formation of inspiralling white dwarf–white dwarf binaries is the natural outcome (e.g., Kremer et al., 2021). As they inspiral, these binaries may be detectable as millihertz gravitational-wave sources by instruments such as LISA (Amaro-Seoane et al., 2017). At merger, they may be detectable at decihertz frequencies by proposed instruments such as DECIGO (e.g., Arca Sedda et al., 2020). Depending on the uncertain details of white dwarf merger physics, these mergers may plausibly lead to Type Ia supernovae (e.g., Webbink, 1984), rejuvenated massive white dwarfs (e.g., Schwab, 2021), or, in the event of collapse, young neutron stars (e.g., Nomoto and Iben, 1985). Neutron stars formed through the latter scenario may be observable in old GCs as young pulsars (e.g., Boyles et al., 2011; Tauris et al., 2013) and may potentially be the source of fast radio bursts similar to FRB20200120E in a GC in M81 (Bhardwaj et al., 2021; Kirsten et al., 2021; Kremer, Piro, and Li, 2021; Lu, Beniamini, and Kumar, 2021).

9 ON THE ORIGIN OF GLOBULAR CLUSTERS

Imagination will often carry us to worlds that never were, but without it we go nowhere.

— Carl Sagan

9.1 THE DARK MATTER FORMATION SCENARIO

There is no doubt that the nature of dark matter (DM) is one of the most elusive concepts in modern day physics. However, the existence of this astrophysical component has been used and required to explain a vast range of phenomena for a considerable amount of time: Back when Zwicky, 1933; Zwicky, 1937 proposed that some sort of non-luminous matter could compose the amount of mass needed to explain the discrepancy between mass measurements of the Coma cluster based on the Virial theorem (e.g., Binney and Tremaine 2008) and based on brightness and number of galaxies, up to recent measurements from the Planck Collaboration et al., 2016; Planck Collaboration et al., 2020 that yield very robust fits of the cosmic microwave background (CMB) using a ΛCDM model accounting for the existence of DM. In between, other important confirmations of this mysterious dark component were provided: Rubin and Ford, 1970; Rubin, Ford, and Thonnard, 1980 showed that the rotation curves of outer stars in nearby galaxies needed an extra amount of mass (compared to observable, luminous matter) to explain their high velocity values and finally, gravitational lensing studies (e.g., Taylor et al. 1998) have also confirmed that the total amount of mass in many galaxy clusters correspond to the dynamical measurements accounting for DM.

Such findings point to the DM as a fundamental component in galaxy formation, present in most galaxies as an enveloping halo, from the smallest to the highest scales. Thus, it seems in principle curious that dense collections of stars spanning from $\sim 10^5 - 10^6$ $M_\odot$ such as globular star clusters (GCs), with some of them thought to be accreted dwarf galaxies (e.g., Majewski et al. 2000; Bekki and Freeman 2003a; Boldrini and Bovy 2021; Pechetti et al. 2021), do not seem to require any significant amount of DM to explain their dynamical mass (e.g., Shin, Kim, and Lee 2013; Conroy, Loeb, and Spergel 2011;Ibata et al. 2013; Moore 1996; Baumgardt et al. 2009; Lane et al. 2010; Feng et al. 2012; Hurst et al. 2015), although some recent works seem to suggest otherwise for a few particular sources (Carlberg and Grillmair, 2022; Errani et al., 2022). In fact, Peebles, 1984 proposed a formation scenario where GCs are formed inside their own DM mini-halo[1], and further studies defended that if formed before re-ionisation[2], GCs could be smaller counterparts of galaxies (e.g., Bromm and

1 Those DM mini-halos could have between $10^6 - 10^8$ $M_\odot$, such as general DM sub-structures or subhalos (Zavala and Frenk, 2019).

2 Which is consistent with GCs having typical ages up to ~ 13 Gyr Marin-Franch et al., 2009.

Clarke 2002, Figure 2 from Mamon et al. 2012 and Silk and Mamon 2012 for a review on galaxy formation).

On the other hand, different formation scenarios, where GCs are not necessarily embedded in DM mini-halos also exist. For instance, GCs could be formed as bound gas clouds (Peebles and Dicke, 1968), as galaxy DM-free fragments (e.g., Searle and Zinn 1978; Abadi, Navarro, and Steinmetz 2006), as relics of young massive clusters (YMC, Portegies Zwart, McMillan, and Gieles 2010a; Longmore, Kruijssen, Bastian, Bally, Rathborne, Testi, Stolte, Dale, Bressert, and Alves 2014) formed in the high-redshift Universe (Kruijssen, 2014; Kruijssen, 2015), or as debris from the galactic disc after merger events (*in-situ* scenario). Moreover, recent cosmological simulations indicate realistic mechanisms through which all these scenarios (i.e., DM and DM-free) can actually happen (Trenti, Padoan, and Jimenez 2015; Kimm et al. 2016; Ricotti, Parry, and Gnedin 2016; Keller et al. 2020; Ma et al. 2020), making it reasonable to argue that GCs likely originate from more than a single formation channel.[3]

Another reason that makes the understanding and further confirmation of different formation channels difficult is that much of the main consequences of these channels are better observable in the outskirts of GCs, where one often lacks good quality data. For example, the detection of tidal tails or stellar streams that might relate to an accretion event can be complicated by an observational bias where the stars in the stream are less luminous than the ones in the central and dense regions of the cluster, and thus more difficult to observe, comparatively (Balbinot and Gieles, 2018). Similarly, a potential DM mini-halo could present a much more diffuse structure than the stellar component, so that its dynamical detectability might only be possible beyond several scale radii (Peñarrubia et al., 2017), where GCs stars are usually confused with galactic field stars.

With the astrometric revolution brought by the *Gaia* mission (Gaia Collaboration et al., 2018a; Gaia Collaboration et al., 2018c; Gaia Collaboration et al., 2021), and the promising future discoveries of the *James Webb Space Telescope* (*JWST*, Gardner et al. 2006) and the *Euclid* mission (Laureijs et al., 2011; Lançon et al., 2021), the need to better constrain the expected differences between the multiple GC formation scenarios is a priority, so that these rich data sets can be fully exploited to better understand the many long-sought questions regarding GC formation. As a matter of fact, although many robust attempts to better model the observational implications of the DM mini-halo scenario have been made, the high computational cost of simulating a GC+DM system in a Milky Way (MW) type of galaxy forced these attempts to be placed in idealised scenarios: for instance, isolated GCs not experiencing tidal forces (Peñarrubia et al., 2017), or orbiting GCs in a static potential (Mashchenko and Sills, 2005). Preferably, simulations with clusters experiencing tidal forces, in a host galaxy fully composed of particles (and not just a static potential) would allow to take into account more correctly dynamical friction and tidal effects between globular clusters and their host galaxy.

In the work from Vitral and Boldrini, 2022, we aimed to clearly separate the observational behaviours of GCs which are formed inside a DM mini-halo and

3 Observational evidence for different GC populations has also been provided, for instance, by noticing significant colour gradients on the GC population from different galaxies (e.g., Cohen, Blakeslee, and Ryzhov 1998; Harris 2009; Wu et al. 2021).

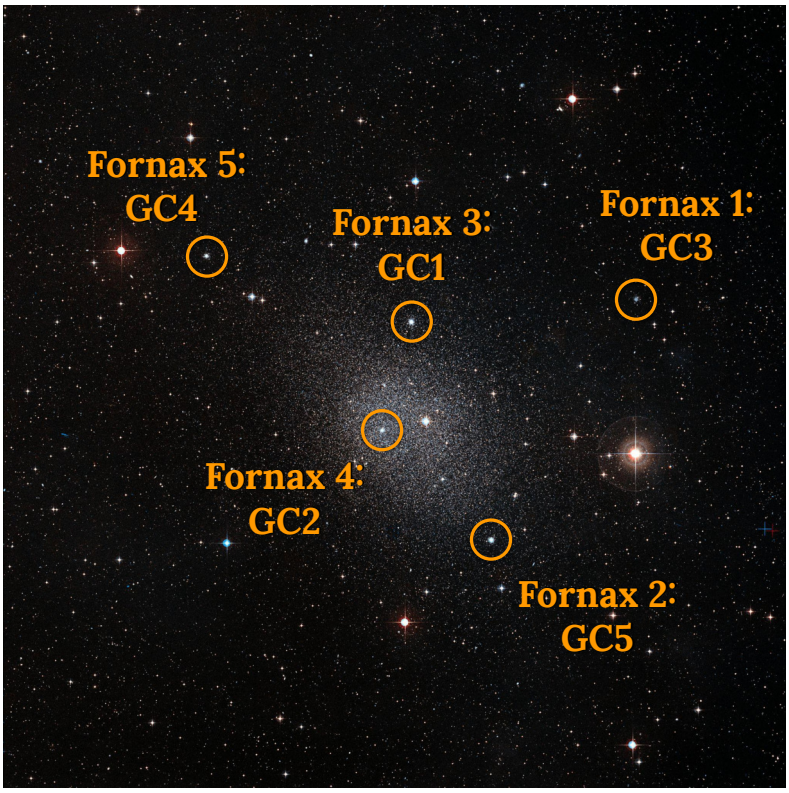

Figure 37: *Globular clusters in Fornax:* Image of the five globular clusters we simulate in the Fornax dwarf spheroidal galaxy, labelled as Vitral and Boldrini, 2022, according to Boldrini, Mohayaee, and Silk, 2020. The original image (without the orange circles and labels) is a composite from Giuseppe Donatiello, constructed with data from ESO and the Digitized Sky Survey 2 (Credit: ESO/Digitized Sky Survey 2, under the CC BY 4.0 licence[4]).

which are devoid of it, both orbiting a host galaxy and thus permanently experiencing a tidal field. We do it by analysing N-body simulations of a GC system with and without a DM embedding mini-halo, alongside with a host galaxy. In order to bypass the high computational cost mentioned above while still keeping a high resolution, we place our GCs in a dwarf spheroidal (dSph) galaxy, following the same prescriptions as the Fornax dSph, in a similar manner than done in Boldrini, Mohayaee, and Silk, 2020. This allows one to consider much less stars than it would be needed if the satellites were orbiting a MW-like galaxy, and also to avoid using a potential instead of particles, which brings unwanted numerical effects. Besides, by taking a real galaxy (i.e., Fornax) as our model, we are likely better exploring the dynamics and orbital evolution of different parameters, and thus reaching more realistic conclusions. I present in the following the findings of this work, and then mention the case of NGC 6397, studied in Boldrini and Vitral, 2021, which brings an interesting discussion to the DM formation scenario. Throughout the rest of the manuscript, I reference the stellar component of the system of GC stars without DM as $\star$, and the stellar component of the system of GCs formed inside DM mini-halos as $\star\bullet$. The dark matter is labelled as $\bullet$.

4 https://creativecommons.org/licenses/by/4.0/.

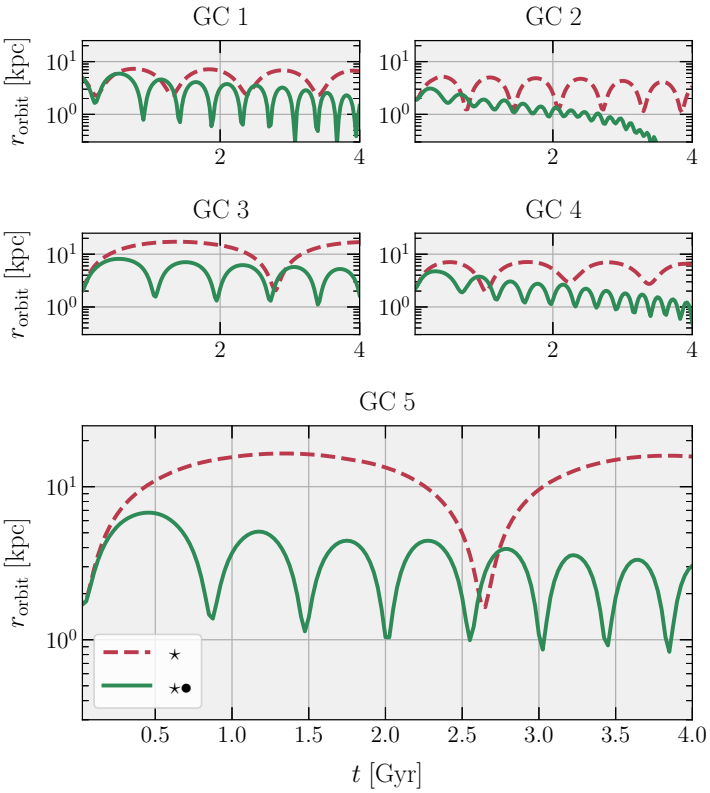

Figure 38: *Fast orbital decay:* We present the evolution of the orbital radius (i.e., the distance to the centre of Fornax) for our five simulated globular clusters. The case without a dark matter mini-halo (⋆) is displayed in dashed red, while the case with a dark matter mini-halo (⋆•) is shown in solid green. This plot exemplifies that systems with dark matter are supposed to sink to the centre faster than the system without the dark matter mini-halo. This figure was originally published in Vitral and Boldrini, 2022.

9.1.1 *Simulations*

Figure 37 illustrates the Fornax-GC system we studied and the labels we use throughout Vitral and Boldrini, 2022. The initial conditions for this system are taken from Boldrini, Mohayaee, and Silk (2020, see their Section 2). We considered the scenario in which the GCs were accreted recently at $z = 0.36$ by Fornax. It ensures that at $z = 0$, the GCs embedded in DM are still orbiting and no star clusters form in the centre of Fornax (in accordance with observations), and also that at 3 Gyr, the cluster's positions relative to Fornax are consistent with their observed projected distances.

9.2 THEORETICAL PREDICTIONS

First, we detail the properties expected from a globular cluster formed inside a dark matter mini-halo. Due to the overall mass increase of the system (GC+DM), some dynamical behaviours can be observed in such a cluster (notably, their orbits become considerably different than the DM-free case). These trends can be whether disruptive or protective, regarding the GC tidal disruption. They can be summarised as:

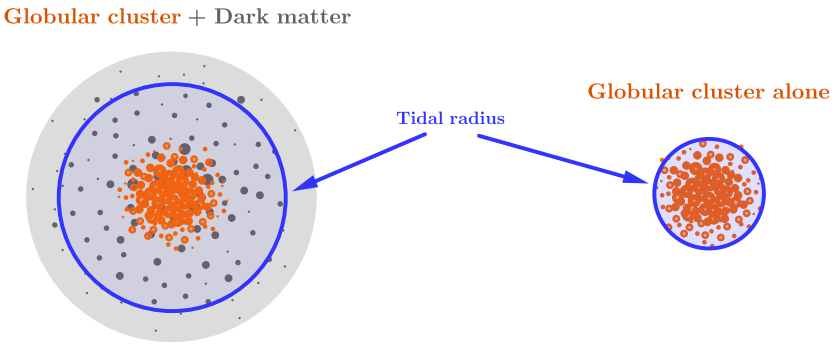

Figure 39: *Tidal radius growth due to an extra dark mass:* Scheme illustrating the increase of tidal radius (*blue*) in the globular cluster system (*orange*) embedded in a dark matter mini-halo (*grey*), in the **left**, in comparison with the globular cluster system without dark matter, in the **right**. This tidal radial expansion is explained by the increase of mass within a region sufficiently small, due to the extra dark matter component (e.g., equation [16]). For our simulations, this increase amounts up to a factor of roughly 2.7. This figure was originally published in Vitral and Boldrini, 2022.

- Dynamical heating from the DM mini-halo and subsequent increase of the stellar velocity dispersion (disruptive).
- Faster orbital decay of the cluster (disruptive).
- Increase of the tidal radius of the system (protective).

Below, we briefly describe them from a theoretical point of view. Next, in the following sections, we balance the effects of each of these trends with the help of our simulations, and explore under which conditions each of these trends prevails over the others.

9.2.1 *Dynamical heating from the dark matter*

For a system in equilibrium, densification due to the increment of DM mass will increase the velocity dispersion throughout the stellar distribution, causing dynamical heating. This is a consequence of the handling of the Virial theorem and has been observed for numerical simulations of isolated GCs embedded in DM mini-halos (see Figure 2 from Peñarrubia et al. 2017).

For isolated systems, the increase of velocity dispersion is likely counterbalanced by the higher gravitational pull of the new more massive system, or in other words, the stars with higher velocity can still be bound to the system due to an increase of the overall escape velocity. However, for orbiting systems experiencing tidal effects, this dynamical heating can help higher velocity stars to escape from the satellite, since the gravitational pull from the main body contributes to decrease the escape velocity of the satellite's stars. Therefore, for orbiting GCs embedded in DM mini-halos, one could, in principle, expect dynamical heating from the DM mass to contribute to the tidal stripping of the cluster.

9.2.2 *Faster orbital decay*

The exchange of energy between the satellite and its host galaxy will lead to the drag of the satellite, also referred to as dynamical friction. This will lead the satellite to lose energy and sink towards the centre of mass of the system. The dynamical friction time of the cluster is the timescale needed for the satellite to reach the centre of mass of the host galaxy. It has been defined in Binney and Tremaine (2008, eq [7-26]), and follows the relation

$$t_{fric} \propto \frac{1}{M} , \tag{117}$$

where M is the satellite's total mass.

Applying this relation to our simulations, where in one case we have a GC system alone of 10^6 $M_\odot$ and in the other case the total system mass is that of the GC plus the DM mini-halo (i.e., 2.1×10^7 $M_\odot$), we find that the system with DM is supposed to sink to the centre roughly twenty times faster than the system without the DM mini-halo. Indeed, when looking at Figure 38, one can notice that the systems with DM (solid green) occupy much shorter radii than the systems without DM (dashed red) throughout their orbits.

As a consequence, systems with a DM mini-halo tend to be located close to their host centres sooner, and thus feel a stronger dynamical heating coming from the host galaxy. This dynamical heating, on its turn, can potentially work to remove more GC stars (along with their DM envelope) than in the case without DM.

9.2.3 *Tidal radius growth*

As presented in Chapter 3, the tidal radius of a satellite of mass M, in a given potential, follows the relation

$$r_t \propto M^{1/3} . \tag{118}$$

Therefore, for our GC system with DM, the respective tidal radius will be roughly 2.7 times greater than the case without dark matter, considering the same distance and enclosed mass from the host. This means that the region where the stars are better protected against tidal stripping is larger in the case with DM than the case without it, and thus one could argue that GCs with DM can be more resilient to tidal forces from their host galaxy. In Figure 39, we illustrate this idea with a scheme where the cluster embedded in DM has a broader tidal radius, and we demonstrate this effect on our simulations in Figure 40.

9.3 DARK MATTER SIGNATURES

In this section, we analyse the main implications of the presence of a DM mini-halo in the overall GC dynamics and morphology, according to the simulations from Vitral and Boldrini, 2022. We remind that our analysis is modelled on the

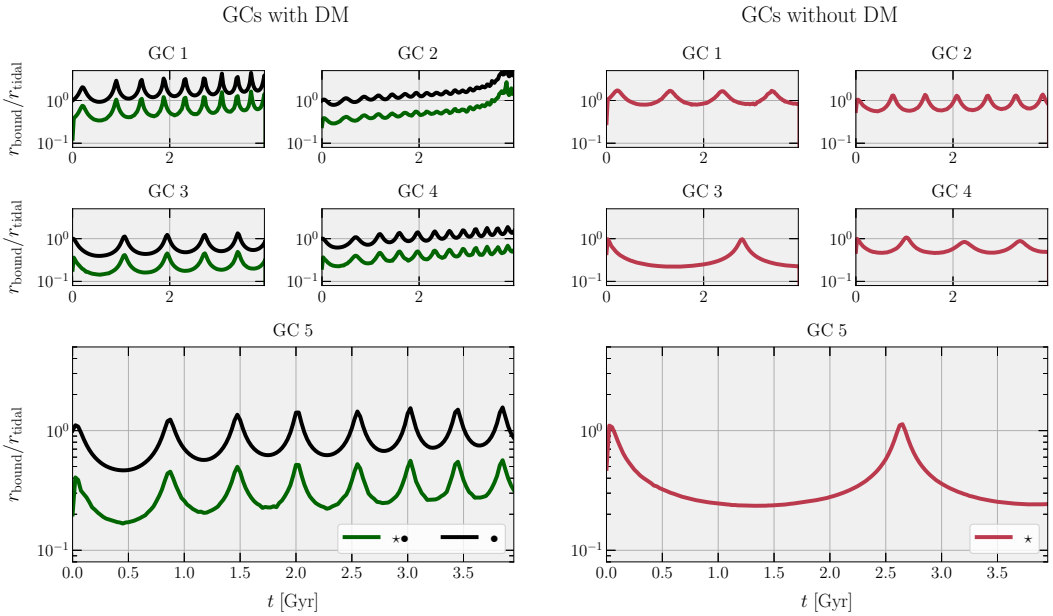

Figure 40: *Evolution of characteristic radii:* We display the evolution of the ratio of bound particles' maximum distance from the globular cluster centre divided by the respective tidal radius of the system, calculated according to section 3. Plots on the **left** indicate the five simulated globular clusters formed inside dark matter mini-halos, with stars (⋆•) in green and dark matter particles (•) in black. The plots on the **right** show, in red, the results of globular clusters formed without dark matter (⋆). Keep in mind that the orbits of globular clusters with and without dark matter are different, and most importantly, their distance to the centre of Fornax is not necessarily the same at a given time, which affects the size of the tidal radius. Notice that a certain tracer (stars or dark matter) is more affected once the ratio r_{bound}/r_{tidal} is greater or comparable to unity, what happens first for the dark matter envelope, on the plots in the left. We argued that this behaviour causes the dark matter mini-halo to act as a shield against tidal stripping of the stellar component. This figure was originally published in Vitral and Boldrini, 2022.

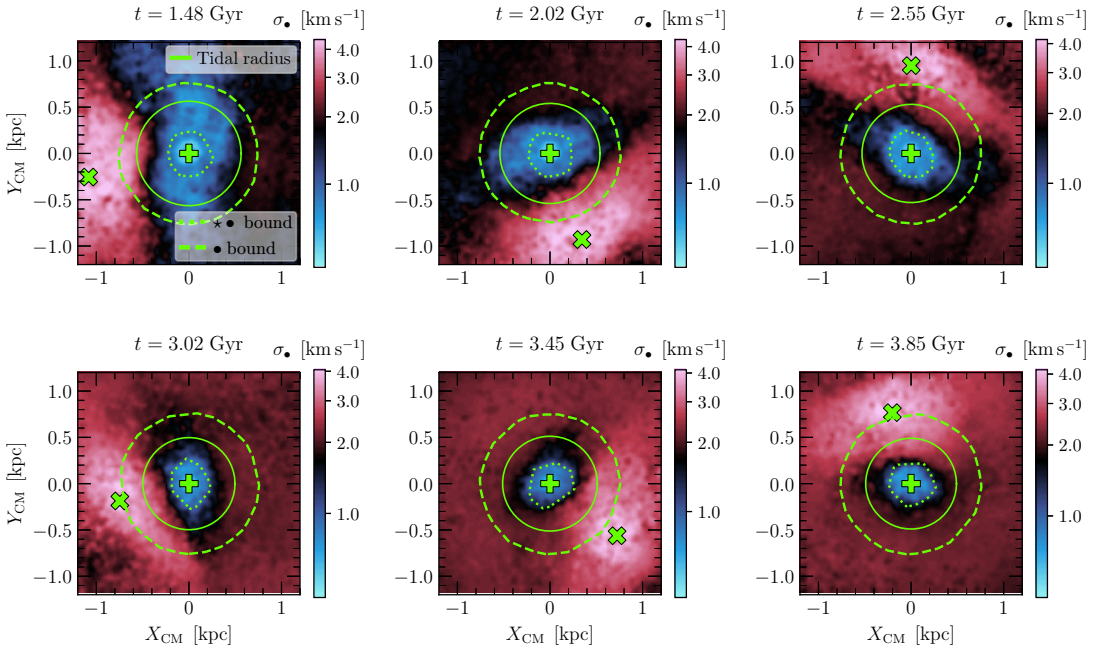

Figure 41: *Dark matter shield:* Velocity dispersion map of dark matter particles for GC5, projected in the X vs. Y plane and centred in the centre of mass of the globular cluster system. We display the last six pericentres of its orbit, where the tidal effects are stronger (as depicted by Figure 40). The extension of bound globular cluster stars and bound dark matter particles are highlighted as dotted and dashed green lines, respectively, while the theoretical tidal radius, calculated according to Chapter 3, is displayed as a solid green circle. The maps are colour-coded logarithmically from blue (lower dispersion) to red (higher dispersion). The centres of Fornax and of the GC are represented as a thick green cross and a plus sign, respectively. For this cluster, notice that the empirical tidal radius, well traced by the blue region, remains always larger than the bound stars radii. This argues in favour of the dynamical presence of a dark matter shield, as illustrated in Figure 39. This figure was originally published in Vitral and Boldrini, 2022.

specific case of the Fornax dSph, in order to probe a realistic scenario. In addition, we keep in mind the points discussed in the previous section concerning disruptive and protective effects on the GC stellar component.

9.3.1 *Dark matter shield*

In the beginning of our simulations with DM mini-halos, all GCs presented a DM envelope massive ($M_\bullet = 2 \times 10^7\ M_\odot$) and concentrated enough ($r_{NFW} \approx 300$ pc, where r_{NFW} is the scale radius of the Navarro, Frenk, and White 1996 profile), so the tidal radius growth explained in section 9.2.3 and illustrated in Figure 39 was observed. In fact, we observed that whenever we had such tidal radius increase, the DM particles are stripped before the GC stars, so the DM envelope works effectively as a shield against tidal stripping of the stellar component, being gradually removed as the system experiences stronger tidal forces from the host galaxy. Indeed, as depicted in Figure 40, one notices that a certain tracer (stars or dark matter) is more affected once the ratio r_{bound}/r_{tidal} is greater or comparable to unity, which happens first for the dark matter envelope, for the plots on the left.

In order to visualise this effect, we created a velocity dispersion map (see appendix B.2.1 for details) of DM particles, which are much more spread than GC stars, and therefore cover better the spatial extent of the tidal radius. Such a map helps us to spot the transitory region where the DM particles start to effectively feel tidal effects of the host galaxy, which is characterised by a steep increase of the velocity dispersion produced by tidal heating of the system.

In Figure 41, we show this velocity dispersion map for GC5, one of the clusters where this DM shield seemed most effective. We display the last six pericentres of its orbit, when the tidal effects are stronger. The extension of bound GC stars and bound DM particles are highlighted as dotted and dashed green lines, respectively, while the theoretical tidal radius, calculated according to section 3 (eq. [16]), is displayed as a solid green circle. The centres of Fornax and of the GC are represented as a thick green cross and a plus sign, respectively.

One also observes (still in Figure 41) a gradual decrease in the extension of the blue region, characterised by a low velocity dispersion, where the DM shield is effective. This means that at first, the DM shield is highly protective, and with time, as DM particles are stripped from the cluster, the system mass decreases (and so does the tidal radius), and the shield becomes weaker. The red colours, on the other hand, point to a region of high dynamical heating, which becomes more intense in the centre of Fornax and favours tidal stripping of the DM shield.

This protective DM shield is a key mechanism to explain most of the DM signatures we observed in GCs embedded in DM. Although this phenomenon is ubiquitous in our GCs formed in DM mini-halos, the survival of such shield depends mostly on the orbital parameters of each cluster, and a specific discussion on this matter is addressed in section 9.4. In the following, we focus on describing the main impacts of such shield with respect to the case where GCs are not embedded in DM mini-halos.

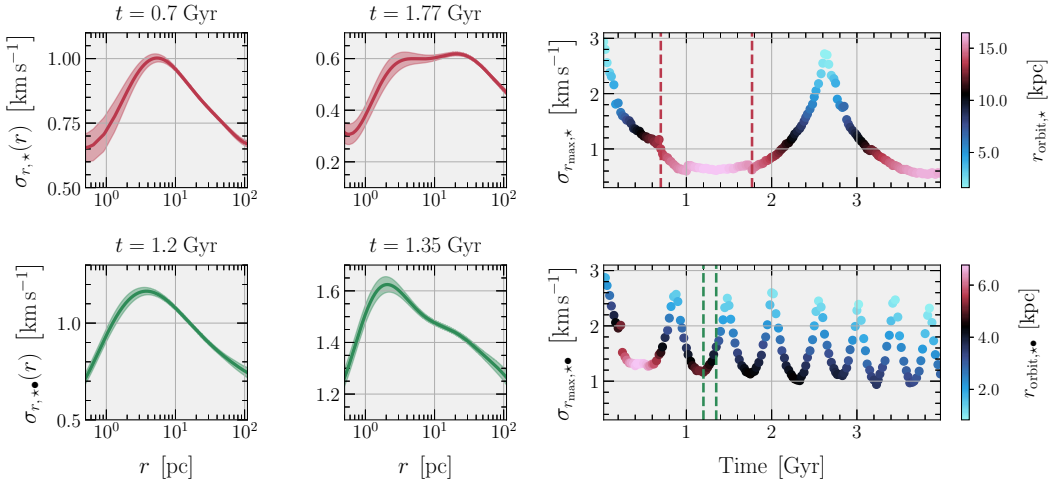

Figure 42: *Stellar velocity dispersion:* Series of plots for GC5. The **upper** plots relate to the simulations devoid of dark matter mini-halos (⋆), while the **lower** plots indicate the results for the globular clusters formed in such mini-halos (⋆•). The two columns on the **left** display hand-picked snapshots where the radial velocity dispersion profile (i.e, $\sigma_r(r)$) resembled better an isolated case without a dark matter mini-halo (left), and with a massive dark matter mini-halo (right), according to Figure 2 from Peñarrubia et al., 2017. The column on the **right** presents the evolution with time of the maximum value of the radial velocity dispersion profile (i.e, $\sigma_{r_{max}}$), for each scenario concerning the dark matter mini-halo, colour-coded according to the distance of the cluster to the centre of the host galaxy (i.e., r_{orbit}), with two vertical dashed lines corresponding to the instants from the two columns on the left. These plots argue that the tidal field from the host galaxy tends to have a much greater impact on inflating the velocity dispersion than the presence of a dark matter mini-halo. In fact, such mini-halos help to *protect* the cluster from tidal effects, rather than contributing to it. This figure was originally published in Vitral and Boldrini, 2022.

9.3.2 *Velocity dispersion profile*

Peñarrubia et al., 2017 simulated isolated GCs embedded in DM mini-halos and showed that due to the extra DM mass, an inflation of the radial velocity dispersion profile towards outer radii[5] is to be expected. In this work, we are able to test such predictions for a more realistic scenario, where the GC+DM subsystem is orbiting a host galaxy, and therefore experiencing tidal effects. For that, we measured the radial velocity dispersion profiles (see section B.2.2 for details) of the bound stars in our clusters in both the cases with and without a DM mini-halo, through the course of the clusters' evolution in the Fornax tidal field.

In Figure 42 (right plots), we show the values of the maximum radial velocity dispersion as a function of time, colour-coded by the distance to the centre of Fornax (i.e., r_{orbit}), in kpc. One of the most important realisations of our analysis is the fact that the overall shape of the velocity dispersion is much more impacted by the host galaxy's tidal field than by an eventual DM mini-

5 Their models presented an inflated structure at roughly $r \approx 20\, r_{1/2}$, where $r_{1/2}$ is the half-mass radius.

halo: The amplitude of the dispersion, traced by its value at the peak follows a periodic variation, with same period than the GC orbit, and has values almost uniquely dependent on the ongoing tidal forces.

In the plot, one can clearly observe that at pericentres (blueish), the velocity dispersion inflates as a whole: the tidal heating from the host galaxy is effectively felt more intensively, leading to a higher velocity dispersion. In contrast, at apocentres (reddish or blackish), the cluster is closer from an ideal isolated scenario, and tidal heating is less effective, leading to low velocity dispersion peaks.

To illustrate the much stronger dependence on tidal forces than on possible DM mini-halos, we selected two snapshots for GC5 (one of the cases where the DM shield seemed most effective) for the case with and without a DM mini-halo (lower and upper plots, respectively). In these snapshots (see Figure 42, four left plots), we can verify that the radial velocity dispersion profile of both the DM and DM-free scenarios assume forms similar to both the isolated cases with no DM mini-halo (left), and with a massive DM mini-halo (right), as presented in Figure 2 of Peñarrubia et al., 2017.

As a general trend, all the clusters had an increasing velocity dispersion close to pericentre, with multiple points of velocity dispersion inflation throughout the GC radial extension. At apocentres, as mentioned above, the clusters resembled better an isolated case (with one or two inflation points), specially for the case with DM mini-halo, where the shapes retrieved by Peñarrubia et al., 2017 could be better spotted. The reason behind the best resemblance in apocentre for the case with DM mini-halos is directly connected to the protective DM shield, which protects the GC stars and approaches better the ideal isolated framework.

9.3.3 *Compactness of the stellar distribution*

An important general characteristic of GCs is that they display a very compact and dense stellar distribution. In our simulations, we observed that the distribution of stars in GCs formed in DM mini-halos is in general more compact and dense than in systems devoid of DM, as a consequence of the protective DM shield. To quantify this trend, we measured the ellipticity (also referred as flattening) and half-number radii for the stellar component of our clusters throughout their evolution, and compared to observational data from GC catalogues. We describe these results below.

9.3.3.1 *Ellipticity (or flattening)*

In order to recreate a two-dimensional ellipticity of the projected density distribution of stars, such as we observe in true data, we placed, for each snapshot, the GC centre in the position $(\alpha, \delta) = (0, 0)$, at five kpc away from the observer[6]. Next, we fitted the distribution of bound stars with a Sérsic (Sérsic, 1963; Sersic,

6 Very high distances would make the stars look closer, which can decrease the precision of our fits, and also erase sky-projection signatures likely to be observed in real data. Very short distances, on the other hand, could have unrealistic sky-projection effects. We argue that 5 kpc is a good compromise, as there is a fair amount of galactic GCs with good data, at roughly this distance.

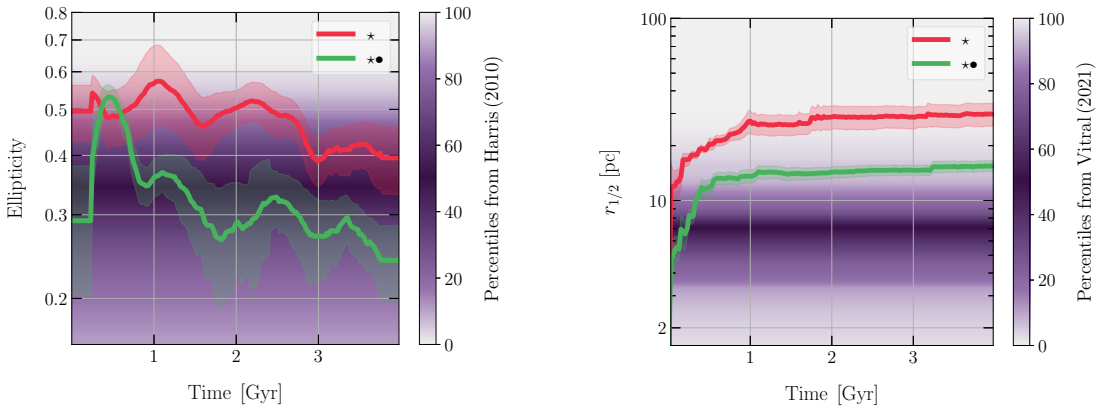

Figure 43: *Ellipticity and half-number radius evolution:* We display the evolution of the mean ellipticity of the projected density distribution of stars of our five simulated globular clusters, in the **left**, and the mean 3D half-number radius evolution of our five simulated globular clusters, in the **right**. The mean of the five globular clusters formed in a dark matter mini-halo ($\star\bullet$) is in *green*, while the mean of the globular clusters without dark matter ($\star$) is in *red*. For the ellipticity plot, as the values fluctuated considerably from one snapshot to another (up to a factor ~ 2), we actually display the running mean over the ten closest snapshots (time-wise). We compared our results of ellipticity with the Harris, 1996; Harris, 2010 catalogue and our half-number radii with the catalogue of Vitral, 2021, by colour-coding their percentiles from white to dark purple. Since the tidal interactions that Milky Way globular clusters suffered can be considerably different from the ones in the Fornax dwarf spheroidal, no strong conclusions should be derived from such a comparison, which rather aims to give a general comparative sample of typical ellipticities and half-number radii values in globular clusters. As a general trend, globular clusters embedded in dark matter mini-halos present more compact shapes (smaller ellipticities and half-number radii) than the case without dark matter, attesting the efficacy of the dark matter shield illustrated in Figures 40 and 41. This figure was originally published in Vitral and Boldrini, 2022.

1968) asymmetric model, using the recipe described in appendix A.3. The fits yielded a semi-major (a) and semi-minor axis (b), from which the ellipticity (or flattening) could be calculated as

$$e = \sqrt{1 - \left(\frac{b}{a}\right)^2}\,. \tag{119}$$

Next, we constructed Figure 43 (left), by computing, at each instant, the mean ellipticity of the five simulated clusters with (green, $\star\bullet$) and without (red, $\star$) DM. The error bars were calculated as $\sqrt{\langle\epsilon\rangle^2 + \sigma_e^2}$, where $\langle\epsilon\rangle$ is the mean uncertainty of the ellipticity fit, and σ_e is the standard deviation of the values from the five clusters. As the values fluctuate (up to a factor ~ 2) from one snapshot to another, we choose to display the running mean over the closest ten points, in order to better observe the evolution of e with time. We then compare it with the values of ellipticity from the Harris, 1996; Harris, 2010 catalogue[7], by plotting the percentiles of their catalogue colour-coded from white to dark purple. Since the tidal interactions that MW GCs suffered can be considerably different from the ones in the Fornax dSph, no strong conclusions should be derived from such a comparison, which rather aims to give a general comparative sample of typical ellipticity values in GCs.

Although we observe a decreasing pattern in the mean ellipticities of both scenarios[8], one also notices that clusters embedded in a DM mini-halo show considerably smaller ellipticities than the clusters devoid of DM. Such relatively small ellipticities are indeed predictable for systems less affected by tidal forces (van den Bergh, 2008), attesting the efficacy of the DM shield illustrated in Figures 40 and 41.

9.3.3.2 *Half-number radius*

Another way to measure the compactness of the cluster is to compute its half-number radius, i.e. the radius wherein half of the bound particles lie. It is a straightforward parameter to look in our simulations as one just needs to sort the stellar distances from the GC centre, and find the mid-point of the respective values. As before, we did that for each snapshot of the cases with and without DM.

In Figure 43 (right), we display the evolution of the mean half-number radius for the five GCs, with error bars computed as the Poisson uncertainty on the mean[9]. In addition, we computed the half-number radius of the GCs analysed in Vitral, 2021 by assuming spherical symmetry and subsequently converting the projected half-number radii into 3D half-number radii[10], and plotting the percentiles of this catalogue colour-coded from white to dark purple.

7 In Harris, 1996; Harris, 2010, the ellipticity is defined as $e = 1 - \frac{b}{a}$, so we convert it to our definition from equation 119.

8 This is expected from orbiting satellites, due to the stripping of outer stars by the tidal field (Akiyama, 1991).

9 The uncertainty ϵ on the mean of n values is $\epsilon = \sigma/\sqrt{n}$, where σ is the standard deviation of those values.

10 The conversion for the Plummer (Plummer, 1911) profile is $r_{1/2} = 1.305\,R_{1/2}$; for the Kazantzidis (Kazantzidis et al., 2004) profile, it is $r_{1/2} = 1.678\,R_{1/2}$; for the Sérsic profile, it depends on the Sérsic index n, so we used the deprojection routine presented in appendix A

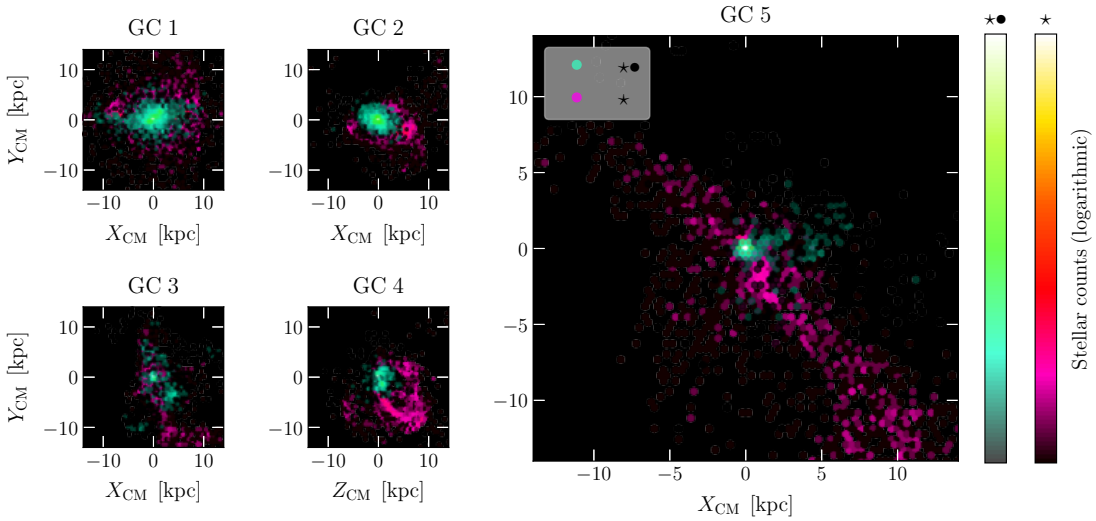

Figure 44: *Dark matter impact on tidal tails:* Stellar distribution of globular clusters formed in dark matter mini-halos (⋆●, turquoise) and globular clusters devoid of dark matter (⋆, magenta) at the last snapshot of our simulations. The hexagonal bins were colour-coded by the bin's stellar counts in a logarithmic scale indicated in the colour-bars. The stellar distribution is projected on the X vs. Y plane for GC1, GC2, GC3 and GC5, while GC4 is projected in the Z vs. Y plane for better visualisation of its particular orbit. This plot highlights more prominent tails in the dark matter-free case, while clusters formed inside dark matter mini-halos present a diffuse stellar envelope with much smaller dimensions than its respective tails. This figure was originally published in Vitral and Boldrini, 2022.

Once again we notice that GCs embedded in DM mini-halos present a more compact structure than in the DM-free case, which this time is characterised by smaller scale radii of the former. The comparison with Milky Way clusters is now more straightforward, as the half-number radii of the true data lies slightly below the mean radii from both scenarios of our simulations, but still closer to the case where GCs do have a DM mini-halo. In spite of the fact that the tidal fields of the MW and of Fornax are different, and therefore these comparisons with MW GCs should not be taken as a settling argument, we argue that Figure 43 still presents an encouraging motivation to further studies concerning the GC formation scenario from Peebles, 1984.

9.3.4 *Tidal tails*

The study of tidal tails in GCs has been revolutionised by *Gaia* data and simulations. For instance, a troubling question that arises when simulating GCs on tidal fields is why these simulations usually predict much more prominent tidal tails (e.g. Boldrini and Vitral 2021; Montuori et al. 2007) than what is observed for the majority of MW clusters? The answer to this question is partially given by Balbinot and Gieles, 2018, who showed with simulations that there is

from Vitral and Mamon (2021, which employs the analytical forms from Lima Neto, Gerbal, and Márquez 1999; Simonneau and Prada 2004; Vitral and Mamon 2020) in order to use the bisection method to invert the number density profile.

a preferential bias towards the escaping of low-mass stars, specially in denser clusters. Such trend reduces considerably the visibility of the tails. In addition, Gieles et al., 2021 recently defended this trend by showing that the visible and extended tails of Palomar 5 are well explained by a supra-massive population of stellar-mass black holes, which is a characteristic associated with less dense GCs (Kremer et al., 2020a). On the other hand, the presence of a DM mini-halo could also reduce the prominence of tidal tails, since the mini-halo is expected to be stripped beforehand GC stars, thus delaying tail formation (e.g., Bromm and Clarke 2002; Mashchenko and Sills 2005; Saitoh et al. 2006; Bekki and Yong 2012; Boldrini and Vitral 2021).

In any case, the increase of better quality data such as *Gaia* EDR3 has allowed to go deeper into this question: Although some GCs, such as NGC 1851 and NGC 7089 (M2), were thought not to have tails based on ground-based imaging (Kuzma et al., 2016; Kuzma, Da Costa, and Mackey, 2018), further *Gaia* studies revealed long tails associated to them (Ibata et al., 2021). However, many clusters with no tidal features, or with only extended envelopes (without tails) are still present[11], and a clear understanding of which mechanisms are behind the lack of very extended tails in these GCs is still not available. On a similar note, Martin et al., 2022 recently used *Gaia* EDR3 and CFHT data to analyse a stellar stream, C-19 (discovered in Ibata et al. 2021), whose metallicity is consistent with it being a remnant of the oldest GC known in our Galaxy, even though the stream still presents a coherent structure to this day, thus requiring some sort of shielding mechanism to protect it from tidal stripping.

We decide to explore the impact of a DM mini-halo on tidal tails by simply plotting, in Figure 44, the stellar distribution of GCs formed in DM mini-halos ($\star\bullet$, turquoise) and GCs devoid of DM ($\star$, magenta) at the last snapshot of our simulations. We also provide a video of the evolution of the tails in the two kind of clusters in the footnote link[12]. We observe much more prominent and obvious tails in the case without DM, with dense streams measuring up to $\gtrsim$ 20 kpc long. In the case where the GCs are formed inside DM mini-halos however, the stellar distribution remains roughly spherical, and with a diffuse stellar envelope of much smaller dimensions than the respective tails. Namely, the extension of the tidal tails around GCs formed in DM mini-halos seems not to exceed $\sim 5-10$ kpc. We connect this difference between two kind of GCs to the protection of the DM shield (as explained in section 9.3.1, and in Figures 39, 40 and 41), which reduces and delays tidal effects on the GCs where it is present.

Therefore, GCs embedded in DM mini-halos are expected to have a roughly spherical, extended ($\sim$ 1 kpc) stellar-envelope, and coherent tails of mild dimension ($\sim 5-10$ kpc)[13], while GCs devoid of DM seem to develop much longer, thicker and well-defined tails extending up to $\gtrsim$ 20 kpc. Evidently, once the DM shield is destroyed, which can happen much before a Hubble time for clusters having specific orbital parameters (see section 9.4), the development of tidal tails can be considered similar to the case without DM, and thus even clusters originally embedded in DM could present extended tails by present the time,

11 See Table 3 from Zhang and Mackey 2021.

12 Link here: https://gitlab.com/eduardo-vitral/vitral_boldrini/-/blob/main/movie.mp4.

13 Such characteristics are in agreement with the recent observations of C-19 (Martin et al., 2022).

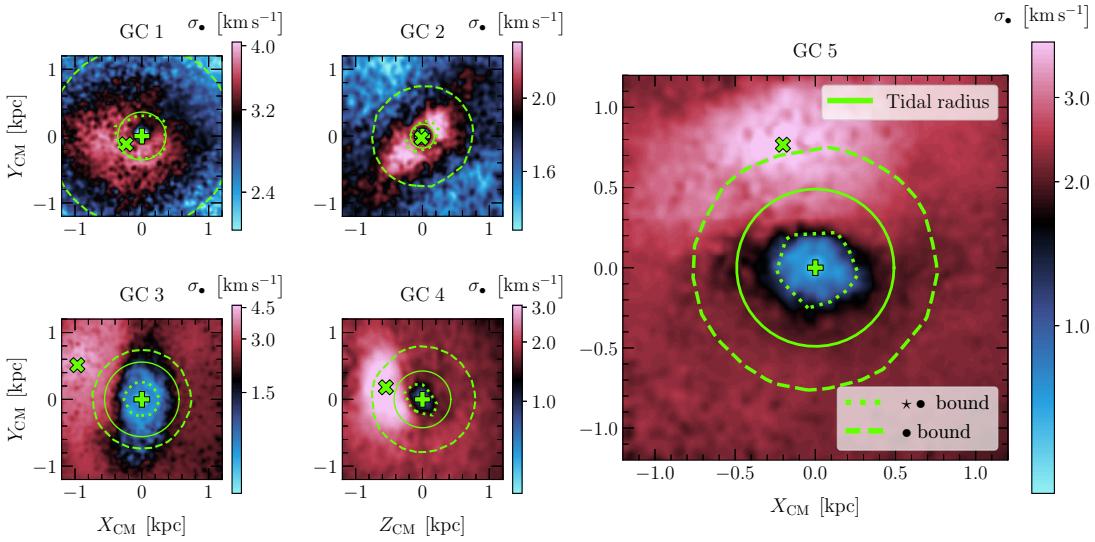

Figure 45: *Survival of the dark matter mini-halo:* Velocity dispersion map of dark matter particles for the five globular clusters we simulated, projected in the X vs. Y plane (with exception of GC4, projected on the Z vs. Y plane for better visualisation of its orbit) and centred in the centre of mass of the globular cluster system. We display the last pericentre passages of their respective orbits, where the tidal effects are stronger. The extension of bound globular cluster stars and bound dark matter particles are highlighted as dotted and dashed green lines, respectively, while the theoretical tidal radius, calculated according to Chapter 3, is displayed as a solid green circle. The maps are colour-coded logarithmically from blue (lower dispersion) to red (higher dispersion). The centres of Fornax and of the GC are represented as a thick green cross and a plus sign, respectively. One can notice that while GCs 3, 4 and 5 manage to keep the dark matter mini-halo (and thus the dark matter shield effect depicted in Figures 40 and 41), GCs 1 and 2 do not. The extent of the red region for GCs 1 and 2 is related to their different orbital parameters. For GCs 3, 4 and 5, we again notice that the empirical tidal radius is well traced by the blue region. This figure was originally published in Vitral and Boldrini, 2022.

in those conditions. Having said that, the DM shield has the effect of delaying tidal effects, by making them much milder while the shield is present.

9.4 SURVIVAL OF THE DARK MATTER MINI-HALO

The DM mini-halo of our simulated GCs was shown to effectively work as a shield against tidal effects. However, not only this mini-halo is gradually removed by being itself stripped before the GC stars, as the increase of mass in the GC+DM system (with respect to the GCs devoid of DM) also brings the system closer to the centre of the host galaxy[14], where tidal effects are stronger. As a result, the DM mini-halo is expected to become negligible with time, so that the question of interest becomes: For how long is the DM mini-halo well preserved in GCs?

The answer to this question is well visible when comparing the five GCs we simulated, and their different orbital parameters. First, we can separate these five GCs into two categories: (1) The GCs where the DM shield is not effective by the end of our simulation and (2) GCs whose shield still manages to protect them against strong tidal effects. Looking at Figure 45, one can clearly assign GCs 1 and 2 to category (1), while GCs 3, 4 and 5 are better suited to category (2). This assignment is due to the fact that the limit of bound stars in GCs 1 and 2 is comparable or greater than the respective tidal radius of the GC+DM system (as shown in Figure 40), meaning that the DM shield illustrated in Figure 39 is no longer well observed.

We argued that the DM loss in GCs 1 and 2 is accelerated by the many pericentre passages (i.e., relatively small orbital periods), as well as the relatively small orbital radii (r_{orbit}) throughout the clusters' orbits. Those factors force these GCs to stay longer next to the centre of the host galaxy, where the tidal interactions are more severe. As a consequence, the DM mini-halos in GCs 1 and 2 suffer from stronger tidal effects and are stripped faster. This can also be checked in Figure 38: GC1 has a short orbital period and small values of r_{orbit}; GC2 has a *very* short orbital period and small values of r_{orbit}; GC3 has a longer orbital period and higher values of r_{orbit}; GC4 has a short orbital period, but not too small values of r_{orbit} (so it still managed to keep the DM shield, although it is more stripped than in GCs 3 and 5); GC5 has an orbital period sufficiently long and higher values of r_{orbit}. Hence, the DM mini-halo survives better to worse, in the following order: GC3, GC5, GC4, GC1 and GC2, respectively.

9.5 DETECTABILITY OF DARK MATTER

If some GCs manage to preserve part of their original DM mini-halo, it is important that we understand the observational limitations that may allow us (or not) to detect this DM component. For instance, as the mini-halo mass distribution is more diffuse than the GC stellar component, one might ask if the DM amount in the GC inner regions is significant. For that purpose, we plot in Figure 46 the mass density ratio between a certain tracer (whether DM or GCs) and

14 Through orbital decay (see section 9.2.2).

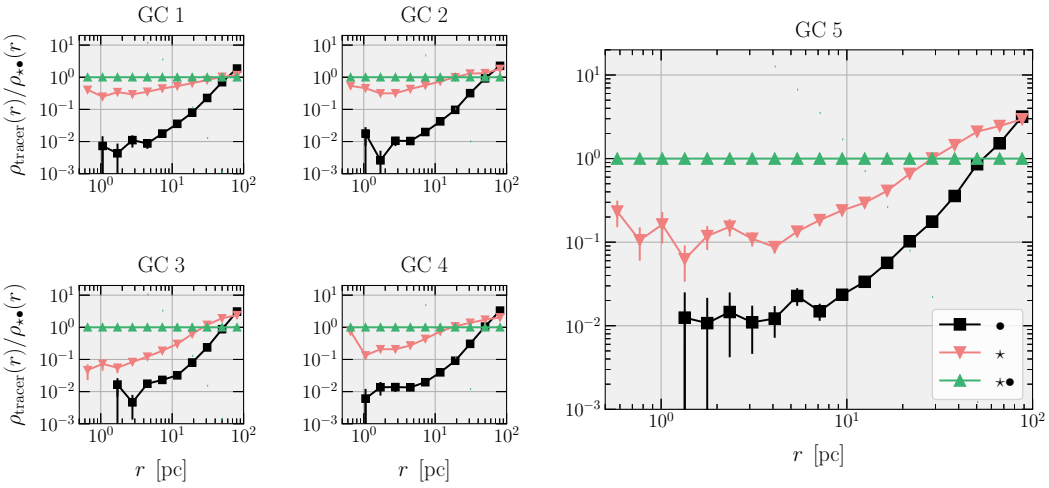

Figure 46: *Density ratio:* We display the density ratio between a certain tracer and the stars from the globular clusters simulated inside dark matter mini-halos (i.e., $\star\bullet$) as a function of distance from the cluster's centre, at the last snapshot of our simulations. The horizontal line of green triangles ($\triangle$) represents the unity ratio, when considering the tracer as the $\star\bullet$ stars themselves. The salmon upside-down triangles ($\triangledown$) have as tracers the stars from globular clusters simulated without dark matter (i.e., $\star$), while the black squares ($\square$) considers the tracer as the dark matter particles (i.e., $\bullet$) from the mini-halos that embed the $\star\bullet$ stars. These plots show that the internal (i.e., $\lesssim$ 10 pc) dynamics of the clusters formed in dark matter mini-halos is not considerably affected by the dark matter, as the density ratio of dark matter particles and stars is of the order of only 1%. This figure was originally published in Vitral and Boldrini, 2022.

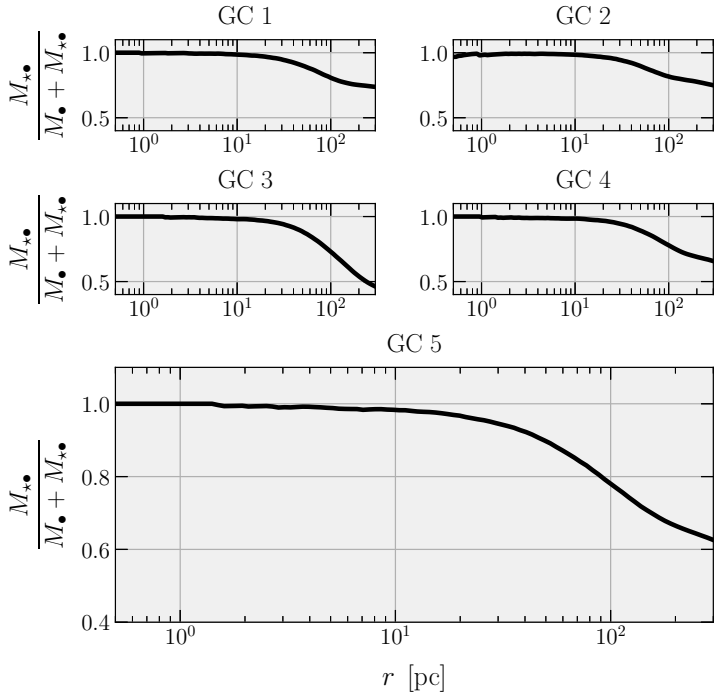

Figure 47: *Cumulative mass ratio:* Comparison of the cumulative mass ratio of stellar to total mass (i.e., $M_{\star\bullet}/[M_\bullet + M_{\star\bullet}]$) as a function of distance to the cluster centre (in pc), for globular clusters simulated inside dark matter mini-halos at the end of our simulations. This plot exalts how difficult it is to detect considerable amounts of dark matter up to hundreds of pc away from the cluster centre. This figure was originally published in Vitral and Boldrini, 2022.

the stars from the GCs simulated inside DM mini-halos (i.e., $\star\bullet$) as a function of distance from the cluster's centre, at the last snapshot of our simulations.

Figure 46 reveals that up to ~ 10 pc, the density ratio between the DM component and the stellar component of the GCs (black squares) is of the order of 1%, meaning that the influence of DM in the internal dynamics of these clusters is mostly negligible[15]. In addition, we also plot in Figure 47, the cumulative mass ratio of stellar to total mass (i.e., $M_{\star\bullet}/[M_\bullet + M_{\star\bullet}]$) as a function of distance to the cluster centre, for the GCs simulated inside DM mini-halos, at the end of our simulations. This latter figure also argues in favour of the difficulty of detecting considerable DM amounts in GCs, even when they were formed inside such mini-halos. Indeed, the cumulative mass ratio of stellar to total mass is of the order of unity up to hundreds of pc away from the clusters' centre.

In the past, many studies (Shin, Kim, and Lee, 2013; Conroy, Loeb, and Spergel, 2011; Ibata et al., 2013; Moore, 1996; Baumgardt et al., 2009; Lane et al., 2010; Feng et al., 2012; Hurst et al., 2015) measured very low mass-to-light ratios in GCs, and sometimes used that as an argument to rule out the presence of dark matter in them. We showed, in agreement with what has been previously pointed out in Bromm and Clarke, 2002; Mashchenko and Sills, 2005; Saitoh et al., 2006; Bekki and Yong, 2012, that GCs originally embedded in DM lose

15 The plot depicts this behaviour at the end of the simulations, but we stress that throughout the evolution of the cluster, typical DM densities remain much lower than the inner GC stellar densities, given the latter's particularly high values.

much of their initial DM content due to tidal interactions. Together with the different density profiles from DM and luminous components, this naturally leads to mass ratios (stellar to total mass) very close to unity, up to distances as far as available data usually go.

Finally, Figure 46 also compares the densities of the GCs formed in DM mini-halos and the ones devoid of it (upside down red triangles). Clearly, clusters with DM have inner stellar densities much higher than GCs devoid of DM, with GCs 3 and 5, which managed to retain most of their initial DM mini-halo, having densities up to ten times higher than their DM-free counterparts. Hence, in addition to denser clusters producing an observational bias where tidal structures are more difficultly detected (Balbinot and Gieles, 2018), we pointed that the ones that might be formed in DM mini-halos also tend to have at the same time higher inner densities and less prominent tidal structures (see section 9.3.4), which can render the search for stellar streams in these GCs particularly hard.

9.6 ENVIRONMENTS FOR DARK MATTER SEARCH

Some signs of shielding structures such as a DM mini-halo (see Figures 39 and 41) can still be noticed in certain sources. For instance, the recent detection of the extremely metal poor stellar stream by Martin et al., 2022, C-19, associated with the oldest known GC, deserves particular attention. Its short orbital time ($\lesssim$ 0.5 Gyr) and low orbital radii[16] imply many passages close to the Galactic centre, in a similar way than our simulated GC+DM systems (Figure 38). Hence, if this 13 Gyr[17] remnant is still well observed, it clearly requires the presence of a shielding mechanism that protected the progenitor GC for long enough so the stream preserves a coherent structure to this day, as the authors do mention.

While Martin et al., 2022 argued that the presence of a DM sub-structure would heat the stellar stream and further disperse it, we emphasise that this is a common misconception, addressed in section 9.3.2: Although the DM mini-halo does heat the stellar component, this heating is negligible when compared to the heating from the host's tidal effects, which in turn are better shielded by the DM in the GCs originally embedded in it. Therefore, we defend that whilst most of the original DM in the C-19 progenitor could have been lost, it portrays a tantalising environment for a DM shield. Indeed, a recent analysis by Errani et al., 2022 proposed that this stream could represent the debris of a DM dominated GC formed at early times. A similar argument was brought up in Boldrini and Vitral, 2021, which we present below.

9.6.1 *Motivations from Boldrini & Vitral (2021)*

In this work, we performed N-body simulations on GPU in an attempt to reproduce the past 10 Gyr of dynamical evolution of a globular cluster presenting similar characteristics to the nearby globular cluster NGC 6397, in the strong

16 Malhan et al., 2022 report a pericentre of 9.3 kpc and an apocentre of 21.6 kpc.

17 The authors find this age by fitting PARSEC isochrones to their observed colour-magnitude diagram.

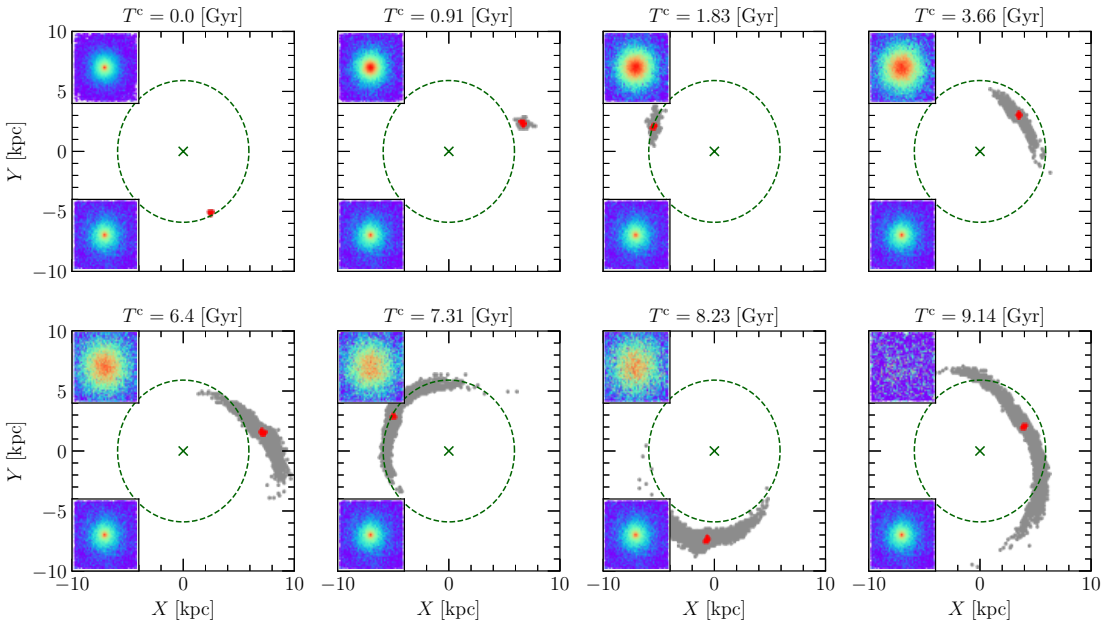

Figure 48: *Formation of tidal tails:* Snapshots of the GC simulated in Boldrini and Vitral, 2021, at different times. Bound and unbounded particles are represented in red and grey, respectively. The subplots on the left are a zoomed-in view of the bound particles at each time, over a region up to ~6 pc from its centre, with the top plots representing the evolving GC in our simulation and the bottom plots depicting a NGC 6397-like GC. The green cross points the centre of the galaxy and the green circle has a radius of 5.91 kpc, i.e. the galactocentric distance of the GC. One can notice extended tidal tails of sizes greater than 1 kpc in roughly 3.66 Gyr, which is well below the age of NGC 6397 (12.87 Gyr). Consequently, we predict that NGC 6397 should exhibit tidal tails and these should be clearly observable. This figure was originally published in Boldrini and Vitral, 2021.

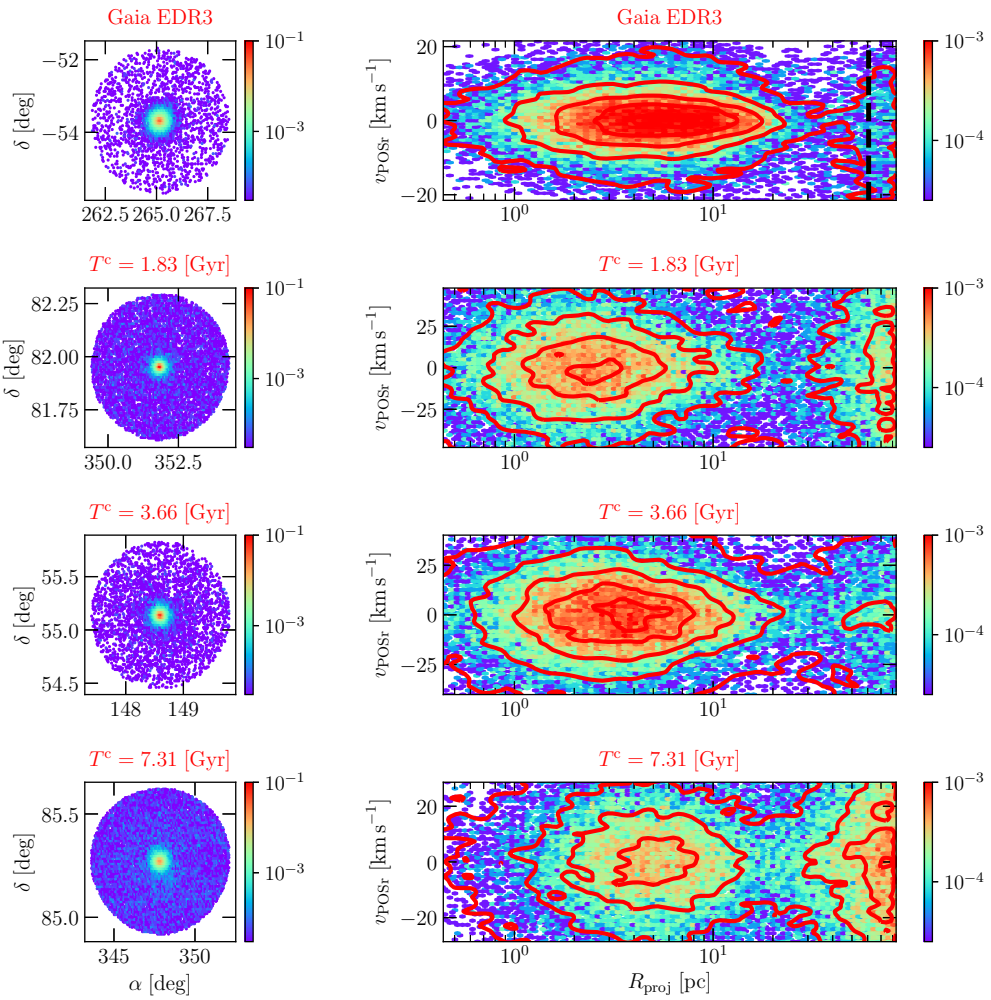

Figure 49: *Discontinuity in density for NGC 6397 from Gaia EDR3 data:* Comparison of *Gaia* EDR3 (first row) and the GC from our simulation, at different times (other rows). *Left:* Projected sky plots. *Right:* Radial direction of the proper motion as a function of the logarithmic binned projected distance along with the tidal radius in dashed black. The colour bars indicate the normalised star counts per bin, with respect to the total number of stars. During the formation of tidal tails for our simulated GC, we observed that a continuity in density, for the radial velocity along the projected radius, emerges below the tidal radius of approximately 100 pc. It shows the presence of potential escapers due to MW tidal effects. In contrast, for NGC 6397, there is a clear cut-off at roughly 30 pc between GC stars and MW interlopers. Indeed, the density transition in observed data seems to correspond to that of a cluster at the very beginning of its evolution in the MW tidal field as the simulated cluster at $T^c = 1.83$ Gyr. We conclude that there is no obvious sign of an ongoing intense tidal disruption for NGC 6397 stars. This figure was originally published in Boldrini and Vitral, 2021.

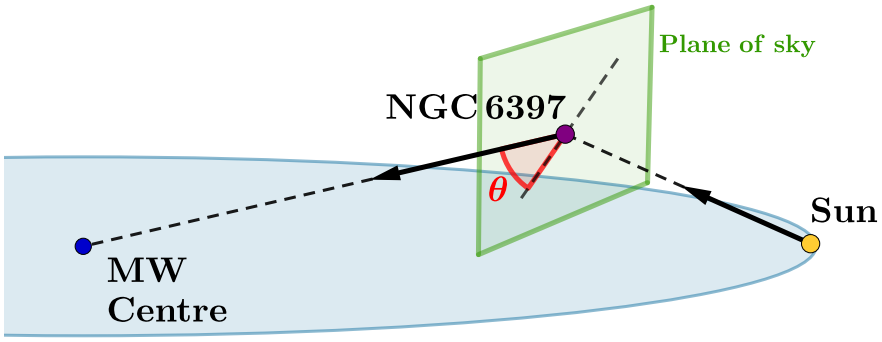

Figure 50: *Geometry of tails:* We represent the projection effects related to tidal tails pointing towards the galactic centre, with θ being the angle between the galactocentric direction and the plane of sky centered on NGC 6397. The positions of the sources are not in agreement with their true positions, for better visualization. This figure was originally published in Boldrini and Vitral, 2021.

tidal field of a Milky Way-like galaxy. We considered a purely baryonic globular cluster, and we used the prescription from Baumgardt and Makino, 2003, in order to access the corrected time of evolution of the cluster, while keeping a feasible mass resolution.

The intense background of dark matter and stars in our simulations is sufficient to disrupt the cluster in a Hubble time. We demonstrated that the lifetime of the simulated cluster depends mainly on its initial density profile and mass. More importantly, we found that more than 6 Gyr ago, right after the first third of the cluster's life, all of our simulated GCs presented tidal tails, which extended farther several kpc long (see Figure 48). We subsequently compared our simulations and observations of NGC 6397 from *Gaia* EDR3 data (see Figure 49). Despite its recent passage through the galactic disk (Rees and Cudworth 2003), we found that several indicators seem to rule out the presence of obvious tidal tails around NGC 6397.

9.6.2 *Robustness tests*

Our observational data analysis established that several indicators such as the stellar distribution and the radial velocity along the projected radius of NGC 6397 seem to rule out the presence of extended tidal tails, contrary to the predictions of our simulations. Here, we provide and evaluate several solutions, which could explain the discrepancy between our simulations and the Gaia EDR3 observations of NGC 6397.

9.6.2.1 *Projection effects*

One of the possible explanations for the lack of tails in the observations could be a projection effect, since the tails could be aligned along the line-of-sight connecting the Sun and NGC 6397. If this is the case, the projection of these tails would be negligible on sky plots, as well as in the outer projected radii of Figure 49.

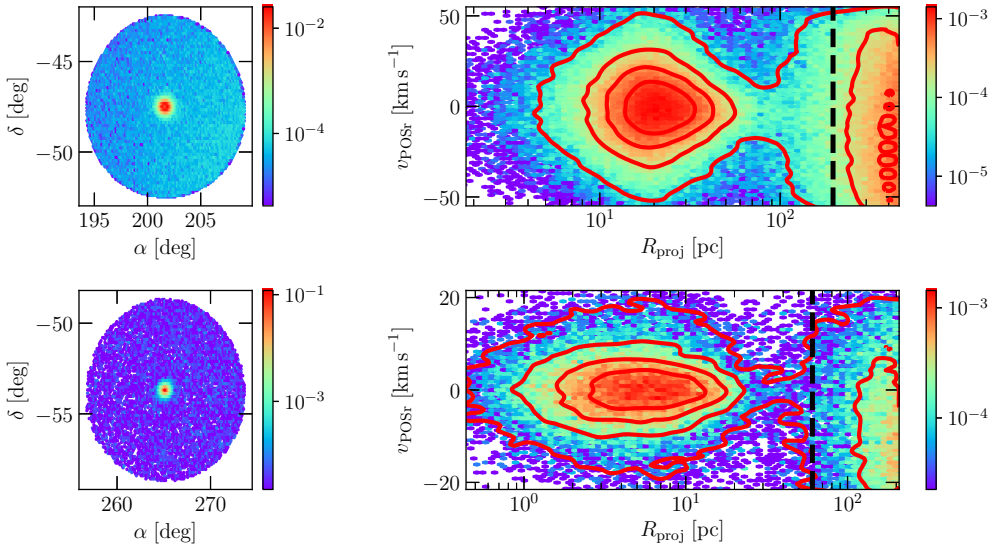

Figure 51: *Comparison with ω Cen:* Analysis of the globular cluster ω Cen, similar to Figure 49, and comparison with NGC 6397. The Gaia EDR3 data, this time observed in a 5-degree cone search, which explains the high number of stars at high projected radii. *Left:* Projected sky plot of the GC. *Right:* Radial direction of the proper motion of the globular cluster as a function of the logarithmic binned projected distance along with the tidal radius of each case in dashed black. The colour bars indicate the normalized star counts per bin, with respect to the total number of stars. We used a distance to the Sun of 5.24 kpc and a tidal radius of 196.46 pc for ω Cen (Baumgardt et al., 2019). The upper plot presents 237692 stars, among which 67639 lie beyond the tidal radius of NGC 5139 and the lower plot displays 44599 stars, among which 9415 lie beyond the tidal radius of NGC 6397. As in our simulations in Figure 49, ω Cen exhibits the continuity in density, for the radial velocity along the projected radius, which indicates the presence of tidal arms. For the observed NGC 6397 extending up to 5 degrees, there is still a clear cut-off and no sign of tidal arms, but only of a stronger MW contamination. This figure was originally published in Boldrini and Vitral, 2021.

In order to test this assumption, we refer to the work of Klimentowski et al., 2009 and Montuori et al., 2007, who analysed the orientation of tidal tails in dwarf spheroidal galaxies and GCs, respectively, by studying the outcome of N−body simulations. Both studies report that in the vicinity of the dwarf or the GC, the tails are typically oriented towards the MW and not along the orbit (see Figures 2 and 3 from Montuori et al. 2007). Indeed, it is in the vicinity of those sources (i.e. at distances closer than ~1 kpc) that the tails are denser and therefore most likely to be detectable. This is well suited for our analysis as we restrict our study to only two (five, in Figure 51) degrees around the cluster centre.

Therefore, we verify if the sky projection of the direction connecting the NGC 6397 and the MW centre is washed out due to an alignment problem (i.e. $\theta \approx 90$ degrees in Figure 50). We derive $\theta = 57.43$ degrees, which is sufficient for us to detect extended tidal tails, since the projection of such components would yield a length of roughly $L \times \cos\theta = L \times 0.54$, with L being the length of the tidal tails in the direction of the MW centre (see Figure 50). The large projection of the tails in the sky derived above is then an important argument for this bias to be neglected.

9.6.2.2 *Limiting magnitude*

Gaia EDR3, as well as its predecessor, has a magnitude limit of $G_{mag} \sim 20$, which basically means that the faintest GC stars, with masses $\lesssim 0.5\ M_\odot$, are not taken into account. Naturally, fainter stars tend to occupy distances farther from the GC centre than brighter stars, due to mass segregation (Binney and Tremaine 2008), and such a relation has been robustly observed by Heyl et al., 2012 and Vitral and Mamon, 2021 for NGC 6397. Therefore, one possibility is that NGC 6397 might have tidal tails which are just not detected by Gaia EDR3, as a consequence of how deep, in magnitude, its observations can probe. However, Vitral and Mamon, 2021 found that, although the fainter stars do follow a more diffuse distribution in space, their radial extent is only about two times greater than the brighter stars (i.e. $R_e = 6.5$ pc), which remains a small radial extent when compared to our simulated GC presenting a Sérsic radius of $R_e \sim 200$ pc and tidal tails of more than 1 kpc long in early stages of the cluster life.

9.6.2.3 *Comparison with other globular clusters*

We now test if this limiting magnitude could affect, for example Figure 49, by blurring or erasing the contribution of faint stars in tidal tails drowned in MW contaminants. For that, we generated plots similar to Figure 49 for GCs known to have obvious tidal tails, such as Pal 5 (Odenkirchen et al. 2001) and NGC 5139 (ω Cen, Ibata et al. 2019).

Indeed, our method was not able to detect strong imprints of the massive tidal tails of Pal 5, given that it is located at roughly 21.6 kpc away from the Sun. As Pal 5 is about nine times more distant than NGC 6397, the limiting magnitude of Gaia EDR3 prevents us from observing many of the faint stars that dominate the tails of the former cluster, whose apparent magnitude depends on their distance to us. Therefore, we decide to test our method with a

closer GC, ω Cen, known to have important tidal tails (e.g. Ibata et al. 2019 and Sollima 2020), and whose distance and MW contamination are not too different from NGC 6397 (the values of distance to the Sun and galactocentric distance of ω Cen are 5.2 kpc and 6.4 kpc, respectively, Harris 2010). Since NGC 5139 is still more distant than NGC 6397, detecting any tidal imprints around it through our method from Figure 49 would indicate the reliability of this procedure.

The first row of Figure 51, which also selects all Gaia EDR3 stars within a 5-σ proper motion region, this time inside a five-degree cone search around ω Cen, shows that although the MW contamination does play a role in blurring the GC escapers, we are still able to observe the continuity in density, for the proper motion radial component along the projected radius, which indicates the presence of tidal tails. Even if Montuori et al. 2007 pointed out that ω Cen has tidal tails deviating from the galactocentric direction and extending toward the galactic plane, our method highlights the external structure. Besides, ω Cen in Figure 51 is similar to second and third snapshots of Figure 49. We display, in the second row, the similar plot of NGC 6397 for comparison. Thus, if ever NGC 6397 has extended tidal tails formed by fainter stars blurred by MW contamination, it would be curious if such an effect is not repeated for ω Cen.

For the observed NGC 6397 extending up to 5 degrees, which is the aperture usually probed in this kind of study (Sollima, 2020), there is still a clear cut-off and no sign of tidal tails, but only of a stronger MW contamination at outer radii (see Figure 51). Indeed, Klimentowski et al. 2009 stress that the most evident signs of tidal structures will be seen closer to the analysed source, where the stars are more clumped together.

9.6.2.4 *Dark matter profile of the MW*

In our MW mass model, we have assumed a NFW profile for the DM halo. However, an evidence for a DM core in the MW was claimed by Portail et al., 2017 in order to explain the high velocity dispersion of the stars in the Galactic bulge. They predicted a small DM core of few kpc in size. In all runs, the GC orbits around the MW centre at a distance between 5.1 and 9.2 kpc. As the GC does not orbit in the regions where a DM core can be produced by feedback (Lazar et al., 2020), it will not feel the dynamical impact of a different DM density profile for the MW. Moreover, we emphasise that the gravitational potential is dominated by stars of the bulge in this inner region of the MW. Therefore, varying the enclosed mass in the inner region of the MW is not a viable solution to efficiently delay the formation of tidal tails around the GC in order to reproduce the Gaia EDR3 observations.

9.6.2.5 *GCs embedded in dark matter*

We now discuss the possible influence of the presence of DM in GCs during their evolution. Contrary to our simulated GCs, which exhibit obvious stellar tidal tails, which are well extended in the sky, we argue that NGC 6397 does not possess such strong tidal imprints, based on Gaia EDR3 data (see Figures 49 and 51). It was claimed that these tidal structures should not form if they were embedded in DM minihalos (Grillmair et al., 1995; Moore, 1996; Mashchenko

and Sills, 2005; Odenkirchen et al., 2003; Vitral and Boldrini, 2022). Indeed, adding this dark component to this GC could help to avoid the formation of stellar tidal tails.

We pointed out that GAIA EDR3 data reveals that stars in the central region of NGC 6397 seem to follow a spherical distribution. Curiously, it was argued that a stellar cluster evolving inside a DM minihalo would have close to this sort of distribution in its denser part, where the stars dominate over DM (Mashchenko and Sills, 2005). We stress that DM provides a potential solution to the case of NGC 6397. A DM minihalo could be responsible for both the inner spherical shape and the absence of tidal tails in this cluster, as the stellar part of a GC embedded in DM would be more resilient to tidal disruption.

9.6.2.6 *Ex-situ origin*

It was also suggested that nuclear star clusters of tidally-stripped galaxies may be the progenitors of GCs, especially massive ones such as G1 and ω Cen (Freeman, 1993; Bekki and Freeman, 2003b; Bekki and Yong, 2012; Böker, 2008; Meylan et al., 2001). They are the most massive clusters of their parent galaxies, M31 and the MW, respectively. Nucleated dwarf galaxies can be transformed into GCs due to tidal stripping of the dwarfs by the strong gravitational field of galaxies (Bekki et al., 2002; Bekki and Freeman, 2003b). It is important to note that this scenario is also motivated by the presence of a far more complex stellar population in clusters such as ω Cen (three distinct populations, Pancino et al. 2003), compared to normal clusters. NGC 6397 hosts only two stellar populations (Milone et al., 2012).

Furthermore, these GC-like systems were embedded in DM halos (Taylor, 2005; Böker et al., 2004; Walcher et al., 2005; Walcher et al., 2006). GCs originated from nucleated dwarfs have therefore formed outside the central regions of the MW. That is the reason why these GC-like systems can have no DM at the present day. In fact, most of the initial DM halo was stripped away from the GC during the first several orbits, even if they are massive at their birth (Wirth, Bekki, and Hayashi, 2020).

The fact that a GC may be a nuclear star cluster remnant could explain the absence of its stripping in the dense MW central region, but it is also used to argue that it may have an intermediate-mass black hole (IMBH) at its centre (Bahcall and Wolf, 1976). Indeed, it was claimed that G1 and ω Cen could contain IMBHs with a mass of 10^4 $M_\odot$ (Gebhardt, Rich, and Ho, 2002; Gebhardt, Rich, and Ho, 2005; van der Marel and Anderson, 2010). However, it was recently demonstrated that the presence of a central IMBH in NGC 6397 was ruled out, in favour of a diffuse dark inner sub-cluster of stellar remnants (Vitral and Mamon, 2021), well explained by a strong concentration of faint white dwarfs (Kremer et al., 2021).

9.6.3 *Conclusions*

Since we believe that the analysis performed with *Gaia* EDR3 data was robust and contradictory to our simulations, where GCs exhibit extended tails, it is much more likely that the cause of such discrepancy is due to the origin scenario of the evolving cluster, as well as some of the environmental conditions

of our simulations. Indeed, we have considered three main factors that could influence the formation of tidal tails in NGC 6397: the dark matter profile of the Milky Way, an extra-galactic origin for this globular cluster, as well as their formation in dark matter minihalos.

We argued that the most likely flaw of our simulation was to consider a purely baryonic globular cluster at the beginning of the simulation. In fact, when assuming a scenario where globular clusters are formed in a dark matter minihalo (Peebles and Dicke 1968; Peebles 1984), one would expect it to protect the cluster stars against intense tidal stripping, which would act as a shield and be itself stripped instead of the luminous matter. The fact that we do not managed to robustly observe considerable amounts of dark matter in globular clusters, and particularly in NGC 6397, could be attributed to such initial dark matter minihalos being stripped by the combination of internal processes of the globular cluster such as stellar evolution and supernovae, and the intense tidal field of the Milky Way.

Part IV

APPENDIX

A

DENSITIES & DEPROJECTIONS

A.1 COEFFICIENTS FOR NEW DEPROJECTED SÉRSIC MODELS

In this appendix, I direct the reader to the tables from Vitral and Mamon, 2020, containing the coefficients a_{ij} in from our Sérsic deprojection formulae, for $\widetilde{f} = \widetilde{\rho}$ and $\widetilde{f} = \widetilde{M}$. The respective table for$\widetilde{f} = \widetilde{\rho}$ is available at https://gitlab.com/eduardo-vitral/vitral_mamon_2020a/-/blob/master/coeff_dens.txt, while the one for $\widetilde{f} = \widetilde{M}$ is available at https://gitlab.com/eduardo-vitral/vitral_mamon_2020a/-/blob/master/coeff_mass.txt.

The tables with the new coefficients computed in Vitral and Mamon, 2021 are available at https://gitlab.com/eduardo-vitral/vitral_mamon_2020b/-/blob/master/coeff_dens.txt for $\widetilde{f} = \widetilde{\rho}$, and at https://gitlab.com/eduardo-vitral/vitral_mamon_2020b/-/blob/master/coeff_mass.txt for $\widetilde{f} = \widetilde{M}$, respectively.

A.2 PROJECTED NUMBER

I present here the complete solution of the centre fit, for a distribution following the Plummer (Plummer, 1911) profile, in the approximation of small cone apertures in the sky (i.e. $R_{max} \ll 1$ radian).

However, whenever $R > R_{max} - d$, the indefinite integral of equation 54 yields:

$$\begin{aligned}\widetilde{N}(x) = &-\frac{a^2 \arccos\left[\frac{R^2+d^2-R_{max}^2}{2Rd}\right]}{\pi(a^2+R^2)} + \\ &\left(\sqrt{\Xi_1}\left(-\sqrt{\Xi_2}\times\right.\right. \\ &\arctan\left[\frac{(d^2-R_{max}^2)^2 - R^2(d^2+R_{max}^2)}{(d^2-R_{max}^2)\sqrt{\Xi_1}}\right] + \\ &\left.\left.(a^2+d^2-R_{max}^2)\arctan\left[\frac{\Xi_3}{\sqrt{\Xi_2}\sqrt{\Xi_1}}\right]\right)\right) \div \\ &\left(2\pi\sqrt{\Xi_2}\sqrt{\Xi_1}\right) + \mathcal{C}\,.\end{aligned} \tag{120}$$

where $\mathcal{C} = 1$ is an integration constant, a is the Plummer effective radius, and Ξ_1, Ξ_2 and Ξ_3 are defined as:

$$\Xi_1 = -d^4 - (R^2 - R_{max}^2)^2 + 2d^2(R^2 + R_{max}^2) \tag{121a}$$

$$\Xi_2 = a^4 + (d^2 - R_{max}^2)^2 + 2a^2(d^2 + R_{max}^2) \tag{121b}$$

$$\Xi_3 = (d^2 - R_{max}^2)^2 + a^2\,(d^2 + R_{max}^2) - R^2\,(a^2 + d^2 + R_{max}^2) \tag{121c}$$

This treatment can be chosen in the BALRoGO method POSITION.FIND_CENTER(), by providing the argument `method="mle_robust"`.

A.3 ASYMMETRIC SURFACE DENSITY

Here I describe how the BALRoGO's POSITION.ELLIPSE_LIKELIHOOD routine performs asymmetric Sérsic fits with (α, δ) data. First, it projects the (α, δ) data according to classical spherical trigonometry relations, translating it so it is centred at the origin:

$$x_p = \cos\delta\,\sin(\alpha - \alpha_0)\,, \tag{122a}$$
$$y_p = \sin\delta\,\cos\delta_0 - \cos\delta\,\sin\delta_0\,\cos(\alpha - \alpha_0)\,, \tag{122b}$$

where (α_0, δ_0) is the centre of the cluster. Next, it rotates the axis so the data can be easily handled:

$$x = x_p\,\cos\theta + y_p\,\sin\theta\,, \tag{123a}$$
$$y = -x_p\,\sin\theta + y_p\,\cos\theta\,, \tag{123b}$$

where θ is the angle between the original reference frame and the new one. With this new set, we are able to define a likelihood function of the stellar distribution as:

$$\mathcal{L} = \prod_i \frac{\Sigma(m)}{N_{tot}}\,. \tag{124}$$

with $m = \sqrt{(x/a)^2 + (y/b)^2}$, and where (a, b) are the semi-axis of the ellipse. The surface density $\Sigma(m)$ and the number of tracers at infinity N_{tot} are defined such as in van de Ven and van der Wel, 2021, so that we have:

$$\frac{\Sigma(m)}{N_{tot}} = \frac{b_n^{2n}\exp\left[-b_n\,m^{1/n}\right]}{2\pi\,a\,b\,n\,\Gamma(2n)}\,. \tag{125}$$

In equation 125, n is the Sérsic index, $\Gamma(x)$ is the gamma function of the variable x and the b_n is computed with the precise approximation from Ciotti and Bertin, 1999. Thus, the fit finds the parameters which maximise $\mathcal{L}$.

Finally, to derive statistical errors of our Bayesian estimates, I use PYTHON's NUMDIFFTOOLS.HESSIAN method to compute the Hessian matrix of the probability distribution function (i.e., eq [125]). After, I assign the uncertainties of each parameter as the square root of the respective diagonal position of the inverted Hessian matrix.

B

GEOMETRY & STATISTICS

B.1 FIELD STARS MOCK DATA

In this section, I derive the equations for random positions and proper motions of field stars, presented in Chapter 6.

B.1.1 *Random positions*

In order to generate n points uniformly distributed in a spherical cap, I shall first considerate Figure 52, with the geometry of the problem. From classical spherical trigonometry relations, it is straightforward to write:

$$\cos R = \sin\delta \sin\delta_0 + \cos\delta \cos\delta_0 \cos(\alpha - \alpha_0) \,, \tag{126a}$$

$$\sin\phi = \frac{\cos\delta \sin(\alpha - \alpha_0)}{\sin R} \,, \tag{126b}$$

$$\sin\delta = \cos R \sin\delta_0 + \sin R \cos\delta_0 \cos\phi \,. \tag{126c}$$

I wish to generate an uniform distribution of points in a spherical cap of radius R_{lim}, so the probability of having a radius smaller than R can be written as:

$$\Pr\{r < R\} = \frac{\text{Surface}(R)}{\text{Surface}(R_{lim})} \,, \tag{127}$$

or, more precisely:

$$\Pr\{r < R\} = \frac{\int_0^R \int_0^{2\pi} \rho^2 \sin\theta d\theta d\varphi}{\int_0^{R_{lim}} \int_0^{2\pi} \rho^2 \sin\theta d\theta d\varphi} = \frac{1 - \cos R}{1 - \cos R_{lim}} \,, \tag{128}$$

where ρ is the radius of the sphere, θ and φ are the longitudinal and latitudinal angles of the sphere, that in our description have their origin at (α_0, δ_0). Similarly, the probability that ϕ is smaller than an angle Θ is:

$$\Pr\{\phi < \Theta\} = \Theta/2\pi \,. \tag{129}$$

Therefore, in order to derive equations for random positions in the sky from Chapter 6, one just needs to invert the relations (128) and (129), with respect to

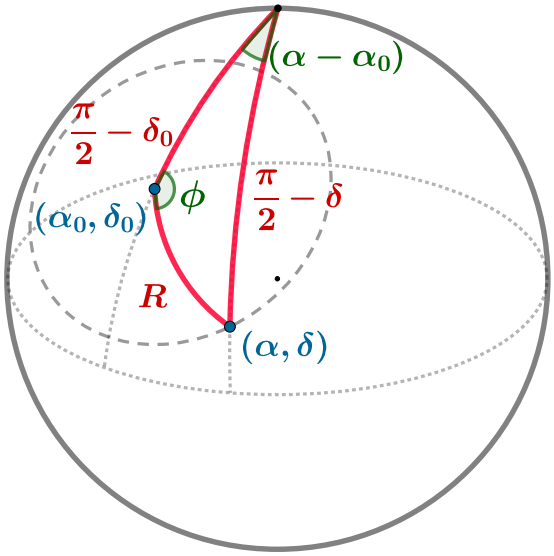

Figure 52: Spherical geometry: Representation of the physical situation of a source projected in the plane of sky.

R and Θ, respectively. The following step, which is to convert the set of known α_0, δ_0, R and ϕ into pairs of (α, δ) is done by first deriving δ with equation (126c) and then α with:

$$\alpha = \begin{cases} \alpha_0 + \arccos(\Lambda_1) & \text{, for } \Lambda_2 > 0 \text{ and } 0 \leqslant \phi \leqslant \pi \\ \alpha_0 + \arccos(-\Lambda_1) & \text{, for } \Lambda_2 < 0 \text{ and } 0 \leqslant \phi \leqslant \pi \\ \alpha_0 - \arccos(\Lambda_1) & \text{, for } \Lambda_2 > 0 \text{ and } \pi < \phi < 2\pi \\ \alpha_0 - \arccos(-\Lambda_1) & \text{, for } \Lambda_2 < 0 \text{ and } \pi < \phi < 2\pi \end{cases} \tag{130}$$

where we have the following correspondences:

$$\Lambda_1 = \sqrt{1 - \frac{\sin^2\phi \, \sin^2 R}{1 - \sin^2\delta}} \tag{131a}$$

$$\Lambda_2 = \frac{\cos R - \sin\delta \sin\delta_0}{\cos\delta \cos\delta_0} \tag{131b}$$

B.1.2 *Random proper motions*

For the field stars, I generated random variables that followed a symmetric Pearson VII distribution. The statistical approach to do so was to invert the probability that a field star proper motion modulus is smaller than M, i.e. the

cumulative distribution function of M for a symmetric Pearson VII distribution of scale radius a and characteristic slope τ:

$$\begin{aligned} \mathrm{CDF}(M) &\equiv \int_0^M f_{PM}(\mu)d\mu \\ &= -\int_0^M \frac{\tau+2}{a}\frac{\mu}{a}\left[1+\left(\frac{\mu}{a}\right)^2\right]^{\tau/2} d\mu\,. \end{aligned} \tag{132}$$

where f_{PM} is the distribution function of proper motions moduli for the Pearson VII symmetric distribution. The result of the integral above is:

$$\mathrm{CDF}(M) = 1 - \left[1+(M/a)^2\right]^{1+\tau/2}\,. \tag{133}$$

Thus, if U is a uniform random variable with boundaries [0, 1] (and thus, $1-U \equiv U$, random PM variables can be generated as presented in Chapter 6.

B.2 VELOCITY DISPERSION

I describe here how I constructed velocity dispersion profiles for the output of our simulations.

B.2.1 *Dispersion map*

The velocity dispersion maps displayed in Figures 41 and 45 was constructed by first binning the projected X vs. Y map with PYTHON's HEXBIN routine, setting the argument `gridsize`= 100. For each bin, I then computed the 1D velocity dispersion of the DM component by summing quadratically the velocity dispersion on X, Y and Z directions and normalising it by the square root of the number of dimensions (i.e., three). Whenever there were more than hundred particles inside the bin, I used all the bin's particles, otherwise I completed the sample by picking the closest particles to the bin's centre of mass, until the threshold of a hundred particles was attained.

The process above assured that each bin had a statistically significant number of tracers, which helped us to reach a better spatial resolution, eventually. However, as the results still presented an important amount of statistical noise, I decided to smooth our maps with PYTHON's GAUSSIAN_FILTER routine, with the argument `sigma`= 3. I finally displayed the outcome of this procedure in a map colour-coded logarithmically from blue (lower dispersion) to red (higher dispersion).

B.2.2 *Dispersion radial profiles*

To build the radial dispersion profiles from Figure 42, I used the routines ANGLE.CART_TO_SPH and DYNAMICS.DISPERSION from the BALROGO PYTHON package, to first convert the data into spherical coordinates and then compute the velocity dispersion of the radial component, as a function of the distance to the

cluster's centre. The way I set BALRoGO to compute this dispersion is by first dividing the radial extent into thirty equally spaced logarithmic bins and then calculating the respective dispersion and Poisson error associated to it.

Next, it smooths the profile in order to remove statistical noise, by fitting a 10-th order polynomial to it with the NUMPY.POLYFIT routine. $1-\sigma$ regions were obtained by following the recipe presented in the footnote link[1]. I finally chose to consider the results inside a more restrict spatial extent in order to neglect the potentially bad fits of the polynomial on the borders of our data.

1 https://stackoverflow.com/questions/28505008/

Abadi, Mario G., Julio F. Navarro, and Matthias Steinmetz (Jan. 2006). "Stars beyond galaxies: the origin of extended luminous haloes around galaxies." In: *MNRAS* 365.3, pp. 747–758. DOI: 10.1111/j.1365-2966.2005.09789.x. eprint: astro-ph/0506659.

Abbott, B. P. et al. (Feb. 2016a). "Observation of Gravitational Waves from a Binary Black Hole Merger." In: *Physical Review Letters* 116.6, 061102, p. 061102. DOI: 10.1103/PhysRevLett.116.061102. eprint: 1602.03837.

Abbott, B. P. et al. (Feb. 2016b). "Observation of Gravitational Waves from a Binary Black Hole Merger." In: *Physical Review Letters* 116.6, 061102, p. 061102. DOI: 10.1103/PhysRevLett.116.061102. arXiv: 1602.03837 [gr-qc].

Abbott, B. P. et al. (2017). "GW170817: Observation of Gravitational Waves from a Binary Neutron Star Inspiral." In: *Physical Review Letters* 119.16, 161101, p. 161101. DOI: 10.1103/PhysRevLett.119.161101. arXiv: 1710.05832 [gr-qc].

Abbott, R. et al. (Apr. 2021). "GWTC-2: Compact Binary Coalescences Observed by LIGO and Virgo during the First Half of the Third Observing Run." In: *Physical Review X* 11.2, 021053, p. 021053. DOI: 10.1103/PhysRevX.11.021053. arXiv: 2010.14527 [gr-qc].

Abel, N. H. (1826). "Auflösung einer mechanisches Aufgabe." In: *Journal für die reine und angewandte Mathematik* 1, pp. 153–157.

Akaike, H. (1983). "Information measures and model selection." In: *Internal-tional Statistical Institute* 44, pp. 277–291.

Akaike, Hirotogu (1973). "Information Theory and an Extension of the Maximum Likelihood Principle." In: *Selected Papers of Hirotugu Akaike*. New York, NY: Springer New York, pp. 199–213.

Akiyama, Kazuhide (Sept. 1991). "Time Variation of Ellipticity of Globular Clusters in the Large Magellanic Cloud." In: *Earth Moon and Planets* 54.3, pp. 203–239. DOI: 10.1007/BF00056321.

Amaro-Seoane, Pau et al. (Feb. 2017). "Laser Interferometer Space Antenna." In: *arXiv e-prints*, arXiv:1702.00786. arXiv: 1702.00786 [astro-ph.IM].

Anderson, Jay et al. (June 2008). "The Acs Survey of Globular Clusters. V. Generating a Comprehensive Star Catalog for each Cluster." In: *Astronomical Journal* 135.6, pp. 2055–2073. DOI: 10.1088/0004-6256/135/6/2055. eprint: 0804.2025.

Anderson, Theodore W and Donald A Darling (1952). "Asymptotic theory of certain" goodness of fit" criteria based on stochastic processes." In: *The annals of mathematical statistics*, pp. 193–212.

Andredakis, Y. C., R. F. Peletier, and M. Balcells (Aug. 1995). "The shape of the luminosity profiles of bulges of spiral galaxies." In: *MNRAS* 275, pp. 874–888. DOI: 10.1093/mnras/275.3.874.

Arca Sedda, Manuel et al. (Nov. 2020). "The missing link in gravitational-wave astronomy: discoveries waiting in the decihertz range." In: *Classical and Quantum Gravity* 37.21, 215011, p. 215011. DOI: 10.1088/1361-6382/abb5c1. arXiv: 1908.11375 [gr-qc].

Arenou, F. et al. (Aug. 2018). "Gaia Data Release 2. Catalogue validation." In: *A&A* 616, A17, A17. DOI: 10.1051/0004-6361/201833234. eprint: 1804.09375.

Aros, Francisco I. et al. (Sept. 2020). "Dynamical modelling of globular clusters: challenges for the robust determination of IMBH candidates." In: *arXiv e-prints*, arXiv:2009.07275. eprint: 2009.07275.

Aros, Francisco I. et al. (Dec. 2021). "Using binaries in globular clusters to catch sight of intermediate-mass black holes." In: *MNRAS* 508.3, pp. 4385–4398. DOI: 10.1093/mnras/stab2872. eprint: 2110.00590.

Ashman, Keith M. and Stephen E. Zepf (2008). *Globular Cluster Systems*.

Askar, Abbas, Manuel Arca Sedda, and Mirek Giersz (Aug. 2018). "MOCCA-SURVEY Database I: Galactic globular clusters harbouring a black hole subsystem." In: *MNRAS* 478.2, pp. 1844–1854.

Askar, Abbas et al. (Jan. 2017). "MOCCA-SURVEY Database - I. Coalescing binary black holes originating from globular clusters." In: *MNRAS* 464.1, pp. L36–L40. DOI: 10.1093/mnrasl/slw177. arXiv: 1608.02520 [astro-ph.HE].

Baes, M. and G. Gentile (Jan. 2011). "Analytical expressions for the deprojected Sérsic model." In: *A&A* 525, A136, A136. DOI: 10.1051/0004-6361/201015716. arXiv: 1009.4713 [astro-ph.CO].

Baes, M. and E. van Hese (Oct. 2011). "Analytical expressions for the deprojected Sérsic model. II. General expressions in terms of the Fox H function." In: *A&A* 534, A69, A69. DOI: 10.1051/0004-6361/201117708. eprint: 1108.1618.

Bahcall, J. N. and R. A. Wolf (Oct. 1976). "Star distribution around a massive black hole in a globular cluster." In: *ApJ* 209, pp. 214–232. DOI: 10.1086/154711.

Bahramian, Arash et al. (July 2020). "The MAVERIC Survey: Chandra/ACIS Catalog of Faint X-ray sources in 38 Galactic globular clusters." In: *arXiv e-prints*, arXiv:2007.04581. eprint: 2007.04581.

Bailyn, Charles D. (Jan. 1995). "Blue Stragglers and Other Stellar Anomalies: Implications for the Dynamics of Globular Clusters." In: *Annual Review of A&A* 33, pp. 133–162. DOI: 10.1146/annurev.aa.33.090195.001025.

Balbinot, Eduardo and Mark Gieles (Feb. 2018). "The devil is in the tails: the role of globular cluster mass evolution on stream properties." In: *MNRAS* 474.2, pp. 2479–2492. DOI: 10.1093/mnras/stx2708. eprint: 1702.02543.

Banik, Nilanjan et al. (Oct. 2021). "Novel constraints on the particle nature of dark matter from stellar streams." In: *JCAP* 2021.10, 043, p. 043. DOI: 10.1088/1475-7516/2021/10/043. eprint: 1911.02663.

Barausse, Enrico and Luciano Rezzolla (2009). "Predicting the Direction of the Final Spin from the Coalescence of Two Black Holes." In: *Astrophysical Journal Letters* 704.1, pp. L40–L44. DOI: 10.1088/0004-637X/704/1/L40. arXiv: 0904.2577 [gr-qc].

Barmby, Pauline et al. (June 2007). "Structural Parameters for Globular Clusters in M31 and Generalizations for the Fundamental Plane." In: *Astronomical Journal* 133.6, pp. 2764–2786. DOI: 10.1086/516777. eprint: 0704.2057.

Bastian, N. et al. (Mar. 2005). "The star cluster population of M 51. II. Age distribution and relations among the derived parameters." In: *A&A* 431.3, pp. 905–924. DOI: 10.1051/0004-6361:20041078. arXiv: astro-ph/0408043 [astro-ph].

Bastian, N. et al. (Dec. 2013). "Early disc accretion as the origin of abundance anomalies in globular clusters." In: *MNRAS* 436.3, pp. 2398–2411. DOI: 10.1093/mnras/stt1745. eprint: 1309.3566.

Bastian, Nate, Ivan Cabrera-Ziri, and Maurizio Salaris (May 2015). "A general abundance problem for all self-enrichment scenarios for the origin of multiple populations in globular clusters." In: *MNRAS* 449.3, pp. 3333–3346. DOI: 10.1093/mnras/stv543. eprint: 1503.03071.

Battaglia, G. et al. (Nov. 2006). "The DART imaging and CaT survey of the Fornax dwarf spheroidal galaxy." In: *A&A* 459, pp. 423–440. DOI: 10.1051/0004-6361:20065720. eprint: astro-ph/0608370.

Baumgardt, H. (Jan. 2017). "N -body modelling of globular clusters: masses, mass-to-light ratios and intermediate-mass black holes." In: *MNRAS* 464.2, pp. 2174–2202. DOI: 10.1093/mnras/stw2488. eprint: 1609.08794.

Baumgardt, H., A. Sollima, and M. Hilker (Nov. 2020). "Absolute V-band magnitudes and mass-to-light ratios of Galactic globular clusters." In: *Publications of the Astron. Soc. of Australia* 37, e046, e046. DOI: 10.1017/pasa.2020.38. eprint: 2009.09611.

Baumgardt, H. and E. Vasiliev (Aug. 2021). "Accurate distances to Galactic globular clusters through a combination of Gaia EDR3, HST, and literature data." In: *MNRAS* 505.4, pp. 5957–5977. DOI: 10.1093/mnras/stab1474. eprint: 2105.09526.

Baumgardt, H. et al. (July 2009). "The velocity dispersion and mass-to-light ratio of the remote halo globular cluster NGC2419." In: *MNRAS* 396.4, pp. 2051–2060. DOI: 10.1111/j.1365-2966.2009.14932.x. arXiv: 0904.3329 [astro-ph.GA].

Baumgardt, H. et al. (Feb. 2019). "Mean proper motions, space orbits, and velocity dispersion profiles of Galactic globular clusters derived from Gaia DR2 data." In: *MNRAS* 482.4, pp. 5138–5155. DOI: 10.1093/mnras/sty2997. eprint: 1811.01507.

Baumgardt, Holger and Junichiro Makino (Mar. 2003). "Dynamical evolution of star clusters in tidal fields." In: *MNRAS* 340.1, pp. 227–246. DOI: 10.1046/j.1365-8711.2003.06286.x. arXiv: astro-ph/0211471 [astro-ph].

Bedin, Luigi R. et al. (May 2008). "Reaching the End of the White Dwarf Cooling Sequence in NGC 6791." In: *Astrophysical Journal* 678.2, pp. 1279–1291. DOI: 10.1086/529370. arXiv: 0801.1346 [astro-ph].

Bekki, K. and K. C. Freeman (Dec. 2003a). "Formation of ω Centauri from an ancient nucleated dwarf galaxy in the young Galactic disc." In: *MNRAS* 346.2, pp. L11–L15. DOI: 10.1046/j.1365-2966.2003.07275.x. eprint: astro-ph/0310348.

Bekki, K. and K. C. Freeman (Dec. 2003b). "Formation of ω Centauri from an ancient nucleated dwarf galaxy in the young Galactic disc." In: *MNRAS* 346.2, pp. L11–L15. DOI: 10.1046/j.1365-2966.2003.07275.x. arXiv: astro-ph/0310348 [astro-ph].

Bekki, K. et al. (Oct. 2002). "Globular cluster formation from gravitational tidal effects of merging and interacting galaxies." In: *MNRAS* 335.4, pp. 1176–1192. DOI: 10.1046/j.1365-8711.2002.05708.x. arXiv: astro-ph/0206008 [astro-ph].

Bekki, Kenji (Apr. 2011). "Secondary star formation within massive star clusters: origin of multiple stellar populations in globular clusters." In: *MNRAS*

412.4, pp. 2241–2259. DOI: 10.1111/j.1365-2966.2010.18047.x. eprint: 1011.5956.

Bekki, Kenji and David Yong (Jan. 2012). "On the origin of the stellar halo and multiple stellar populations in the globular cluster NGC 1851." In: *MNRAS* 419.3, pp. 2063–2076. DOI: 10.1111/j.1365-2966.2011.19856.x. arXiv: 1109.4463 [astro-ph.GA].

Bellini, A. et al. (Dec. 2014). "Hubble Space Telescope Proper Motion (HST-PROMO) Catalogs of Galactic Globular Clusters. I. Sample Selection, Data Reduction, and NGC 7078 Results." In: *Astrophysical Journal* 797.2, 115, p. 115. DOI: 10.1088/0004-637X/797/2/115. eprint: 1410.5820.

Bellini, A. et al. (Aug. 2017). "The State-of-the-art HST Astro-photometric Analysis of the Core of ω Centauri. III. The Main Sequence's Multiple Populations Galore." In: *ApJ* 844.2, 164, p. 164. DOI: 10.3847/1538-4357/aa7b7e. eprint: 1706.07063.

Bellini, Andrea et al. (Jan. 2018). "The HST Large Programme on ω Centauri. II. Internal Kinematics." In: *Astrophysical Journal* 853.1, 86, p. 86. DOI: 10.3847/1538-4357/aaa3ec. arXiv: 1801.01504 [astro-ph.GA].

Bellm, Eric C. et al. (Jan. 2019). "The Zwicky Transient Facility: System Overview, Performance, and First Results." In: *Publications of the ASP* 131.995, p. 018002. DOI: 10.1088/1538-3873/aaecbe. arXiv: 1902.01932 [astro-ph.IM].

Benvenuto, O. G. and M. A. De Vito (Sept. 2005). "The formation of helium white dwarfs in close binary systems - II." In: *MNRAS* 362.3, pp. 891–905. DOI: 10.1111/j.1365-2966.2005.09315.x.

Bertin, G. and A. L. Varri (Dec. 2008a). "The Construction of Nonspherical Models of Quasi-Relaxed Stellar Systems." In: *ApJ* 689.2, pp. 1005–1019. DOI: 10.1086/592684. eprint: 0808.2432.

Bertin, G. and A. L. Varri (Dec. 2008b). "The Construction of Nonspherical Models of Quasi-Relaxed Stellar Systems." In: *ApJ* 689.2, pp. 1005–1019. DOI: 10.1086/592684. arXiv: 0808.2432 [astro-ph].

Bhardwaj, M. et al. (Apr. 2021). "A Nearby Repeating Fast Radio Burst in the Direction of M81." In: *Astrophysical Journal Letters* 910.2, L18, p. L18. DOI: 10.3847/2041-8213/abeaa6. arXiv: 2103.01295 [astro-ph.HE].

Bhattacharya, D. and E. P. J. van den Heuvel (Jan. 1991). "Formation and evolution of binary and millisecond radio pulsars." In: *Physics Reports* 203.1-2, pp. 1–124. DOI: 10.1016/0370-1573(91)90064-S.

Bianchini, P., R. Ibata, and B. Famaey (Dec. 2019). "Exploring the Outskirts of Globular Clusters: The Peculiar Kinematics of NGC 3201." In: *Astrophysical Journal Letters* 887.1, L12, p. L12. DOI: 10.3847/2041-8213/ab58d1. eprint: 1912.02195.

Bianchini, P. et al. (June 2016a). "A novel look at energy equipartition in globular clusters." In: *MNRAS* 458.4, pp. 3644–3654. DOI: 10.1093/mnras/stw552. arXiv: 1603.00878 [astro-ph.GA].

Bianchini, P. et al. (Mar. 2016b). "The Effect of Unresolved Binaries on Globular Cluster Proper-motion Dispersion Profiles." In: *Astrophysical Journal Letters* 820.1, L22, p. L22. DOI: 10.3847/2041-8205/820/1/L22. eprint: 1603.02280.

Bianchini, P. et al. (Dec. 2018). "The internal rotation of globular clusters revealed by Gaia DR2." In: *MNRAS* 481.2, pp. 2125–2139. DOI: 10.1093/mnras/sty2365. eprint: 1806.02580.

Binney, J. and G. A. Mamon (July 1982). "M/L and velocity anisotropy from observations of spherical galaxies, of must M 87 have a massive black hole ?" In: *MNRAS* 200, pp. 361–375. DOI: 10.1093/mnras/200.2.361.

Binney, James and Scott Tremaine (2008). *Galactic Dynamics: Second Edition*.

Böker, Torsten (Jan. 2008). "Are Globular Clusters the Remnant Nuclei of Progenitor Disk Galaxies?" In: *ApJ Letters* 672.2, p. L111. DOI: 10.1086/527033. arXiv: 0711.4542 [astro-ph].

Böker, Torsten et al. (Jan. 2004). "A Hubble Space Telescope Census of Nuclear Star Clusters in Late-Type Spiral Galaxies. II. Cluster Sizes and Structural Parameter Correlations." In: *Astronomical Journal* 127.1, pp. 105–118. DOI: 10.1086/380231. arXiv: astro-ph/0309761 [astro-ph].

Boldrini, Pierre and Jo Bovy (June 2021). "No globular cluster progenitors in Milky Way satellite galaxies." In: *arXiv e-prints*, arXiv:2106.09419. eprint: 2106.09419.

Boldrini, Pierre, Roya Mohayaee, and Joseph Silk (Mar. 2020). "Embedding globular clusters in dark matter minihaloes solves the cusp-core and timing problems in the Fornax dwarf galaxy." In: *MNRAS* 492.3, pp. 3169–3178. DOI: 10.1093/mnras/staa011. arXiv: 1909.07404 [astro-ph.GA].

Boldrini, Pierre and Eduardo Vitral (July 2021). "Absence of obvious tidal tails around the globular cluster NGC 6397." In: *MNRAS*. DOI: 10.1093/mnras/stab2035.

Bonatto, Charles et al. (Feb. 2019). "J-PLUS: A wide-field multi-band study of the M 15 globular cluster. Evidence of multiple stellar populations in the RGB." In: *A&A* 622, A179, A179. DOI: 10.1051/0004-6361/201732441. eprint: 1804.03966.

Boyles, J. et al. (Nov. 2011). "Young Radio Pulsars in Galactic Globular Clusters." In: *Astrophysical Journal* 742.1, 51, p. 51. DOI: 10.1088/0004-637X/742/1/51. arXiv: 1108.4402 [astro-ph.SR].

Breen, P. G. and D. C. Heggie (July 2013). "Dynamical evolution of black hole subsystems in idealized star clusters." In: *MNRAS* 432, pp. 2779–2797.

Breivik, Katelyn et al. (July 2020). "COSMIC Variance in Binary Population Synthesis." In: *Astrophysical Journal* 898.1, 71, p. 71. DOI: 10.3847/1538-4357/ab9d85. arXiv: 1911.00903 [astro-ph.HE].

Bressan, Alessandro et al. (Nov. 2012). "PARSEC: stellar tracks and isochrones with the PAdova and TRieste Stellar Evolution Code." In: *MNRAS* 427.1, pp. 127–145. DOI: 10.1111/j.1365-2966.2012.21948.x. eprint: 1208.4498.

Bromm, Volker and Cathie J. Clarke (Feb. 2002). "The Formation of the First Globular Clusters in Dwarf Galaxies before the Epoch of Reionization." In: *ApJ Letters* 566.1, pp. L1–L4. DOI: 10.1086/339440. arXiv: astro-ph/0201066 [astro-ph].

Burnham, K. P. and D. R. Anderson (2002). *A Practival Information-Theoretic Approach*. 2nd ed. New York: Springer.

Calcaferro, Leila M., Leandro G. Althaus, and Alejandro H. Córsico (June 2018). "The coolest extremely low-mass white dwarfs." In: *A&A* 614, A49, A49. DOI: 10.1051/0004-6361/201732551. eprint: 1802.06753.

Caon, N., M. Capaccioli, and M. D'Onofrio (Dec. 1993). "On the Shape of the Light Profiles of Early Type Galaxies." In: *MNRAS* 265, pp. 1013–1021.

Carlberg, Raymond G. and Carl J. Grillmair (Mar. 2022). "The Dark Matter Halo of M54." In: *arXiv e-prints*, arXiv:2203.01365. eprint: 2203.01365.

Carretta, E. et al. (Oct. 2009a). "Na-O anticorrelation and HB. VII. The chemical composition of first and second-generation stars in 15 globular clusters from GIRAFFE spectra." In: *A&A* 505.1, pp. 117–138. DOI: 10.1051/0004-6361/200912096. eprint: 0909.2938.

Carretta, E. et al. (2009b). "Na-O anticorrelation and HB. VIII. Proton-capture elements and metallicities in 17 globular clusters from UVES spectra." In: *A&A* 505.1, pp. 139–155. DOI: 10.1051/0004-6361/200912097. eprint: 0909.2941.

Chandrasekhar, S. (July 1931). "The Maximum Mass of Ideal White Dwarfs." In: *ApJ* 74, p. 81. DOI: 10.1086/143324.

Chandrasekhar, S. (1942). *Principles of Stellar Dynamics*. University of Chicago Press.

Chandrasekhar, S. (Mar. 1943). "Dynamical Friction. I. General Considerations: the Coefficient of Dynamical Friction." In: *Astrophysical Journal* 97, pp. 255–262.

Chatterjee, Sourav et al. (Mar. 2013). "Understanding the dynamical state of globular clusters: core-collapsed versus non-core-collapsed." In: *MNRAS* 429.4, pp. 2881–2893. DOI: 10.1093/mnras/sts464. eprint: 1207.3063.

Chen, Yang et al. (Nov. 2014). "Improving PARSEC models for very low mass stars." In: *MNRAS* 444.3, pp. 2525–2543. DOI: 10.1093/mnras/stu1605. eprint: 1409.0322.

Chen, Yang et al. (Sept. 2015). "PARSEC evolutionary tracks of massive stars up to 350 $M_\odot$ at metallicities $0.0001 \leqslant Z \leqslant 0.04$." In: *MNRAS* 452.1, pp. 1068–1080. DOI: 10.1093/mnras/stv1281. eprint: 1506.01681.

Chilingarian, Igor V. et al. (Aug. 2018). "A Population of Bona Fide Intermediate-mass Black Holes Identified as Low-luminosity Active Galactic Nuclei." In: *Astrophysical Journal* 863.1, 1, p. 1. DOI: 10.3847/1538-4357/aad184. arXiv: 1805.01467 [astro-ph.GA].

Ciotti, L. and G. Bertin (Dec. 1999). "Analytical properties of the $R^{1/m}$ law." In: *A&A* 352, pp. 447–451. eprint: astro-ph/9911078.

Ciotti, Luca, Antonio Mancino, and Silvia Pellegrini (Dec. 2019). "A new class of galaxy models with a central BH - I. The spherical case." In: *MNRAS* 490.2, pp. 2656–2667. DOI: 10.1093/mnras/stz2636. eprint: 1909.09639.

Cohen, J. G. (Feb. 1976). "Mass loss in globular-cluster red giants." In: *ApJ Letters* 203, pp. L127–L129. DOI: 10.1086/182035.

Cohen, Judith G., John P. Blakeslee, and Anton Ryzhov (Mar. 1998). "The Ages and Abundances of a Large Sample of M87 Globular Clusters." In: *Astrophysical Journal* 496.2, pp. 808–826. DOI: 10.1086/305429. eprint: astro-ph/9709192.

Cohn, H. (Dec. 1980). "Late core collapse in star clusters and the gravothermal instability." In: *Astrophysical Journal* 242, pp. 765–771. DOI: 10.1086/158511.

Conroy, Charlie, Abraham Loeb, and David N. Spergel (Nov. 2011). "Evidence against Dark Matter Halos Surrounding the Globular Clusters MGC1 and NGC 2419." In: *Astrophysical Journal* 741.2, 72, p. 72. DOI: 10.1088/0004-637X/741/2/72. arXiv: 1010.5783 [astro-ph.GA].

Cordoni, G. et al. (May 2019). "Three-Component Kinematics of Multiple Stellar Populations in Globular Clusters with Gaia and VLT." In: *arXiv e-prints*, arXiv:1905.09908. eprint: 1905.09908.

Cordoni, G. et al. (Jan. 2020). "Three-component Kinematics of Multiple Stellar Populations in Globular Clusters with Gaia and VLT." In: *Astrophysical Journal* 889.1, 18, p. 18. DOI: 10.3847/1538-4357/ab5aee. arXiv: 1905.09908 [astro-ph.SR].

Croton, D. J. et al. (Jan. 2006). "The many lives of active galactic nuclei: cooling flows, black holes and the luminosities and colours of galaxies." In: *MNRAS* 365, pp. 11–28. DOI: 10.1111/j.1365-2966.2005.09675.x. eprint: astro-ph/0508046.

Cummings, Jeffrey D. et al. (Oct. 2018). "The White Dwarf Initial-Final Mass Relation for Progenitor Stars from 0.85 to 7.5 $M_{\odot}$." In: *Astrophysical Journal* 866.1, 21, p. 21. DOI: 10.3847/1538-4357/aadfd6. arXiv: 1809.01673 [astro-ph.SR].

D'Antona, Francesca et al. (Oct. 2014). "Pre-main-sequence accretion and the formation of multiple populations in globular clusters." In: *MNRAS* 443.4, pp. 3302–3308. DOI: 10.1093/mnras/stu1380. eprint: 1407.2424.

D'Ercole, Annibale et al. (Dec. 2008). "Formation and dynamical evolution of multiple stellar generations in globular clusters." In: *MNRAS* 391.2, pp. 825–843. DOI: 10.1111/j.1365-2966.2008.13915.x. eprint: 0809.1438.

Dalessandro, E. et al. (Sept. 2018). "The Unexpected Kinematics of Multiple Populations in NGC 6362: Do Binaries Play a Role?" In: *ApJ* 864.1, 33, p. 33. DOI: 10.3847/1538-4357/aad4b3. eprint: 1807.07918.

Dalessandro, Emanuele et al. (Oct. 2019). "A Family Picture: Tracing the Dynamical Path of the Structural Properties of Multiple Populations in Globular Clusters." In: *ApJ Letters* 884.1, L24, p. L24. DOI: 10.3847/2041-8213/ab45f7. eprint: 1910.00613.

Davies, Melvyn B. (Jan. 2015). "Formation Channels for Blue Straggler Stars." In: *Astrophysics and Space Science Library*. Ed. by Henri M. J. Boffin, Giovanni Carraro, and Giacomo Beccari. Vol. 413. Astrophysics and Space Science Library, p. 203. DOI: 10.1007/978-3-662-44434-4_9. eprint: 1406.3477.

Decressin, T. et al. (Mar. 2007). "Fast rotating massive stars and the origin of the abundance patterns in galactic globular clusters." In: *A&A* 464.3, pp. 1029–1044. DOI: 10.1051/0004-6361:20066013. eprint: astro-ph/0611379.

Di Carlo, Ugo N. et al. (Sept. 2020). "Binary black holes in the pair instability mass gap." In: *MNRAS* 497.1, pp. 1043–1049. DOI: 10.1093/mnras/staa1997. arXiv: 1911.01434 [astro-ph.HE].

Djorgovski, S. and I. R. King (June 1986). "A Preliminary Survey of Collapsed Cores in Globular Clusters." In: *Astrophysical Journal Letters* 305, p. L61. DOI: 10.1086/184685.

Douchin, F. and P. Haensel (Dec. 2001). "A unified equation of state of dense matter and neutron star structure." In: *A&A* 380, pp. 151–167. DOI: 10.1051/0004-6361:20011402. eprint: astro-ph/0111092.

Einasto, J. (1965). In: *Trudy Inst. Astroz. Alma-Ata* 51, p. 87.

Emsellem, Eric and Glenn van de Ven (Feb. 2008). "Formation of Central Massive Objects via Tidal Compression." In: *ApJ* 674.2, pp. 653–659. DOI: 10.1086/524720. eprint: 0710.3161.

Erkal, Denis and Vasily Belokurov (Dec. 2015). "Properties of dark subhaloes from gaps in tidal streams." In: *MNRAS* 454.4, pp. 3542–3558. DOI: 10.1093/mnras/stv2122. eprint: 1507.05625.

Erkal, Denis, Sergey E. Koposov, and Vasily Belokurov (Sept. 2017). "A sharper view of Pal 5's tails: discovery of stream perturbations with a novel non-parametric technique." In: *MNRAS* 470.1, pp. 60–84. DOI: 10.1093/mnras/stx1208. eprint: 1609.01282.

Errani, Raphaël et al. (Mar. 2022). "The Pristine survey XVIII: C-19: Tidal debris of a dark matter-dominated globular cluster?" In: *arXiv e-prints*, arXiv:2203.02513. eprint: 2203.02513.

Event Horizon Telescope Collaboration et al. (Apr. 2019). "First M87 Event Horizon Telescope Results. I. The Shadow of the Supermassive Black Hole." In: *Astrophysical Journal Letters* 875.1, L1, p. L1. DOI: 10.3847/2041-8213/ab0ec7. eprint: 1906.11238.

Fardal, Mark A. et al. (Feb. 2021). "Mapping Gaia Parallax Systematic Errors over the Sky with Faint Milky Way Stars." In: *Astronomical Journa* 161.2, 58, p. 58. DOI: 10.3847/1538-3881/abcccf. eprint: 2011.10553.

Farmer, R. et al. (Dec. 2019). "Mind the Gap: The Location of the Lower Edge of the Pair-instability Supernova Black Hole Mass Gap." In: *Astrophysical Journal* 887.1, 53, p. 53. DOI: 10.3847/1538-4357/ab518b. arXiv: 1910.12874 [astro-ph.SR].

Feng, Lei et al. (Apr. 2012). "Search for dark matter signals with Fermi-LAT observation of globular clusters NGC 6388 and M 15." In: *Journal of Cosmology and Astroparticle Physics* 2012.4, 030, p. 030. DOI: 10.1088/1475-7516/2012/04/030. arXiv: 1112.2438 [astro-ph.HE].

Franklin, B. and J. Sparks (1839). *The Works of Benjamin Franklin: Containing Several Political and Historical Tracts Not Included in Any Former Ed., and Many Letters Official and Private, Not Hitherto Published; with Notes and a Life of the Author*. The Works of Benjamin Franklin: Containing Several Political and Historical Tracts Not Included in Any Former Ed., and Many Letters Official and Private, Not Hitherto Published; with Notes and a Life of the Author v. 9. Hillard, Gray. URL: https://books.google.fr/books?id=uu8_AAAAYAAJ.

Freeman, K. C. (Jan. 1993). "Globular Clusters and Nucleated Dwarf Ellipticals." In: *The Globular Cluster-Galaxy Connection*. Ed. by Graeme H. Smith and Jean P. Brodie. Vol. 48. Astronomical Society of the Pacific Conference Series, p. 608.

Fregeau, John M. and Frederic A. Rasio (Apr. 2007). "Monte Carlo Simulations of Globular Cluster Evolution. IV. Direct Integration of Strong Interactions." In: *Astrophysical Journal* 658.2, pp. 1047–1061. DOI: 10.1086/511809. eprint: astro-ph/0608261.

Fryer, Chris L. (Sept. 1999). "Mass Limits For Black Hole Formation." In: *ApJ* 522.1, pp. 413–418. DOI: 10.1086/307647. eprint: astro-ph/9902315.

Fusi Pecci, F. et al. (Mar. 1993). "On the Effects of Cluster Density and Concentration on the Horizontal Branch Morphology: The Origin of the Blue Tails." In: *Astronomical Journal* 105, p. 1145. DOI: 10.1086/116500.

Gaia Collaboration et al. (Nov. 2016). "The Gaia mission." In: *A&A* 595, A1, A1. DOI: 10.1051/0004-6361/201629272. arXiv: 1609.04153 [astro-ph.IM].

Gaia Collaboration et al. (Aug. 2018a). "Gaia Data Release 2. Kinematics of globular clusters and dwarf galaxies around the Milky Way." In: *A&A* 616, A12, A12. DOI: 10.1051/0004-6361/201832698. eprint: 1804.09381.

Gaia Collaboration et al. (Aug. 2018b). "Gaia Data Release 2. Kinematics of globular clusters and dwarf galaxies around the Milky Way." In: *A&A* 616, A12, A12. DOI: 10.1051/0004-6361/201832698. eprint: 1804.09381.

Gaia Collaboration et al. (Aug. 2018c). "Gaia Data Release 2. Observational Hertzsprung-Russell diagrams." In: *A&A* 616, A10, A10. DOI: 10.1051/0004-6361/201832843. eprint: 1804.09378.

Gaia Collaboration et al. (Aug. 2018d). "Gaia Data Release 2. The celestial reference frame (Gaia-CRF2)." In: *A&A* 616, A14, A14. DOI: 10.1051/0004-6361/201832916. eprint: 1804.09377.

Gaia Collaboration et al. (May 2021). "Gaia Early Data Release 3. Summary of the contents and survey properties." In: *A&A* 649, A1, A1. DOI: 10.1051/0004-6361/202039657. eprint: 2012.01533.

Galilei, G. and O. GRASSI (1618). *The Assayer, Etc. (Translated ... by Stillman Drake.)*. URL: https://books.google.fr/books?id=uSctMwEACAAJ.

Gardner, Jonathan P. et al. (Apr. 2006). "The James Webb Space Telescope." In: *Space Science Reviews* 123.4, pp. 485–606. DOI: 10.1007/s11214-006-8315-7. eprint: astro-ph/0606175.

Gebhardt, Karl, R. M. Rich, and Luis C. Ho (Oct. 2002). "A 20,000 M_{solar} Black Hole in the Stellar Cluster G1." In: *ApJ Letters* 578.1, pp. L41–L45. DOI: 10.1086/342980. arXiv: astro-ph/0209313 [astro-ph].

Gebhardt, Karl, R. M. Rich, and Luis C. Ho (Dec. 2005). "An Intermediate-Mass Black Hole in the Globular Cluster G1: Improved Significance from New Keck and Hubble Space Telescope Observations." In: *ApJ* 634.2, pp. 1093–1102. DOI: 10.1086/497023. arXiv: astro-ph/0508251 [astro-ph].

Gerosa, Davide and Maya Fishbach (July 2021). "Hierarchical mergers of stellar-mass black holes and their gravitational-wave signatures." In: *Nature Astronomy* 5, pp. 749–760. DOI: 10.1038/s41550-021-01398-w. arXiv: 2105.03439 [astro-ph.HE].

Gerosa, Davide and Michael Kesden (June 2016). "precession: Dynamics of spinning black-hole binaries with python." In: *Physical Review D* 93.12, 124066, p. 124066. DOI: 10.1103/PhysRevD.93.124066. arXiv: 1605.01067 [astro-ph.HE].

Gieles, Mark et al. (Feb. 2021). "A supra-massive population of stellar-mass black holes in the globular cluster Palomar 5." In: *arXiv e-prints*, arXiv:2102.11348. eprint: 2102.11348.

Giersz, Mirek et al. (Dec. 2015). "MOCCA code for star cluster simulations - IV. A new scenario for intermediate mass black hole formation in globular clusters." In: *MNRAS* 454.3, pp. 3150–3165. DOI: 10.1093/mnras/stv2162. eprint: 1506.05234.

Giesers, Benjamin et al. (Mar. 2018). "A detached stellar-mass black hole candidate in the globular cluster NGC 3201." In: *MNRAS* 475.1, pp. L15–L19. DOI: 10.1093/mnrasl/slx203. eprint: 1801.05642.

Giesers, Benjamin et al. (Dec. 2019). "A stellar census in globular clusters with MUSE: Binaries in NGC 3201." In: *A&A* 632, A3, A3. DOI: 10.1051/0004-6361/201936203. arXiv: 1909.04050 [astro-ph.SR].

Goldsbury, Ryan, Jeremy Heyl, and Harvey Richer (Nov. 2013). "Quantifying Mass Segregation and New Core Radii for 54 Milky Way Globular Clusters." In: *Astrophysical Journal* 778.1, 57, p. 57. DOI: 10.1088/0004-637X/778/1/57. eprint: 1308.3706.

Goldsbury, Ryan et al. (Dec. 2010). "The ACS Survey of Galactic Globular Clusters. X. New Determinations of Centers for 65 Clusters." In: *Astronomical Journal* 140.6, pp. 1830–1837. DOI: 10.1088/0004-6256/140/6/1830. eprint: 1008.2755.

González, Elena et al. (Feb. 2021). "Intermediate-mass Black Holes from High Massive-star Binary Fractions in Young Star Clusters." In: *Astrophysical Journal Letters* 908.2, L29, p. L29. DOI: 10.3847/2041-8213/abdf5b. eprint: 2012.10497.

Goodman, J. (Jan. 1993). "The Theory of Pre Core Collapse and POST Core Collapse Evolution and Gravothermal Oscillations." In: *Structure and Dynamics of Globular Clusters*. Ed. by S. G. Djorgovski and Georges Meylan. Vol. 50. Astronomical Society of the Pacific Conference Series, p. 87.

Graham, Alister W. and Simon P. Driver (Jan. 2005). "A Concise Reference to (Projected) Sérsic $R^{1/n}$ Quantities, Including Concentration, Profile Slopes, Petrosian Indices, and Kron Magnitudes." In: *Publications of the Astron. Soc. of Australia* 22.2, pp. 118–127. DOI: 10.1071/AS05001. eprint: astro-ph/0503176.

Graham, Alister W. and Lee R. Spitler (Aug. 2009). "Quantifying the coexistence of massive black holes and dense nuclear star clusters." In: *MNRAS* 397.4, pp. 2148–2162. DOI: 10.1111/j.1365-2966.2009.15118.x. eprint: 0907.5250.

Gratton, Raffaele et al. (Nov. 2019). "What is a globular cluster? An observational perspective." In: *A&Ar* 27.1, 8, p. 8. DOI: 10.1007/s00159-019-0119-3. eprint: 1911.02835.

Greene, Jenny E., Jay Strader, and Luis C. Ho (Aug. 2020). "Intermediate-Mass Black Holes." In: *Annual Review of A&A* 58, pp. 257–312. DOI: 10.1146/annurev-astro-032620-021835. arXiv: 1911.09678 [astro-ph.GA].

Grillmair, Carl J. et al. (June 1995). "Globular Clusters with Tidal Tails: Deep Two-Color Star Counts." In: *Astronomical Journal* 109, p. 2553. DOI: 10.1086/117470. arXiv: astro-ph/9502039 [astro-ph].

Haehnelt, Martin G. and Martin J. Rees (July 1993). "The formation of nuclei in newly formed galaxies and the evolution of the quasar population." In: *MNRAS* 263.1, pp. 168–178. DOI: 10.1093/mnras/263.1.168.

Haiman, Zoltán (2013). "The Formation of the First Massive Black Holes." In: *The First Galaxies*. Ed. by Tommy Wiklind, Bahram Mobasher, and Volker Bromm. Vol. 396. Astrophysics and Space Science Library, p. 293. DOI: 10.1007/978-3-642-32362-1_6.

Harris, William E. (1996). "A Catalog of Parameters for Globular Clusters in the Milky Way." In: *Astronomical Journal* 112, p. 1487. DOI: 10.1086/118116.

Harris, William E. (July 2009). "Globular Cluster Systems in Giant Ellipticals: The Mass/Metallicity Relation." In: *Astrophysical Journal* 699.1, pp. 254–280. DOI: 10.1088/0004-637X/699/1/254. eprint: 0904.4208.

Harris, William E. (Dec. 2010). "A New Catalog of Globular Clusters in the Milky Way." In: *arXiv e-prints*, arXiv:1012.3224. eprint: 1012.3224.

Harwit, Martin (1988). *Astrophysical Concepts*.

Hawking, Stephen (Jan. 1971). "Gravitationally collapsed objects of very low mass." In: *MNRAS* 152, p. 75. DOI: 10.1093/mnras/152.1.75.

Haywood, M. et al. (Aug. 2018). "In Disguise or Out of Reach: First Clues about In Situ and Accreted Stars in the Stellar Halo of the Milky Way from Gaia

DR2." In: *ApJ* 863.2, 113, p. 113. DOI: 10.3847/1538-4357/aad235. eprint: 1805.02617.

Heggie, D. C. (Dec. 1975). "Binary evolution in stellar dynamics." In: *MNRAS* 173, pp. 729–787. DOI: 10.1093/mnras/173.3.729.

Heggie, D. C. (Aug. 1979). "A theory of core collapse in clusters." In: *MNRAS* 76.3, pp. 525–554. DOI: 10.1093/mnras/188.3.525.

Heggie, D. C. and P. Hut (Jan. 1996). "Dark Matter in Globular Clusters." In: *Dynamical Evolution of Star Clusters: Confrontation of Theory and Observations*. Ed. by Piet Hut and Junichiro Makino. Vol. 174. IAU Symposium, p. 303. eprint: astro-ph/9511115.

Helmi, Amina (Aug. 2020). "Streams, Substructures, and the Early History of the Milky Way." In: *Annual Review of A&A* 58, pp. 205–256. DOI: 10.1146/annurev-astro-032620-021917. eprint: 2002.04340.

Helmi, Amina and Simon D. M. White (Aug. 1999). "Building up the stellar halo of the Galaxy." In: *MNRAS* 307.3, pp. 495–517. DOI: 10.1046/j.1365-8711.1999.02616.x. eprint: astro-ph/9901102.

Helmi, Amina et al. (Nov. 1999). "Debris streams in the solar neighbourhood as relicts from the formation of the Milky Way." In: *Nature* 402.6757, pp. 53–55. DOI: 10.1038/46980. eprint: astro-ph/9911041.

Helmi, Amina et al. (2018). "The merger that led to the formation of the Milky Way's inner stellar halo and thick disk." In: *Nature* 563.7729, pp. 85–88. DOI: 10.1038/s41586-018-0625-x. eprint: 1806.06038.

Hénault-Brunet, V. et al. (2015). "Multiple populations in globular clusters: the distinct kinematic imprints of different formation scenarios." In: *MNRAS* 450.2, pp. 1164–1198. DOI: 10.1093/mnras/stv675. eprint: 1503.07532.

Hénon, M. (Feb. 1961). "Sur l'évolution dynamique des amas globulaires." In: *Annales d'Astrophysique* 24, p. 369.

Hernquist, L. (June 1990). "An analytical model for spherical galaxies and bulges." In: *Astrophysical Journal* 356, pp. 359–364.

Herschel, William (Jan. 1786). "Catalogue of One Thousand New Nebulae and Clusters of Stars. By William Herschel, LL.D. F. R. S." In: *Philosophical Transactions of the Royal Society of London Series I* 76, pp. 457–499.

Hertzsprung, Ejnar (Jan. 1911). "Ueber die Verwendung photographischer effektiver Wellenlaengen zur Bestimmung von Farbenaequivalenten." In: *Publikationen des Astrophysikalischen Observatoriums zu Potsdam* 63.

Heyl, J. S. et al. (Dec. 2012). "Deep Hubble Space Telescope Imaging in NGC 6397: Stellar Dynamics." In: *Astrophysical Journal* 761.1, 51, p. 51. DOI: 10.1088/0004-637X/761/1/51. eprint: 1210.0826.

Hills, J. G. (1975). "Encounters between binary and single stars and their effect on the dynamical evolution of stellar systems." In: *Astronomical Journal* 80, pp. 809–825. DOI: 10.1086/111815.

Hills, J. G. and C. A. Day (Feb. 1976). "Stellar Collisions in Globular Clusters." In: *Astrophysics Letters* 17, p. 87.

Hopkins, Philip F. et al. (Mar. 2006). "A Unified, Merger-driven Model of the Origin of Starbursts, Quasars, the Cosmic X-Ray Background, Supermassive Black Holes, and Galaxy Spheroids." In: *Astrophysical Journals* 163.1, pp. 1–49. DOI: 10.1086/499298. eprint: astro-ph/0506398.

Hoyle, F. and William A. Fowler (Feb. 1963). "Nature of Strong Radio Sources." In: *Nature* 197.4867, pp. 533–535. DOI: 10.1038/197533a0.

Hurst, Travis J. et al. (May 2015). "Indirect probes of dark matter and globular cluster properties from dark matter annihilation within the coolest white dwarfs." In: *Physical Review D* 91.10, 103514, p. 103514. DOI: 10.1103/PhysRevD.91.103514. arXiv: 1410.3925 [astro-ph.CO].

Hurvich, Clifford M. and Chih-Ling Tsai (1989). "Regression and time series model selection in small samples." In: *Biometrika* 76.2, pp. 297–307.

Husser, Tim-Oliver et al. (Apr. 2016). "MUSE crowded field 3D spectroscopy of over 12 000 stars in the globular cluster NGC 6397. I. The first comprehensive HRD of a globular cluster." In: *A&A* 588, A148, A148. DOI: 10.1051/0004-6361/201526949. eprint: 1602.01649.

Hut, P. (Sept. 1983). "Binaries as a heat source in stellar dynamics - Release of binding energy." In: *ApJ Letters* 272, pp. L29–L33. DOI: 10.1086/184111.

Hut, P. and J. N. Bahcall (May 1983). "Binary-single star scattering. I - Numerical experiments for equal masses." In: *ApJ* 268, pp. 319–341. DOI: 10.1086/160956.

Ibata, R. A., G. Gilmore, and M. J. Irwin (July 1994). "A dwarf satellite galaxy in Sagittarius." In: *Nature* 370.6486, pp. 194–196. DOI: 10.1038/370194a0.

Ibata, R. et al. (Feb. 2013). "Do globular clusters possess dark matter haloes? A case study in NGC 2419." In: *MNRAS* 428.4, pp. 3648–3659. DOI: 10.1093/mnras/sts302. eprint: 1210.7787.

Ibata, Rodrigo A. et al. (Apr. 2019). "Identification of the long stellar stream of the prototypical massive globular cluster ω Centauri." In: *Nature Astronomy* 3, pp. 667–672. DOI: 10.1038/s41550-019-0751-x. eprint: 1902.09544.

Ibata, Rodrigo et al. (June 2021). "Charting the Galactic Acceleration Field. I. A Search for Stellar Streams with Gaia DR2 and EDR3 with Follow-up from ESPaDOnS and UVES." In: *Astrophysical Journal* 914.2, 123, p. 123. DOI: 10.3847/1538-4357/abfcc2. eprint: 2012.05245.

Iben I., Jr. (May 1986). "On the Evolution of Binary Components Which First Fill Their Roche Lobes after the Exhaustion of Central Helium." In: *ApJ* 304, p. 201. DOI: 10.1086/164154.

Iben I., Jr. and A. Renzini (Jan. 1983). "Asymptotic giant branch evolution and beyond." In: *Annual Review of A&A* 21, pp. 271–342. DOI: 10.1146/annurev.aa.21.090183.001415.

Ivanova, N. et al. (July 2010). "Formation of Black Hole X-ray Binaries in Globular Clusters." In: *Astrophysical Journal* 717.2, pp. 948–957. DOI: 10.1088/0004-637X/717/2/948. arXiv: 1001.1767 [astro-ph.HE].

Jaffe, W. (Mar. 1983). "A simple model for the distribution of light in spherical galaxies." In: *MNRAS* 202, pp. 995–999. DOI: 10.1093/mnras/202.4.995.

Jain, Rashi et al. (Mar. 2020). "NGC 6397: The metallicity trend along the isochrone revisited." In: *A&A* 635, A161, A161. DOI: 10.1051/0004-6361/201936952. arXiv: 2002.07702 [astro-ph.SR].

Jeans, J.H. (1942). *Physics and Philosophy*. Dover classics of science and mathematics. Dover Publications. ISBN: 9780486119175. URL: https://books.google.fr/books?id=3STDAgAAQBAJ.

Joshi, Kriten J., Frederic A. Rasio, and Simon Portegies Zwart (Sept. 2000). "Monte Carlo Simulations of Globular Cluster Evolution. I. Method and Test Calculations." In: *Astrophysical Journal* 540.2, pp. 969–982. DOI: 10.1086/309350. arXiv: astro-ph/9909115 [astro-ph].

Kaaret, P. et al. (Feb. 2001). "Chandra High-Resolution Camera observations of the luminous X-ray source in the starburst galaxy M82." In: *MNRAS* 321.2, pp. L29–L32. DOI: 10.1046/j.1365-8711.2001.04064.x. eprint: astro-ph/0009211.

Kamann, S. et al. (Apr. 2016). "MUSE crowded field 3D spectroscopy of over 12 000 stars in the globular cluster NGC 6397. II. Probing the internal dynamics and the presence of a central black hole." In: *A&A* 588, A149, A149. DOI: 10.1051/0004-6361/201527065. eprint: 1602.01643.

Kazantzidis, Stelios et al. (2004). "Density Profiles of Cold Dark Matter Substructure: Implications for the Missing-Satellites Problem." In: *Astrophysical Journal* 608.2, pp. 663–679. DOI: 10.1086/420840. eprint: astro-ph/0312194.

Keller, Benjamin W. et al. (July 2020). "Where did the globular clusters of the Milky Way form? Insights from the E-MOSAICS simulations." In: *MNRAS* 495.4, pp. 4248–4267. DOI: 10.1093/mnras/staa1439. eprint: 2005.05342.

Kimm, Taysun et al. (May 2016). "Formation of Globular Clusters in Atomic-cooling Halos Via Rapid Gas Condensation and Fragmentation during the Epoch of Reionization." In: *Astrophysical Journal* 823.1, 52, p. 52. DOI: 10.3847/0004-637X/823/1/52. eprint: 1510.05671.

King, Ivan R. (Feb. 1966). "The structure of star clusters. III. Some simple dynamical models." In: *Astronomical Journal* 71, p. 64. DOI: 10.1086/109857.

King, Ivan (June 1962). "The structure of star clusters. I. an empirical density law." In: *Astronomical Journal* 67, p. 471. DOI: 10.1086/108756.

Kirsten, F. et al. (May 2021). "A repeating fast radio burst source in a globular cluster." In: *arXiv e-prints*, arXiv:2105.11445. arXiv: 2105.11445 [astro-ph.HE].

Klimentowski, Jarosław et al. (Dec. 2009). "The orientation and kinematics of inner tidal tails around dwarf galaxies orbiting the Milky Way." In: *MNRAS* 400.4, pp. 2162–2168. DOI: 10.1111/j.1365-2966.2009.15626.x. eprint: 0908.4022.

Kolmogorov, Andrey (1933). "Sulla determinazione empirica di una lgge di distribuzione." In: *Inst. Ital. Attuari, Giorn.* 4, pp. 83–91.

Kremer, Kyle, Anthony L. Piro, and Dongzi Li (Aug. 2021). "Dynamical Formation Channels for Fast Radio Bursts in Globular Clusters." In: *Astrophysical Journal Letters* 917.1, L11, p. L11. DOI: 10.3847/2041-8213/ac13a0. arXiv: 2107.03394 [astro-ph.HE].

Kremer, Kyle et al. (Jan. 2018a). "Accreting Black Hole Binaries in Globular Clusters." In: *Astrophysical Journal* 852.1, 29, p. 29. DOI: 10.3847/1538-4357/aa99df. arXiv: 1709.05444 [astro-ph.HE].

Kremer, Kyle et al. (Mar. 2018b). "How Black Holes Shape Globular Clusters: Modeling NGC 3201." In: *Astrophysical Journal Letters* 855.2, L15, p. L15. DOI: 10.3847/2041-8213/aab26c. arXiv: 1802.09553 [astro-ph.HE].

Kremer, Kyle et al. (Jan. 2019a). "How Initial Size Governs Core Collapse in Globular Clusters." In: *Astrophysical Journal* 871.1, 38, p. 38. DOI: 10.3847/1538-4357/aaf646. arXiv: 1808.02204 [astro-ph.GA].

Kremer, Kyle et al. (Aug. 2019b). "Tidal Disruptions of Stars by Black Hole Remnants in Dense Star Clusters." In: *Astrophysical Journal* 881.1, 75, p. 75. DOI: 10.3847/1538-4357/ab2e0c. arXiv: 1904.06353 [astro-ph.HE].

Kremer, Kyle et al. (Apr. 2020a). "Modeling Dense Star Clusters in the Milky Way and Beyond with the CMC Cluster Catalog." In: *Astrophysical Journals* 247.2, 48, p. 48. DOI: 10.3847/1538-4365/ab7919. eprint: 1911.00018.

Kremer, Kyle et al. (Nov. 2020b). "Populating the Upper Black Hole Mass Gap through Stellar Collisions in Young Star Clusters." In: *Astrophysical Journal* 903.1, 45, p. 45. DOI: 10.3847/1538-4357/abb945. arXiv: 2006.10771 [astro-ph.HE].

Kremer, Kyle et al. (Jan. 2020c). "The Role of "black hole burning" in the evolution of dense star clusters." In: *Star Clusters: From the Milky Way to the Early Universe*. Ed. by Angela Bragaglia et al. Vol. 351, pp. 357–366. DOI: 10.1017/S1743921319007269. eprint: 1907.12564.

Kremer, Kyle et al. (Aug. 2021). "White Dwarf Subsystems in Core-Collapsed Globular Clusters." In: *Astrophysical Journal* 917.1, 28, p. 28. DOI: 10.3847/1538-4357/ac06d4. eprint: 2104.11751.

Kremer, Kyle et al. (Jan. 2022). "Hydrodynamics of Collisions and Close Encounters between Stellar Black Holes and Main-sequence Stars." In: *arXiv e-prints*, arXiv:2201.12368. arXiv: 2201.12368 [astro-ph.HE].

Kruijssen, J. M. Diederik (Dec. 2014). "Globular cluster formation in the context of galaxy formation and evolution." In: *Classical and Quantum Gravity* 31.24, 244006, p. 244006. DOI: 10.1088/0264-9381/31/24/244006. eprint: 1407.2953.

Kruijssen, J. M. Diederik (Dec. 2015). "Globular clusters as the relics of regular star formation in 'normal' high-redshift galaxies." In: *MNRAS* 454.2, pp. 1658–1686. DOI: 10.1093/mnras/stv2026. eprint: 1509.02163.

Kulkarni, S. R., Piet Hut, and Steve McMillan (July 1993). "Stellar black holes in globular clusters." In: *Nature* 364.6436, pp. 421–423. DOI: 10.1038/364421a0.

Kuzma, P. B., G. S. Da Costa, and A. D. Mackey (Jan. 2018). "The outer envelopes of globular clusters. II. NGC 1851, NGC 5824 and NGC 1261*." In: *MNRAS* 473.3, pp. 2881–2898. DOI: 10.1093/mnras/stx2353. eprint: 1709.02915.

Kuzma, P. B. et al. (Oct. 2016). "The outer envelopes of globular clusters - I. NGC 7089 (M2)." In: *MNRAS* 461.4, pp. 3639–3652. DOI: 10.1093/mnras/stw1561. eprint: 1606.05949.

LSST Science Collaboration et al. (Dec. 2009). "LSST Science Book, Version 2.0." In: *arXiv e-prints*, arXiv:0912.0201. arXiv: 0912.0201 [astro-ph.IM].

Lançon, Ariane et al. (Dec. 2021). "Extragalactic globular clusters with Euclid and other wide surveys." In: *arXiv e-prints*, arXiv:2110.13783. eprint: 2110.13783.

Lane, Richard R. et al. (Aug. 2010). "Halo globular clusters observed with AAOmega: dark matter content, metallicity and tidal heating." In: *MNRAS* 406.4, pp. 2732–2742. DOI: 10.1111/j.1365-2966.2010.16874.x. arXiv: 1004.4696 [astro-ph.GA].

Laplace, P.S. (1810). "Mémoire sur les approximations des formules qui sont fonctions de très grands nombres et sur leur application aux probabilités." In: *Mémoires de l'Académie Royale des Sciences de Paris* 10, p. 301.

Larson, R. B. (1984). "Black hole remnants in globular clusters." In: *MNRAS* 210, pp. 763–777. DOI: 10.1093/mnras/210.4.763.

Laureijs, R. et al. (2011). "Euclid Definition Study Report." In: *arXiv e-prints*, arXiv:1110.3193. eprint: 1110.3193.

Lazar, Alexandres et al. (July 2020). "A dark matter profile to model diverse feedback-induced core sizes of ΛCDM haloes." In: *MNRAS* 497.2, pp. 2393–2417. DOI: 10.1093/mnras/staa2101. arXiv: 2004.10817 [astro-ph.GA].

Lee, Jae-Woo (July 2017). "Multiple Stellar Populations of Globular Clusters from Homogeneous Ca-CN Photometry. II. M5 (NGC 5904) and a New Filter System." In: *ApJ* 844.1, 77, p. 77. DOI: 10.3847/1538-4357/aa7b8c. eprint: 1706.07969.

Lee, Jae-Woo (Oct. 2018). "Multiple Stellar Populations of Globular Clusters from Homogeneous Ca-CN Photometry. III. NGC 6752." In: *ApJs* 238.2, 24, p. 24. DOI: 10.3847/1538-4365/aadcad. eprint: 1901.10107.

Leigh, Nathan W. C. et al. (Mar. 2013). "Gas depletion in primordial globular clusters due to accretion on to stellar-mass black holes." In: *MNRAS* 429.4, pp. 2997–3006. DOI: 10.1093/mnras/sts554. arXiv: 1212.1461 [astro-ph.SR].

Leonard, Peter J. T. (July 1989). "Stellar Collisions in Globular Clusters and the Blue Straggler Problem." In: *Astronomical Journal* 98, p. 217. DOI: 10.1086/115138.

Leonard, Peter J. T. (1996). "The Implications of the Binary Properties of the M67 Blue Stragglers." In: *ApJ* 470, p. 521. DOI: 10.1086/177884.

Lewis, Antony and Sarah Bridle (Nov. 2002). "Cosmological parameters from CMB and other data: A Monte Carlo approach." In: *Physical Review D* 66.10, 103511, p. 103511. DOI: 10.1103/PhysRevD.66.103511. eprint: astro-ph/0205436.

Li, Hefan et al. (July 2021). "Gaia EDR3 Proper Motions of Milky Way Dwarfs. I. 3D Motions and Orbits." In: *ApJ* 916.1, 8, p. 8. DOI: 10.3847/1538-4357/ac0436. eprint: 2104.03974.

Libralato, Mattia et al. (July 2018). "Hubble Space Telescope Proper Motion (HSTPROMO) Catalogs of Galactic Globular Cluster. VI. Improved Data Reduction and Internal-kinematic Analysis of NGC 362." In: *Astrophysical Journal* 861.2, 99, p. 99. DOI: 10.3847/1538-4357/aac6c0. arXiv: 1805.05332 [astro-ph.SR].

Libralato, Mattia et al. (Mar. 2019). "The Hubble Space Telescope UV Legacy Survey of Galactic Globular Clusters. XVIII. Proper-motion Kinematics of Multiple Stellar Populations in the Core Regions of NGC 6352." In: *Astrophysical Journal* 873.2, 109, p. 109. DOI: 10.3847/1538-4357/ab0551. arXiv: 1902.02787 [astro-ph.SR].

Lima Neto, G. B., D. Gerbal, and I. Márquez (Oct. 1999). "The specific entropy of elliptical galaxies: an explanation for profile-shape distance indicators?" In: *MNRAS* 309.2, pp. 481–495. DOI: 10.1046/j.1365-8711.1999.02849.x. eprint: astro-ph/9905048.

Lin, Dacheng et al. (Apr. 2020). "Multiwavelength Follow-up of the Hyperluminous Intermediate-mass Black Hole Candidate 3XMM J215022.4-055108." In: *Astrophysical Journal Letters* 892.2, L25, p. L25. DOI: 10.3847/2041-8213/ab745b. eprint: 2002.04618.

Lindegren, L. et al. (Aug. 2018). "Gaia Data Release 2. The astrometric solution." In: *A&A* 616, A2, A2. DOI: 10.1051/0004-6361/201832727. eprint: 1804.09366.

Lindegren, L. et al. (May 2021). "Gaia Early Data Release 3. The astrometric solution." In: *A&A* 649, A2, A2. DOI: 10.1051/0004-6361/202039709. eprint: 2012.03380.

Loeb, Abraham and Frederic A. Rasio (Sept. 1994). "Collapse of Primordial Gas Clouds and the Formation of Quasar Black Holes." In: *Astrophysical Journal* 432, p. 52. DOI: 10.1086/174548. eprint: astro-ph/9401026.

Łokas, E. L. and G. A. Mamon (Feb. 2001). "Properties of spherical galaxies and clusters with an NFW density profile." In: *MNRAS* 321, pp. 155–166. DOI: 10.1046/j.1365-8711.2001.04007.x. eprint: astro-ph/0002395.

Longmore, S. N. et al. (Jan. 2014). "The Formation and Early Evolution of Young Massive Clusters." In: *Protostars and Planets VI*. Ed. by Henrik Beuther et al., p. 291. DOI: 10.2458/azu_uapress_9780816531240-ch013. eprint: 1401.4175.

Lousto, Carlos O. et al. (June 2010). "Remnant masses, spins and recoils from the merger of generic black hole binaries." In: *Classical and Quantum Gravity* 27.11, 114006, p. 114006. DOI: 10.1088/0264-9381/27/11/114006. arXiv: 0904.3541 [gr-qc].

Lousto, Carlos O. et al. (Apr. 2012). "Gravitational recoil from accretion-aligned black-hole binaries." In: *Physical Review D* 85.8, 084015, p. 084015. DOI: 10.1103/PhysRevD.85.084015. arXiv: 1201.1923 [gr-qc].

Lu, Wenbin, Paz Beniamini, and Pawan Kumar (July 2021). "Implications of a rapidly varying FRB in a globular cluster of M81." In: *arXiv e-prints*, arXiv:2107.04059. arXiv: 2107.04059 [astro-ph.HE].

Lynden-Bell, D. and Roger Wood (Jan. 1968). "The gravo-thermal catastrophe in isothermal spheres and the onset of red-giant structure for stellar systems." In: *MNRAS* 138, p. 495. DOI: 10.1093/mnras/138.4.495.

Márquez, I. et al. (Jan. 2000). "Gravo-thermal properties and formation of elliptical galaxies." In: *A&A* 353, pp. 873–886.

Ma, Xiangcheng et al. (Apr. 2020). "Self-consistent proto-globular cluster formation in cosmological simulations of high-redshift galaxies." In: *MNRAS* 493.3, pp. 4315–4332. DOI: 10.1093/mnras/staa527. eprint: 1906.11261.

Mackey, A. D. et al. (July 2007). "The effect of stellar-mass black holes on the structural evolution of massive star clusters." In: *MNRAS* 379.1, pp. L40–L44.

Madau, Piero and Martin J. Rees (Apr. 2001). "Massive Black Holes as Population III Remnants." In: *Astrophysical Journal Letters* 551.1, pp. L27–L30. DOI: 10.1086/319848. arXiv: astro-ph/0101223 [astro-ph].

Majewski, S. R. et al. (Jan. 2000). "ω Centauri : Nucleus of a milky way dwarf spheroidal ?" In: *Liege International Astrophysical Colloquia*. Ed. by A. Noels et al. Vol. 35. Liege International Astrophysical Colloquia, p. 619. eprint: astro-ph/9910278.

Makino, Junichiro and Piet Hut (Dec. 1991). "On Core Collapse." In: *Astrophysical Journal* 383, p. 181. DOI: 10.1086/170774.

Malhan, Khyati and Rodrigo A. Ibata (July 2018). "STREAMFINDER - I. A new algorithm for detecting stellar streams." In: *MNRAS* 477.3, pp. 4063–4076. DOI: 10.1093/mnras/sty912. eprint: 1804.11338.

Malhan, Khyati et al. (Feb. 2022). "The Global Dynamical Atlas of the Milky Way Mergers: Constraints from Gaia EDR3-based Orbits of Globular Clusters, Stellar Streams, and Satellite Galaxies." In: *ApJ* 926.2, 107, p. 107. DOI: 10.3847/1538-4357/ac4d2a. eprint: 2202.07660.

Mamon, G. A. et al. (Jan. 2012). "Predicting the Frequencies of Young and of Tiny Galaxies." In: *Dwarf Galaxies: Keys to Galaxy Formation and Evolution*. Vol. 28. Astrophysics and Space Science Proceedings, p. 39. DOI: 10.1007/978-3-642-22018-0_3. eprint: 1103.5349.

Mamon, Gary A., Andrea Biviano, and Gwenaël Boué (Mar. 2013). "MAMPOSSt: Modelling Anisotropy and Mass Profiles of Observed Spherical Systems - I. Gaussian 3D velocities." In: *MNRAS* 429.4, pp. 3079–3098. DOI: 10.1093/mnras/sts565. eprint: 1212.1455.

Mamon, Gary A. and Ewa L. Łokas (Nov. 2005). "Dark matter in elliptical galaxies - II. Estimating the mass within the virial radius." In: *MNRAS* 363.3, pp. 705–722. DOI: 10.1111/j.1365-2966.2005.09400.x. eprint: astro-ph/0405491.

Mann, Christopher R. et al. (Apr. 2019). "A Multimass Velocity Dispersion Model of 47 Tucanae Indicates No Evidence for an Intermediate-mass Black Hole." In: *Astrophysical Journal* 875.1, 1, p. 1. DOI: 10.3847/1538-4357/ab0e6d. eprint: 1807.03307.

Marigo, Paola et al. (Jan. 2017). "A New Generation of PARSEC-COLIBRI Stellar Isochrones Including the TP-AGB Phase." In: *Astrophysical Journal* 835.1, 77, p. 77. DOI: 10.3847/1538-4357/835/1/77. eprint: 1701.08510.

Marin-Franch, Antonio et al. (Apr. 2009). "The ACS Survey of Galactic Globular Clusters. VII. Relative Ages." In: *Astrophysical Journal* 694.2, pp. 1498–1516. DOI: 10.1088/0004-637X/694/2/1498. eprint: 0812.4541.

Martin, Nicolas F. et al. (Jan. 2022). "A stellar stream remnant of a globular cluster below the metallicity floor." In: *Nature* 601.7891, pp. 45–48. DOI: 10.1038/s41586-021-04162-2. eprint: 2201.01309.

Martinazzi, E. et al. (Aug. 2014). "Probing mass segregation in the globular cluster NGC 6397." In: *MNRAS* 442.4, pp. 3105–3111. DOI: 10.1093/mnras/stu1032. eprint: 1411.6327.

Mashchenko, Sergey and Alison Sills (Jan. 2005). "Globular Clusters with Dark Matter Halos. II. Evolution in a Tidal Field." In: *Astrophysical Journal* 619.1, pp. 258–269. DOI: 10.1086/426133. eprint: astro-ph/0409606.

Mazure, A. and H. V. Capelato (Jan. 2002). "Exact solutions for the spatial de Vaucouleurs and Sérsic laws and related quantities." In: *A&A* 383, pp. 384–389. DOI: 10.1051/0004-6361:20011751. eprint: astro-ph/0112147.

Mazzali, Paolo A. et al. (Feb. 2007). "A Common Explosion Mechanism for Type Ia Supernovae." In: *Science* 315.5813, p. 825. DOI: 10.1126/science.1136259. eprint: astro-ph/0702351.

McConnachie, Alan W. and Kim A. Venn (Dec. 2020). "Updated Proper Motions for Local Group Dwarf Galaxies Using Gaia Early Data Release 3." In: *Research Notes of the American Astronomical Society* 4.12, 229, p. 229. DOI: 10.3847/2515-5172/abd18b. eprint: 2012.03904.

McCrea, W. H. (Jan. 1964). "Extended main-sequence of some stellar clusters." In: *MNRAS* 128, p. 147. DOI: 10.1093/mnras/128.2.147.

McDonald, I. and A. A. Zijlstra (Mar. 2015). "Mass-loss on the red giant branch: the value and metallicity dependence of Reimers' η in globular clusters." In: *MNRAS* 448.1, pp. 502–521. DOI: 10.1093/mnras/stv007. eprint: 1501.00874.

McKee, Christopher F., Antonio Parravano, and David J. Hollenbach (Nov. 2015). "Stars, Gas, and Dark Matter in the Solar Neighborhood." In: *Astrophysical Journal* 814.1, 13, p. 13. DOI: 10.1088/0004-637X/814/1/13. eprint: 1509.05334.

Mellier, Y. and G. Mathez (Mar. 1987). "Deprojection of the de Vaucouleurs R exp 1/4 brightness profile." In: *A&A* 175.1-2, pp. 1–3.

Merritt, D. (June 1985). "Spherical stellar systems with spheroidal velocity distributions." In: *Astronomical Journal* 90, pp. 1027–1037. DOI: 10.1086/113810.

Merritt, D. et al. (Dec. 2006). "Empirical Models for Dark Matter Halos. I. Nonparametric Construction of Density Profiles and Comparison with Parametric Models." In: *Astronomical Journal* 132, pp. 2685–2700. eprint: arXiv:astro-ph/0509417.

Merritt, David (Feb. 1987). "The Distribution of Dark Matter in the Coma Cluster." In: *Astrophysical Journal* 313, p. 121. DOI: 10.1086/164953.

Merritt, David et al. (June 2004). "Core Formation by a Population of Massive Remnants." In: *Astrophysical Journal Letters* 608.1, pp. L25–L28.

Merritt, David et al. (May 2005). "A Universal Density Profile for Dark and Luminous Matter?" In: *ApJl* 624.2, pp. L85–L88. DOI: 10.1086/430636. eprint: astro-ph/0502515.

Messier, Charles (Jan. 1781). *Catalogue des Nébuleuses et des Amas d'Étoiles (Catalog of Nebulae and Star Clusters)*. Connoissance des Temps ou des Mouvements Célestes.

Meylan, G. et al. (Aug. 2001). "Mayall II=G1 in M31: Giant Globular Cluster or Core of a Dwarf Elliptical Galaxy?" In: *Astronomical Journal* 122.2, pp. 830–841. DOI: 10.1086/321166. arXiv: astro-ph/0105013 [astro-ph].

Michie, R. W. (Jan. 1963). "The dynamics of spherical stellar systems, IV." In: *MNRAS* 126, p. 499. DOI: 10.1093/mnras/126.6.499.

Miki, Yohei and Masayuki Umemura (Apr. 2017). "GOTHIC: Gravitational octtree code accelerated by hierarchical time step controlling." In: *New Astronomy* 52, pp. 65–81. DOI: 10.1016/j.newast.2016.10.007. arXiv: 1610.07279 [astro-ph.IM].

Miki, Yohei and Masayuki Umemura (Apr. 2018). "MAGI: many-component galaxy initializer." In: *MNRAS* 475.2, pp. 2269–2281. DOI: 10.1093/mnras/stx3327. eprint: 1712.08760.

Miller, M. Coleman and Douglas P. Hamilton (Feb. 2002). "Production of intermediate-mass black holes in globular clusters." In: *MNRAS* 330.1, pp. 232–240. DOI: 10.1046/j.1365-8711.2002.05112.x. eprint: astro-ph/0106188.

Milone, A. P. et al. (Jan. 2012). "A Double Main Sequence in the Globular Cluster NGC 6397." In: *Astrophysical Journal* 745.1, 27, p. 27. DOI: 10.1088/0004-637X/745/1/27. eprint: 1110.1077.

Milone, A. P. et al. (Oct. 2018). "Gaia unveils the kinematics of multiple stellar populations in 47 Tucanae." In: *MNRAS* 479.4, pp. 5005–5011. DOI: 10.1093/mnras/sty1873. eprint: 1807.03511.

Montuori, M. et al. (Apr. 2007). "Tidal Tails around Globular Clusters: Are They a Good Tracer of Cluster Orbits?" In: *ApJ* 659.2, pp. 1212–1221. DOI: 10.1086/512114. eprint: astro-ph/0611204.

Moore, Ben (Apr. 1996). "Constraints on the Global Mass-to-Light Ratios and on the Extent of Dark Matter Halos in Globular Clusters and Dwarf Spheroidals." In: *Astrophysical Journal Letters* 461, p. L13. DOI: 10.1086/309998. arXiv: astro-ph/9511147 [astro-ph].

Morscher, Meagan et al. (Feb. 2015). "The Dynamical Evolution of Stellar Black Holes in Globular Clusters." In: *Astrophysical Journal* 800.1, 9, p. 9. DOI: 10.1088/0004-637X/800/1/9. arXiv: 1409.0866 [astro-ph.GA].

Muñoz, Ricardo R. et al. (June 2018). "A MegaCam Survey of Outer Halo Satellites. III. Photometric and Structural Parameters." In: *ApJ* 860.1, 66, p. 66. DOI: 10.3847/1538-4357/aac16b.

Navarro, J. F. et al. (Apr. 2004). "The inner structure of ΛCDM haloes - III. Universality and asymptotic slopes." In: *MNRAS* 349, pp. 1039–1051.

Navarro, Julio F., Carlos S. Frenk, and Simon D. M. White (May 1996). "The Structure of Cold Dark Matter Halos." In: *Astrophysical Journal* 462, p. 563. DOI: 10.1086/177173. eprint: astro-ph/9508025.

Nomoto, K. (Feb. 1984). "Evolution of 8-10 solar mass stars toward electron capture supernovae. I - Formation of electron-degenerate O + NE + MG cores." In: *ApJ* 277, pp. 791–805. DOI: 10.1086/161749.

Nomoto, K. and Jr. Iben I. (1985). "Carbon ignition in a rapidly accreting degenerate dwarf - A clue to the nature of the merging process in close binaries." In: *Astrophysical Journal* 297, pp. 531–537. DOI: 10.1086/163547.

Nusser, Adi (July 2019). "A scenario for ultra-diffuse satellite galaxies with low velocity dispersions." In: *arXiv e-prints*, arXiv:1907.08035. eprint: 1907.08035.

Odenkirchen, Michael et al. (Feb. 2001). "Detection of Massive Tidal Tails around the Globular Cluster Palomar 5 with Sloan Digital Sky Survey Commissioning Data." In: *ApJ Letters* 548.2, pp. L165–L169. DOI: 10.1086/319095. eprint: astro-ph/0012311.

Odenkirchen, Michael et al. (Nov. 2003). "The Extended Tails of Palomar 5: A 10^{o} Arc of Globular Cluster Tidal Debris." In: *Astronomical Journal* 126.5, pp. 2385–2407. DOI: 10.1086/378601. arXiv: astro-ph/0307446 [astro-ph].

Olver, F. W. J. (1972). "in Handbook of Mathematical Functions, Ed. M. Abramowitz and I. Stegun, chap. 9." In: Dover. Chap. 9.

Oosterhoff, P. T. (Apr. 1939). "Some remarks on the variable stars in globular clusters." In: *The Observatory* 62, pp. 104–109.

Oppenheimer, J. R. and H. Snyder (Sept. 1939). "On Continued Gravitational Contraction." In: *Physical Review* 56.5, pp. 455–459. DOI: 10.1103/PhysRev.56.455.

Osipkov, L. P. (1979). "Spherical systems of gravitating bodies with an ellipsoidal velocity distribution." In: *Soviet Astronomy Letters* 5, pp. 42–44.

Ostriker, J. P. (Jan. 1985). "Physical interactions between stars." In: *Dynamics of Star Clusters*. Ed. by J. Goodman and P. Hut. Vol. 113, pp. 347–357.

Pancino, E. et al. (Oct. 2003). "The multiple stellar population in ω Centauri: spatial distribution and structural properties." In: *MNRAS* 345.2, pp. 683–690. DOI: 10.1046/j.1365-8711.2003.06981.x. arXiv: astro-ph/0305524 [astro-ph].

Pastorelli, Giada et al. (June 2019). "Constraining the thermally pulsing asymptotic giant branch phase with resolved stellar populations in the Small Magellanic Cloud." In: *MNRAS* 485.4, pp. 5666–5692. DOI: 10.1093/mnras/stz725. eprint: 1903.04499.

Peñarrubia, Jorge et al. (Oct. 2017). "Stellar envelopes of globular clusters embedded in dark mini-haloes." In: *MNRAS* 471.1, pp. L31–L35. DOI: 10.1093/mnrasl/slx094. eprint: 1706.02710.

Pearson, Karl (Jan. 1916). "Mathematical Contributions to the Theory of Evolution. XIX. Second Supplement to a Memoir on Skew Variation." In: *Philo-*

sophical Transactions of the Royal Society of London Series A 216, pp. 429–457. DOI: 10.1098/rsta.1916.0009.

Pechetti, Renuka et al. (Nov. 2021). "Detection of a ~100,000 $M_\odot$ black hole in M31's most massive globular cluster: A tidally stripped nucleus." In: *arXiv e-prints*, arXiv:2111.08720. eprint: 2111.08720.

Peebles, P. J. E. (Feb. 1984). "Dark matter and the origin of galaxies and globular star clusters." In: *Astrophysical Journal* 277, pp. 470–477. DOI: 10.1086/161714.

Peebles, P. J. E. and R. H. Dicke (Dec. 1968). "Origin of the Globular Star Clusters." In: *Astrophysical Journal* 154, p. 891. DOI: 10.1086/149811.

Peres, A. (Dec. 1962). "Classical Radiation Recoil." In: *Phys. Rev.* 128 (5), pp. 2471–2475. DOI: 10.1103/PhysRev.128.2471. URL: https://link.aps.org/doi/10.1103/PhysRev.128.2471.

Perets, Hagai B. et al. (June 2016). "Micro-tidal Disruption Events by Stellar Compact Objects and the Production of Ultra-long GRBs." In: *Astrophysical Journal* 823.2, 113, p. 113. DOI: 10.3847/0004-637X/823/2/113. arXiv: 1602.07698 [astro-ph.HE].

Planck Collaboration et al. (Sept. 2016). "Planck 2015 results. XIII. Cosmological parameters." In: *A&A* 594, A13, A13. DOI: 10.1051/0004-6361/201525830. eprint: 1502.01589.

Planck Collaboration et al. (Sept. 2020). "Planck 2018 results. VI. Cosmological parameters." In: *A&A* 641, A6, A6. DOI: 10.1051/0004-6361/201833910. eprint: 1807.06209.

Plummer, H. C. (Mar. 1911). "On the problem of distribution in globular star clusters." In: *MNRAS* 71, pp. 460–470.

Portail, Matthieu et al. (Feb. 2017). "Dynamical modelling of the galactic bulge and bar: the Milky Way's pattern speed, stellar and dark matter mass distribution." In: *MNRAS* 465.2, pp. 1621–1644. DOI: 10.1093/mnras/stw2819. arXiv: 1608.07954 [astro-ph.GA].

Portegies Zwart, S. F. et al. (Aug. 1999). "Star cluster ecology. III. Runaway collisions in young compact star clusters." In: *A&A* 348, pp. 117–126. eprint: astro-ph/9812006.

Portegies Zwart, Simon F. and Stephen L. W. McMillan (Jan. 2000). "Black Hole Mergers in the Universe." In: *Astrophysical Journal Letters* 528.1, pp. L17–L20. DOI: 10.1086/312422. arXiv: astro-ph/9910061 [astro-ph].

Portegies Zwart, Simon F. and Stephen L. W. McMillan (Sept. 2002). "The Runaway Growth of Intermediate-Mass Black Holes in Dense Star Clusters." In: *Astrophysical Journal* 576.2, pp. 899–907. DOI: 10.1086/341798. eprint: astro-ph/0201055.

Portegies Zwart, Simon F., Stephen L. W. McMillan, and Mark Gieles (Sept. 2010a). "Young Massive Star Clusters." In: *Annual Review of A&A* 48, pp. 431–493. DOI: 10.1146/annurev-astro-081309-130834. eprint: 1002.1961.

Portegies Zwart, Simon F., Stephen L. W. McMillan, and Mark Gieles (Sept. 2010b). "Young Massive Star Clusters." In: *Annual Review of A&A* 48, pp. 431–493. DOI: 10.1146/annurev-astro-081309-130834. arXiv: 1002.1961 [astro-ph.GA].

Prugniel, P. and F. Simien (May 1997). "The fundamental plane of early-type galaxies: non-homology of the spatial structure." In: *A&A* 321, pp. 111–122.

Quinlan, Gerald D. (Nov. 1996). "The time-scale for core collapse in spherical star clusters." In: *New Astronomy* 1.3, pp. 255–270. DOI: 10.1016/S1384-1076(96)00018-8. eprint: astro-ph/9606182.

Rastello, Sara, Giovanni Carraro, and Roberto Capuzzo-Dolcetta (June 2020). "Effect of Binarity in Star Cluster Dynamical Mass Determination." In: *Astrophysical Journal* 896.2, 152, p. 152. DOI: 10.3847/1538-4357/ab910b. eprint: 2005.03037.

Read, J. I. et al. (Feb. 2021). "Breaking beta: a comparison of mass modelling methods for spherical systems." In: *MNRAS* 501.1, pp. 978–993. DOI: 10.1093/mnras/staa3663. arXiv: 2011.09493 [astro-ph.GA].

Rees, R. F. and K. M. Cudworth (Dec. 2003). "Did the Globular Cluster NGC 6397 Trigger the Formation of the Young Open Cluster NGC 6231?" In: *American Astronomical Society Meeting Abstracts*. Vol. 203. American Astronomical Society Meeting Abstracts, p. 10.06.

Reiz, Anders (Sept. 1954). "The Structure of Stars with Negligible Content of Heavy Elements." In: *ApJ* 120, p. 342. DOI: 10.1086/145920.

Rezzolla, Luciano, Elias R. Most, and Lukas R. Weih (Jan. 2018). "Using Gravitational-wave Observations and Quasi-universal Relations to Constrain the Maximum Mass of Neutron Stars." In: *Astrophysical Journal Letters* 852.2, L25, p. L25. DOI: 10.3847/2041-8213/aaa401. arXiv: 1711.00314 [astro-ph.HE].

Ricotti, Massimo, Owen H. Parry, and Nickolay Y. Gnedin (Nov. 2016). "A Common Origin for Globular Clusters and Ultra-faint Dwarfs in Simulations of the First Galaxies." In: *Astrophysical Journal* 831.2, 204, p. 204. DOI: 10.3847/0004-637X/831/2/204. eprint: 1607.04291.

Riello, M. et al. (May 2021). "Gaia Early Data Release 3. Photometric content and validation." In: *A&A* 649, A3, A3. DOI: 10.1051/0004-6361/202039587. eprint: 2012.01916.

Robin, A. C. et al. (2003). "A synthetic view on structure and evolution of the Milky Way." In: *A&A* 409, pp. 523–540. DOI: 10.1051/0004-6361:20031117.

Rodrigues, O. (1840). "Des lois géométriques qui régissent les déplacements d'un système solide dans l'espace, et de la variation des coordonnées provenant de ces déplacements considérés indépendamment des causes qui peuvent les produire." In: *Journal de Mathématiques Pures et Appliquées, vol. 5, pages 380-440.*

Rodriguez, Carl L. et al. (Dec. 2016). "Million-body star cluster simulations: comparisons between Monte Carlo and direct N-body." In: *MNRAS* 463.2, pp. 2109–2118. DOI: 10.1093/mnras/stw2121. arXiv: 1601.04227 [astro-ph.IM].

Rodriguez, Carl L. et al. (Dec. 2018). "Post-Newtonian dynamics in dense star clusters: Formation, masses, and merger rates of highly-eccentric black hole binaries." In: *Physical Review D* 98.12, 123005, p. 123005. DOI: 10.1103/PhysRevD.98.123005. arXiv: 1811.04926 [astro-ph.HE].

Rodriguez, Carl L. et al. (Aug. 2019). "Black holes: The next generation—repeated mergers in dense star clusters and their gravitational-wave properties." In: *Physical Review D* 100.4, 043027, p. 043027. DOI: 10.1103/PhysRevD.100.043027. arXiv: 1906.10260 [astro-ph.HE].

Rodriguez, Carl L. et al. (Jan. 2021). "The Observed Rate of Binary Black Hole Mergers can be Entirely Explained by Globular Clusters." In: *Research Notes of the American Astronomical Society* 5.1, 19, p. 19. DOI: 10.3847/2515-5172/abdf54. eprint: 2101.07793.

Rodriguez, Carl L. et al. (Feb. 2022). "Modeling Dense Star Clusters in the Milky Way and beyond with the Cluster Monte Carlo Code." In: *ApJ* 258.2, 22, p. 22. DOI: 10.3847/1538-4365/ac2edf. eprint: 2106.02643.

Rood, Robert T. (Sept. 1973). "Metal-Poor Stars. V. Horizontal-Branch Morphology." In: *ApJ* 184, pp. 815–838. DOI: 10.1086/152373.

Rubin, V. C., Jr. Ford W. K., and N. Thonnard (June 1980). "Rotational properties of 21 SC galaxies with a large range of luminosities and radii, from NGC 4605 (R=4kpc) to UGC 2885 (R=122kpc)." In: *ApJ* 238, pp. 471–487. DOI: 10.1086/158003.

Rubin, Vera C. and Jr. Ford W. Kent (Feb. 1970). "Rotation of the Andromeda Nebula from a Spectroscopic Survey of Emission Regions." In: *ApJ* 159, p. 379. DOI: 10.1086/150317.

Rui, Nicholas Z. et al. (May 2021a). "Matching Globular Cluster Models to Observations." In: *Astrophysical Journal* 912.2, 102, p. 102. DOI: 10.3847/1538-4357/abed49. arXiv: 2103.05033 [astro-ph.GA].

Rui, Nicholas Z. et al. (Mar. 2021b). "No Black Holes in NGC 6397." In: *Research Notes of the American Astronomical Society* 5.3, 47, p. 47. DOI: 10.3847/2515-5172/abee77. eprint: 2103.06273.

Russell, Henry Norris (May 1914). "Relations Between the Spectra and Other Characteristics of the Stars." In: *Popular Astronomy* 22, pp. 275–294.

Saitoh, Takayuki R. et al. (Mar. 2006). "Tidal Disruption of Dark Matter Halos around Proto-Globular Clusters." In: *ApJ* 640.1, pp. 22–30. DOI: 10.1086/500104. arXiv: astro-ph/0511692 [astro-ph].

Salpeter, Edwin E. (Jan. 1955). "The Luminosity Function and Stellar Evolution." In: *Astrophysical Journal* 121, p. 161. DOI: 10.1086/145971.

Sandage, Allan (Aug. 1993). "Temperature, Mass, and Luminosity of RR Lyrae Stars as Function of Metallicity at the Blue Fundamental Edge. II." In: *Astronomical Journal* 106, p. 703. DOI: 10.1086/116676.

Scheepmaker, R. A. et al. (July 2007). "ACS imaging of star clusters in M 51. I. Identification and radius distribution." In: *A&A* 469.3, pp. 925–940. DOI: 10.1051/0004-6361:20077511. arXiv: 0704.3604 [astro-ph].

Schmidt, M. (Mar. 1963). "3C 273 : A Star-Like Object with Large Red-Shift." In: *Nature* 197.4872, p. 1040. DOI: 10.1038/1971040a0.

Schwab, Josiah (Jan. 2021). "Evolutionary Models for the Remnant of the Merger of Two Carbon-Oxygen Core White Dwarfs." In: *Astrophysical Journal* 906.1, 53, p. 53. DOI: 10.3847/1538-4357/abc87e. arXiv: 2011.03546 [astro-ph.SR].

Schwarz, Gideon (July 1978). "Estimating the Dimension of a Model." In: *Annals of Statistics* 6.2, pp. 461–464.

Schwarzschild, M., L. Searle, and R. Howard (Sept. 1955). "On the Colors of Subdwarfs." In: *ApJ* 122, p. 353. DOI: 10.1086/146094.

Searle, L. and R. Zinn (Oct. 1978). "Composition of halo clusters and the formation of the galactic halo." In: *Astrophysical Journal* 225, pp. 357–379. DOI: 10.1086/156499.

Sérsic, J. L. (1963). In: *Bull. Assoc. Argentina de Astron.* 6, p. 41.

Sersic, J. L. (1968). *Atlas de galaxias australes*. Cordoba, Argentina: Observatorio Astronomico.

Shin, Jihye, Sungsoo S. Kim, and Young-Wook Lee (Aug. 2013). "Dark Matter Content in Globular Cluster NGC 6397." In: *Journal of Korean Astronomical Society* 46.4, pp. 173–181. DOI: 10.5303/JKAS.2013.46.4.173.

Shipp, N. et al. (Aug. 2018). "Stellar Streams Discovered in the Dark Energy Survey." In: *ApJ* 862.2, 114, p. 114. DOI: 10.3847/1538-4357/aacdab. eprint: 1801.03097.

Silk, Joseph and Gary A. Mamon (Aug. 2012). "The current status of galaxy formation." In: *Research in Astronomy and Astrophysics* 12.8, pp. 917–946. DOI: 10.1088/1674-4527/12/8/004. eprint: 1207.3080.

Silverman, B. W. (1986). *Density estimation for statistics and data analysis*.

Simonneau, E. and F. Prada (1999). "Structural properties of spherical galaxies obeying the Sersic Rî/n law: a semi-analytical approach." In: unpublished preprint, submitted to MNRAS, arXiv:astro-ph/9906151.

Simonneau, E. and F. Prada (Apr. 2004). "Structural Properties of Spherical Galaxies: a Semi-Analytical Approach." In: *Revista Mexicana de Astronomia y Astrofisica* 40, pp. 69–79.

Smirnov, Nikolai V (1939). "On the estimation of the discrepancy between empirical curves of distribution for two independent samples." In: *Bull. Math. Univ. Moscou* 2.2, pp. 3–14.

Sollima, A. (June 2020). "The eye of Gaia on globular clusters structure: tidal tails." In: *MNRAS* 495.2, pp. 2222–2233. DOI: 10.1093/mnras/staa1209. eprint: 2004.13754.

Sollima, A. and H. Baumgardt (Nov. 2017). "The global mass functions of 35 Galactic globular clusters: I. Observational data and correlations with cluster parameters." In: *MNRAS* 471.3, pp. 3668–3679. DOI: 10.1093/mnras/stx1856. eprint: 1708.09529.

Sollima, A., H. Baumgardt, and M. Hilker (May 2019). "The eye of Gaia on globular clusters kinematics: internal rotation." In: *MNRAS* 485.1, pp. 1460–1476. DOI: 10.1093/mnras/stz505. eprint: 1902.05895.

Spera, Mario, Michela Mapelli, and Alessand ro Bressan (Aug. 2015). "The mass spectrum of compact remnants from the PARSEC stellar evolution tracks." In: *MNRAS* 451.4, pp. 4086–4103. DOI: 10.1093/mnras/stv1161. arXiv: 1505.05201 [astro-ph.SR].

Spitzer Lyman, Jr. and Michael H. Hart (Mar. 1971). "Random Gravitational Encounters and the Evolution of Spherical Systems. I. Method." In: *ApJ* 164, p. 399. DOI: 10.1086/150855.

Spitzer, Lyman (1987). *Dynamical evolution of globular clusters*.

Stetson, Peter B., Don A. Vandenberg, and Michael Bolte (July 1996). "The Relative Ages of Galactic Globular Clusters." In: *Publications of the ASP* 108, p. 560. DOI: 10.1086/133766. eprint: astro-ph/9605064.

Stodolkiewicz, J. S. (Jan. 1982). "Dynamical evolution of globular clusters. I." In: *Acta Astronomica* 32.1-2, pp. 63–91.

Strader, Jay et al. (2012). "Two stellar-mass black holes in the globular cluster M22." In: *Nature* 490.7418, pp. 71–73. DOI: 10.1038/nature11490. arXiv: 1210.0901 [astro-ph.HE].

Strigari, Louis E., James S. Bullock, and Manoj Kaplinghat (Mar. 2007). "Determining the Nature of Dark Matter with Astrometry." In: *Astrophysical Journal Letters* 657.1, pp. L1–L4. DOI: 10.1086/512976. eprint: astro-ph/0701581.

Stryker, L. L. (1993). "Blue Stragglers." In: *Publications of the ASP* 105, p. 1081. DOI: 10.1086/133286.

Sugiura, N. (1978). "Further analysts of the data by Akaike's information criterion and the finite corrections." In: *Communications in Statistics - Theory and Methods* 7.1, pp. 13–26. DOI: 10.1080/03610927808827599.

Tauris, T. M. et al. (2013). "Evolution towards and beyond accretion-induced collapse of massive white dwarfs and formation of millisecond pulsars." In: *A&A* 558, A39, A39. DOI: 10.1051/0004-6361/201321662. arXiv: 1308.4887 [astro-ph.SR].

Taylor, A. N. et al. (July 1998). "Gravitational Lens Magnification and the Mass of Abell 1689." In: *ApJ* 501.2, pp. 539–553. DOI: 10.1086/305827. eprint: astro-ph/9801158.

Taylor, M. B. (2005). "TOPCAT & STIL: Starlink Table/VOTable Processing Software." In: *Astronomical Data Analysis Software and Systems XIV*. Ed. by P. Shopbell, M. Britton, and R. Ebert. Vol. 347. Astronomical Society of the Pacific Conference Series, p. 29.

The LIGO Scientific Collaboration et al. (Sept. 2020). "GW190521: A Binary Black Hole Merger with a Total Mass of 150 $M_\odot$." In: *arXiv e-prints*, arXiv:2009.01075. eprint: 2009.01075.

Thomas, G. F. et al. (Jan. 2018). "Stellar streams as gravitational experiments. II. Asymmetric tails of globular cluster streams." In: *A&A* 609, A44, A44. DOI: 10.1051/0004-6361/201731609. eprint: 1709.01934.

Thompson, Todd A. et al. (May 2020). "Response to Comment on "A noninteracting low-mass black hole-giant star binary system"." In: *Science* 368.6491, eaba4356, eaba4356. DOI: 10.1126/science.aba4356. arXiv: 2005.07653 [astro-ph.HE].

Tiongco, Maria A., Enrico Vesperini, and Anna Lisa Varri (Aug. 2019). "Kinematical evolution of multiple stellar populations in star clusters." In: *MNRAS* 487.4, pp. 5535–5548. DOI: 10.1093/mnras/stz1595. eprint: 1907.05901.

Tiret, O. et al. (Dec. 2007). "Velocity dispersion around ellipticals in MOND." In: *A&A* 476, pp. L1–L4. eprint: arXiv:0710.4070.

Tremaine, S. D., J. P. Ostriker, and Jr. Spitzer L. (Mar. 1975). "The formation of the nuclei of galaxies. I. M31." In: *ApJ* 196, pp. 407–411. DOI: 10.1086/153422.

Tremou, Evangelia et al. (July 2018). "The MAVERIC Survey: Still No Evidence for Accreting Intermediate-mass Black Holes in Globular Clusters." In: *Astrophysical Journal* 862.1, 16, p. 16. DOI: 10.3847/1538-4357/aac9b9. eprint: 1806.00259.

Trenti, Michele, Paolo Padoan, and Raul Jimenez (Aug. 2015). "The Relative and Absolute Ages of Old Globular Clusters in the LCDM Framework." In: *Astrophysical Journal Letters* 808.2, L35, p. L35. DOI: 10.1088/2041-8205/808/2/L35. eprint: 1502.02670.

Trenti, Michele and Roeland van der Marel (Nov. 2013). "No energy equipartition in globular clusters." In: *MNRAS* 435.4, pp. 3272–3282. DOI: 10.1093/mnras/stt1521. arXiv: 1302.2152 [astro-ph.GA].

Trujillo, I. et al. (July 2002). "Triaxial stellar systems following the $r^{1/n}$ luminosity law: an analytical mass-density expression, gravitational torques and the bulge/disc interplay." In: *MNRAS* 333.3, pp. 510–516. DOI: 10.1046/j.1365-8711.2002.05367.x. eprint: astro-ph/0201485.

VandenBerg, Don A. et al. (Oct. 2013). "The Ages of 55 Globular Clusters as Determined Using an Improved ΔV_{TO}^{HB} Method along with Color-Magnitude

Diagram Constraints, and Their Implications for Broader Issues." In: *Astrophysical Journal* 775.2, 134, p. 134. DOI: 10.1088/0004-637X/775/2/134. eprint: 1308.2257.

Vasiliev, Eugene (Jan. 2019a). "AGAMA: action-based galaxy modelling architecture." In: *MNRAS* 482.2, pp. 1525–1544. DOI: 10.1093/mnras/sty2672. eprint: 1802.08239.

Vasiliev, Eugene (Apr. 2019b). "Proper motions and dynamics of the Milky Way globular cluster system from Gaia DR2." In: *MNRAS* 484.2, pp. 2832–2850. DOI: 10.1093/mnras/stz171. eprint: 1807.09775.

Vasiliev, Eugene (Oct. 2019c). "Systematic errors in Gaia DR2 astrometry and their impact on measurements of internal kinematics of star clusters." In: *MNRAS* 489.1, pp. 623–640. DOI: 10.1093/mnras/stz2100. eprint: 1811.05345.

Vasiliev, Eugene and Holger Baumgardt (Aug. 2021). "Gaia EDR3 view on galactic globular clusters." In: *MNRAS* 505.4, pp. 5978–6002. DOI: 10.1093/mnras/stab1475. eprint: 2102.09568.

Vesperini, Enrico et al. (Mar. 2013). "Dynamical evolution and spatial mixing of multiple population globular clusters." In: *MNRAS* 429.3, pp. 1913–1921. DOI: 10.1093/mnras/sts434. eprint: 1212.2651.

Vitral, Eduardo (June 2021). "BALRoGO: Bayesian Astrometric Likelihood Recovery of Galactic Objects - Global properties of over one hundred globular clusters with Gaia EDR3." In: *MNRAS* 504.1, pp. 1355–1369. DOI: 10.1093/mnras/stab947. eprint: 2102.04841.

Vitral, Eduardo and Pierre Boldrini (2022). "Properties of globular clusters formed in dark matter mini-halos." In: *arXiv e-prints*, arXiv:2112.01265. eprint: 2112.01265.

Vitral, Eduardo and Gary A. Mamon (Mar. 2020). "A precise analytical approximation for the deprojection of the Sérsic profile." In: *A&A* 635, A20, A20. DOI: 10.1051/0004-6361/201937202.

Vitral, Eduardo and Gary A. Mamon (Feb. 2021). "Does NGC 6397 contain an intermediate-mass black hole or a more diffuse inner subcluster?" In: *A&A* 646, A63, A63. DOI: 10.1051/0004-6361/202039650. eprint: 2010.05532.

Vitral, Eduardo et al. (July 2022). "Stellar graveyards: clustering of compact objects in globular clusters NGC 3201 and NGC 6397." In: *MNRAS* 514.1, pp. 806–825. DOI: 10.1093/mnras/stac1337. eprint: 2202.01599.

Volonteri, Marta (July 2010). "Formation of supermassive black holes." In: *A&Ar* 18.3, pp. 279–315. DOI: 10.1007/s00159-010-0029-x. eprint: 1003.4404.

Walcher, C. J. et al. (Jan. 2005). "Masses of Star Clusters in the Nuclei of Bulgeless Spiral Galaxies." In: *ApJ* 618.1, pp. 237–246. DOI: 10.1086/425977. arXiv: astro-ph/0409216 [astro-ph].

Walcher, C. J. et al. (Oct. 2006). "Stellar Populations in the Nuclei of Late-Type Spiral Galaxies." In: *ApJ* 649.2, pp. 692–708. DOI: 10.1086/505166. arXiv: astro-ph/0604138 [astro-ph].

Wan, Zhen et al. (Apr. 2021). "The dynamics of the globular cluster NGC 3201 out to the Jacobi radius." In: *MNRAS* 502.3, pp. 4513–4525. DOI: 10.1093/mnras/stab306. eprint: 2102.01472.

Wang, Long et al. (May 2016). "The DRAGON simulations: globular cluster evolution with a million stars." In: *MNRAS* 458.2, pp. 1450–1465.

Watkins, Laura L. et al. (Apr. 2015). "Hubble Space Telescope Proper Motion (HSTPROMO) Catalogs of Galactic Globular Cluster. II. Kinematic Profiles and Maps." In: *Astrophysical Journal* 803.1, 29, p. 29. DOI: 10.1088/0004-637X/803/1/29. eprint: 1502.00005.

Weatherford, Newlin C. et al. (Aug. 2020). "A Dynamical Survey of Stellar-mass Black Holes in 50 Milky Way Globular Clusters." In: *Astrophysical Journal* 898.2, 162, p. 162. DOI: 10.3847/1538-4357/ab9f98. eprint: 1911.09125.

Webbink, R. F. (Feb. 1984). "Double white dwarfs as progenitors of R Coronae Borealis stars and type I supernovae." In: *Astrophysical Journal* 277, pp. 355–360. DOI: 10.1086/161701.

Webbink, R. F. (Jan. 1985). "Structure parameters of galactic globular clusters." In: *Dynamics of Star Clusters*. Ed. by J. Goodman and P. Hut. Vol. 113, pp. 541–577.

Wells, H.G. (1898). *The Time Machine*. ISBN: 9781463570644. URL: https://books.google.fr/books?id=xAGAZwEACAAJ.

Widrow, Lawrence M. and John Dubinski (Oct. 2005). "Equilibrium Disk-Bulge-Halo Models for the Milky Way and Andromeda Galaxies." In: *ApJ* 631.2, pp. 838–855. DOI: 10.1086/432710. eprint: astro-ph/0506177.

Wirth, Henriette, Kenji Bekki, and Kohei Hayashi (May 2020). "Formation of massive globular clusters with dark matter and its implication on dark matter annihilation." In: *MNRAS* 496.1, pp. L70–L74. DOI: 10.1093/mnrasl/slaa089. arXiv: 2005.07128 [astro-ph.GA].

Woosley, S. E. (Feb. 2017). "Pulsational Pair-instability Supernovae." In: *Astrophysical Journal* 836.2, 244, p. 244. DOI: 10.3847/1538-4357/836/2/244. arXiv: 1608.08939 [astro-ph.HE].

Wu, Yiming et al. (Dec. 2021). "The Color Gradients of the Globular Cluster Systems in M87 and M49." In: *arXiv e-prints*, arXiv:2112.12334. eprint: 2112.12334.

Zavala, Jesús and Carlos S. Frenk (Sept. 2019). "Dark Matter Haloes and Subhaloes." In: *Galaxies* 7.4, p. 81. DOI: 10.3390/galaxies7040081. eprint: 1907.11775.

Zel'dovich, Ya. B. and I. D. Novikov (Jan. 1966). "The Hypothesis of Cores Retarded during Expansion and the Hot Cosmological Model." In: *Astronomicheskii Zhurnal* 43, p. 758.

Zhang, Shumeng and Dougal Mackey (Nov. 2021). "A search for stellar structures around nine outer halo globular clusters in the Milky Way." In: *arXiv e-prints*, arXiv:2111.09072. eprint: 2111.09072.

Zhao, Hongsheng (Jan. 1996). "Analytical models for galactic nuclei." In: *MNRAS* 278.2, pp. 488–496. DOI: 10.1093/mnras/278.2.488. eprint: astro-ph/9509122.

Zocchi, Alice, Mark Gieles, and Vincent Hénault-Brunet (Feb. 2019). "The effect of stellar-mass black holes on the central kinematics of ω Cen: a cautionary tale for IMBH interpretations." In: *MNRAS* 482.4, pp. 4713–4725. DOI: 10.1093/mnras/sty1508. eprint: 1806.02157.

Zwicky, F. (Jan. 1933). "Die Rotverschiebung von extragalaktischen Nebeln." In: *Helvetica Physica Acta* 6, pp. 110–127.

Zwicky, F. (Oct. 1937). "On the Masses of Nebulae and of Clusters of Nebulae." In: *ApJ* 86, p. 217. DOI: 10.1086/143864.

de Vaucouleurs, G. (Jan. 1948). "Recherches sur les Nebuleuses Extragalactiques." In: *Annales d'Astrophysique* 11, pp. 247–287.

den Brok, Mark et al. (Feb. 2014). "The central mass and mass-to-light profile of the Galactic globular cluster M15." In: *MNRAS* 438.1, pp. 487–493. DOI: 10.1093/mnras/stt2221. eprint: 1311.3303.

van de Ven, G. et al. (Jan. 2006). "The dynamical distance and intrinsic structure of the globular cluster ω Centauri." In: *A&A* 445.2, pp. 513–543. DOI: 10.1051/0004-6361:20053061. eprint: astro-ph/0509228.

van de Ven, Glenn and Arjen van der Wel (June 2021). "Deprojecting Sérsic Profiles for Arbitrary Triaxial Shapes: Robust Measures of Intrinsic and Projected Galaxy Sizes." In: *ApJ* 914.1, 45, p. 45. DOI: 10.3847/1538-4357/abf047. eprint: 2104.01810.

van den Bergh, Sidney (May 2008). "The Flattening of Globular Clusters." In: *Astronomical Journal* 135.5, pp. 1731–1737. DOI: 10.1088/0004-6256/135/5/1731. eprint: 0802.4061.

van der Marel, R. P. (Sept. 1994). "Velocity profiles of galaxies with claimed black holes - III. Observations and models for M 87." In: *MNRAS* 270, pp. 271–297. DOI: 10.1093/mnras/270.2.271.

van der Marel, Roeland P. and Jay Anderson (Feb. 2010). "New Limits on an Intermediate-Mass Black Hole in Omega Centauri. II. Dynamical Models." In: *Astrophysical Journal* 710.2, pp. 1063–1088. DOI: 10.1088/0004-637X/710/2/1063. eprint: 0905.0638.

COLOPHON

This document was typeset using the typographical look-and-feel `classicthesis` developed by André Miede. The style was inspired by Robert Bringhurst's seminal book on typography "*The Elements of Typographic Style*". `classicthesis` is available for both LaTeX and LyX:

https://bitbucket.org/amiede/classicthesis/

Happy users of `classicthesis` usually send a real postcard to the author, a collection of postcards received so far is featured here:

http://postcards.miede.de/

Final Version as of September 14, 2022 (`classicthesis` version 4.2).